

© 2015 by Julia A. Plews. All rights reserved.

MULTISCALE ANALYSIS OF LOCALIZED, NONLINEAR, THREE-DIMENSIONAL
THERMO-STRUCTURAL EFFECTS

BY

JULIA A. PLEWS

DISSERTATION

Submitted in partial fulfillment of the requirements
for the degree of Doctor of Philosophy in Civil Engineering
in the Graduate College of the
University of Illinois at Urbana-Champaign, 2015

Urbana, Illinois

Doctoral Committee:

Professor C. Armando Duarte, Chair and Director of Research
Doctor Thomas G. Eason III, U.S. Air Force Research Laboratory
Professor Arif Masud
Associate Professor Luke Olson

Abstract

There are a wide range of computational modeling challenges associated with structures subjected to sharp, local heating effects. Problems of this nature are prevalent in diverse engineering applications such as structural analysis of hypersonic flight vehicles in extreme environments, computational modeling of weld processes, and development of semiconductor processing technology. Complex temperature gradients in the materials cause three-dimensional, localized, intense thermomechanical stress/strain variation and residual deformations, making multiphysics analysis necessary to accurately predict structural response. Localized damage or deformation may impact global structural behavior, yet bridging spatial scales between local- and structural-scale response is a nontrivial task. Because of these issues, standard finite element analysis techniques lead to cumbersome and prohibitively expensive numerical simulations for this class of problems.

This study proposes a Generalized or eXtended Finite Element Method (G/XFEM) for analyzing three-dimensional solid, coupled physics problems exhibiting localized heating and thermomechanical effects. The method is based on the GFEM with global–local enrichment functions (GFEM^{gl}), which involves the solution of interdependent coarse- (global) and fine-scale (local) problems. The global problem captures coarse-scale behavior, while local problems resolve sharp solution features in regions where fine-scale phenomena may govern the overall structural response. To address the intrinsic coupling of scales, local solution information is embedded in the global solution space via a partition of unity approach. This method extends the capabilities of traditional *hp*-adaptive FEM or GFEM—consisting of heavy mesh refinement (*h*) and local high-order polynomial approximations (*p*)—to one-way coupled thermo-structural problems, providing meshing flexibility while remaining accurate and efficient. Linear thermoelasticity and nonlinear thermoplasticity problems are considered, involving both steady-state and transient heating effects.

The GFEM^{gl} is further extended to capture multiscale thermal and thermomechanical effects induced by material-scale heterogeneity, which may also impact structural behavior at the coarse scale. Due to the extraordinary level of fidelity required to resolve fine-scale effects at the global scale, strategies for distributing large workloads on a parallel computer and improving the computational efficiency of the proposed method are needed. Studies have shown that the GFEM^{gl} benefits from straightforward parallelism. However, inexact, coarse-scale boundary conditions on fine-scale may lead to large errors in global solutions. Traditional strategies aimed at improving or otherwise lessening the effect

of poor local boundary conditions in the GFEM^{gl} may be impractically expensive in the problems of interest, such as transient or nonlinear simulations involving many time or load steps. Thus, inexpensive and optimized approaches for improving boundary conditions on local problems in both linear and nonlinear problems are identified.

The performance of the method is assessed on representative, large-scale, nonlinear, coupled thermo-structural problems exhibiting phenomena spanning global (structural) and local (component or even material) scales.

Acknowledgments

I would like to begin by thanking my committee members, and especially my advisor, Professor Armando Duarte, for his continuous support and valuable guidance during my graduate studies. His inspirational dedication to high-quality, pragmatic research and passion for developing excellent computational tools played no small part in the completion of this dissertation.

I greatly appreciate the continued financial support I have received from the Collaborative Center in Structural Sciences (C²S²) at the Ohio State University and the former Midwest Structural Sciences Center (MSSC) at the University of Illinois, supported by the U.S. Air Force Research Laboratory (AFRL) at Wright-Patterson Air Force Base. I would also like to thank my committee member and collaborator, Doctor Tom Eason, as well as Doctor Ravi Chona of AFRL for their similarly unwavering support and helpful suggestions during my research efforts. I am grateful to my collaborator and former colleague Doctor Pat O'Hara, also at AFRL, not only for his fruitful advice and discussions, but also for the contributions of his dissertation, which have provided a strong foundation for my research. I would thus also like to acknowledge my colleague Haoyang Li and Professor Dae-Jin Kim, whose contributions were similarly crucial to this research.

Thanks also go to my friends and colleagues during my Ph.D. studies, especially Varun Gupta, Mark Messner, and Tim Truster, for their openness to questions, discussions, complaints, etc., which led to many memorable conversations and made graduate school a positive experience. I would be remiss to fail to mention my fellow hockey players and numerous friends who have made the University of Illinois and Champaign-Urbana a wonderful place to call home. A special thanks to Dan and Jeni Hoeflinger for their friendship and generosity.

Finally, I would like to express my gratitude to my family: to my parents, for their patience and support, and for always granting me freedom in my pursuits, and to my brother.

Table of Contents

List of Tables	vii
List of Figures	ix
Chapter 1 Introduction	1
1.1 Background	1
1.1.1 Thermo-structural modeling of hypersonic flight vehicles	2
1.1.2 Computational welding mechanics	3
1.1.3 Modeling of material-scale thermomechanical effects	3
1.2 Available approaches	4
1.2.1 Multiscale methods	5
1.2.2 Coupled physics and multiscale approaches to coupled physics problems	7
1.3 Research objectives	8
1.4 Outline	10
Chapter 2 A GFEM approach for capturing localized thermomechanical effects	11
2.1 Problem definition	12
2.1.1 Steady-state heat transfer	12
2.1.2 Thermoelasticity	12
2.2 GFEM approximations	13
2.2.1 GFEM ^{gl}	16
2.3 GFEM ^{gl} formulation for coupled heat transfer and thermoelasticity	17
2.3.1 Steady-state heat transfer	18
2.3.2 Thermoelasticity	21
2.4 A coupled physics framework for efficient thermomechanical analysis	25
2.4.1 Current approaches and limitations	25
2.4.2 GFEM coupling	25
2.4.3 GFEM ^{gl} coupling	26
2.4.4 Coupling implementation	26
2.5 Numerical examples	26
2.5.1 L-shaped domain	26
2.5.2 Laser-heated beam	27
2.5.3 Laser-heated stiffened panel	33
2.6 Summary	36
Chapter 3 A GFEM for resolving fine-scale material heterogeneity	37
3.1 Scale-bridging with GFEM ^{gl}	38
3.1.1 GFEM ^{gl} with sub-local domains	38
3.1.2 Parallelization of sub-local computations	39
3.1.3 Numerical integration of weak form	40
3.1.4 Multiscale effects on sub-local boundaries	41
3.1.5 Improvement of boundary conditions on sub-local problems	41

3.2	Numerical examples	43
3.2.1	Homogeneous laser-heated beam	43
3.2.2	Square domain with material microstructure	45
3.2.3	Laser-heated beam with material heterogeneity	56
3.2.4	L-shaped domain	61
3.2.5	Heterogeneous beam under thermomechanical bending	67
3.3	Summary	68
Chapter 4 GFEM^{gl} for nonlinear thermomechanical problems with time-dependent behavior		71
4.1	Problem definition	72
4.1.1	Transient heat transfer	72
4.1.2	Thermoplasticity	73
4.2	GFEM ^{gl} formulation for coupled transient heat transfer and thermoplasticity	75
4.2.1	GFEM ^{gl} for general time-dependent problems	75
4.2.2	Transient heat transfer	75
4.2.3	Nonlinear thermoplasticity	79
4.3	Numerical examples	90
4.3.1	Bi-material bar with confined plastic region	91
4.3.2	Thermo-elasto-plastic laser-heated beam	98
4.3.3	Heterogeneous thermo-elasto-plastic beam	112
4.3.4	Hat-stiffened panel	115
4.4	Summary	128
Chapter 5 Contributions and prospects for future work		129
5.1	Contributions	129
5.2	Future directions	130
5.2.1	Improved physics	130
5.2.2	Multiple spatial scales	131
5.2.3	Efficient linear solvers	132
5.2.4	Integration with practical analysis tools	132
Appendix A Thermomechanical coupling implementation for GFEM		134
A.1	<i>hp</i> -GFEM coupling	134
A.2	GFEM ^{gl} coupling	135
A.2.1	Global thermo-structural problems	136
A.2.2	Local thermo-structural problems	136
Appendix B GFEM^{gl} parallel improvements		140
B.1	Sub-local problem boundary condition computation	140
B.1.1	Boundary conditions from coarse-scale solution	140
B.1.2	Boundary conditions from enriched global solution	142
B.1.3	Numerical example: transient heat transfer	142
B.2	Parallel assembly	148
B.2.1	Tetrahedral mesh	149
B.2.2	Hexahedral mesh	150
B.2.3	Element coloring scheme performance	153
Appendix C GFEM^{gl} nonlinear solution algorithms for time-dependent shape functions		154
References		158

List of Tables

2.1	Comparison of global and pointwise thermoelasticity quantities under each method for the laser-heated beam.	31
2.2	Comparison of degrees of freedom (dofs) used in each method for the laser-heated beam.	32
2.3	Comparison of physics coupling methods for assembly of the laser-heated beam thermoelasticity problem	32
2.4	Wall times (in seconds) in each solution phase for all load cases in the stiffened panel problem.	36
3.1	Sub-local problem details from GFEM ^{gl} analyses of the laser-heated beam problem.	43
3.2	Comparison of GFEM ^{gl} solution of the bi-material unit cell with adaptive GFEM DFEA for verification (heat transfer only).	49
3.3	Parallel local problem assembly wall times for each global–local iteration of the 2×2 square example.	53
3.4	Comparison of actual times to solution for the large square domain using GFEM ^{gl} and DFEA.	55
3.5	Laser-heated beam with material heterogeneous material problem size details.	57
3.6	Comparison of L-shaped domain solutions from various boundary conditions on the local problem(s).	62
3.7	L-shaped domain GFEM ^{gl} sub-local problem sizes.	65
3.8	Memory usage in L-shaped domain solutions using the GFEM ^{gl} for various numbers of sub-local problems.	65
3.9	Comparison of L-shaped domain solutions using the GFEM ^{gl} for various numbers of sub-local problems.	65
3.10	Comparison of GFEM ^{gl} parallel performance in L-shaped domain solutions with various numbers of sub-local problems.	66
3.11	Thermoelasticity problem size details in degrees of freedom (dofs) for the heterogeneous beam.	67
3.12	Wall times for each GFEM ^{gl} thermoelasticity solution phase for the heterogeneous thermomechanical beam.	68
4.1	Classical rate-independent J_2 flow theory.	74
4.2	Comparison of maximum axial displacements u_y^{\max} obtained from GFEM ^{gl} solutions of the bi-material bar, relative to the <i>hp</i> -GFEM reference.	95
4.3	Comparison of Newton-Raphson iterations required for convergence of the GFEM ^{gl} global bi-material bar problem, relative to the <i>hp</i> -GFEM reference	96
4.4	Comparison of Newton-Raphson iterations required for convergence of the GFEM ^{gl} local bi-material bar problem, relative to the <i>hp</i> -GFEM reference.	97
4.5	Thermo-elasto-plastic laser-heated beam material properties.	98
4.6	Wall time spent assembling/solving the global nonlinear laser-heated beam problem (moving flux) at $t = 0.75$; GFEM ^{gl} vs. <i>hp</i> -GFEM reference.	110
4.7	Thermo-elasto-plastic heterogeneous beam material properties.	112
4.8	Thermoplasticity problem size details in degrees of freedom (dofs) for the heterogeneous beam.	112
4.9	Comparison of GFEM ^{gl} solution of the heterogeneous thermo-elasto-plastic beam to the equivalent <i>hp</i> -GFEM DFEA.	113
4.10	Comparison of wall times of <i>hp</i> -GFEM DFEA and each GFEM ^{gl} thermoplasticity solution phase for the heterogeneous thermomechanical beam.	113

4.11	Newton-Raphson iterations required to solve the heterogeneous thermo-elasto-plastic beam problem with each method.	113
4.12	Comparison of wall times for assembly of the global heterogeneous thermo-elasto-plastic beam thermoplasticity problem in both GFEM ^{gl} and <i>hp</i> -GFEM DFEA on 24 CPUs.	115
4.13	Hat-stiffened panel material properties.	116
4.14	Hat-stiffened panel sharp flux locations.	118
4.15	Hat-stiffened panel GFEM ^{gl} problem size details in degrees of freedom (dofs).	120
4.16	Wall times required for GFEM ^{gl} simulation of the hat-stiffened panel problem; sharp flux in Region A.	122
B.1	Comparison of parallel efficiency of <i>hp</i> -GFEM and GFEM ^{gl} transient heat transfer solutions of the laser-heated beam.	147

List of Figures

1.1	Illustration of shock wave interaction on a hypersonic leading edge.	2
1.2	Temperatures on the skin of a NASA concept hypersonic vehicle.	3
1.3	Typical distribution of plastic regions in a laser welding process.	4
2.1	Construction of a GFEM shape function.	14
2.2	Typical single-physics coarse-scale global domain and refined local problem	17
2.3	The GFEM ^{gl} for sequentially-coupled thermo-structural problems	19
2.4	Geometry and <i>hp</i> -GFEM mesh of the L-shaped domain.	27
2.5	<i>hp</i> -GFEM solutions of a thermoelastic L-shaped domain.	28
2.6	Gaussian laser flux applied to the surface of the laser-heated beam.	29
2.7	Meshes used to solve the laser-heated beam problem with the GFEM ^{gl}	30
2.8	<i>hp</i> -GFEM mesh of the laser-heated beam problem.	30
2.9	GFEM ^{gl} and <i>hp</i> -GFEM DFEA solution contours of the laser-heated beam problem.	31
2.10	Enriched global thermoelasticity assembly time of brute force versus optimized coupling methods at various global-to-local mesh size ratios (H/h) for the laser-heated beam.	33
2.11	Critical loading locations on the stiffened panel.	34
2.12	GFEM ^{gl} solution contours of von Mises stress in the stiffened panel problem.	35
3.1	Coarse global mesh and four sample sub-local domains	39
3.2	Global mesh and overlapping patches ω_1 and ω_2 used to generate sub-local problems.	40
3.3	Laser-heated beam GFEM ^{gl} solution contours using sub-local problems at various global mesh refinement levels.	44
3.4	Laser-heated beam von Mises stress field under the sharp heating.	45
3.5	Convergence of relative difference in the energy norm of laser-heated beam GFEM ^{gl} solutions at various global mesh sizes H after global–local iterations.	46
3.6	Pointwise convergence of maximum von Mises stress in laser-heated beam GFEM ^{gl} solutions at various global mesh sizes H after global–local iterations.	47
3.7	Geometry of the square unit cell domain with bi-material microstructure.	48
3.8	GFEM meshes used to solve the 1×1 cell with each method.	48
3.9	Convergence of relative error in the energy norm of GFEM ^{gl} heat transfer solutions of the 2×2 square domain after global–local iterations.	50
3.10	Enriched global flux magnitude contours of the 2×2 square example.	51
3.11	Convergence of relative error in the energy norm of GFEM ^{gl} thermoelasticity solutions of the 2×2 square domain after global–local iterations.	52
3.12	GFEM ^{gl} von Mises stress contours after three global–local iterations on the 2×2 square problem.	52
3.13	Geometry of the largest (4×4) square domain with bi-material microstructure.	54
3.14	Coarse, global GFEM ^{gl} mesh used to solve the largest (4×4) square domain example.	54
3.15	Vertical temperature profile in the 4×4 square domain.	55
3.16	Heterogeneous laser-heated beam geometry in a localized region surrounding the sharp laser heating.	56
3.17	GFEM ^{gl} reference solution contours from the laser-heated beam with material heterogeneity.	57

3.18	Laser-heated beam with material heterogeneity solution contours from GFEM ^{gl} at various global mesh refinement levels.	58
3.19	Convergence of relative error in the energy norm of heterogeneous laser-heated beam GFEM ^{gl} solutions at various global mesh refinement levels H after global–local iterations.	60
3.20	Pointwise convergence of von Mises stress in the heterogeneous laser-heated beam from GFEM ^{gl} solutions at various global mesh refinement levels H after global–local iterations.	61
3.21	Geometry of the L-shaped domain with bi-material microstructure near the reentrant inner corner.	62
3.22	Coarse global mesh and a sub-local domain used to generate GFEM ^{gl} enrichment functions for the L-shaped domain example.	63
3.23	L-shaped domain temperature profile approaching the reentrant corner at $x = 50$	63
3.24	Magnitude of heat flux singularity at the reentrant inner corner of the L-shaped domain.	64
3.25	Temperature profile in L-shaped domain approaching the reentrant corner at $x = 50$	66
3.26	Mesh and thermomechanical boundary conditions on the heterogeneous beam.	67
3.27	Heterogeneous beam solution contours from GFEM ^{gl} simulations.	69
4.1	The GFEM ^{gl} for time-dependent thermo-structural problems	76
4.2	Nonlinear stress–strain relationships for, e.g., nonlinear elastic or elasto-plastic materials.	80
4.3	Geometry and boundary conditions of the elasto-plastic bi-material bar.	91
4.4	hp -GFEM mesh of the bi-material bar problem.	91
4.5	Meshes used to solve the bi-material bar problem with the GFEM ^{gl}	92
4.6	Contours of residual axial stress σ_{yy} in the bi-material bar problem from GFEM ^{gl} and hp -GFEM solutions at the final load step.	93
4.7	GFEM ^{gl} load–displacement curve of the bi-material bar problem based on incremental enrichments, compared to hp -GFEM.	94
4.8	GFEM ^{gl} load–displacement curve of the bi-material bar problem based on total enrichments, compared to hp -GFEM.	94
4.9	GFEM ^{gl} load–displacement curve of the bi-material bar problem based on global–local enrichments computed from the ultimate load step, $\lambda = \lambda_{\max} = 1.0$, compared to hp -GFEM.	95
4.10	Time evolution of the maximum magnitude (at $x = 9.3$) of the stationary laser flux applied to the thermo-elasto-plastic laser-heated beam.	99
4.11	hp -GFEM mesh of the thermo-elasto-plastic beam subjected to stationary laser heating.	100
4.12	Meshes used to solve the thermo-elasto-plastic laser-heated problem with the GFEM ^{gl} (stationary heating).	100
4.13	Contours of maximum temperature and axial stress in the thermo-elasto-plastic laser-heated beam problem from GFEM ^{gl} and hp -GFEM solutions.	101
4.14	Contours of axial displacement u_x at the maximum temperature load step in the thermo-elasto-plastic laser-heated beam problem from GFEM ^{gl} local (top) and corresponding enriched global (bottom) solutions with different choices of local boundary conditions.	102
4.15	Pointwise maximum temperature and von Mises stress along the central axis ($y = 0.25, z = 0.22$) of the thermo-elasto-plastic laser-heated beam from the hp -GFEM reference and GFEM ^{gl} solutions with time-dependent shape functions.	103
4.16	Pointwise maximum temperature and von Mises stress along the central axis ($y = 0.25, z = 0.22$) of the thermo-elasto-plastic laser-heated beam from the hp -GFEM reference and GFEM ^{gl} solutions with <i>time-independent</i> shape functions.	104
4.17	Residual deformed configurations of the thermo-elasto-plastic laser-heated beam from hp -GFEM and GFEM ^{gl} solutions.	105
4.18	Pointwise residual displacements, after cooling to room temperature, of the thermo-elasto-plastic laser-heated beam from the hp -GFEM reference and GFEM ^{gl} solutions with time-dependent shape functions.	106
4.19	Pointwise residual displacements, after cooling to room temperature, of the thermo-elasto-plastic laser-heated beam from the hp -GFEM reference and a GFEM ^{gl} solution with <i>time-independent</i> shape functions.	107

4.20	Time evolution of the maximum magnitude (at $x = 9.25 + 0.125t$) of the moving laser flux applied to the thermo-elasto-plastic laser-heated beam.	108
4.21	hp -GFEM mesh of the thermo-elasto-plastic beam subjected to moving laser heating.	108
4.22	Meshes used to solve the thermo-elasto-plastic laser-heated problem with the GFEM ^{gl} (moving heat flux).	109
4.23	Temperature profiles along the central axis of the thermo-elasto-plastic laser-heated beam subjected to a transient, moving laser flux at various times t	110
4.24	Axial stress profiles along the central axis of the thermo-elasto-plastic laser-heated beam subjected to a transient, moving laser flux at various times t	111
4.25	Contours of equivalent plastic strain $\bar{\epsilon}^p$ at the final time/load step for the thermo-elasto-plastic laser-heated beam subjected to a moving laser heating.	111
4.26	Heterogeneous thermo-elasto-plastic beam von Mises stress contours from GFEM ^{gl} simulations.	114
4.27	Geometry of the hat-stiffened panel problem. Overall size of the panel in-plane is 10.0×7.5	116
4.28	Time variation of peak flux intensity (i.e., at $x = b$, $z_{min} \leq z \leq z_{max}$) applied to the hat-stiffened panel problem in each local region of interest.	117
4.29	Global hexahedral mesh and local problem regions in the hat-stiffened panel problem	118
4.30	Tetrahedral local problem meshes used in each sharp flux case for the hat-stiffened panel problem.	119
4.31	Cutaway view of typical tetrahedral local problem meshes used in regions with spot welds in the hat-stiffened panel problem.	119
4.32	GFEM ^{gl} global temperature contours at the maximum heat flux ($t = 2.5$) in the hat-stiffened panel problem.	121
4.33	Strain energy and internal heat energy in the hat-stiffened panel problem, GFEM ^{gl} vs. coarse scale hexahedral mesh.	122
4.34	Von Mises stress contours in the panel at maximum load ($t = 2.5$) and final ($t = 25.0$) time steps from GFEM ^{gl} and coarse global simulations of the hat-stiffened panel problem; sharp flux in Region A.	123
4.35	Von Mises stress contours in the panel at maximum load ($t = 2.5$) and final ($t = 25.0$) time steps from GFEM ^{gl} and coarse global simulations of the hat-stiffened panel problem; sharp flux in Region B.	124
4.36	Cutaway view of von Mises stress contours in the stiffeners at maximum load ($t = 2.5$) from GFEM ^{gl} and coarse global simulations of the hat-stiffened panel problem; sharp flux in Region A.	124
4.37	Cutaway view of von Mises stress contours in the stiffeners at maximum load ($t = 2.5$) from GFEM ^{gl} and coarse global simulations of the hat-stiffened panel problem; sharp flux in Region B.	125
4.38	GFEM ^{gl} parallel speedup in the steady-state hat-stiffened panel problem, relative to a serial GFEM ^{gl} simulation.	126
4.39	Parallel vs. serial solution wall times spent in each solution phase in the steady-state hat-stiffened panel problem.	127
A.1	Algorithm showing communication between physics problems in the hp -GFEM case.	135
A.2	Algorithm showing communication between GFEM ^{gl} global thermo-structural problem and global heat transfer problems.	137
A.3	Algorithm showing communication between GFEM ^{gl} local thermo-structural problems and the global heat transfer problem.	138
B.1	Coarse-scale computation of boundary conditions on sub-local problems <i>without</i> global–local enrichment functions in the global problem.	141
B.2	Local problem descendant relationships for optimized computation of boundary conditions on sub-local problems <i>with</i> global–local enrichment functions in the global problem.	143
B.3	Fine-scale, master descendant mesh.	144
B.4	Internal energies of GFEM ^{gl} and hp -GFEM transient heat transfer solutions of the laser-heated beam.	145
B.5	Cumulative wall time required for transient heat transfer simulation of the laser-heated beam, brute force computation of local problem boundary conditions.	146
B.6	Cumulative wall time required for assembly of local problems in GFEM ^{gl} transient heat transfer simulations of the laser-heated beam.	146
B.7	Cumulative wall time required for transient heat transfer simulation of the laser-heated beam, optimized computation of local problem boundary conditions.	147

B.8	Comparison of wall times for transient heat transfer simulations of the laser-heated beam with and without storage of (sub-)local problem factorizations.	148
B.9	Different OpenMP parallel assembly strategies considered: atomic updating (<code>atomic</code>) versus critical region (<code>critical</code>), from [57].	149
B.10	Simple parallel assembly benchmark problem; a 4-node tetrahedral mesh of a linear elastic domain under uniform tension.	149
B.11	Speedup in parallel assembly for the benchmark problem with 4-node tetrahedral elements for various global polynomial orders of the approximation.	151
B.12	Simple parallel assembly benchmark problem; an 8-node hexahedral mesh of a linear elastic domain under uniform tension.	152
B.13	Speedup in parallel assembly for the benchmark problem with 8-node hexahedral elements.	152
B.14	Comparison of the number of elements per color in each mesh considered for the benchmark problem.	153

Chapter 1

Introduction

1.1 Background

A growing number of problems encountered in engineering practice today require consideration of phenomena encompassing multiple spatial scales of interest. This work considers a current challenge in several engineering disciplines, which is the computational modeling of localized, intense structural heating effects. Rapid variations in thermomechanical stresses can arise from localized, external heat sources, sharp geometrical features in the structure, or material interfaces. Application areas of special interest are thermo-structural modeling of hypersonic aircraft as well as prediction of residual stress fields in laser welding, but problems of this nature also exist in areas such as semiconductor manufacturing technology and composite materials.

Engineering solutions in these application areas first require high-fidelity numerical models which can accurately depict structural response under representative loading scenarios. However, realistic thermal and mechanical loadings for this class of problems are in general quite complex and potentially difficult to characterize because of extreme variations of physical quantities of interest in both space and time. Effective analysis tools and methods must incorporate multiphysics capabilities to capture interactions between temperature and stress gradients, and simultaneously bridge spatial scales between local and structural-level response.

The *hp*-adaptive version of the finite element method (*hp*-FEM), which controls solution quality through mesh refinement (*h*) and high-order polynomial enrichment (*p*), has been identified as optimal for problems of interest [108, 126]. Commercial finite element analysis (FEA) software packages are commonly used for traditional design practice in the engineering areas of interest. Unfortunately, performing *hp*-adaptivity in available FEA software is often prohibitively difficult or, in many cases, even impossible. Additionally, treatment of sharp, localized thermal loads requires special attention; if these loadings are applied on meshes designed to capture only the global response of the structure, the error of the finite element solution may be large even far away from the localized features due to well-known pollution error [3, 90]. Finite element models may also be very large in order to accurately represent structural geometry, making further adaptive global mesh refinement too expensive. Complications arise in *transient* regimes, where solution reliability can be very sensitive to global remeshing, and localized refinement may necessitate

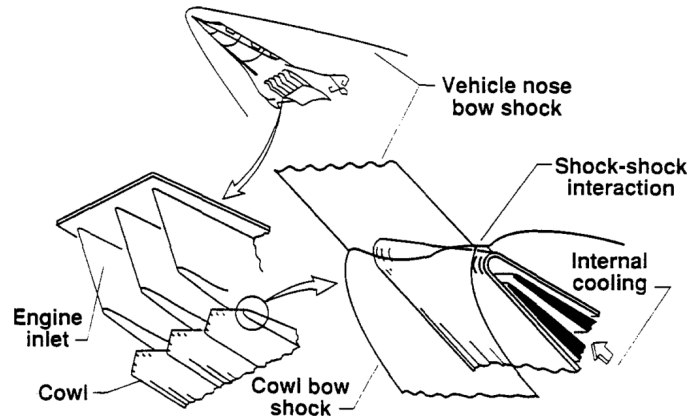


Figure 1.1: Illustration of shock wave interaction on a hypersonic leading edge, from [102].

prohibitively small time steps, bottlenecking solution time. Localized thermal gradients may also induce *nonlinear*, *elasto-plastic* behavior in the material. Although plasticity may be confined to just a small region, the global structural model must be treated as nonlinear, and multiple computationally expensive nonlinear solution iterations—involving reassembly and refactorization of the resulting linearized global system of equations—are typically necessary under *hp*-adaptive methods. *hp*-adaptive remeshing in nonlinear analyses with history-dependent materials presents another challenge, since material state variables and three-dimensional solutions must be transferred from one mesh to the next in time for convergence of the nonlinear solution scheme [67, 95, 104].

1.1.1 Thermo-structural modeling of hypersonic flight vehicles

One example of particular interest, which is a large part of the motivation behind this work, lies in the structural analysis of hypersonic flight vehicles. At very high airspeeds, rapid variations in the density and temperature of the compressible flow lead to shock wave impingements on the skin of the vehicle. Interactions between shock waves, as illustrated in Figure 1.1, typically occur most severely on leading edges and have been shown to lead to very intense, localized temperature gradients and pressure loadings. An example of the intense nature of the temperature fields experienced by hypersonic air vehicles is depicted in Figure 1.2, which shows results from a NASA concept hypersonic vehicle at Mach 8.0. Characterization of these complicated aerodynamic effects itself has been an active research topic [16, 41, 42, 87, 131, 137, 138]. A comprehensive, historical overview of the challenges posed by aero-thermomechanical effects in hypersonic structures and their importance can be found in [127].

Based on experimental investigations, intense, localized heat fluxes may be concentrated on an area just microns in width—that is, many orders of magnitude smaller than the structure. However, the sharp thermomechanical gradients have been known to cause localized failures and instabilities, thereby drastically impacting the global behavior of the structural system; thus, the two disparate spatial scales may not, in general, be considered separately. It has also

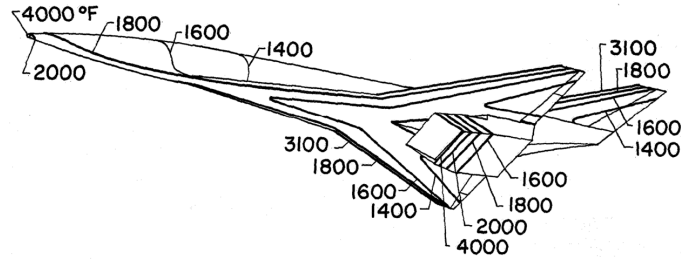


Figure 1.2: Temperatures on the skin of a NASA concept hypersonic vehicle flight at Mach 8.0, from [53].

been shown that aerodynamic heating on hypersonic vehicles may reach such extreme levels that thermomechanical properties of the structural materials are significantly altered, and in some cases viscoplastic behavior can be observed [101, 102, 128, 129]. Thus, many additional modeling challenges are presented by the highly nonlinear behavior of the structure.

1.1.2 Computational welding mechanics

Computational modeling of laser welding processes is another interesting and challenging potential application of the work presented herein. Residual stress prediction is critical in determining the fatigue life of welded structures, and the very localized nature of welding heat sources necessitates a multiphysics analysis coupling heat transfer and thermomechanical response.

Furthermore, extreme temperature gradients near the heat source cause complex, highly nonlinear thermo-viscoplastic behavior in the material [12, 85]. Adding to this challenge is a phase change in the material directly under the laser heating, leading to a so-called ‘keyhole,’ which is yet another example of a localized, nonlinear, rapidly evolving phenomenon that may potentially govern the overall behavior of the welded structure [69]. Figure 1.3 shows typical plastic regions in a specimen undergoing laser welding.

In practice, as in the case of hypersonic vehicles, quasistatic analysis is usually considered to be sufficient [69]; however, fast-moving heat sources lead to highly transient heat transfer phenomena. Recent examples of computational modeling efforts include work by Moraitis and Labeas [86], Tsirkas et al. [130], and Carmignani et al. [12]. In traditional approaches, heavy finite element mesh refinement along the weld is required to resolve the localized thermal and thermomechanical effects of interest, making transient analysis difficult and extraordinarily expensive. A comprehensive summary of the multiphysics computational modeling challenges inherent in this class of problems is given by Lindgren in [69].

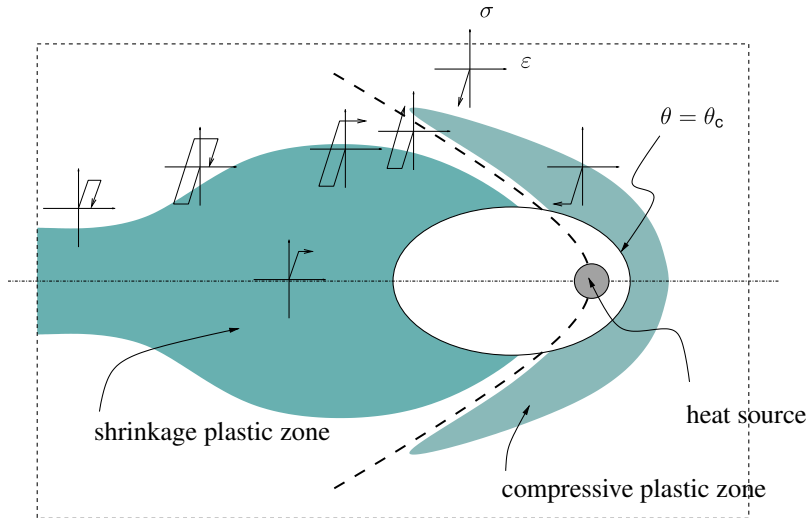


Figure 1.3: Typical distribution of plastic regions in laser welding process, from [85].

1.1.3 Modeling of material-scale thermomechanical effects

In many applications, for instance, in the field of materials science, even smaller physical scales must be considered to obtain an accurate picture of system behavior. Highly localized thermomechanical behavior in structures may often arise in the presence of heterogeneous materials and fine-scale material interfaces due to material property mismatch, which is a very common problem in semiconductor manufacturing [117, 125] and other various composite materials applications [134]. Structural failure is caused by the onset of localized damage at a scale orders of magnitude smaller than the overall structural dimensions, such as delamination, cracking, or shear banding. Fine-scale material characteristics like heterogeneities and inclusions may interact with these localized phenomena, affecting structural behavior and patterns of damage evolution. Material- and structural-level phenomena may be intrinsically coupled, but the fidelity required to capture physics at each scale is extraordinarily expensive under traditional analysis techniques.

1.2 Available approaches

A summary of current methods relevant to the issues examined in this study is loosely broken into three categories:

- (i) methods developed to bridge solution characteristics from fine to structural (or micro to macro) scales, or so-called ‘multiscale’ methods,
- (ii) methods for multiphysics problems and applications related to the localized effects of interest in this study, and
- (iii) methods which incorporate both coupled physics *and* fine-scale features on global, structural-scale problems.

The latter two categories are grouped together in the following sections.

1.2.1 Multiscale methods

A well-known method for capturing localized behavior in structural-scale models is the global–local finite element method [19, 88]. This procedure consists of two basic steps. First, a coarse-scale, global structural analysis is performed. A subdomain containing a feature of interest, such as a fracture, is extracted from the global model, which is then analyzed independently, subject to boundary conditions from the coarse-scale solution. This local solution is taken as a better approximation of the global solution over the local subdomain. However, local solutions can be highly variable in quality as a result of inaccuracies in local boundary conditions from the initial, coarse-scale analysis. Also, local solution characteristics can potentially impact the global behavior of the system, which cannot be considered in the global–local FEM. Iterative improvement of the global–local FEM is proposed in [136]. A similar global–local coupling strategy for capturing localized *nonlinear* behavior is proposed by Gendre et al. [44].

Several superposition-based methods for capturing fine-scale approximations in the neighborhood of localized features on a structural-scale model have been proposed, such as the *s*-version of the FEM proposed by Fish [39] as well as the *hp-d* method of Krause and Rank [112]. In these methods, coarse, structural-scale meshes are used to represent the smooth, global solution behavior (in the *hp-d* method, this is termed the ‘base’ approximation), while localized solution features are captured over heavily refined, fine-scale domains (the ‘overlay’ approximation, in *hp-d* terminology). However, both methods experience several limitations. In order to guarantee C^0 continuity of the solution at the interface between coarse-scale and fine-scale approximations, homogeneous Dirichlet boundary conditions must be applied on the fine-scale boundaries. Furthermore, the global model comprises coarse-scale or base in addition to *all* fine-scale or overlay degrees of freedom, leading to very large systems of equations. The *hp-d* method leverages a block Gauss-Seidel iterative solution scheme to treat the linear system of equations, but convergence issues have been observed in this strategy.

The *hp-d* method has been extended to handle several problems of interest exhibiting localized phenomena. Düster also introduced the idea of incorporating fully three-dimensional effects into two-dimensional structural models (so-called ‘dimensionally reduced modeling’ or DRM) using the *hp-d* method [33, 34]. The goal of this method is to be able to capture structural response in a computationally efficient manner, since three-dimensional finite element models are quite often prohibitively expensive for large-scale, structural problems of interest; however, important localized phenomena generally exhibit fully three-dimensional characteristics, and must be considered in regions of interest. Aspects of the *hp-d* method as well as partition of unity methods [2, 4, 80] are also borrowed in the framework of the Finite Cell Method presented in [58] in order to model material interfaces on non-matching meshes.

The Generalized or eXtended Finite Element Method (GFEM or XFEM) [7, 24, 82, 89, 123], based on the addition of special enrichment functions to the FEM approximation, has also seen extensions to multiscale application. For instance, in [139], a special XFEM enrichment function is adopted for yield line analysis in plates. The primary goal

of the enrichment is to capture high gradient zones (HGZs) within plates, while maintaining C^1 continuity of the solution. Liu et al. [71] have presented an XFEM enrichment strategy for heat transfer problems in composites which exhibit both weak (heat flux) and strong (temperature) discontinuities across internal material interfaces. The GFEM based on concepts of the global–local FEM presented for localized fracture and transient heat transfer applications [23, 26, 90, 91] is a multiscale method which is studied in detail in this work, and is discussed extensively in subsequent chapters of this dissertation.

The Variational Multiscale (VMS) method proposed by Hughes et al. [56] is an example of a method adopting a separation of fine-scale and coarse-scale solution features, in which the fine-scale approximation involves residual-free ‘bubble’ functions. The VMS has been applied to challenging multiphysics problems, as well, such as fluid-structure interaction (FSI) [60].

The Multiscale FEM (MsFEM) of Hou and Wu [54] is a parallelizable technique for predicting macro-scale response without resolving fine-scale effects, often used in porous media applications. The fine-scale is resolved by shape functions obtained from the numerical solution of fine-scale boundary value problems; however, boundary conditions on these problems pose an issue. Efendiev and others [31, 35] have extended this work and attempted to address these challenges. Additional work by Zhang et al. [143] proposes the extended MsFEM (EMsFEM) for modeling heterogeneous materials.

Multigrid and domain decomposition techniques have also seen use in multiscale problems. For instance, multigrid techniques have been applied to finite element problems with localized *hp*-adaptive mesh refinement [6, 55, 81], and the domain decomposition-based FETI-DP method of Farhat et al. [36] has been developed and used for multiscale. However, local nonlinearities may pose a challenge in traditional multigrid and domain decomposition approaches [11, 15]. Pebrel et al. [103] present a domain decomposition technique specifically aimed at problems with nonlinear behavior.

Yet another class of methods, homogenization-based techniques have also been immensely popular tools in the modeling of multiscale problems. De Borst [17] gives a broad overview of the state-of-the-art in computational methods for resolving multiscale features, primarily with application to materials science. It is important to mention the FE^2 and related methods of Feyel, Chaboche, Unger, Özdemir, et al. [37, 38, 99, 100, 133], which derive homogenized macro-scale material properties from the solution of micro-scale boundary value problems at integration points in the macro-scale model. Many additional homogenization approaches are reviewed in Chapter 3. However, homogenized properties cannot adequately characterize fine-scale behavior in the neighborhood of localized solution features such as sharp gradients and singularities; thus, homogenization approaches may not be applicable in the problems of interest in this study, which exhibit very localized temperature and stress/strain gradients.

1.2.2 Coupled physics and multiscale approaches to coupled physics problems

In the application area of laser welding, Montalvo-Urquiza et al. [85] employ an adaptive FEM for transient modeling of the sharp laser flux and resulting thermoplastic effects. By refining and unrefining the three-dimensional finite element mesh over the course of the simulation, the sharp temperature gradients as well as the highly localized, nonlinear effects around the laser heating can be captured effectively. However, adaptive refinement on the structural-scale domain leads to expensive computations at each time step of the laser welding analysis, and the tradeoff between solution quality and computational expense is highly sensitive to the adaptive FEM error estimation scheme. The authors also note that post-welding cooling stages are much simpler to model, since there is no additional adaptivity effort required to track the sharp, rapidly evolving laser heat source. Runnemalm and Hyun [115] similarly apply an adaptive FEM strategy aimed at solving the challenging problem of localized thermo-viscoplastic effects due to laser welding. These authors further note that adaptive methods are complicated by the fact that error estimates must account for localized evolution of both thermal and mechanical behavior. Souloumiac et al. [122] and Duan et al. [21] acknowledge the large computational cost of using a fully three-dimensional model to bridge localized, residual post-welding deformations to the structural scale in order to predict residual global distortions. Instead, they propose a global–local technique based on local three-dimensional approximations in the neighborhood of localized thermomechanical phenomena, while adopting plate or shell elements to model the global structure away from the weld.

A number of multiscale methods have also been extended to coupled physics problems. The previously mentioned VMS [56] has been adapted by Oskay [97, 98], leading to so-called Variational Multiscale Enrichment (VME), the goal of which is accurate resolution of fine-scale effects in regions of interest in multiphysics problems. This method has been applied to the coupled mechano-diffusion problem for modeling the multiscale diffusion of oxygen into titanium, as well as diffusion and elasticity problems featuring material microstructures and inclusions. In VME, the microscale ‘enrichment domains’ coincide with global (macroscale) elements, and in order to enforce continuity of the global solution, in [97], homogeneous boundary conditions must be applied on the microscale problems (leading to the residual-free bubble functions of VMS fame). The sensitivity of VME solutions to microscale boundary conditions is acknowledged in [98], which proposes the use of so-called ‘canopy functions’ to relax the homogeneous Dirichlet requirement, and introduces mixed-type boundary conditions on microscale problems. However, the mixed boundary conditions have been shown to lead to complications in the parallelization of the method. Similarly, building on the MsFEM and the EMsFEM of Zhang et al. previously described, Yang et al. [140] introduce the EMsFEM methodology for nonlinear, coupled thermoelastic problems.

Several methods have been presented in the literature within the framework of the XFEM for addressing challenging localized thermomechanical and other multiphysics effects relevant to this work. The majority of these methods

are based upon analytically defined enrichment functions in order to accurately represent localized solution characteristics on non-matching meshes, which greatly reduces manual effort in finite element mesh generation. Duflot [30] introduces analytical enrichment functions for representing fractures in thermoelasticity, treating (i) the adiabatic crack, where the temperature field in general experiences a jump across the crack surface, and the heat flux exhibits singularities at the crack tip; as well as (ii) the isothermal crack, where the temperature is held constant over the crack surface, and thus Dirichlet boundary conditions must be applied over the crack surface. Each of these cases is analyzed using specially tailored enrichment functions, and localized solution gradients surrounding the discontinuities are effectively resolved. This work is extended by Zamani et al. [142], who adopt similar enrichment strategies, and are especially concerned with the computation of stress intensity factors (SIFs) in thermoelastic fracture mechanics problems of interest. Khoei et al. [59] present an XFEM approach for coupled, time-dependent thermo-hydro-mechanical modeling of porous media exhibiting discontinuities.

Also worth mentioning are several homogenization methods for resolving fine-scale thermomechanical effects. A homogenization technique based on the FE^2 method is proposed for heat transfer in heterogeneous materials by Özdemir et al. in [99]. These authors extend their work on heat transfer to the multiphysics problem of thermomechanical coupling in [100]. It is important to note that the authors assume a scale separation, and thus they also note that the method may not be valid in applications where the macro-scale temperature gradients are extremely sharp and may be significant even at the micro-scale. Macri and Littlefield [76] also present a work based on the multiscale enriched partition of unity method developed in [40, 75] which adopts principles from homogenization theory as well as partition of unity methods to generate special enrichment functions to transfer microscale thermomechanical effects to the macroscale.

1.3 Research objectives

The Generalized or eXtended Finite Element Method (G/XFEM) [7, 24, 82, 89, 123], a traditional finite element formulation augmented with custom-designed enrichment functions to capture specific solution features of interest, is presented in this work as a candidate to alleviate many of the aforementioned difficulties with present approaches to problems of interest. Specifically, this study presents a GFEM aimed at resolving the challenging multiscale, multidisciplinary, nonlinear phenomena within the framework of the GFEM with global–local enrichment functions (GFEM^{gl}) [23, 26]. The GFEM^{gl} hybridizes standard global–local analysis and GFEM; custom shape functions are generated numerically from the solution of hp -adapted GFEM local or fine-scale boundary value problems subject to boundary conditions from a coarse-scale, initial global analysis of the structure. These custom, fine-scale, so-called ‘global–local’ shape functions are embedded in the global approximation space via a partition of unity approach,

thereby enabling localized solution features to be represented on a regular, coarse global mesh. The method has already been shown to provide effective solutions to both steady-state and transient heat transfer problems exhibiting localized, sharp temperature gradients [90–93].

In the scope of this work GFEM and the GFEM^{gl} are extended to handle coupled physics (thermomechanical) problems, which introduces an additional set of challenges due to the special enrichment functions, heavy mesh refinement, and high-order polynomial approximations inherent in typical GFEM simulations. Sharp temperature and stress/strain gradients may be present *within elements* in the GFEM mesh, represented by numerically generated GFEM enrichment functions from fine-scale problems. Thus, typical thermomechanical coupling techniques adopted in the industry, such as transferring interpolated or nodal temperatures to the global structural model, as well as other ad-hoc approaches, are insufficient to accurately resolve the sharp, localized features of interest. Because of the high level of mesh adaptivity, the exchange of information between physics problems may be very expensive. This work presents a novel coupling scheme which takes advantage of special features of the GFEM^{gl} to make multiphysics solutions both feasible and efficient.

The GFEM^{gl} is also adapted for the analysis of localized thermo-structural effects due to material-scale heterogeneity, or multiscale problems. In contrast to many typical multiscale methods, the use of a partition of unity affords this method *no restrictions on inter-compatibility and continuity among micro or local solutions*, which is a primary concern in many existing multiscale techniques. Studies have shown that GFEM^{gl} local problems are intrinsically and rapidly parallelizable [63], which is especially beneficial when intense levels of mesh refinement are required, as is the case in the presence of material-scale heterogeneity. Some analysis of the parallel performance of the method as it is applied to this class of problems is included in the scope of this work. However, the quality of global–local enrichments for this class of problems is sensitive to the accuracy of local problem boundary conditions from coarse-scale, global solutions, especially when hundreds or thousands of local problems are analyzed in parallel; thus, efficient boundary condition improvement strategies are also discussed.

Furthermore, in order to address the nonlinear nature of many problems within the target application areas, the GFEM and GFEM^{gl} are also extended to handle localized thermoplastic effects. The GFEM^{gl} has effectively modeled problems exhibiting confined plastic behavior in [52, 64]. These previous applications focused on structures subjected to uniform, monotonic loading scenarios, where nonlinear behavior is confined to a single region (e.g., around a crack tip or other localized stress concentration) and evolves only moderately and, moreover, proportionally in between time or load steps. In application areas of interest, however, localized thermomechanical loads generally evolve in both time and space. Furthermore, predicting residual stress and strain fields in the material is paramount in determining the damaged state, or, in the case of laser welding, the *initial* state of the structure, so consideration of time-dependent cooling effects is necessary. Leveraging the previously cited work on the GFEM^{gl} for transient heat transfer and

nonlinear applications, this work presents an extension of the GFEM^{gl} to nonlinear, thermoplastic problems utilizing *time-dependent* global–local shape functions to characterize the highly localized thermo-elasto-plastic features of interest on the coarse-scale, global structural problem.

The primary goal these extensions of the GFEM^{gl} is therefore the computational simulation of realistic, industrial-scale multiphysics problems under extreme, localized thermomechanical loading scenarios in a parallel and computationally efficient manner, with particular emphasis on generality and extensibility of the methods presented.

1.4 Outline

In Chapter 2, the extension of the GFEM and GFEM^{gl} to coupled, multidisciplinary problems—in this case, thermo-structural interaction—is presented. This chapter also gives a detailed introduction to the GFEM and GFEM^{gl}. Chapter 3 discusses in detail the modeling of localized thermal and thermomechanical effects due to material-scale heterogeneity using the GFEM^{gl}. Chapter 4 presents the GFEM^{gl} for modeling localized, *nonlinear* elasto-plastic and multiphysics thermoplastic effects as well as residual thermomechanical stresses and strains, considering the effects of time-dependent loading scenarios. Chapters 3 and 4 also provide some discussion on the parallel computing aspects of the GFEM^{gl}, since computational efficiency is extremely important in representative problems, which are generally quite large and expensive to solve when using traditional direct analysis methods to achieve a comparable level of fidelity. Finally, overall conclusions and a proposal of future work is given in Chapter 5.

Chapter 2

A GFEM approach for capturing localized thermomechanical effects

The goal of this work is to provide an efficient means of analyzing thermo-structural interaction problems while maintaining compatibility with the proposed Generalized Finite Element Method (GFEM) approach. The most common solution techniques used in the industry involve decoupling thermal and structural analyses, pre-designing a mesh for each discipline, and often then solving using separate software packages tailored for each physics discipline, for instance, as in [114] for the case of composite structures. The heat transfer problem may generally be discretized with 3D solid finite elements, while the mechanical model may be meshed using more efficient, dimensionally reduced plate or shell finite elements. Interfacing the disparate models is nontrivial, as it requires interpolation or assumptions about variation of the temperature field through the thickness dimension of the plate or shell. However, sharp temperature gradients in the presence of intense heat sources, internal material interfaces, or complicated structural geometry cannot always be adequately characterized by interpolated or smoothed quantities, or analytical polynomial expressions through the thickness. In traditional software packages detailed redesign of each mesh may also be required to accommodate all critical load cases. All of these issues increase both computational and manual effort in exchanging information between and analyzing multiphysics problems.

The GFEM^{gl} [23, 26, 90] is an established method in the modeling of localized heating and structural effects based on the use of enrichment functions generated from the solution of high-fidelity local problems in the global GFEM approximation. This work presents the first extension of the GFEM^{gl} to multiphysics (thermomechanical) problems, as presented in [107]. Because special or numerical-generated enrichment functions are used in GFEM, detailed, localized information about variation of multiphysics solution fields of interest is required within individual elements in the domain, making multiphysics analysis under these methods potentially very expensive. To address this, this chapter presents an optimized approach for exchanging information in the analysis of thermo-structural problems discretized using *hp*-adaptive GFEM (*hp*-GFEM) and, moreover, the GFEM^{gl}, which avoids computational expense related to expensive searching and mapping between physics meshes. Additionally, the approach takes advantage of features of the GFEM^{gl} to enable multiphysics analysis under this method while incurring little to no additional cost compared to single-physics analysis. These extensions of the GFEM to one-way-coupled thermo-structural problems provide meshing flexibility at both local—component- or material-level—and structural scales while remaining

competitive with traditional approaches. Furthermore, the straightforward parallelism of the GFEM^{sl} is exploited to provide efficient, high-fidelity solutions to multiphysics problems of interest. The method is applied to several coupled thermomechanical problems highlighting its potential applications, and its computational benefits are also discussed.

2.1 Problem definition

The problem of interest in this chapter is one-way-coupled, steady-state, linear thermoelasticity in three dimensions, though the approach presented is extensible to other physics as well as transient and nonlinear problems (demonstrated in Chapter 4). The problem is defined over a domain $\Omega \in \mathbb{R}^3$. The formulation is presented in a staggered sense, as is typical of analyses carried out in the target application areas.

2.1.1 Steady-state heat transfer

The steady-state heat transfer problem is defined over a domain $\Omega^\theta \in \mathbb{R}^3$, $\Omega^\theta = \Omega$, with boundary $\partial\Omega^\theta = \Gamma^\theta \cup \Gamma^f \cup \Gamma^c$, where $\Gamma^\theta \cap \Gamma^f = \emptyset$, $\Gamma^\theta \cap \Gamma^c = \emptyset$, and $\Gamma^c \cap \Gamma^f = \emptyset$. Although this is a coupled thermo-structural problem, in the problems of interest, the heating contribution due to mechanical deformation can be neglected [127, 128]. The strong form of the governing partial differential equation is given by

$$\nabla \cdot (\boldsymbol{\kappa} \nabla \theta) = -Q(\mathbf{x}) \quad \text{in } \Omega^\theta, \quad (2.1)$$

where $\theta = \theta(\mathbf{x})$ is the temperature field, $\boldsymbol{\kappa} = \boldsymbol{\kappa}(\mathbf{x})$ the thermal conductivity tensor, and $Q(\mathbf{x})$ the internal heat source.

Boundary conditions on $\partial\Omega^\theta$ are given by

$$\begin{aligned} \theta &= \bar{\theta} \quad \text{on } \Gamma^\theta \\ -\boldsymbol{\kappa} \nabla \theta \cdot \mathbf{n} &= \bar{f} \quad \text{on } \Gamma^f \\ -\boldsymbol{\kappa} \nabla \theta \cdot \mathbf{n} &= h_c(\theta - \theta_\infty) \quad \text{on } \Gamma^c, \end{aligned} \quad (2.2)$$

where \mathbf{n} is the outward unit normal to Γ^f and Γ^c , and \bar{f} and $\bar{\theta}$ are prescribed normal heat flux and temperature, respectively, h_c is the convective coefficient, and θ_∞ is the ambient temperature.

2.1.2 Thermoelasticity

The linear elastic problem is also defined over a three-dimensional domain $\Omega^u \in \mathbb{R}^3$, $\Omega^u = \Omega$, with boundary $\partial\Omega^u = \Gamma^u \cup \Gamma^t$, where $\Gamma^u \cap \Gamma^t = \emptyset$. In the problems of interest, quasistatic response is expected; that is, inertial effects can be

neglected [127]. The steady-state governing equations are

$$\begin{aligned}
\nabla \cdot \boldsymbol{\sigma} &= -\mathbf{b}(\mathbf{x}) \quad \text{in } \Omega^u \\
\boldsymbol{\sigma} &= \mathbf{C} : \boldsymbol{\varepsilon}^m \\
\boldsymbol{\varepsilon}^m &= \boldsymbol{\varepsilon} - \boldsymbol{\varepsilon}^\theta \\
\boldsymbol{\varepsilon} &= \frac{1}{2} (\nabla \mathbf{u} + \nabla \mathbf{u}^T) \\
\boldsymbol{\varepsilon}^\theta &= \boldsymbol{\alpha}_\theta (\theta - \theta_\infty),
\end{aligned} \tag{2.3}$$

with $\boldsymbol{\sigma}$ the Cauchy stress tensor, and \mathbf{b} the body force. $\mathbf{C} = \mathbf{C}(\mathbf{x})$ is Hooke's tensor of material moduli,

$$\mathbf{C}(\mathbf{x}) = B\mathbf{1} \otimes \mathbf{1} + 2\mu \left[\mathbf{I} + \frac{1}{3} \mathbf{1} \otimes \mathbf{1} \right],$$

where $B = B(\mathbf{x})$ is the material bulk modulus, $\mu = \mu(\mathbf{x})$ the shear modulus, and $\mathbf{1}$ and \mathbf{I} signify the second- and fourth-order identity tensors, respectively. $\boldsymbol{\varepsilon}$, $\boldsymbol{\varepsilon}^m$, $\boldsymbol{\varepsilon}^\theta$ represent the total, mechanical, and thermal strain tensors, respectively, $\mathbf{u} = \mathbf{u}(\mathbf{x})$ the displacement field, and $\boldsymbol{\alpha}_\theta$ the tensor of thermal expansion coefficients. In all cases, isotropic thermal expansion is assumed, that is, $\boldsymbol{\alpha}_\theta = \alpha_\theta \mathbf{1}$.

Boundary conditions on $\partial\Omega^u$ are

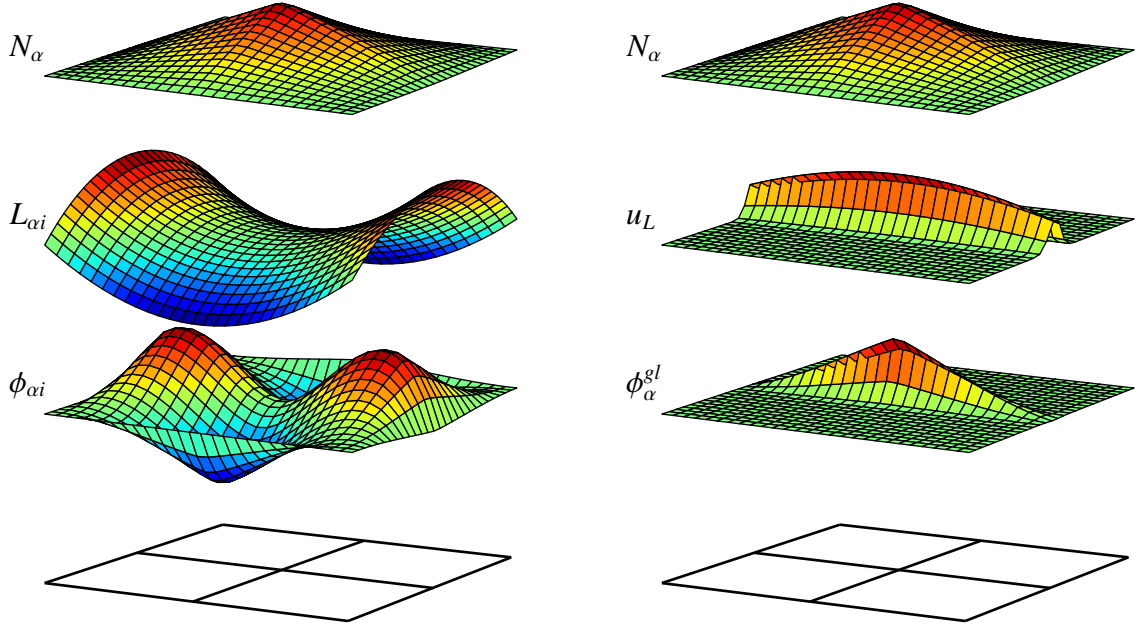
$$\begin{aligned}
\mathbf{u} &= \bar{\mathbf{u}} \quad \text{on } \Gamma^u \\
\boldsymbol{\sigma} \cdot \mathbf{n} &= \bar{\mathbf{t}} \quad \text{on } \Gamma^t,
\end{aligned} \tag{2.4}$$

where $\bar{\mathbf{u}}$ is the prescribed displacement, \mathbf{n} is the outward unit normal to Γ^t , and $\bar{\mathbf{t}}$ is the specified traction.

2.2 GFEM approximations

The Generalized Finite Element Method (GFEM) is adopted in this study to discretize the partial differential equations formulated in the above section. The Generalized or eXtended Finite Element Method [7, 24, 82, 89, 123] is an instance of the Partition of Unity Method (PUM) of Babuška et al. [2, 4, 80] and Duarte and Oden [27–29, 89]. A history of Generalized/eXtended FEMs is given in [9].

The standard Lagrangian finite element shape functions N_α , $\alpha \in I_h = \{1, \dots, k\}$, in a mesh with k nodes covering



(a) Polynomial enrichment

(b) Numerical enrichment

Figure 2.1: Construction of a GFEM shape function—from top to bottom, the FEM partition of unity φ_α , an enrichment function, and the resulting shape function.

a domain Ω , are chosen as the partition of unity in GFEM, since

$$\sum_{\alpha \in I_h} N_\alpha(\mathbf{x}) = 1 \quad \forall \mathbf{x} \in \Omega.$$

The GFEM hinges on the idea that the partition of unity can then be enriched, or combined with local function approximation spaces built around a priori knowledge of a given problem's solution behavior. A generalized finite element shape function $\phi_{\alpha i}(\mathbf{x})$ is constructed as

$$\phi_{\alpha i}(\mathbf{x}) = N_\alpha(\mathbf{x})L_{\alpha i}(\mathbf{x}) \quad (\text{no summation on } \alpha), \quad (2.5)$$

where $N_\alpha(\mathbf{x})$ is a finite element shape function and $L_{\alpha i}(\mathbf{x})$ is an enrichment function, $\alpha \in I_h^e \subset I_h$ is the index of a node in a FE mesh, and $i \in \mathcal{I}(\alpha) = \{1, \dots, m_\alpha\}$ is the index of the enrichment at the node. Figure 2.1a illustrates shape function construction using a standard polynomial enrichment. Nodes *not* in I_h^e have only the linear FE shape function N_α . The support of $N_\alpha(\mathbf{x})$, denoted by cloud or patch ω_α , is simply the union of all finite elements sharing node α , and

enrichment functions $\{L_{\alpha i}\}_{i=1}^{m_\alpha}$ form a basis of *patch space* $\chi_\alpha(\omega_\alpha)$.

The test and trial GFEM space \mathbb{S}_{GFEM} is obtained by hierarchically augmenting the standard FEM space \mathbb{S}_{FEM} with the global enrichment space \mathbb{S}_{ENR} ; that is,

$$\mathbb{S}_{GFEM} = \mathbb{S}_{FEM} + \mathbb{S}_{ENR}, \quad (2.6)$$

where

$$\begin{aligned} \mathbb{S}_{FEM} &= \sum_{\alpha \in I_h} \hat{\mathbf{u}}_\alpha N_\alpha, \quad \hat{\mathbf{u}}_\alpha \in \mathbb{R}, \\ \text{and} \quad \mathbb{S}_{ENR} &= \sum_{\alpha \in I_h^e} N_\alpha \chi_\alpha, \quad \chi_\alpha = \text{span}\{L_{\alpha i}\}_{i=1}^{m_\alpha}. \end{aligned} \quad (2.7)$$

Patch spaces $\chi_\alpha(\omega_\alpha)$, $\alpha \in I_h$, use the orthotropic polynomial enrichment functions presented in [22, 24, 89]. The polynomial degree of FEM or GFEM shape functions in the coordinate directions $\{x, y, z\}$ is denoted by $\mathbf{p} = \{p_x, p_y, p_z\}$. For instance the shape functions at a node $\alpha \in I_h$ with polynomial degree $\mathbf{p} = \{2, 2, 1\}$ are given by

$$\begin{aligned} \phi_{\alpha 0} &= N_\alpha \\ \phi_{\alpha 1} &= N_\alpha \frac{x - x_\alpha}{h_\alpha} \\ \phi_{\alpha 2} &= N_\alpha \frac{y - y_\alpha}{h_\alpha}, \end{aligned}$$

where h_α is a scaling factor taken as the diameter of the largest element sharing the node and $\mathbf{x}_\alpha = (x_\alpha, y_\alpha, z_\alpha)$ are the nodal coordinates. In this example, then, patch enrichment space $\chi_\alpha(\omega_\alpha) = \text{span}\{\frac{x-x_\alpha}{h_\alpha}, \frac{y-y_\alpha}{h_\alpha}\}$. A node with only the standard FEM shape function N_α has a polynomial degree $\mathbf{p} = \{1, 1, 1\}$.

The shape functions in \mathbb{S}_{ENR} are computed using (2.5). The GFEM approximation, θ^{hp} , of a scalar field θ (e.g., temperature) can thus be written as

$$\theta^{hp}(\mathbf{x}) = \underbrace{\sum_{\alpha \in I_h} \hat{\theta}_\alpha N_\alpha(\mathbf{x})}_{\text{Standard FEM approximation}} + \underbrace{\sum_{\alpha \in I_h^e} N_\alpha(\mathbf{x}) \sum_{i=1}^{m_\alpha} \tilde{\theta}_{\alpha i} L_{\alpha i}(\mathbf{x})}_{\text{GFEM enriched approximation}}, \quad \hat{\theta}_\alpha, \tilde{\theta}_{\alpha i} \in \mathbb{R}. \quad (2.8)$$

A GFEM approximation \mathbf{u}^{hp} of vector field \mathbf{u} (e.g., displacement) is exactly analogous:

$$\mathbf{u}^{hp}(\mathbf{x}) = \sum_{\alpha \in I_h} \hat{\mathbf{u}}_\alpha N_\alpha(\mathbf{x}) + \sum_{\alpha \in I_h^e} N_\alpha(\mathbf{x}) \sum_{i=1}^{m_\alpha} \tilde{\mathbf{u}}_{\alpha i} L_{\alpha i}(\mathbf{x}), \quad \hat{\mathbf{u}}_\alpha, \tilde{\mathbf{u}}_{\alpha i} \in \mathbb{R}^3. \quad (2.9)$$

The GFEM has been utilized successfully in the simulation of fracture mechanics [25, 83], polycrystalline [119] and fiber-reinforced [109, 110] microstructures, heat transfer with sharp temperature gradients [90], and several other examples where closed-form, analytical enrichment functions are available.

2.2.1 GFEM^{gl}

Although traditional GFEM applications have relied on analytical enrichments designed around prior knowledge of problem physics, convenient analytical functions do not exist for all classes of problems. Combining aspects of GFEM with the global–local FEM [19, 88], the GFEM with global–local enrichment functions (GFEM^{gl}) [23, 26] enables the user to automatically generate special, numerical enrichments ϕ_α^{gl} for the structural-scale problem through the solution of *hp*-adapted local problems designed to capture localized features of interest. Thus, expensive mesh refinement and high-order polynomial enrichment are restricted to the local mesh, and only a few degrees of freedom are added to the global problem in the form of numerically built enrichment functions, making the method especially useful in large problems where concentrated global mesh refinement proves too computationally expensive. The GFEM^{gl} has seen several applications, including transient heat transfer [91], fracture [61, 62], and localized plasticity [64].

GFEM^{gl} analyses of steady-state, single-physics problems consist of three essential steps:

- (i) solution of the coarse, global boundary value problem, termed the *initial global problem*,
- (ii) extraction and solution of *local problems* using the initial global solution as a boundary condition, and
- (iii) reanalysis of the *enriched global problem* based on local solutions.

Detailed formulation of these steps for the more complex case of coupled heat transfer and thermoelasticity is included in Section 2.3. Figure 2.2 illustrates the exchange of information between global and local domains.

2.2.1.1 Global–local enrichment improvement strategies

An important issue pertaining to the GFEM^{gl} procedure is that discretization error in coarse-scale initial global solutions in both heat transfer and thermoelastic problems leads to inexact boundary conditions on local problems, the effect of which has been a topic of recent study [51, 106]. In some cases boundary conditions may be poor, leading to poor-quality global–local enrichments. To obtain higher-quality local solutions (leading to better enrichment functions for the global problem), one such strategy used in this work is carrying out *multiple global–local iterations*:

- (i) local problem boundary conditions from coarse-scale, initial global solutions are updated based on improved, enriched global solutions,
- (ii) local problems are solved again, and

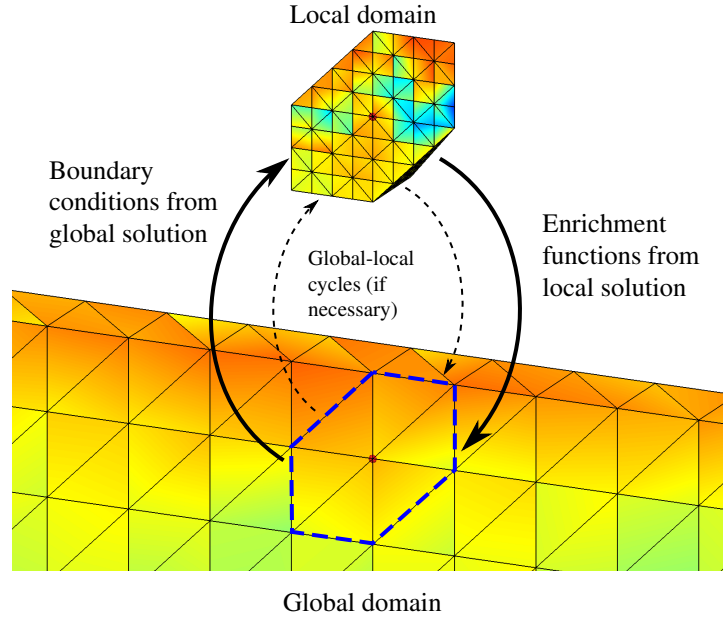


Figure 2.2: Typical single-physics coarse-scale global domain and hp -adapted local problem which encloses a localized solution feature like a singularity, sharp gradient, or material interface.

(iii) global–local enrichments are updated.

This procedure is also illustrated pictorially in Figure 2.2, denoted by dashed arrows.

2.3 GFEM^{gl} formulation for coupled heat transfer and thermoelasticity

In contrast to the single-physics version of GFEM^{gl}, the one-way-coupled thermo-structural problem involves additional steps and complexity, summarized as follows:

A. Heat transfer problem

- (i) Solution of the coarse, initial global heat transfer problem,
- (ii) extraction and solution of heat transfer local problems using the initial global heat transfer solution as a boundary condition, and
- (iii) reanalysis of the enriched global heat transfer problem based on local heat transfer solutions.

B. Thermoelasticity problem

- (i) Solution of the initial global thermoelastic problem based on thermal stresses computed from the enriched global temperature,
- (ii) extraction and solution of thermoelastic local problems using the initial global thermoelastic solution as a boundary condition, computing thermal stresses from the enriched global temperature, and

(iii) reanalysis of the enriched global thermoelastic problem based on local thermoelastic solutions.

Detailed formulation of the GFEM^{gl} for coupled heat transfer and thermoelasticity is included in Section 2.3. Figure 2.3 illustrates this exchange of information between global and local domains. While the above procedure designates one potential GFEM^{gl} coupling scheme in which thermal stresses in the elastic problem are based on the *enriched global* temperature field (the coupling sequence adopted in all examples shown), other sequences are possible; for instance, the *coarse, initial global* or *local* temperature solutions could be used to compute thermal stresses in initial global and local thermoelastic problems, respectively.

2.3.1 Steady-state heat transfer

Adopting (2.8) to approximate temperature field θ using GFEM and rewriting in matrix form,

$$\theta(\mathbf{x}) \approx \theta^{hp}(\mathbf{x}) = \bar{\mathbf{N}}^\theta(\mathbf{x})\mathbf{d}^\theta \quad (2.10)$$

where

$$\bar{\mathbf{N}}^\theta = [\bar{\mathbf{N}}_1^\theta \cdots \bar{\mathbf{N}}_n^\theta], \quad \bar{\mathbf{N}}_\alpha^\theta = [N_\alpha \quad \phi_{\alpha 1} \cdots \phi_{\alpha m_\alpha}].$$

The temperature gradient $\nabla\theta$, as it appears in (2.1), can then be approximated in a straightforward manner using (2.10) as

$$\nabla\theta(\mathbf{x}) \approx \nabla\theta^{hp}(\mathbf{x}) = \bar{\mathbf{B}}^\theta(\mathbf{x})\mathbf{d}^\theta, \quad (2.11)$$

where

$$\bar{\mathbf{B}}^\theta(\mathbf{x}) = \nabla \otimes \bar{\mathbf{N}}^\theta(\mathbf{x}).$$

2.3.1.1 Initial global problem

On the coarse-scale, global domain $\bar{\Omega}^\theta = \Omega^\theta \cup \partial\Omega^\theta$, the initial global problem is formulated as: Find $\theta^0 \in \mathbb{S}_G^0(\Omega^\theta) \subset \mathbb{S}_{GFEM}(\Omega^\theta)$ such that for all $\delta\theta^0 \in \mathbb{S}_G^0(\Omega^\theta)$,

$$\begin{aligned} \int_{\Omega^\theta} \nabla\theta^0 \boldsymbol{\kappa} \nabla\delta\theta^0 \, d\Omega + \eta \int_{\Gamma^\theta} \theta^0 \delta\theta^0 \, d\Gamma + \int_{\Gamma^c} h_c \theta^0 \delta\theta^0 \, d\Gamma \\ = \int_{\Omega^\theta} Q \delta\theta^0 \, d\Omega + \int_{\Gamma^f} \bar{f} \delta\theta^0 \, d\Gamma + \eta \int_{\Gamma^\theta} \bar{\theta} \delta\theta^0 \, d\Gamma + \int_{\Gamma^c} h_c \theta_\infty \delta\theta^0 \, d\Gamma, \end{aligned} \quad (2.12)$$

where η is a penalty parameter for enforcement of Dirichlet boundary conditions.

Introducing (2.10) and (2.11) for the temperature field θ^0 in (2.12), the discrete form of the problem may be written

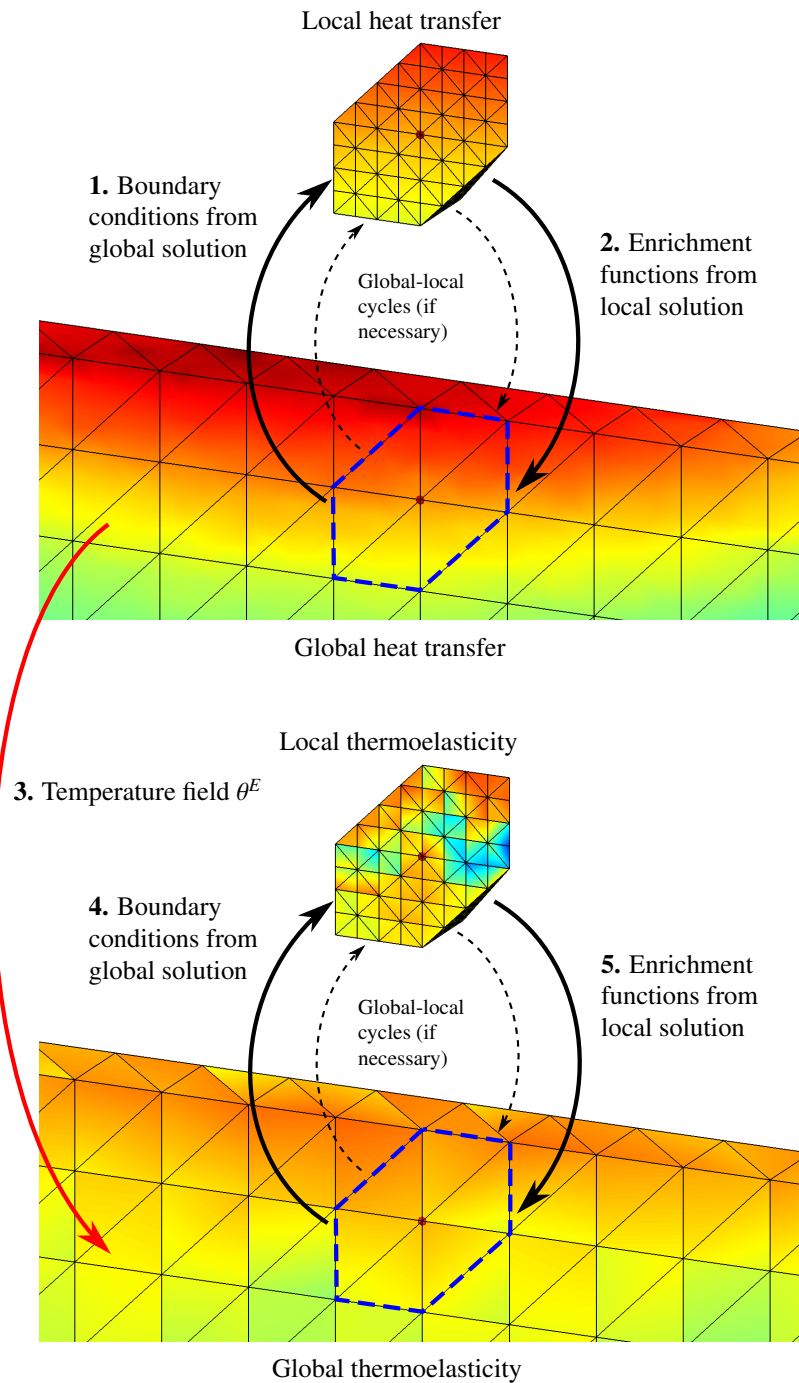


Figure 2.3: The GFEM^{gl} for sequentially-coupled thermo-structural problems, as detailed in Section 2.3. The coarse-scale global problem and hp -adapted local problem which resolves localized solution features such as singularities, sharp gradients, or material interfaces are shown in each discipline.

as

$$\mathbf{K}^\theta \mathbf{d}^\theta = \mathbf{f}_{\text{ext}}^\theta, \quad (2.13)$$

where

$$\begin{aligned} \mathbf{K}^\theta &= \int_{\Omega^\theta} \bar{\mathbf{B}}^{\theta T} \boldsymbol{\kappa} \bar{\mathbf{B}}^\theta \, d\Omega + \eta \int_{\Gamma^\theta} \bar{\mathbf{N}}^{\theta T} \bar{\mathbf{N}}^\theta \, d\Gamma + \int_{\Gamma^c} h_c \bar{\mathbf{N}}^{\theta T} \bar{\mathbf{N}}^\theta \, d\Gamma, \\ \mathbf{f}_{\text{ext}}^\theta &= \int_{\Omega^\theta} \bar{\mathbf{N}}^{\theta T} \bar{Q} \, d\Omega + \int_{\Gamma^f} \bar{\mathbf{N}}^{\theta T} \bar{f} \, d\Gamma + \eta \int_{\Gamma^\theta} \bar{\mathbf{N}}^{\theta T} \bar{\theta} \, d\Gamma + \int_{\Gamma^c} h_c \bar{\mathbf{N}}^{\theta T} \theta_\infty \, d\Gamma. \end{aligned}$$

2.3.1.2 Local problem(s)

The local domain $\bar{\Omega}_L = \Omega_L \cup \partial\Omega_L$, where $\Omega_L \subseteq \Omega$, is selected from Ω as the support of a set of ‘seed’ patches, \mathcal{I}^{sl} , or

$$\Omega_L^\theta = \bigcup_{\alpha \in \mathcal{I}^{sl}} \omega_\alpha. \quad (2.14)$$

A sample local mesh is shown in Figure 2.2.

Using the initial global solution θ^0 obtained from (2.12) as a coarse boundary condition on $\partial\Omega_L$, each local problem is solved independently of all other local problems, so that no communication among local problems is required, and local solutions are used only to generate enrichment functions ϕ_α^{sl} for the global solution space. This condition also allows for enforcement of the boundary condition as Dirichlet, Neumann, or Cauchy [62], since there are no constraints on solution continuity among local problems.

The initial global and local problem steps are equivalent to standard global–local analysis [19, 88].

The local heat transfer problem is formulated as follows: Find $\theta_L \in \mathbb{S}_L(\Omega_L^\theta) \subset \mathbb{S}_{GFEM}(\Omega_L^\theta)$ such that for all $\delta\theta_L \in \mathbb{S}_L(\Omega_L^\theta)$,

$$\begin{aligned} & \int_{\Omega_L^\theta} \nabla \theta_L \boldsymbol{\kappa} \nabla \delta\theta_L \, d\Omega + \eta \int_{\partial\Omega_L^\theta \setminus (\partial\Omega_L^\theta \cap (\Gamma^f \cup \Gamma^c))} \theta_L \delta\theta_L \, d\Gamma + \int_{\partial\Omega_L^\theta \cap \Gamma^c} h_c \theta_L \delta\theta_L \, d\Gamma \\ &= \eta \int_{\partial\Omega_L^\theta \setminus (\partial\Omega_L^\theta \cap \partial\Omega^\theta)} \theta^0 \delta\theta_L \, d\Gamma + \eta \int_{\partial\Omega_L^\theta \cap \Gamma^\theta} \bar{\theta} \delta\theta_L \, d\Gamma + \int_{\Omega_L^\theta} q \delta\theta_L \, d\Omega + \int_{\partial\Omega_L^\theta \cap \Gamma^f} \bar{f} \delta\theta_L \, d\Gamma \\ & \quad + \int_{\partial\Omega_L^\theta \cap \Gamma^c} h_c \theta_\infty \delta\theta_L \, d\Gamma. \end{aligned} \quad (2.15)$$

As in the global problem, using (2.10) and (2.11) for the temperature field θ_L in (2.15), the discrete form of the problem may be written as

$$\mathbf{K}_L^\theta \mathbf{d}_L^\theta = \mathbf{f}_{\text{ext},L}^\theta, \quad (2.16)$$

where

$$\begin{aligned} \mathbf{K}_L^\theta &= \int_{\Omega_L^\theta} \bar{\mathbf{B}}_L^{\theta T} \kappa \bar{\mathbf{B}}_L^\theta d\Omega + \eta \int_{\partial\Omega_L^\theta \setminus (\partial\Omega_L^\theta \cap (\Gamma^f \cup \Gamma^c))} \bar{\mathbf{N}}_L^{\theta T} \bar{\mathbf{N}}_L^\theta d\Gamma + \int_{\partial\Omega_L^\theta \cap \Gamma^c} h_c \bar{\mathbf{N}}_L^{\theta T} \bar{\mathbf{N}}_L^\theta d\Gamma, \\ \mathbf{f}_{\text{ext},L}^\theta &= \eta \int_{\partial\Omega_L^\theta \setminus (\partial\Omega_L^\theta \cap \partial\Omega^\theta)} \bar{\mathbf{N}}_L^{\theta T} \theta^0 d\Gamma + \eta \int_{\partial\Omega_L^\theta \cap \Gamma^\theta} \bar{\mathbf{N}}_L^{\theta T} \bar{\theta} d\Gamma + \int_{\Omega_L^\theta} \bar{\mathbf{N}}_L^{\theta T} \mathcal{Q} d\Omega + \int_{\partial\Omega_L^\theta \cap \Gamma^f} \bar{\mathbf{N}}_L^{\theta T} \bar{f} d\Gamma \\ &\quad + \int_{\partial\Omega_L^\theta \cap \Gamma^c} h_c \bar{\mathbf{N}}_L^{\theta T} \theta_\infty d\Gamma. \end{aligned}$$

2.3.1.3 Enriched global problem

Traditional global–local methods may suffer from the limitation that local solutions may not satisfactorily represent true solution behavior over the local region $\Omega \cap \Omega_L$ due to inaccurate boundary conditions from the initial, coarse-scale solution. In general, localized solution characteristics resolved in local problems may also impact the overall structural-scale behavior. Thus, in GFEM^{gl}, local problem solutions θ_L are used directly as numerical enrichments in the global problem (2.12),

$$\phi_\alpha^{gl}(\mathbf{x}) = N_\alpha(\mathbf{x})\theta_L(\mathbf{x}), \quad (2.17)$$

and the global GFEM space hierarchically enriched with global–local shape functions is given by

$$\mathbb{S}_{GFEM}^E = \mathbb{S}_{GFEM}^0 + \{N_\alpha \theta_\alpha^{gl} \text{ (no summation on } \alpha), \alpha \in \mathcal{I}^{gl}\}, \quad (2.18)$$

where \mathbb{S}_{GFEM}^0 is the GFEM space of the initial global problem,

$$\theta_\alpha^{gl}(\mathbf{x}) = \tilde{\theta}_\alpha \theta_L(\mathbf{x}), \quad \tilde{\theta}_\alpha \in \mathbb{R}$$

is an approximation defined over patch ω_α , $\alpha \in \mathcal{I}^{gl}$, $\tilde{\theta}_\alpha$ is a global degree of freedom. The solution of the enriched global heat transfer problem is denoted hereafter θ^E .

2.3.2 Thermoelasticity

Adopting (2.9) and rewriting in matrix form, the GFEM approximation \mathbf{u}^{hp} of a displacement field \mathbf{u} can be written as

$$\mathbf{u}(\mathbf{x}) \approx \mathbf{u}^{hp}(\mathbf{x}) = \bar{\mathbf{N}}^{\mathbf{u}}(\mathbf{x})\mathbf{d}^{\mathbf{u}}, \quad (2.19)$$

where

$$\bar{\mathbf{N}}^{\mathbf{u}} = [\bar{\mathbf{N}}_1^{\mathbf{u}} \cdots \bar{\mathbf{N}}_k^{\mathbf{u}}], \quad \bar{\mathbf{N}}_\alpha^{\mathbf{u}} = \begin{bmatrix} \mathbf{N}_{\alpha 0}^{\mathbf{u}} & \mathbf{N}_{\alpha 1}^{\mathbf{u}} & \cdots & \mathbf{N}_{\alpha m_\alpha}^{\mathbf{u}} \end{bmatrix},$$

PoU
Enrichment

and

$$\mathbf{N}_{\alpha 0}^{\mathbf{u}} = \begin{bmatrix} N_{\alpha} & 0 & 0 \\ 0 & N_{\alpha} & 0 \\ 0 & 0 & N_{\alpha} \end{bmatrix}, \quad \mathbf{N}_{\alpha i}^{\mathbf{u}} = \begin{bmatrix} \phi_{\alpha i} & 0 & 0 \\ 0 & \phi_{\alpha i} & 0 \\ 0 & 0 & \phi_{\alpha i} \end{bmatrix}.$$

Applying the fourth equation in (2.3) to (2.19), it then follows that the approximation $\boldsymbol{\varepsilon}^{hp}$ of the strain tensor $\boldsymbol{\varepsilon}$ is given by

$$\boldsymbol{\varepsilon}(\mathbf{u}) \approx \boldsymbol{\varepsilon}^{hp}(\mathbf{u}^{hp}) = \bar{\mathbf{B}}^{\mathbf{u}}(\mathbf{x})\mathbf{d}^{\mathbf{u}} \quad (2.20)$$

where $\bar{\mathbf{B}}^{\mathbf{u}}$ denotes the strain operator in Voigt notation,

$$\bar{\mathbf{B}}^{\mathbf{u}} = [\bar{\mathbf{B}}_1^{\mathbf{u}} \cdots \bar{\mathbf{B}}_k^{\mathbf{u}}],$$

with

$$\bar{\mathbf{B}}_{\alpha}^{\mathbf{u}} = \begin{bmatrix} \mathbf{B}_{\alpha 0}^{\mathbf{u}} & \mathbf{B}_{\alpha 1}^{\mathbf{u}} & \cdots & \mathbf{B}_{\alpha m_{\alpha}}^{\mathbf{u}} \\ \text{PoU} & \text{Enrichment} & & \end{bmatrix}$$

and

$$\mathbf{B}_{\alpha 0}^{\mathbf{u}} = \begin{bmatrix} N_{,x}^{\alpha} & 0 & 0 \\ 0 & N_{,y}^{\alpha} & 0 \\ 0 & 0 & N_{,z}^{\alpha} \\ N_{,y}^{\alpha} & N_{,x}^{\alpha} & 0 \\ N_{,z}^{\alpha} & 0 & N_{,x}^{\alpha} \\ 0 & N_{,z}^{\alpha} & N_{,y}^{\alpha} \end{bmatrix}, \quad \mathbf{B}_{\alpha i}^{\mathbf{u}} = \begin{bmatrix} \phi_{,x}^{\alpha i} & 0 & 0 \\ 0 & \phi_{,y}^{\alpha i} & 0 \\ 0 & 0 & \phi_{,z}^{\alpha i} \\ \phi_{,y}^{\alpha i} & \phi_{,x}^{\alpha i} & 0 \\ \phi_{,z}^{\alpha i} & 0 & \phi_{,x}^{\alpha i} \\ 0 & \phi_{,z}^{\alpha i} & \phi_{,y}^{\alpha i} \end{bmatrix}.$$

The GFEM^{gl} formulated for thermoelasticity follows analogously to the heat transfer case.

2.3.2.1 Initial global problem

The variational formulation of the global linear thermoelasticity problem is as follows:

Find $\mathbf{u}^0 \in \mathbb{S}_G^0(\Omega^{\mathbf{u}}) \subset \mathbb{S}_{GFEM}(\Omega^{\mathbf{u}})$ such that, $\forall \delta \mathbf{u}^0 \in \mathbb{S}_G^0(\Omega^{\mathbf{u}})$,

$$\int_{\Omega^{\mathbf{u}}} \boldsymbol{\sigma}(\mathbf{u}^0) : \boldsymbol{\varepsilon}(\delta \mathbf{u}^0) \, d\Omega + \eta \int_{\Gamma^{\mathbf{u}}} \mathbf{u}^0 \cdot \delta \mathbf{u}^0 \, d\Gamma = \int_{\Gamma^{\mathbf{t}}} \bar{\mathbf{t}} \cdot \delta \mathbf{u}^0 \, d\Gamma + \eta \int_{\Gamma^{\mathbf{u}}} \bar{\mathbf{u}} \cdot \delta \mathbf{u}^0 \, d\Gamma, \quad (2.21)$$

where η is a penalty parameter. As this is a linear problem, in practice the Cauchy stress σ is decomposed as

$$\begin{aligned}\sigma &= \tilde{\sigma} - \sigma^\theta \\ \tilde{\sigma}(\mathbf{u}^0) &= \mathbf{C} : \boldsymbol{\varepsilon}(\mathbf{u}^0) \\ \sigma^\theta(\theta^E) &= \mathbf{C} : \boldsymbol{\varepsilon}^\theta(\theta^E).\end{aligned}\tag{2.22}$$

The thermal stress contributions, σ^θ , are then treated on the right-hand side of (2.21).

Introducing (2.19) and (2.22) in (2.21), the discrete form of the problem may be written as

$$\mathbf{K}^u \mathbf{d}^u = \mathbf{f}_{\text{ext}}^u - \mathbf{f}_{\text{int}}^u,\tag{2.23}$$

where

$$\begin{aligned}\mathbf{K}^u &= \int_{\Omega^u} \bar{\mathbf{B}}^{uT} \mathbf{C} \bar{\mathbf{B}}^u d\Omega + \eta \int_{\Gamma^u} \bar{\mathbf{N}}^{uT} \bar{\mathbf{N}}^u d\Gamma, \\ \mathbf{f}_{\text{ext}}^u &= \int_{\Gamma^t} \bar{\mathbf{N}}^{uT} \bar{\mathbf{t}} d\Gamma + \eta \int_{\Gamma^u} \bar{\mathbf{N}}^{uT} \bar{\mathbf{u}} d\Gamma, \\ \mathbf{f}_{\text{int}}^u &= - \int_{\Omega^u} \bar{\mathbf{B}}^{uT} \mathbf{C} \alpha_\theta \theta^E d\Omega,\end{aligned}$$

and θ^E is known and may be obtained directly from (2.10).

The enriched global temperature field θ^E from the GFEM^{el} analysis of the global heat transfer problem (2.12) provides the best estimate of the global temperature field. Thus, θ^E is used to compute the thermal stress contribution even in the coarse, initial elasticity problem. In general, $\theta^E \in \mathbb{S}_{GFEM}^E$, and \mathbb{S}_{GFEM}^E has numerical enrichment functions defined on a refined, local mesh; thus, extra care must be taken to accurately integrate the thermal stress contribution in the coarse-scale, global thermoelasticity problem, which is described in Section 2.4.3.

2.3.2.2 Local problem(s)

Local domain Ω_L^u denotes a subdomain of Ω^u , constructed precisely analogously to local problems in the heat transfer case described in Section 2.3.1.

The local thermoelasticity problem is formulated as follows:

Find $\mathbf{u}_L \in \mathbb{S}_L(\Omega_L^u) \subset \mathbb{S}_{GFEM}(\Omega_L^u)$ such that, $\forall \delta \mathbf{u}_L \in X_L^{hp}(\Omega_L^u)$,

$$\begin{aligned} \int_{\Omega_L^u} \boldsymbol{\sigma}(\mathbf{u}_L) : \boldsymbol{\varepsilon}(\delta \mathbf{u}_L) \, d\Omega + \eta \int_{\partial\Omega_L^u \setminus (\partial\Omega_L^u \cap \Gamma^u)} \mathbf{u}_L \cdot \delta \mathbf{u}_L \, d\Gamma \\ = \eta \int_{\partial\Omega_L^u \setminus (\partial\Omega_L^u \cap \partial\Omega^u)} \mathbf{u}^0 \cdot \delta \mathbf{u}_L \, d\Gamma + \eta \int_{\partial\Omega_L^u \cap \Gamma^u} \bar{\mathbf{u}} \cdot \delta \mathbf{u}_L \, d\Gamma + \int_{\partial\Omega_L^u \cap \Gamma^t} \bar{\mathbf{t}} \cdot \delta \mathbf{u}_L \, d\Gamma. \end{aligned} \quad (2.24)$$

The same decomposition of the stress field $\boldsymbol{\sigma}$ for analyzing thermal stress contributions given in (2.22) is applied. Just as in the heat transfer case, a key aspect of problem (2.24) is the use of the generalized FEM solution of the coarse-scale, global problem, \mathbf{u}^0 , as a displacement boundary condition on $\partial\Omega_L^u \setminus (\partial\Omega_L^u \cap \partial\Omega^u)$. Enforcement of the global solution boundary condition as tractions or springs is also permitted on $\partial\Omega_L^u \setminus (\partial\Omega_L^u \cap \partial\Omega^u)$.

Introducing (2.19) and (2.22) in (2.24), the discrete form of the problem may be written as

$$\mathbf{K}_L^u \mathbf{d}_L^u = \mathbf{f}_{\text{ext},L}^u - \mathbf{f}_{\text{int},L}^u, \quad (2.25)$$

where

$$\begin{aligned} \mathbf{K}_L^u &= \int_{\Omega_L^u} \bar{\mathbf{B}}_L^{uT} \mathbf{C} \bar{\mathbf{B}}_L^u \, d\Omega + \eta \int_{\partial\Omega_L^u \setminus (\partial\Omega_L^u \cap \Gamma^u)} \bar{\mathbf{N}}_L^{uT} \bar{\mathbf{N}}_L^u \, d\Gamma \\ \mathbf{f}_{\text{ext},L}^u &= \eta \int_{\partial\Omega_L^u \setminus (\partial\Omega_L^u \cap \partial\Omega^u)} \bar{\mathbf{N}}_L^{uT} \mathbf{u}^0 \, d\Gamma + \eta \int_{\partial\Omega_L^u \cap \Gamma^u} \bar{\mathbf{N}}_L^{uT} \bar{\mathbf{u}} \, d\Gamma + \int_{\partial\Omega_L^u \cap \Gamma^t} \bar{\mathbf{N}}_L^{uT} \bar{\mathbf{t}} \, d\Gamma, \\ \mathbf{f}_{\text{int},L}^u &= \int_{\Omega_L^u} \bar{\mathbf{B}}_L^{uT} \mathbf{C} \alpha_\theta \theta^E \, d\Omega, \end{aligned}$$

and again θ^E may be obtained directly from (2.10).

2.3.2.3 Enriched global problem

The global thermoelasticity problem (2.21) is reanalyzed, hierarchically adding global–local enrichments generated from the local problem solution,

$$\boldsymbol{\phi}_\alpha^{gl}(\mathbf{x}) = N_\alpha(\mathbf{x}) \mathbf{u}_L(\mathbf{x}), \quad (2.26)$$

where the GFEM space \mathbb{S}_{GFEM}^E is defined just as in the heat transfer case (2.18), noting, however, that the spaces of the heat transfer and thermoelasticity problems may be entirely different and independent of one another.

2.4 A coupled physics framework for efficient thermomechanical analysis

2.4.1 Current approaches and limitations

In target applications of this method—that is, modeling of thermomechanical effects due to local heating—engineers typically adopt a sequential or one-way-coupled solution scheme due to the weakly coupled nature of the physics of interest. While under certain circumstances heating effects due to rapid mechanical deformations may be significant, the intensity of localized temperature gradients due to thermal loadings (e.g., from fluids or other external heat sources) is generally orders of magnitude higher [127, 128]. This allows for the use of separate software packages tailored to heat transfer and structural analysis of each separate problem, as well as different, specially designed finite element meshes for heat transfer and structural models. Coupling between thermal and structural problems is often achieved by passing nodal or interpolated temperature information from the heat transfer solver to the structural analysis code.

The GFEM has shown promise in capturing localized heating effects [90, 91]. However, when considering multi-physics coupling, the use of high-order polynomial, numerical, or otherwise special enrichment functions to describe the solution in GFEM means smoothed or nodally interpolated temperature fields may not be sufficient to describe the high solution gradients in the neighborhood of, for example, thermal shocks or other sharp heat sources, which may be localized within a single element in the mesh.

2.4.2 GFEM coupling

Adaptive GFEM solutions typically employ high-order polynomial approximations (p -refinement) and heavy mesh refinement (h -refinement) in the neighborhood of localized solution features. Thus, when modeling thermomechanical effects, *physical quantities* defined at a physical point in the domain must be shared between heat transfer and structural models. However, if different mesh geometries are adopted in each physics problem, mapping of physical coordinates between physics meshes can be expensive and potentially problematic due to heavy localized mesh refinement.

In order to avoid expensive mappings between physics problems for the one-way coupled case, in the GFEM approach *identical mesh geometries* are used in both heat transfer and structural problems. This simplification allows for increased efficiency in exchanging information between physics problems due to the one-to-one correspondence of finite elements, as well as exact numerical integration of the thermal stress contribution over the structural mesh. Furthermore, only one instance of the mesh geometry needs to be stored. Although the mesh geometries are identical, no such restriction is imposed on the GFEM enrichment spaces, as defined in Section 2.2, in each physics discipline, so the desired solution fidelity can be achieved in each physics problem via, for instance, p -refinements.

2.4.3 GFEM^{gl} coupling

The GFEM^{gl} introduces additional complexities into the multiphysics coupling framework. Because a sequential coupling is adopted, the most accurate, enriched global heat transfer solution θ^E computed from (2.12) is used to compute thermal stress contributions in each of the initial global, local, and enriched global structural problems, as described previously in Section 2.3.2. However, θ^E is represented using global–local shape functions (2.17) generated by the solution of *hp*-adapted heat transfer local problems (2.15), which are defined over refined local meshes. Thus, additional assumptions are necessary in the GFEM^{gl} to maintain computational efficiency and compatibility with the framework design.

Under the GFEM^{gl}, in order to avoid expensive mappings between meshes, not only are the global heat transfer and structural mesh geometries identical, but the *local problem meshes* must also have the same one-to-one correspondence. Just as in the *hp*-GFEM, only the geometry of the mesh must be the same, however, an arbitrary choice of enrichment functions is possible.

2.4.4 Coupling implementation

A detailed description of the specific computational issues related to the coupling of physics problems within the GFEM framework as well as diagrams illustrating the important exchange of multiphysics information is available in Appendix A.

2.5 Numerical examples

2.5.1 L-shaped domain

A three-dimensional L-shaped domain is subjected to uniform temperatures applied at the right and top faces, as shown in Figure 2.4. The domain is restricted only against rigid body motion. In this example, fine-scale solution features or sharp gradients are introduced by the reentrant inner corner. Thus, it primarily serves to verify that the GFEM and coupled physics framework are able to handle sharp solution features without the need to resolve complex and localized applied loadings.

This problem was solved using the *hp*- or adaptive version of the GFEM with geometric mesh refinement at the inner corner. A uniform polynomial approximation in the heat transfer problem of the degree $\mathbf{p}^\theta = \{2, 2, 1\}$ and in the thermoelasticity problem of $\mathbf{p}^\theta = \{3, 3, 2\}$ was used.

It is clear from Figure 2.5 that both heat flux and stress singularities exist at the reentrant corner, despite the smooth nature of the temperature distribution and boundary conditions.

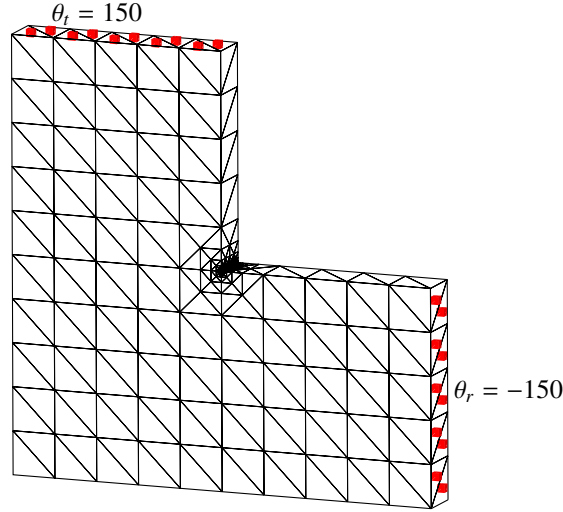


Figure 2.4: Geometry and hp -GFEM mesh of the L-shaped domain.

2.5.2 Laser-heated beam

The second example presented is a small, three-dimensional coupon beam of dimensions $12 \text{ in} \times 0.5 \text{ in} \times 0.24 \text{ in}$ with uniform conductivity $\kappa = 2.92 \frac{\text{ft-lbf}}{\text{s-in}^2\text{F}}$ and elastic properties $E = 55 \text{ ksi}$, $\nu = 0.3$, and $\alpha_\theta = 2.75 \times 10^{-6} \text{ }^\circ\text{F}^{-1}$. The beam is subjected to localized, steady-state Gaussian laser heating on its front surface, given by

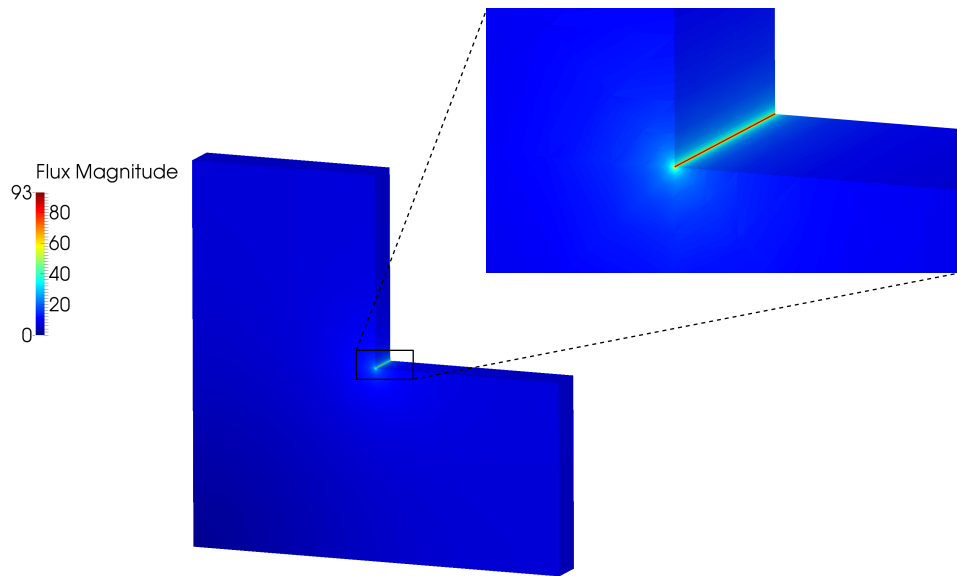
$$\bar{f}(\mathbf{x}) = \frac{I_0}{2\pi a^2} \exp\left(\frac{-(x-b)^2}{2a^2}\right), \quad 8.0 \leq x \leq 10.0.$$

Here, parameter $I_0 = 295 \frac{\text{ft-lbf}}{\text{s}}$ is the laser flux intensity, $a = 0.025 \text{ in}$ is the laser focus, or width, and $b = 9.3 \text{ in}$ dictates the x -coordinate of the center of the flux. Convection boundary conditions are applied elsewhere on the domain at an ambient temperature $\theta_\infty = 70 \text{ }^\circ\text{F}$, and the ends of the beam are fixed against axial deformation. The flux function is shown in Figure 2.6.

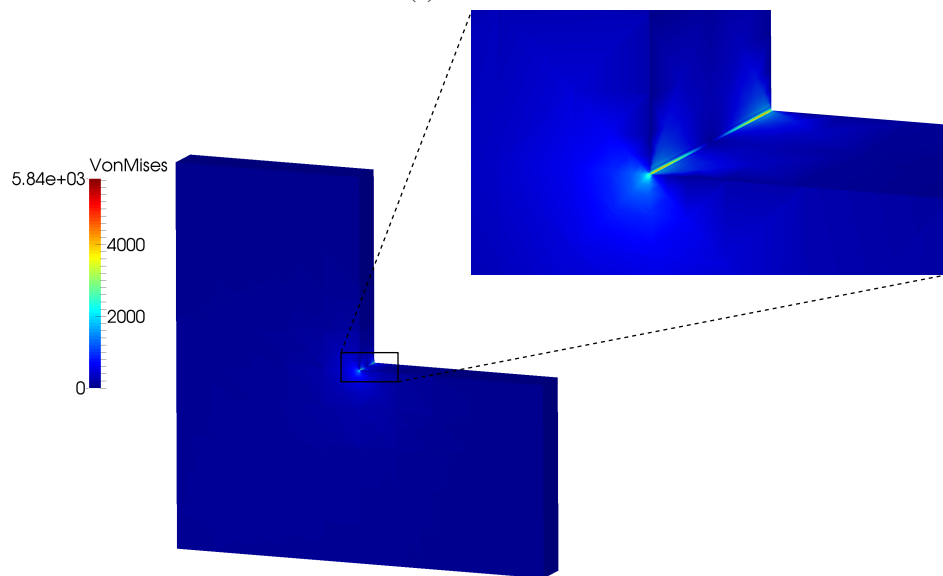
The sharply varying laser flux necessitates high solution fidelity close to the laser heating in order to adequately characterize local as well as global solution behavior in both the heat transfer and thermoelastic problem.

2.5.2.1 GFEM^{gl}

The problem is first solved using the GFEM^{gl} and a coarse structural mesh (global element size $H = 0.5$), while mesh refinement and polynomial enrichment are carried out in a local problem enclosing the localized laser flux. The global mesh size remains coarse and regular throughout, while local problem mesh refinement is carried out to obtain a sufficient level of fidelity locally surrounding the sharp flux. In the global heat transfer problem, a uniform polynomial order $\mathbf{p}^\theta = \{2, 2, 2\}$ is used. The local problem is selected as a small region surrounding the sharp laser flux between $8.0 \leq x \leq 10.5$, which has 10 levels of adaptive mesh refinement and $\mathbf{p}_L^\theta = \{3, 2, 2\}$. The enriched global problem



(a) Heat flux



(b) von Mises stress

Figure 2.5: hp -GFEM solutions of a thermoelastic L-shaped domain showing localized effects due to a singularity.

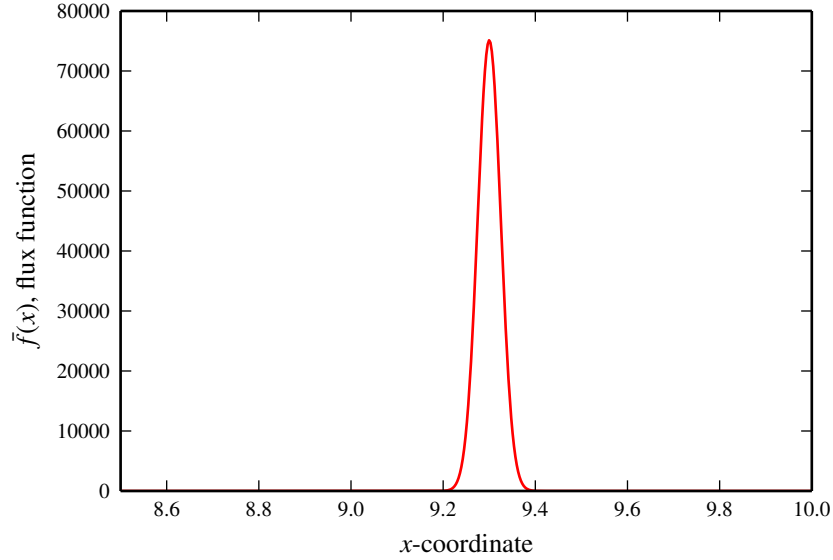
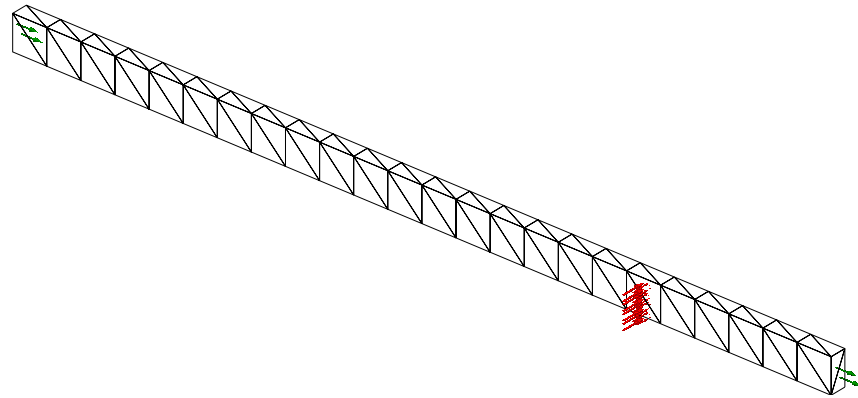


Figure 2.6: Gaussian laser flux applied to the surface of the laser-heated beam.

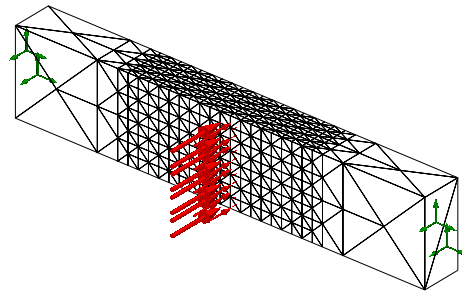
has the same polynomial order as the initial global problem plus global–local enrichments in the neighborhood of the thermal spike. Accordingly, the thermoelastic problem has $\mathbf{p}^u = \{3, 3, 3\}$, and the corresponding local problem uses $\mathbf{p}_L^u = \{4, 3, 3\}$, one order higher than the heat transfer problem in order to be able to represent the thermal strain due to the numerical solution for the temperature field. The geometry, boundary conditions, and GFEM^{gl} local problem and global problem meshes are shown in Figure 2.7.

The adaptive or *hp*-GFEM, on the other hand, which involves both mesh refinement and higher-order polynomial enrichment of the solution in regions of interest, is optimal for this type of problem, and is thus used to generate an *equivalent* solution (also denoted the *hp*-GFEM DFEA solution hereafter). This solution has 10 levels of localized global mesh refinement, a global polynomial order of approximation in the heat transfer (thermoelasticity) problem of $\mathbf{p}^\theta = \{2, 2, 2\}$ ($\mathbf{p}^u = \{3, 3, 3\}$), and a polynomial order $\mathbf{p}^\theta = \{3, 3, 3\}$ ($\mathbf{p}^u = \{4, 4, 4\}$) in the neighborhood of the sharp heating. This DFEA solution is thus equivalent to the GFEM^{gl} solutions detailed above for direct comparison. The heavy, localized refinement necessary to resolve the spike on the global mesh is demonstrated in Figure 2.8 (cf. the coarse mesh in Fig. 2.7a).

Solution contours from DFEA and GFEM^{gl} simulations of the laser-heated beam problem are shown in Figure 2.9. Qualitatively, the GFEM^{gl} enriched with the numerically generated local problem solution compares very favorably with DFEA. Quantitative measures of the GFEM^{gl} solution accuracy compared to DFEA are also provided in Table 2.1. Since GFEM^{gl} solutions are compared to an equivalent DFEA using *hp*-GFEM, the global accuracy of the solution



(a) GFEM^{gl} global problem



(b) GFEM^{gl} local problem

Figure 2.7: Meshes used to solve the laser-heated beam problem with the GFEM^{gl}.

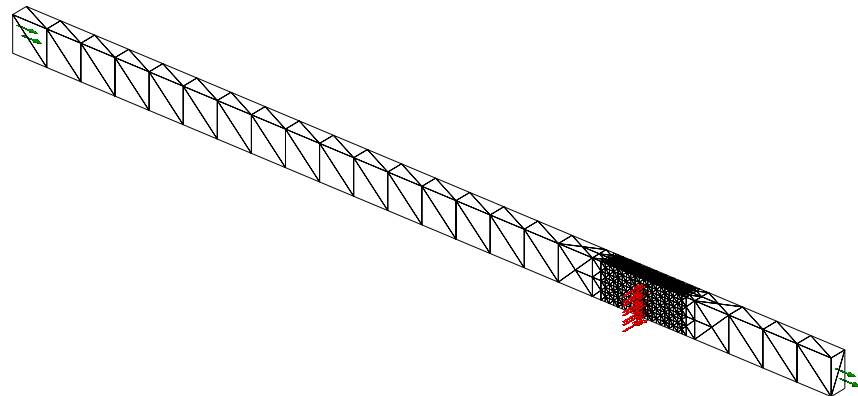


Figure 2.8: *hp*-GFEM mesh of the laser-heated beam problem.

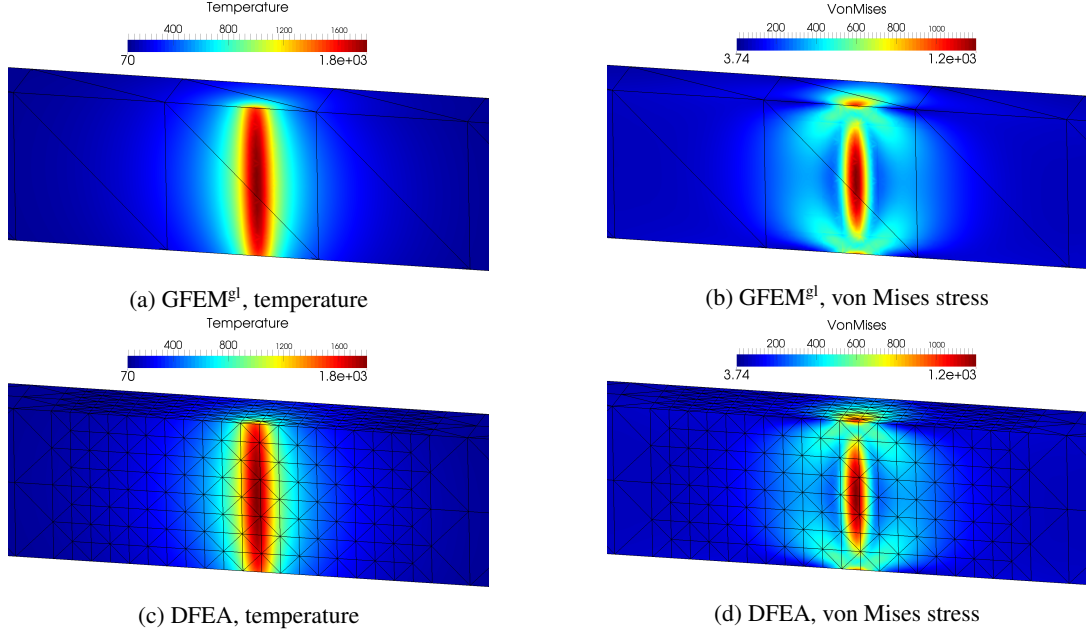


Figure 2.9: GFEM^{gl} and *hp*-GFEM DFEA solution contours of the laser-heated beam problem.

Table 2.1: Comparison of global and pointwise thermoelasticity quantities under each method for the laser-heated beam.

Method	Max. von Mises	% difference	Strain energy	$e_{E,\mathbf{u}}^{r,\text{diff}}$
DFEA (<i>hp</i> -GFEM)	1198.0	—	4.588×10^{-3}	—
GFEM ^{gl} global	943.5	21.2%	12.23×10^{-3}	1.291
local	1198.6	0.05%	—	—
enriched	1198.7	0.05%	4.587×10^{-3}	0.014

is measured as relative difference in the energy norm,

$$e_{E,\theta}^{r,\text{diff}} = \frac{\sqrt{|\mathcal{B}(\theta_{hp}^{\text{eq}}, \theta_{hp}^{\text{eq}}) - \mathcal{B}(\theta_{gl}, \theta_{gl})|}}{\sqrt{|\mathcal{B}(\theta_{hp}^{\text{eq}}, \theta_{hp}^{\text{eq}})|}} \quad (2.27)$$

in the heat transfer case, and

$$e_{E,\mathbf{u}}^{r,\text{diff}} = \frac{\sqrt{|\mathcal{B}(\mathbf{u}_{hp}^{\text{eq}}, \mathbf{u}_{hp}^{\text{eq}}) - \mathcal{B}(\mathbf{u}_{gl}, \mathbf{u}_{gl})|}}{\sqrt{|\mathcal{B}(\mathbf{u}_{hp}^{\text{eq}}, \mathbf{u}_{hp}^{\text{eq}})|}} \quad (2.28)$$

for the elasticity problem, where $(\)_{hp}^{\text{eq}}$ denotes the equivalent *hp*-GFEM DFEA solution, and $(\)_{gl}$ denotes a GFEM^{gl} solution, while $\mathcal{B}(\ , \)$ indicates the bilinear form associated with each problem. Despite the relatively poor quality of the initial global solution in both local and global measures—maximum von Mises stress and strain energy, respectively—the enriched global problem effectively resolves the localized thermal stress spike on the coarse mesh, which has a drastic impact on global error in the solution, as well. Furthermore, the GFEM^{gl} achieves a high level

Table 2.2: Comparison of degrees of freedom (dofs) used in each method for the laser-heated beam.

Method	Problem size	
	Heat transfer	Thermoelasticity
DFEA (<i>hp</i> -GFEM)	22,376	151,374
GFEM ^{gl} global	400	3,000
local	22,216	149,958
enriched	416	3,048

Table 2.3: Comparison of physics coupling methods for assembly of the laser-heated beam thermoelasticity problem (wall time) on a serial computer.

	Assembly time (s)		Time savings (%)
	Brute force	Optimized	
Initial global	1.629	0.184	88.7%
Local	5.972	1.607	73.1%
Enriched global	8.247	1.311	84.1%
<i>Total</i>	15.848	3.102	80.4%

of accuracy while maintaining substantial computational savings in the global problem, adding only a few degrees of freedom to the problem in the form of global–local enrichments; the numbers of degrees of freedom used in each method are summarized in Table 2.2.

Finally, the efficiency of the proposed framework to couple each physics problem under the GFEM^{gl} is examined. The ‘optimized’ framework described in Section 2.4.3, which leverages identical mesh geometry and nested descendant information in order to efficiently transfer solution information between disciplines and accurately integrate multiphysics contributions, is compared to the alternative, or the ‘brute force’ method, where the solution is obtained using only the physical or global coordinate information. In the latter instance, there is no reliance on identical mesh geometry or highly refined, nested local problem mesh information; instead, expensive searching for the correct element in the heat transfer global problem is necessary. To account for this increase in computational effort, the following results were obtained using lower-order polynomial approximations in the GFEM solutions, $\mathbf{p}^\theta = \{1, 1, 1\}$, $\mathbf{p}_L^\theta = \{2, 2, 2\}$, $\mathbf{p}^u = \{2, 2, 2\}$, and $\mathbf{p}_L^u = \{3, 3, 3\}$.

Table 2.3 summarizes the serial wall time spent assembling the thermoelasticity problem in GFEM^{gl} simulations of the laser-heated beam problem using both the brute force method and the optimized coupling framework. In all cases, the optimized framework provides a noticeable time savings compared to brute force searching, especially in initial and enriched global problems. Additionally, Figure 2.10 shows assembly times from each enriched global thermoelasticity problem for various levels of mesh refinement in the local problem. For minimal levels of mesh refinement in the local problem relative to the global mesh, obtaining the temperature field from the heat transfer problem using the global coordinate is nearly as efficient as the optimized framework. However, it is clear that computational effort increases

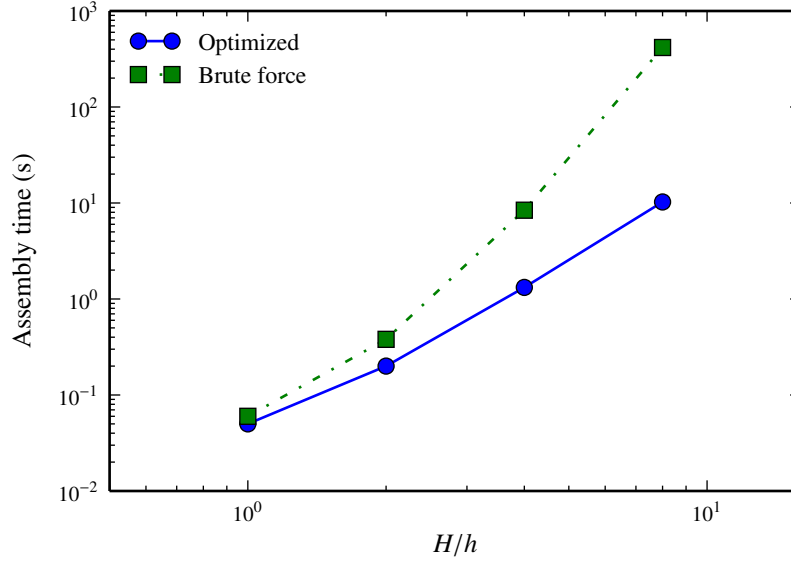


Figure 2.10: Enriched global thermoelasticity assembly time of brute force versus optimized coupling methods at various global-to-local mesh size ratios (H/h) for the laser-heated beam.

drastically as the local mesh is refined, and brute force searching/mapping between local and global domains becomes prohibitively expensive; at the highest level of local mesh refinement, the optimized framework yields a time savings of over 93%.

2.5.3 Laser-heated stiffened panel

The final example presented in this chapter is a larger, more representative problem exhibiting complicated geometrical features, and comprising many degrees of freedom in the global problem in order to accurately represent the structure. In this type of problem, several different critical load cases might need examining. The GFEM^{gl} allows for great flexibility in analyzing multiple localized load cases because the same global, structural mesh can be used in each analysis. In each case, only the location of the local problem enclosing the localized feature changes, and heavy mesh refinement and higher-order polynomial enrichment are restricted to the local problems. Because the global model does not change, a partitioning of the GFEM system of equations $\mathbf{K}\mathbf{u} = \mathbf{f}$ of the form

$$\begin{bmatrix} \mathbf{K}^0 & \mathbf{K}^{0,gl} \\ \mathbf{K}^{gl,0} & \mathbf{K}^{gl} \end{bmatrix} \begin{bmatrix} \underline{\mathbf{u}}^0 \\ \underline{\mathbf{u}}^{gl} \end{bmatrix} = \begin{bmatrix} \mathbf{f}^0 \\ \mathbf{f}^{gl} \end{bmatrix} \quad (2.29)$$

where $()^0$ corresponds to degrees of freedom from the global model, $()^{gl}$ corresponds to degrees of freedom associated with the GFEM^{gl}, and $()^{0,gl}$ or $()^{gl,0}$ correspond to coupling terms between the global and global-local dofs. This reanalysis algorithm is detailed in [23, 62]. In cases where the global problem is very large, direct finite

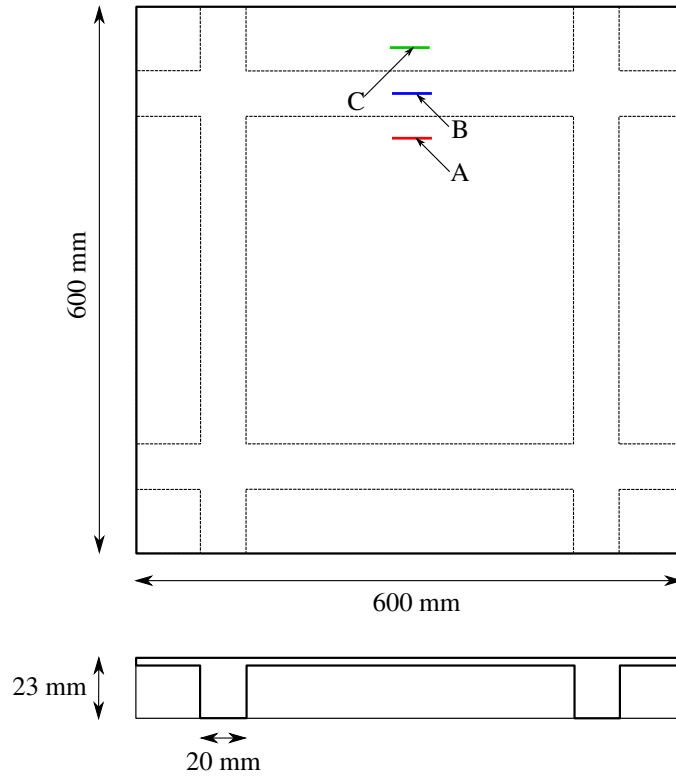
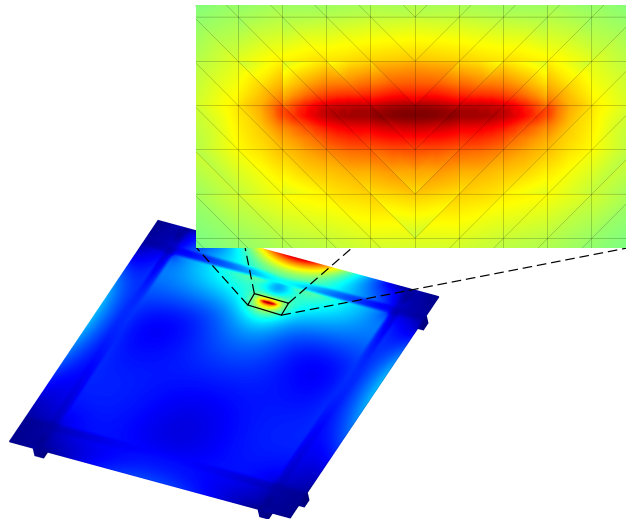


Figure 2.11: Critical loading locations on the stiffened panel.

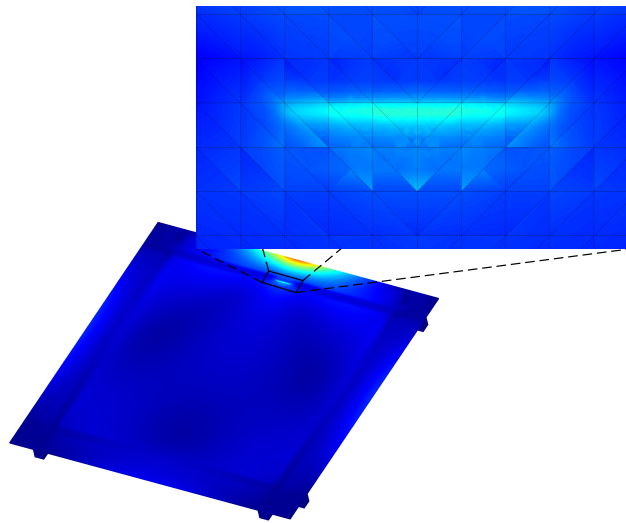
element analysis, which requires high levels of localized mesh refinement, is prohibitively expensive. Furthermore, because global–local enrichments are hierarchical, the initial factorization of the global stiffness matrix can be saved and reused for each case, reducing the computational expense when many cases are necessary.

This example is a 600×600 mm thin panel with stiffener beams along each edge. Three different sharp, Gaussian flux loading cases are analyzed in this problem, as illustrated, along with the geometry of the panel, in Figure 2.11. The sharp fluxes are applied on the top of the panel, near a stiffener beam, and temperature boundary conditions are applied on the panel edges perpendicular to the spike. The domain is insulated elsewhere. In case “A,” the flux lies on the interior of the panel, in case “B,” directly on top of the edge stiffener beam, and case “C,” on the outside of the panel, close to the edge. In the structural analysis, the panel is allowed to expand freely, and is only constrained against rigid body motion. The effect of varying the location of the spike on the resulting thermal and structural quantities of interest is examined.

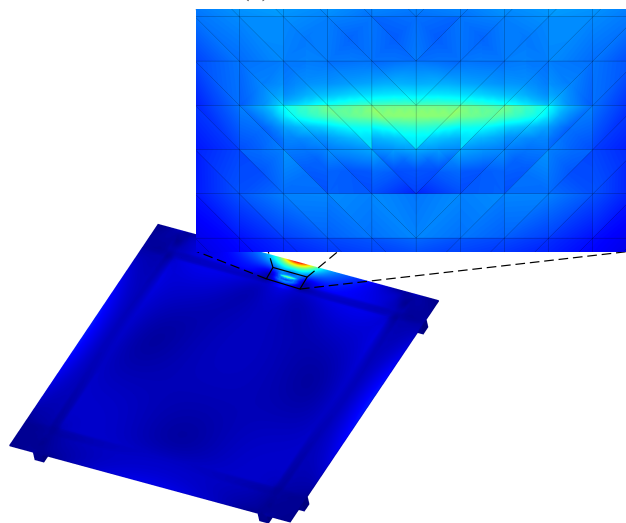
Figure 2.12 shows the von Mises stress fields resulting from each analysis case. The stress as well as temperature magnitude are affected significantly by the location of the sharp laser heating with respect to the stiffener beam. Just as in the case of the laser-heated beam, the stress field in the vicinity of each thermal load case is *still intense*, regardless of the lack of global structural constraints. Furthermore, it is noteworthy that the resolution of the intense, localized loading is critical to the global behavior of the system in all cases.



(a) Load case A



(b) Load case B



(c) Load case C

Figure 2.12: GFEM^{gl} solution contours of von Mises stress in the stiffened panel problem.

Table 2.4: Wall times (in seconds) in each solution phase for all load cases in the stiffened panel problem.

Load case	Initial		Local		Enriched		Total	
	Assemble	Solve	Assemble	Solve	Assemble	Solve		
Heat transfer	A		1.34	5.82	5.47	3.98		
	B	0.32	1.16	4.89	58.89	16.88	6.34	121.03
	C			1.27	5.32	4.94	4.41	
Thermoelasticity	A			27.86	91.10	19.79	222.20	
	B	18.78	151.56	104.93	1345.95	74.76	516.56	2954.63
	C			26.16	83.16	18.43	253.40	

Table 2.4 summarizes computation times for each aspect of the problem—initial global, local, and enriched global stages for both heat transfer and thermoelasticity. It is very noticeable that the expense associated with resolving localized stress/strain fields due to sharp heating is orders of magnitude higher than the effort required for the heat transfer solution. It is also clear that the parallelization of local computations based on techniques developed in [63, 106] is necessary to reduce computational effort in local problems. However, reuse of the initial global solution via the system partitioning (2.29) and reanalysis algorithm above provides some savings in this large example.

2.6 Summary

This chapter presents the extension of the *hp*-GFEM and GFEM^{gl} to thermomechanical problems exhibiting challenging localized solution characteristics. The framework presented for coupling the multidisciplinary problems exploits special features of the method to accomplish an efficient and reliable exchange of information. Traditional coupling techniques often involve communication between separate analysis codes requiring interpolation of the solution or nodal quantities, which is impractical for problems of interest with very high, localized gradients contained within individual mesh elements. This framework has been shown to lead to vastly improved efficiency in the class of problems of interest where extremely high levels of local mesh refinement are required to resolve sharp solution gradients, compared to traditional coupling techniques.

The robust combination of accuracy and computationally efficient physics coupling enables high-fidelity simulation of three-dimensional, localized thermomechanical effects on the coarse, structural scale, yielding results which are comparable to direct finite element analysis (DFEA) for the problems examined.

The extremely high temperatures and temperature gradients in problems of interest in this study, however, quite often lead to localized plasticity and damage evolution in the material. Thus, an analogous extension of this method to thermoplasticity problems is required to obtain realistic and useful results in the prediction of residual deformations of structures in relevant application areas; this extension of the method to nonlinear problems is detailed in Chapter 4.

Chapter 3

A GFEM for resolving fine-scale material heterogeneity

Another important class of problems exhibiting multiscale thermomechanical features discussed in the introductory segment of this study is those problems with internal material interfaces and fine-scale heterogeneity. The primary class of methods aimed at bridging between micro- and macro-level effects has historically been homogenization-based methods. It is therefore necessary to mention quite a few additional methods beyond those described in Section 1.2 detailed in the literature which attempt to solve this problem. Among recent works, representative examples are coupled hierarchical multiscale approaches like the previously discussed FE^2 (Feyel, Chaboche, Unger, Özdemir et al.) [37, 38, 99, 100, 133]. The gradient-enhanced FE^2 of Kouznetsova, Geers, and Brekelmans [65] addresses some of the limitations of the original FE^2 related to the presence of discontinuities in the analysis domain. Belytschko et al. [8, 74] present the multiscale projection method, another example of a continuous–discontinuous homogenization scheme where the XFEM [7, 82] is used to incorporate discontinuities at the macro-scale. The Multiscale Aggregating Discontinuities (MAD) method introduced by Belytschko et al. [10, 120] is an extension of the FE^2 which is able to model macro cracks, in which cohesive forces on crack faces are calculated from the fine scale problems. Similarly Matouš et al. [77] propose a multiscale FE^2 which is also able to consistently handle macro-scale cohesive cracks.

Concurrent embedded multiscale methods, in which two disparate scales are discretized simultaneously, include the Voronoi Cell Finite Element Method of Ghosh et al. [45–48, 111], the multiscale approach of Liu et al. [72, 78, 79], and the method of Cloirec et al. [14]. Lagrange multiplier methods are typically used to couple the macro- and micro-scale discretizations in this class of methods, such as the Mortar method [66] or the Arlequin method of Ben-Dhia [18].

Additional examples of multiscale methods proposed in recent years include domain decomposition methods, like the FETI-DP method of Farhat et al. [36], the variation of this method proposed by Lloberas-Valls et al. [73], the domain decomposition-based method of Guidault et al. [49], and the multigrid method proposed in [113]; the method of Fish et al. based on a decomposition of the fine scale displacement field into eigenstrains and eigenseparations [96, 141]; the variational multiscale enrichment method (VME) of Oskay [97, 98]; and the Multiscale FEM of Tom Hou et al. [35, 54].

The above list of multiscale methods is far from exhaustive; a recent review of the state-of-the-art in multiscale

computational homogenization techniques is available in [43].

Nearly all hierarchical multiscale approaches achieve coupling between scales of interest by the numerical solution of a macroscale boundary value problem using homogenized or upscaled properties from micro-scale problem solutions. A persistent limitation in these approaches is that homogenized parameters may misrepresent complex solution behavior in the vicinity of localized phenomena such as stress raisers, fractures or sharp temperature gradients. The solution of the homogenized equations u_H has been shown to be a good approximation to the solution u of the original problem in the L^2 norm, but not, in general, in the energy norm [5]. Thus, quantities such as strains and stresses computed from u_H may be inaccurate, since the derivatives of u are large and oscillatory in regions containing localized effects, yet understanding the behavior of local stress and strain fields around sharp solution gradients is necessary to quantify failure initiation and evolution in heterogeneous materials and structures.

For a detailed description of GFEM and the GFEM^{gl}, please refer to Section 2.2. In Section 3.1 the GFEM^{gl} is extended for the case of heterogeneous materials, as presented in [106], in which the global problem resolves the overall structural response, while local problems are solved *in parallel* to capture and bridge information about fine-scale material heterogeneities back to the coarse scale. This method is demonstrated on several three-dimensional heat transfer problems which have fine-scale material features combined with localized solution behavior in Section 3.2 to explore its accuracy, computational efficiency, and flexibility relative to a direct analysis approach.

3.1 Scale-bridging with GFEM^{gl}

To resolve localized solution effects due to material microstructural features, the particular application of this work, local problems typically require extensive mesh refinement, and physical regions of the global domain where global–local enrichments are necessary may also be large. In this instance, local problems enclosing the solution behavior of interest comprise prohibitively many degrees of freedom and the cost of a GFEM^{gl} analysis becomes comparable to a DFEA. Since DFEA is widely regarded as an unrealistic option for this class of problems featuring highly disparate spatial scales, an approach which has been identified to drastically reduce the computational cost per GFEM^{gl} local problem is dividing large local problems into smaller, ‘sub-local’ domains [63].

3.1.1 GFEM^{gl} with sub-local domains

Just as in the standard GFEM^{gl} approach described previously, a local problem domain Ω_L is selected according to (2.14) which encloses a region or localized solution feature of interest, and mesh adaptivity is performed. However, in the GFEM^{gl} with sub-local problems, this local domain is automatically subdivided into smaller, more computationally

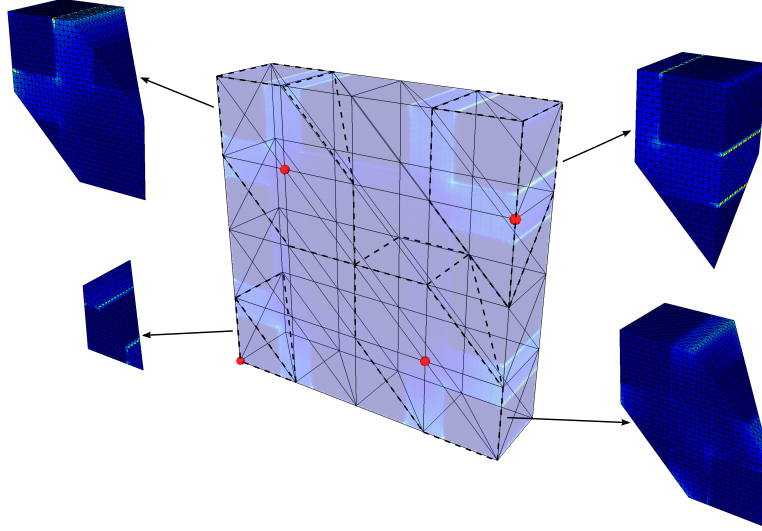


Figure 3.1: Coarse global mesh and four sample sub-local domains used to generate GFEM^{gl} enrichment functions for each global patch—50 sub-local domains are used in the actual analysis of this problem. The boundaries of sub-local domains are indicated with dashed lines.

manageable sub-local problems, each of which corresponds to a global patch ω_α used to seed the local problem, i.e.,

$$\Omega_{L\alpha} = \omega_\alpha, \quad \alpha \in \mathcal{I}^{gl}. \quad (3.1)$$

This concept is demonstrated in Figure 3.1, which shows just a few example sub-local domains (though 50 sub-local problems are actually extracted and solved in the illustrated example).

In the context of multiscale problems, each sub-local domain could be viewed as a sort of ‘unit cell’ to represent a single microstructural feature. However, a key difference is that, inherently, sub-local domains of adjacent global patches overlap, as in Figure 3.2, which shows two global patches used to generate a local problem. This overlap leads to some additional computational effort compared to the traditional GFEM^{gl} with monolithic local problems, since the same physical region in the global domain may be solved multiple times in several independent sub-local problems. However, since each sub-local problem is solved independently of each other, the cost of solving all sub-local problems on a parallel computer is smaller than solving a single large local problem (cf. Section 3.1.2). Furthermore, because sub-local solutions are inserted into the global approximation space using a partition of unity, continuity at sub-local boundaries is trivially enforced in the GFEM^{gl}.

3.1.2 Parallelization of sub-local computations

Each sub-local problem depends only upon the initial global solution for boundary conditions and, therefore, is solved independently of and free of communication with all other sub-local problems, which allows for efficient and straight-

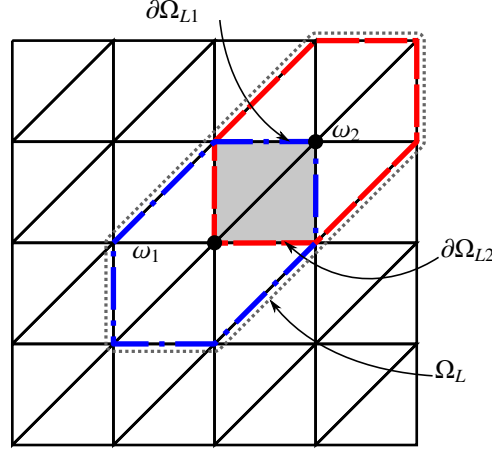


Figure 3.2: Global mesh and overlapping patches ω_1 and ω_2 used to generate sub-local problems. Part of the boundary $\partial\Omega_{L1}$ is interior to ω_2 , while part of $\partial\Omega_{L2}$ is also interior to ω_1 . The overlapping region is shaded. The equivalent local problem domain Ω_L is also denoted by a dotted outline, constructed according to (2.14).

Algorithm 3.1 Parallel solution of GFEM^{gl} sub-local problems.

```

create  $n_{loc}$  sub-local problems (as in Section 3.1.1), collect and sort in a list;
initialize number of problems solved  $i \leftarrow 0$ ;
while  $i < n_{loc}$  in parallel do
    select next problem  $i$  from list;
     $i \leftarrow i + 1$ ;
    solve sub-local problem  $i$ ;
end while

```

forward parallelization of the GFEM^{gl} [63]. In the class of problems of interest, where a very large number of sub-local problems may be necessary to effectively bridge spatial scales, parallel speed-up is crucial to the practicality of the method.

The simplicity of GFEM^{gl} parallelization is described in Algorithm 3.1. The only caveat is that sub-local problems must be selected in only one thread at a time and subsequently delegated to another thread in the team in order to avoid a race condition. Additionally, because sub-local problems may vary in size and expense, for example, close to the global boundary as opposed to on the interior of the domain (compare bottom left and top left sub-local problem domains in Figure 3.1), the order in which they are solved may affect parallel efficiency, and thus sorting may be necessary. A much more detailed discussion of the parallelism of the method as well as additional implementational details are available in [63].

3.1.3 Numerical integration of weak form

Because neighboring patches of elements are enriched with *different* sub-local solutions, and thus defined on different sub-local domains, integration of the enriched global weak form can, in general, be complicated in the overlap region, due to the highly adapted nature of sub-local problems and potential mesh incompatibility issues. However, in the

GFEM^{gl}, since all refinement is performed on the local mesh *before* subdivision into sub-local problems, adjacent sub-local problems have matching meshes where they overlap. This greatly simplifies numerical integration of global–local shape functions in the global problem, since sub-local solutions can then be integrated exactly using the refined, unsubdivided local mesh. Further explanation of this issue can be found in [63].

Moreover, in order to resolve fine-scale material effects, accurate integration of the left hand side is crucial, due to rapid spatial variation in the thermal conductivity $\kappa(\mathbf{x})$. In the coarse-scale, initial global analysis given by (2.12) or (2.21), however, *only coarse-scale integration* of the left hand side is used, since only coarse-scale response is needed to generate boundary conditions for fine-scale problems. On the other hand, in the local and enriched global problems, the left hand side can be integrated exactly using the heavily refined local mesh. Global integration is carried out using a parallel implementation, as discussed in Appendix B.

3.1.4 Multiscale effects on sub-local boundaries

A major challenge when dealing with material heterogeneities is the oscillations, high gradients, and singularities of the exact solution. The initial global problem is discretized using a coarse mesh designed to capture only smooth, structural-scale behavior; therefore, boundary conditions on sub-local domains are also smooth. The fine-scale behavior of the exact solution is then lost at individual sub-local boundaries. As made clear by Figure 3.2, however, in the GFEM^{gl} each sub-local problem boundary lying on the interior of the global domain, i.e., $\partial\Omega_L \setminus (\partial\Omega_L \cap \partial\Omega)$ is *interior to another sub-local problem* on an adjacent patch in the overlap region. Therefore, resulting global–local enrichment functions are able to capture highly oscillatory fine-scale effects *even across element or sub-local problem boundaries*. This is in contrast to competing methods, which may require harsh constraints on fine-scale approximation functions at local boundaries, thereby potentially losing important localized solution characteristics. Strategies to further improve the boundary conditions applied to sub-local problems are discussed in the next section.

3.1.5 Improvement of boundary conditions on sub-local problems

Inexact and often poor boundary conditions on local problems from the coarse-scale global solution are the primary controlling factor in the quality of GFEM^{gl} solutions. Based on detailed studies of the method as it is applied to several classes of problems, solution behavior due to local boundary conditions can be problem-dependent [51]. In GFEM^{gl} analyses with sub-local problems, the effect of the boundary conditions becomes even more important, due to the inherently smaller local problems and resulting proximity of local boundaries to sharp solution features. Two strategies have been identified in [51] to improve their quality:

- (i) multiple global–local iterations, and/or

(ii) use of a ‘buffer zone’ to dampen the effect of error in boundary conditions altogether.

3.1.5.1 Global–local iteration

As previously described in Chapter 2, carrying out multiple global–local iterations is one promising method for improving GFEM^{gl} solutions [51, 90]. After the initial GFEM^{gl} analysis according to Section 2.2.1, sub-local problems are solved again, substituting the enriched global solution θ^E or \mathbf{u}^E , in heat transfer and thermoelasticity, respectively, for the initial global solution θ^0 or \mathbf{u}^0 , providing an improved estimate of the global solution as a boundary condition on the sub-local problems. This iteration can be carried out as many times as needed. It should be noted that unlike traditional iterative methods, typically only a few iterations are sufficient to obtain an accurate solution. However, inherent in this approach is the additional computational expense of solving each highly refined sub-local problem and enriched global problem multiple times—fortunately, in the case of linear problems, this entails only forward and backward substitutions, since the stiffness matrices of sub-local problems do not change between iterations.

An additional issue associated with global–local iteration in problems where extensive mesh refinement is present at each sub-local problem boundary may impact computational efficiency. Bridging the enriched global solution, which is based on local enrichments defined on the *previous* heavily refined local problem, to the boundary of the *current* similarly heavily refined local problem is necessary (and the same issue appears, as will be demonstrated in Chapter 4, for time-dependent problems, when local boundary conditions at each time step are derived from enriched global solutions at the previous time step). This requires expensive searching and mapping algorithms to transfer information between the *first* enriched global solution and *second* local problem(s), which can be complex and even unreliable for extreme levels of mesh refinement in local problems. However, the topology of local meshes remains the same in between local problem iterations, and a one-to-one correspondence exists between each sub-local problem element in overlapping regions. Leveraging this information, an optimized approach (similar in nature to the multi-physics coupling framework detailed in Chapter 2 and Appendix A) can be adopted to more efficiently map enriched global solutions onto the boundary of each sub-local problem; the implementation of this approach is explained in Appendix B.

3.1.5.2 Buffer zone

The buffer zone strategy consists of selecting a *larger* sub-local domain than the corresponding global region enriched by that sub-local solution. In terms of seed patches, this can be interpreted as $\mathcal{I}_{\text{enriched}}^{gl} \subset \mathcal{I}_{\text{local problem}}^{gl}$.

The buffer zone approach is the simplest strategy, as it involves solving the initial global, local, and enriched global problems only once, potentially saving substantial computational effort compared to global–local iteration, and is straightforward to implement. In this study, this approach is not used because of the larger and more expensive sub-

Table 3.1: Sub-local problem details from GFEM^{gl} analyses of the laser-heated beam problem: (enriched) global problem sizes (in degrees of freedom) relative to DFEA and sizes of the largest sub-local problems at each global mesh size.

Method	Sub-local problems	Global problem size		Max. local problem size		
		Heat	Elasticity	Heat	Elasticity	
DFEA (<i>hp</i> -GFEM)	—	146,142	949,968	—	—	
GFEM ^{gl}	H_1	45	673	4,845	81,081	513,513
	H_2	275	1,823	12,435	11,169	70,737
	H_3	1,589	8,393	55,797	1,701	10,773

local problems which result. The effect of using a buffer zone in parallel sub-local problems is unclear and potentially interesting, however, and is left for future investigation.

3.2 Numerical examples

3.2.1 Homogeneous laser-heated beam

In order to most directly compare the performance of the parallel GFEM^{gl} to the traditional GFEM^{gl} with monolithic local problems, before moving to problems exhibiting fine-scale material features, the *homogeneous* thermoelastic laser-heated beam problem of Section 2.5.2 is revisited; in this chapter, the identical problem is solved using the parallel approach with sub-local problems. It has already been shown that parallel efficiency of the method improves as the number of sub-local problems is increased by slightly refining the global mesh H while holding constant the local mesh size h , i.e., reducing the ratio H/h . This gain in efficiency is due to the lower computational cost of individual problems and a more uniform load balance, and comes without a significant impact on overall solution accuracy.

In each case, the coarse global mesh shown in Figure 2.7a ($H = 0.5$) is refined gradually in the neighborhood of the sharp laser flux, resulting in global mesh sizes of $H_1 = 0.25$, $H_2 = 0.125$, and $H_3 = 0.0625$. Corresponding global meshes are superimposed on contour plots shown in Figure 3.3. The global heat transfer and thermoelasticity problems have polynomial orders of approximation $\mathbf{p}^\theta = \{2, 2, 2\}$ and $\mathbf{p}^u = \{3, 3, 3\}$, respectively, while all sub-local problems use $\mathbf{p}_L^\theta = \{3, 3, 2\}$ and $\mathbf{p}_L^u = \{4, 4, 3\}$. The element size in sub-local problems in each case is $h \approx 0.0078$. Sub-local problem details for this example are given in Table 3.1. Unless otherwise noted, all examples are solved using 24 CPUs on a shared memory machine with 384 GB RAM, and a direct linear solver is used in all cases.

Because local problems are subdivided into smaller sub-local domains, inherently more local boundaries are created in the parallel version of the GFEM^{gl}; thus, error in boundary conditions from the coarse-scale global problem solution on local problems may often govern overall error in the final, enriched global solution. As previously dis-

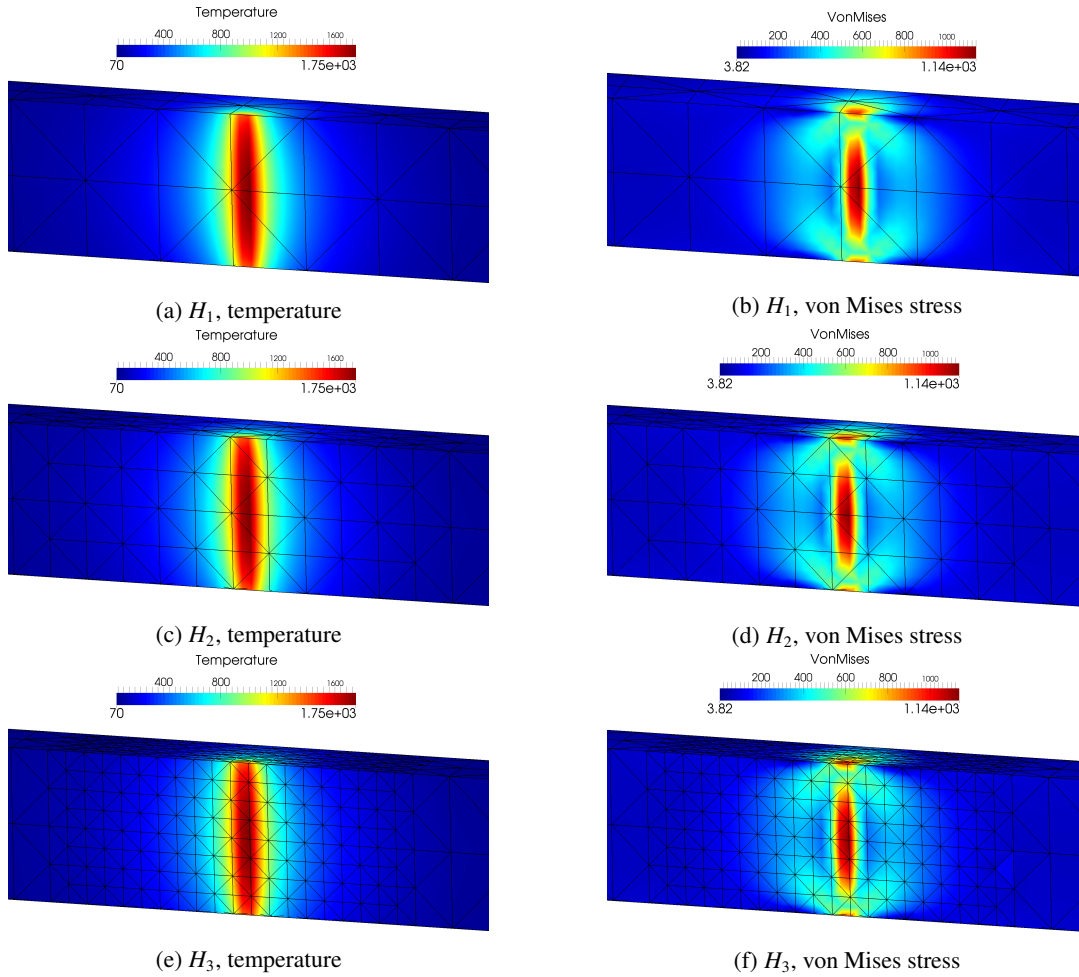


Figure 3.3: Laser-heated beam GFEM^{gl} solution contours using sub-local problems at various global mesh refinement levels.

cussed, strategies have been identified to improve these inexact boundary conditions [51, 106]. One such improvement strategy is the use of multiple global–local iterations, which replaces the coarse-scale, initial solution as a boundary condition on local problems with the better-quality enriched global solution. Multiple global–local iterations are carried out on the laser-heated beam at each global mesh refinement level. GFEM^{gl} solution contours from the parallel approach using sub-local domains at each global mesh refinement level are shown in Figure 3.3. Solutions are shown at the final global–local iteration in each case. Figure 3.4 demonstrates the evolution of von Mises stress under the sharp laser heating at global mesh size H_2 in each enriched global solution. The stress is shown along the centerline of the beam, at a depth $z = 0.16$ below the surface upon which the laser heating is applied. It is apparent from this figure that oscillations in the solution may be present near local problem boundaries due to poor-quality boundary conditions from the coarse-scale global solution. However, after even just one additional global–local iteration, the smoothness of the solution in the vicinity of the sharp thermal gradient is improved drastically.

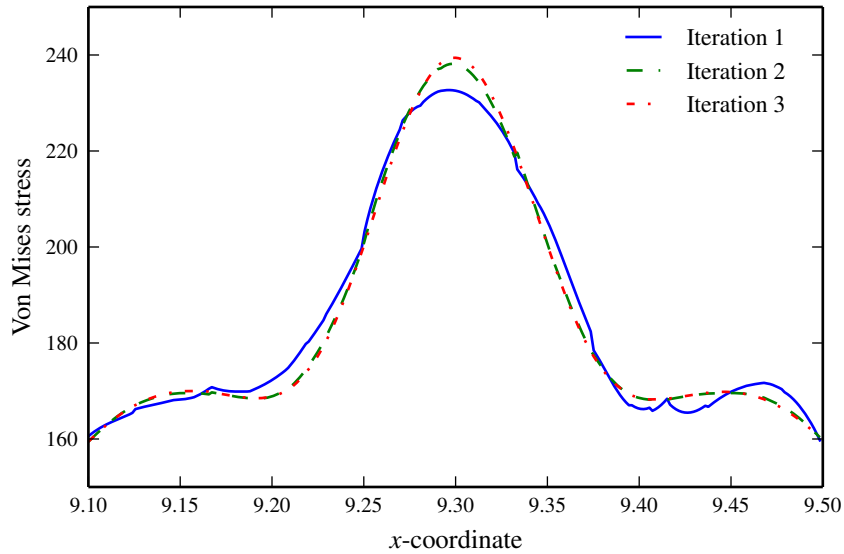


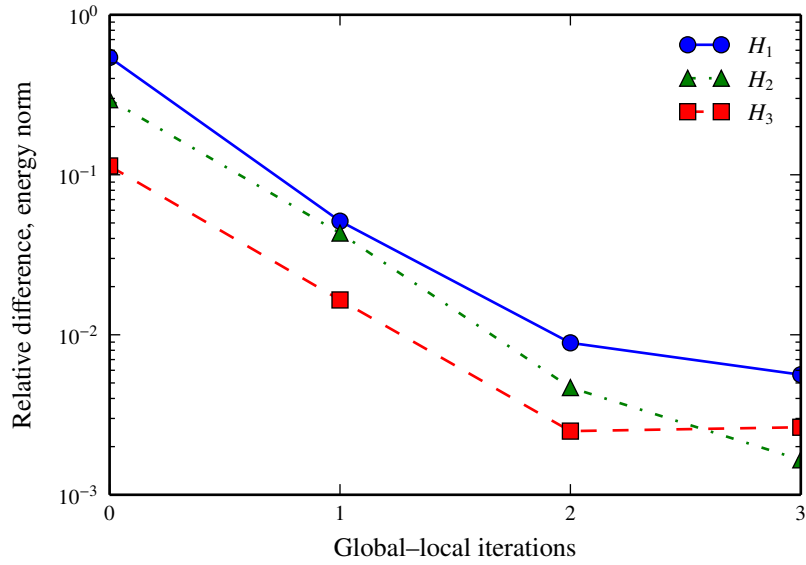
Figure 3.4: Laser-heated beam von Mises stress field under the sharp heating along the center of the beam, at depth $z = 0.16$, at each global–local iteration.

In order to better quantify the accuracy of the GFEM^{gl} solutions, Figure 3.5 shows convergence of global error measures—in this case, relative difference in the energy norm of each solution, computed using (2.27) and (2.28)—of both heat transfer and thermoelasticity solutions at each global mesh size with respect to an equivalent direct finite element analysis. The equivalent DFEA employs the *hp*-adaptive GFEM with an identical localized mesh refinement level and polynomial order of the approximation as GFEM^{gl} simulations, as described previously. After global–local iterations, the GFEM^{gl} at each global mesh size converges to a solution very similar to the equivalent DFEA in both heat transfer and thermoelasticity problems, resulting in all cases in a relative difference in the energy norm of under 1%. For a given mesh refinement level (local mesh refinement in GFEM^{gl}; localized global mesh refinement in the DFEA) it is therefore possible to obtain a global accuracy level with GFEM^{gl} which is on par with optimal *hp*-adaptive approaches for this problem.

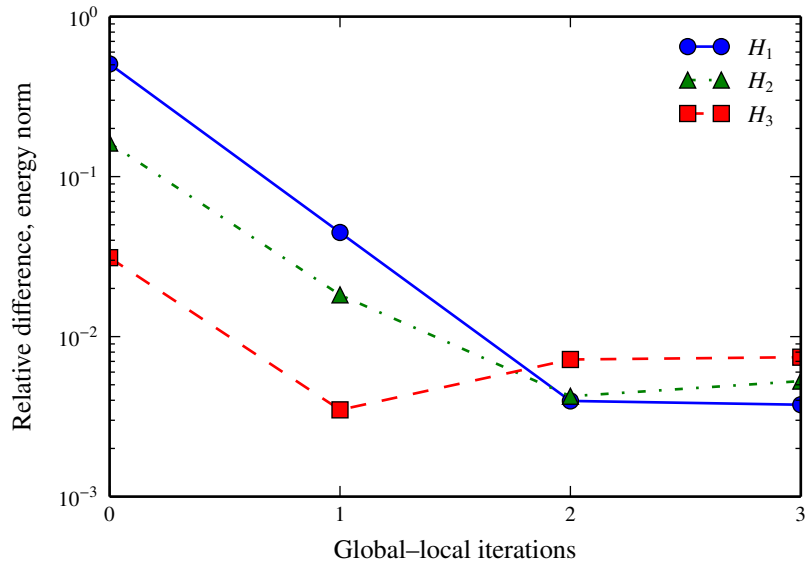
In addition to global measures of solution quality, local or pointwise quantities are also considered. Thus, maximum von Mises stresses from GFEM^{gl} thermoelasticity solutions are compared in Figure 3.6. The pointwise quantities of interest in the neighborhood of localized features obtained from GFEM^{gl} simulations are shown to be accurate when compared to a direct finite element analysis, converging to relative difference levels well under 1%.

3.2.2 Square domain with material microstructure

The next example presented exhibits multiscale effects in the form of material heterogeneity: a three-dimensional, square domain with a bi-material “microstructure”, inspired by [98], subjected to strong convective boundary con-



(a) Heat transfer



(b) Thermoelasticity

Figure 3.5: Convergence of relative difference in the energy norm of laser-heated beam GFEM^{gl} solutions at various global mesh sizes H after global-local iterations with respect to equivalent DFEA. Iteration zero represents the coarse-scale initial global solution.

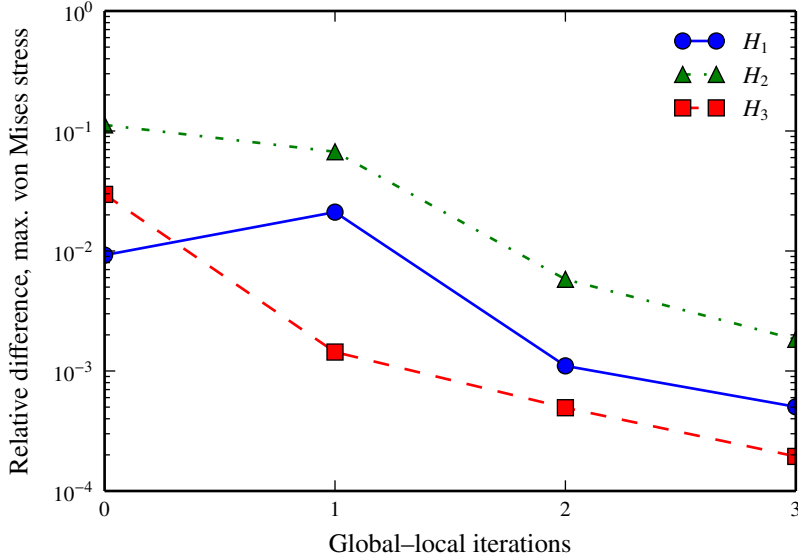


Figure 3.6: Pointwise convergence of maximum von Mises stress in laser-heated beam GFEM^{gl} solutions at various global mesh sizes H after global–local iterations, computed with respect to DFEA. Iteration zero represents the coarse-scale initial global solution.

ditions on top (θ_{top}) and bottom (θ_{bottom}), and left (θ_{left}) and right (θ_{right}) faces to induce a nearly two-dimensional steady-state heat diffusion through the domain. When the thermoelasticity problem is solved, homogeneous displacement boundary conditions are applied on top, bottom, left, and right faces. This problem is solved for various resolutions (1×1 , 2×2 , and 4×4) of the repeating microstructural pattern, as described in more detail for each case to follow.

3.2.2.1 1×1 (unit) cell

Geometry and boundary conditions of this simplest, “unit cell” case are depicted in Figure 3.7. This example is solved for the heat transfer problem only. The ratio of conductivities of each material phase is $\kappa_a/\kappa_b = 50$. This example serves to verify that the GFEM^{gl} is able to reproduce a reference hp - or adaptive GFEM direct finite element analysis (DFEA) on a coarse mesh in the presence of material heterogeneity.

The hp -GFEM DFEA employs heavy, uniform mesh refinement and polynomial order $\mathbf{p}_{\text{DFEA}} = \{2, 2, 1\}$. On the other hand the GFEM^{gl} global mesh is much coarser, with $\mathbf{p} = \{1, 1, 1\}$, or only the linear partition of unity. The GFEM^{gl} local problem is chosen accordingly as the *entire unit cell* domain, which provides exact boundary conditions from the global domain, since $\partial\Omega_L = \partial\Omega$, the simplest possible case. The GFEM^{gl} local problem also uses the same mesh refinement level and polynomial order $\mathbf{p}_{\text{loc}} = \mathbf{p}_{\text{DFEA}}$ as the DFEA, so that the two solutions are identical. Figure 3.8 demonstrates the DFEA (and, thus, also the GFEM^{gl} local problem) mesh, as well as the coarse, global mesh used in the GFEM^{gl}, all consisting of structured, 4-node GFEM tetrahedra. While the material microstructure is selected to

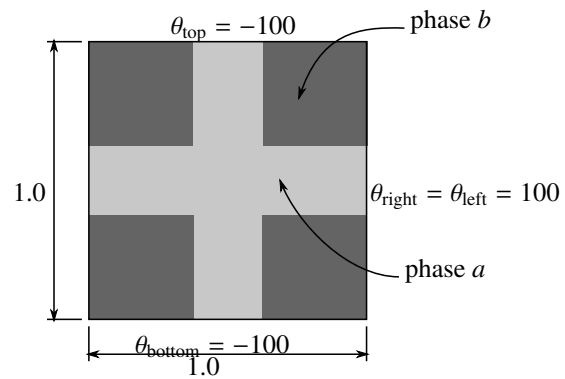


Figure 3.7: Geometry of the square unit cell domain with bi-material microstructure.

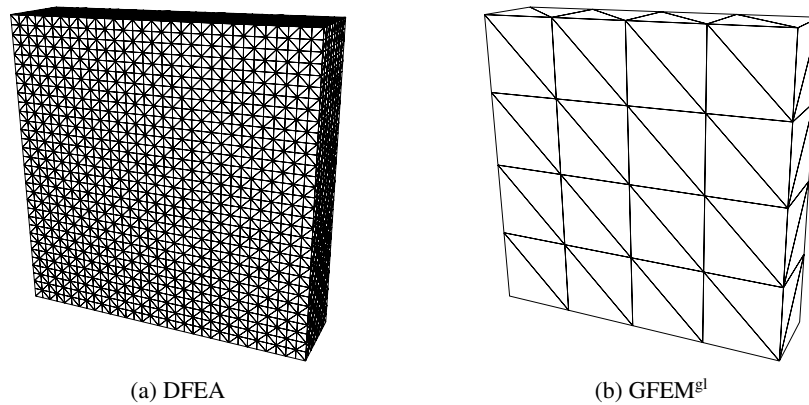


Figure 3.8: GFEM meshes used to solve the 1×1 cell with each method. The adaptive GFEM DFEA mesh is identical to the mesh used in the GFEM^{gl} local problem.

Table 3.2: Comparison of GFEM^{gl} solution of the bi-material unit cell with adaptive GFEM DFEA for verification (heat transfer only).

Method		Global dofs	Energy ($\times 10^5$)	% difference
DFEA		53,979	3.094	–
GFEM ^{gl}	initial	50	4.322	39.68%
	local	53,979	3.094	0.00%
	enriched	100	3.099	0.15%

fit the mesh refinement pattern in all examples presented for simplicity’s sake, arbitrary microstructural features may also be modeled in through the use of GFEM enrichments like those described in [1, 84, 124].

A summary of the numerical simulation results is given in Table 3.2. As expected, DFEA and GFEM^{gl} local problem solutions are identical, and using only the partition of unity and global–local enrichment functions, the GFEM^{gl} is able to reproduce the reference solution with fine-scale details on the coarse, global mesh for this special case.

3.2.2.2 2×2 cells

To determine the impact of local boundary conditions on GFEM^{gl} solutions to the multiscale problems of interest, as well as the effectiveness of proposed boundary condition improvement strategies, the next case is a slightly larger problem than the above example, consisting of 4 of the microstructural unit cells—2 in the x - and 2 in the y -direction—with otherwise identical geometry and boundary conditions. This example, however, is analyzed using the multiphysics coupling framework for the thermoelastic solution. The coarse global mesh is shown in Figure 3.10. Now adopting the sub-local GFEM^{gl} approach, global–local enrichment functions are constructed from numerical solutions of 50 hp -adapted sub-local problems.

As in the previous example, both DFEA and GFEM^{gl} meshes consist of structured, 4-node tetrahedral elements. In this case, *two* hp -GFEM direct analyses are carried out: one is an ‘equivalent’ hp -GFEM solution with an equivalent level of fidelity to GFEM^{gl} simulations, while the other is used as a reference solution to which both the equivalent DFEA and GFEM^{gl} solutions are compared. The *equivalent* DFEA uses heavy, uniform mesh refinement and global polynomial degree $\mathbf{p}_{\text{DFEA}}^\theta = \{2, 2, 1\}$ in the heat transfer problem. The *reference* DFEA, on the other hand, has the same level of mesh refinement, while $\mathbf{p}_{\text{DFEA}}^\theta = \{3, 3, 2\}$. In GFEM^{gl} simulations $\mathbf{p}^\theta = \{1, 1, 1\}$ globally, while adapted sub-local problems use $\mathbf{p}_{\text{loc}}^\theta = \{2, 2, 1\}$. In all instances, the thermoelasticity problem uses one polynomial order higher than the heat transfer problem.

Unlike the 1×1 verification example, however, local problem boundaries which lie on the interior of the global domain introduce *inexact* boundary conditions from the coarse-scale solution. Of the two boundary condition improvement strategies discussed in Section 3.1.5, only the strategy involving multiple global–local iterations is examined for

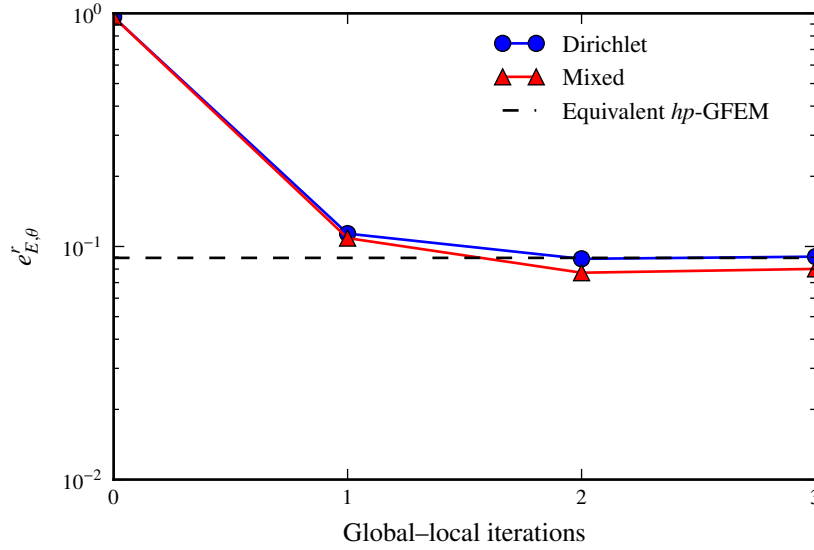


Figure 3.9: Convergence of relative error in the energy norm of GFEM^{gl} heat transfer solutions of the 2×2 square domain after global–local iterations, using various local boundary condition types. Zero global–local iterations indicates the coarse-scale, initial global solution. The dashed line represents the relative error (with respect to the hp -GFEM reference solution) of the equivalent hp -GFEM solution.

each boundary condition type. Because of the large number of local problems and high level of local mesh refinement, the buffer zone strategy for boundary condition improvement is not considered, so as to incur a lower computational cost per sub-local problem.

Convergence of GFEM^{gl} solutions with respect to the reference DFEA solution after global–local iterations for each boundary condition type in the heat transfer problem is shown in Figure 3.9. The equivalent DFEA is also shown for comparison. Relative error in the energy norm of each solution θ_h with respect to the reference solution θ^{ref} is computed as

$$e_{E,\theta}^r = \frac{\sqrt{|\mathcal{B}(\theta^{\text{ref}}, \theta^{\text{ref}}) - \mathcal{B}(\theta_h, \theta_h)|}}{\sqrt{|\mathcal{B}(\theta^{\text{ref}}, \theta^{\text{ref}})|}}.$$

After just two global–local iterations, in the Dirichlet case, the relative difference in the energy norm between GFEM^{gl} and the equivalent DFEA is on the order of 1%, whereas mixed boundary conditions on sub-local problems yield a result which is slightly closer to the reference solution. No significant further improvement in the solution is observed past two iterations for any boundary condition type tested. The enriched global flux field contours after three iterations resulting from each type of boundary condition on sub-local problems in the GFEM^{gl} are also shown in Figure 3.10. The presence of fine-scale singularities at sharp material interfaces and across global element boundaries can be observed; localized, sharp gradients in the flux field are accurately resolved across scales by the GFEM^{gl}.

Analogous results for the thermoelastic problem are given in Figure 3.11, where relative error in the energy norm

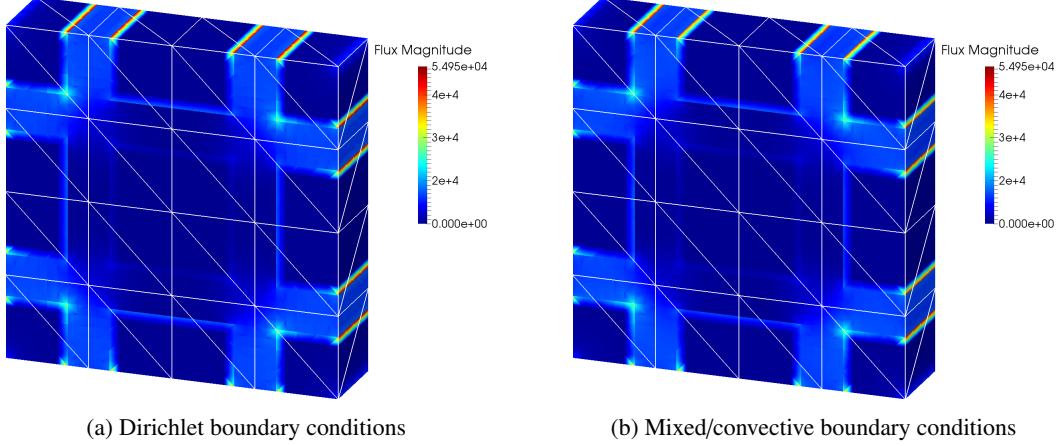


Figure 3.10: Enriched global flux magnitude contours of the 2×2 square example solved with GFEM^{gl} after three global–local cycles, based on Dirichlet and convective boundary conditions in sub-local problems. The coarse global mesh is also superimposed in each case.

of the each solution \mathbf{u}_h with respect to the reference solution \mathbf{u}^{ref} is given by

$$e_{E,\mathbf{u}}^r = \frac{\sqrt{|\mathcal{B}(\mathbf{u}^{\text{ref}}, \mathbf{u}^{\text{ref}}) - \mathcal{B}(\mathbf{u}_h, \mathbf{u}_h)|}}{\sqrt{|\mathcal{B}(\mathbf{u}^{\text{ref}}, \mathbf{u}^{\text{ref}})|}}.$$

Dirichlet and mixed boundary conditions exhibit a similar convergence behavior with respect to the reference DFEA, both attaining an error level close to or better than the equivalent direct analysis in this case. Unlike the heat transfer problem, Dirichlet boundary conditions on sub-local problems converge to a lower error level relative to the reference hp -GFEM solution more quickly than spring boundary conditions. The converged von Mises stress contours after three global–local cycles in the thermoelasticity problem are shown in Figure 3.12.

Based on results from both heat transfer and thermoelasticity, in Figures 3.9 and 3.11, respectively, discrepancies between Dirichlet and mixed boundary conditions may be attributed to problem-specific behavior. In general, it may be difficult to choose an optimal, representative spring stiffness or convective coefficient to ensure a low error level in GFEM^{gl} enriched global solutions relative to DFEA; Dirichlet boundary conditions, on the other hand, are straightforward and provide accuracy levels which are generally very similar or better than mixed boundary conditions. Regardless of the type of boundary conditions chosen for the GFEM^{gl} simulation, as error due to inaccurate boundary conditions in local problems decreases (i.e., as the quality of the global solution improves), *discretization error* in local problems, which is independent of the local boundary conditions, governs the overall solution accuracy.

Numerical results for the time required to assemble local problems during each global–local iteration are given in Table 3.3; results from both brute force and optimized approaches to assembling local problem boundary conditions, as described in Section 3.1.5, are included for comparison. Based on these results, it is clear that sub-local assembly

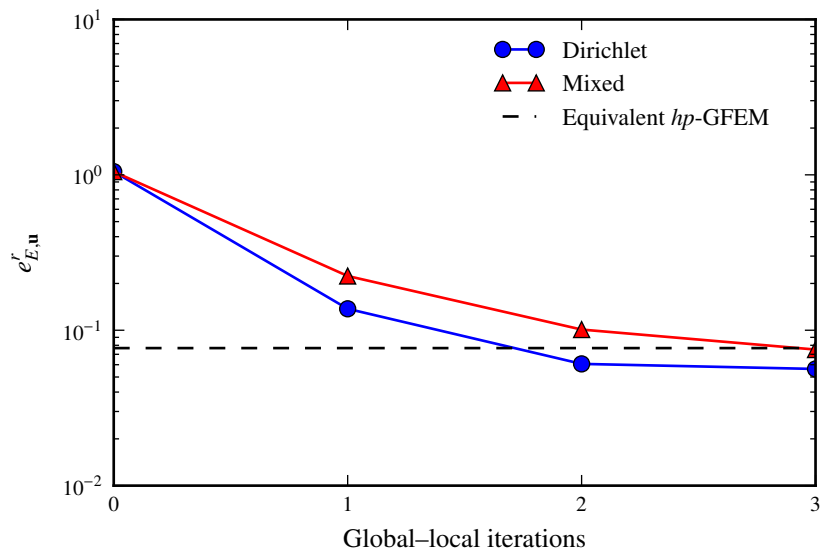


Figure 3.11: Convergence of relative error in the energy norm of GFEM^{gl} thermoelasticity solutions of the 2×2 square domain after global–local iterations, using various local boundary condition types. Zero global–local iterations indicates the coarse-scale, initial global solution. The dashed line represents the relative error (with respect to the hp -GFEM reference solution) of the equivalent hp -GFEM solution.

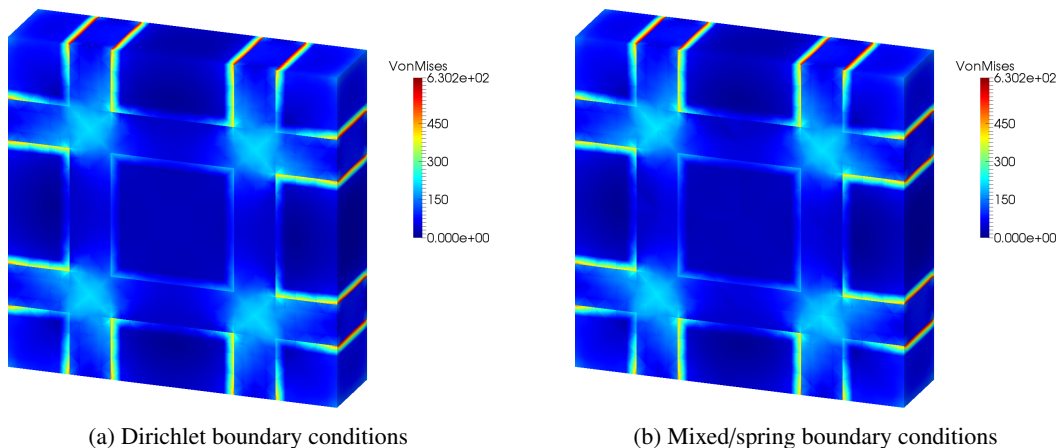


Figure 3.12: GFEM^{gl} von Mises stress contours of the 2×2 square problem after three global–local iterations with various local problem boundary condition types.

Table 3.3: Parallel local problem assembly wall times for each global–local iteration of the 2×2 square example (24 CPUs); brute force approach to assembling boundary conditions versus an optimized approach based on sub-local mesh topology. Heat transfer (Ω_L^θ) and thermoelasticity (Ω_L^u), respectively, are given.

B.C. type	Iteration	Brute force (s)		Optimized (s)		Speedup	
		Ω_L^θ	Ω_L^u	Ω_L^θ	Ω_L^u	Ω_L^θ	Ω_L^u
Dirichlet	1	0.57	18.40	0.56	19.81	0.99	0.93
	2	24.86	63.77	0.60	20.60	41.74	3.10
	3	23.47	64.22	0.55	21.69	42.84	2.96
Mixed	1	0.57	19.59	0.49	18.80	1.16	1.04
	2	25.25	112.66	0.55	24.71	45.89	4.56
	3	25.29	109.08	0.69	21.87	36.82	4.99

times are bottlenecked by the computation of boundary contributions. Using the brute force approach, initial local problems are the least expensive to assemble, since their boundary conditions are derived from the smooth, initial global solution, defined over a coarse mesh. However, computational effort is drastically increased in both heat transfer and thermoelastic problems after further iterations due to the substantial cost of searching and mapping of the enriched global solution quantities onto local problem boundaries. On the other hand, use of the topology of sub-local problem meshes at the boundary leads to assembly times which are on the same order as the initial global problem; in heat transfer, this leads to a 98% time savings, and 67% in the case of thermoelasticity. This drastic reduction in assembly effort affords the use of global–local iterations as a practical boundary condition improvement strategy, even in cases which require very high levels of mesh refinement in fine-scale, sub-local problems.

3.2.2.3 4×4 cells

To explore the computational efficiency of the method in large simulations, another example is provided, which is composed of 16 of the unit cells described in Section 3.2.2.1—4 in the x - and 4 in the y -direction. This problem is solved for heat transfer physics only. The geometry and boundary conditions of the larger problem are illustrated in Figure 3.13. Direct finite element analysis and a GFEM^{gl} solution are again compared. As in previous cases, global polynomial order in the reference solution is $\mathbf{p}_{\text{DFEA}} = \{2, 2, 1\}$, while in the GFEM^{gl} the coarse-scale global solution uses $\mathbf{p} = \{1, 1, 1\}$. 162 sub-local problems are solved in this instance with heavy mesh refinement and $\mathbf{p}_{\text{loc}} = \{2, 2, 1\}$.

The DFEA is comprised of over 1.6 million dofs, but the largest—and thus most computationally expensive—GFEM^{gl} sub-local problem is just under 54000 dofs, or roughly *30 times smaller* than the DFEA. The GFEM^{gl} enriched global problem, on the other hand, consists of only 324 dofs. The coarse, global mesh of structured, 4-node GFEM tetrahedral elements utilized to solve this example using GFEM^{gl} is shown in Figure 3.14. Only one global–local cycle (i.e., no additional boundary condition improvement strategy) is considered in this case.

To carry out the computations, the *hp*-GFEM DFEA utilizes a parallel implementation with 6 CPUs for assembly

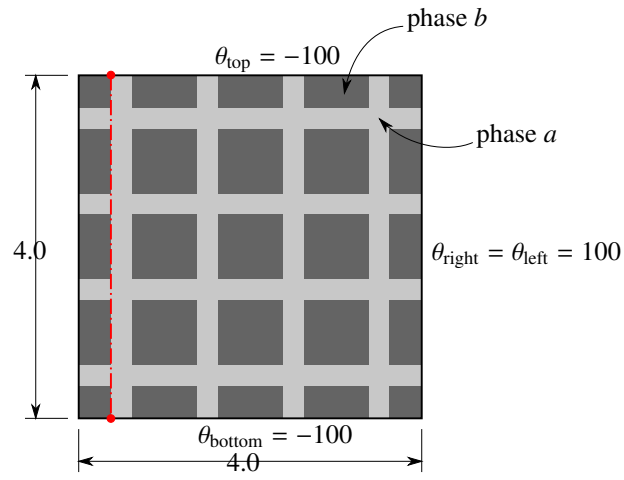


Figure 3.13: Geometry of the largest (4×4) square domain with bi-material microstructure.

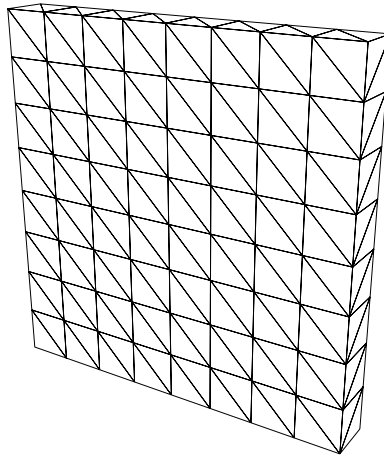


Figure 3.14: Coarse, global GFEM^{gl} mesh used to solve the largest (4×4) square domain example.

Table 3.4: Comparison of actual times to solution for the large square domain using GFEM^{gl} and DFEA.

Method	Assembly (s)	Solution (s)	Total (s)
DFEA	18.84	164.30	183.14
GFEM ^{gl} initial	0.00	0.01	
162 sub-local problems	24.42	90.75	
enriched	22.67	0.01	137.86

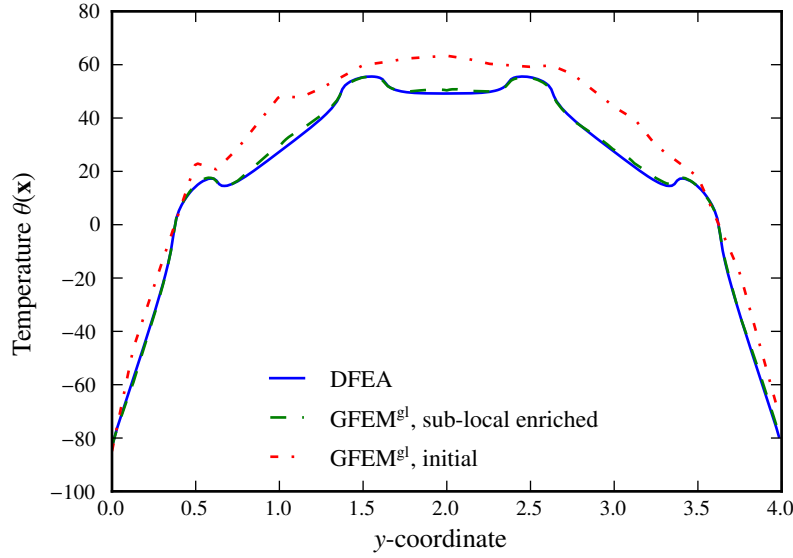


Figure 3.15: Vertical temperature profile in the 4×4 square domain at $x = 0.375$ (denoted by the dotted line in Figure 3.13): DFEA reference versus GFEM^{gl} coarse-scale, initial global and enriched solutions.

and solution of the global problem. Analogously, in the GFEM^{gl}, the 162 sub-local problems are assembled and solved in parallel using 6 CPUs, and assembly and solution of the global problem are also carried out in parallel. The solution times resulting from each method are provided in Table 3.4.

The GFEM^{gl} gives noticeably better computational efficiency—over 30% time savings—than the DFEA under the parallel implementation, even on a very small number of CPUs. While assembly of the DFEA is just slightly more efficient than assembly of the enriched global problem, which can be attributed to the cost of assembling global–local enrichment functions, factorization and solution of the global system of equations in the DFEA is the clear bottleneck on solution time. On the other hand, in the GFEM^{gl}, solving the 162 local problems is the most involved computation. On a larger computer with additional CPUs it is expected that the GFEM^{gl} would provide vastly better efficiency in terms of total time to solution.

It has already been verified that global measures, such as energy, between *hp*-GFEM DFEA and GFEM^{gl} simulations agree well, so in this case local or pointwise accuracy of the global solution under each method is also explored in Figure 3.15. The initial global solution provides an upper bound to the reference solution; however, it is clear

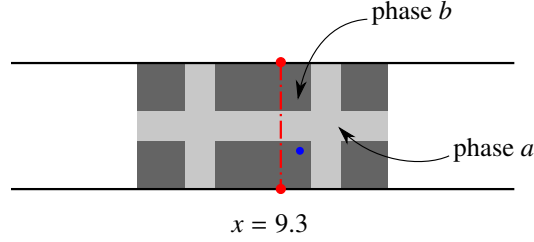


Figure 3.16: Heterogeneous laser-heated beam geometry in a localized region surrounding the sharp laser heating. The center of the applied sharp laser heating is indicated by a dashed line. The single dot indicates the location at which pointwise quantities are compared in each simulation.

that no local characteristics, such as sharp gradients in the temperature field can be captured on the structural-scale mesh without special enrichment functions. Despite inexact boundary conditions from the coarse-scale solution on the GFEM^{gl} sub-local problems, however, pointwise temperature from the enriched global solution compares very well with the reference solution. The GFEM^{gl} provides both improved computational efficiency and comparable accuracy to DFEA for this problem.

3.2.3 Laser-heated beam with material heterogeneity

Combining aspects of the laser-heated beam and square domain examples presented in Sections 3.2.1 and 3.2.2, the presence of material heterogeneity is considered in a localized region under the sharp flux on the same laser-heated beam of Sections 3.2.1 and 2.5.2. Thus, this example serves to combine the multiscale effects of both very localized thermomechanical loading as well as material heterogeneity. The cruciform material pattern depicted on the beam in Figure 3.16. In this problem, material properties are such that the ratio of heat conductivities $\kappa_a/\kappa_b = 5.0$. Similarly, thermoelastic properties are such that the ratio of Young's moduli $E_a/E_b = 5.0$, thermal expansion coefficients $\alpha_a/\alpha_b = 5.0$, and Poisson's ratios $\nu_a = \nu_b$. In each case, material properties are chosen such that the volume-averaged properties are equivalent to the properties chosen in the homogeneous beam in Section 3.2.1.

Because of localized stress concentrations and singularities due to material interfaces, this problem requires very high local solution fidelity, which makes DFEA impractical due to the extreme level of mesh refinement required to resolve localized stress gradients. However, the GFEM^{gl} with sub-local domains allows for substantially better resolution of local fields due to the lower computational cost of individual fine-scale problems, even at very high levels of mesh refinement. Thus, since it has been shown that GFEM^{gl} can obtain an accuracy level comparable to DFEA, in this case the GFEM^{gl} is used to generate a reference solution. This reference solution has a global mesh refinement level leading to 1,589 sub-local problems, each of which has a local element size $h \approx 0.0039$; in comparison, the coarsest global mesh has $H = 0.5$. Polynomial orders used in the global and local problems, respectively, are $\mathbf{p}^\theta = \{2, 2, 2\}$, $\mathbf{p}^u = \{3, 3, 3\}$, $\mathbf{p}_L^\theta = \{3, 3, 2\}$, and $\mathbf{p}_L^u = \{4, 4, 3\}$. The thermoelasticity DFEA which

Table 3.5: Laser-heated beam with heterogeneous material problem size details (in degrees of freedom) from the GFEM^{gl} reference solution versus the equivalent direct simulation. 1,589 sub-local problems are solved in the GFEM^{gl} reference solution. The DFEA is prohibitively large and thus *not* solved in this case, but only shown for comparison.

Method	Problem size	
	Heat transfer	Thermoelasticity
DFEA (<i>hp</i> -GFEM)	1,104,611	7,153,071
GFEM ^{gl} Initial global	6,804	51,030
GFEM ^{gl} Largest local	11,169	70,737
GFEM ^{gl} Enriched global	8,393	55,797

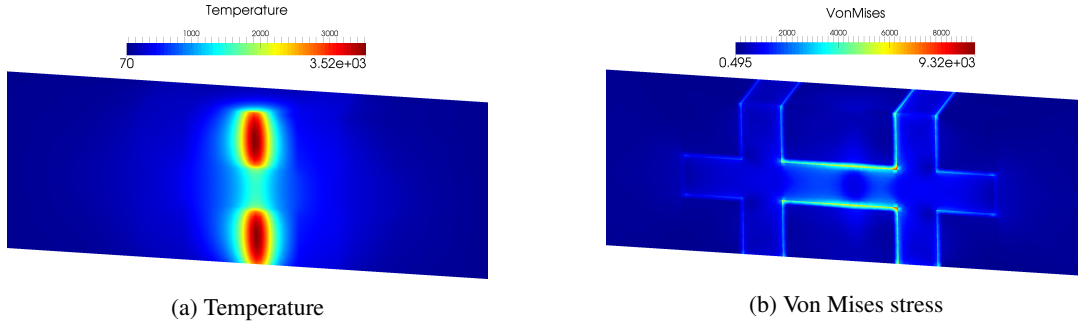


Figure 3.17: GFEM^{gl} reference solution contours from the laser-heated beam with material heterogeneity.

is hypothetically equivalent to this reference solution (i.e., identical mesh refinement level and polynomial order of approximation) consists of over 7 million degrees of freedom and is too large to be stored in memory on the computational resources used to obtain these results. Details of the size of the GFEM^{gl} reference solution as compared to its equivalent DFEA solution are given in Table 3.5. Qualitative contours of the GFEM^{gl} reference solution are shown in Figure 3.17.

Just as in the case of the homogeneous beam in Section 3.2.1, the problem is solved with various global mesh sizes H in order to generate varying numbers and sizes of sub-local problems in the GFEM^{gl}, where $H_1 = 0.25$, $H_2 = 0.125$, and $H_3 = 0.0625$. In all cases, the resulting local mesh size is $h \approx 0.0078$. Global problem and sub-local problem sizes are identical to those from the homogeneous beam example, shown in Table 3.1. Solution contours at each global mesh refinement level are given in Figure 3.18.

Convergence behavior of GFEM^{gl} solutions after global–local iterations with respect to the reference solution is also examined in this case. Relative error in the energy norm in global solutions, with respect to the reference GFEM^{gl} solution, from both heat transfer and thermoelasticity solutions are shown in Figure 3.19. In this case, relative error in the energy norm is computed as

$$e_{E,\theta}^r = \frac{\sqrt{|\mathcal{B}(\theta_{gl}^{\text{ref}}, \theta_{gl}^{\text{ref}}) - \mathcal{B}(\theta_{gl}, \theta_{gl})|}}{\sqrt{|\mathcal{B}(\theta_{gl}^{\text{ref}}, \theta_{gl}^{\text{ref}})|}}$$

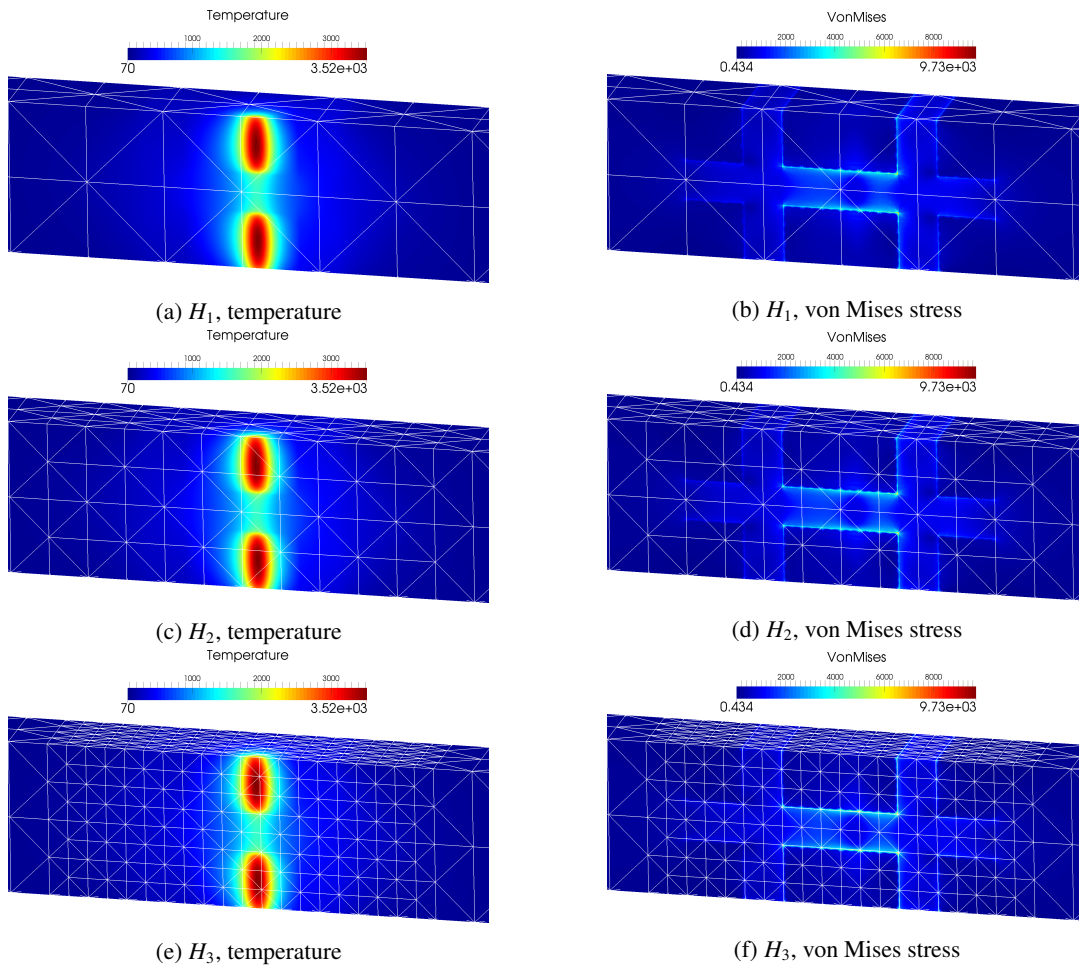


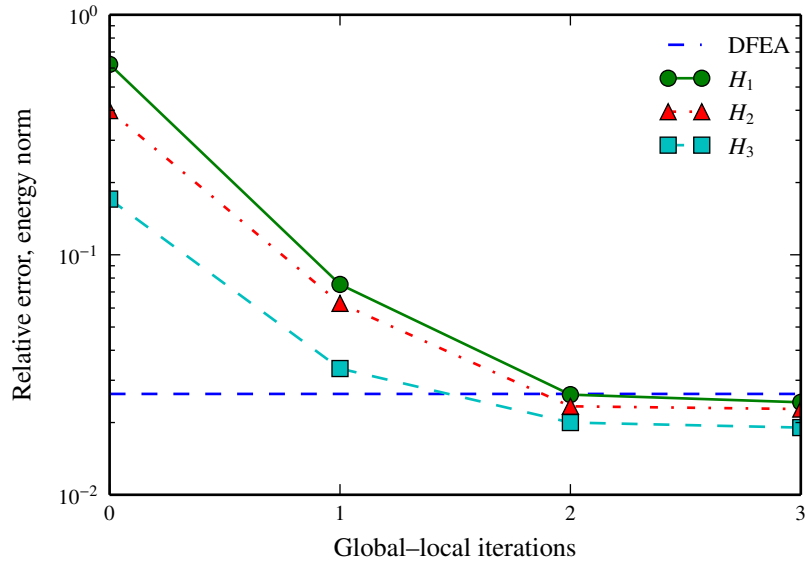
Figure 3.18: Laser-heated beam with material heterogeneity solution contours from GFEM^{gl} at various global mesh refinement levels.

in heat transfer, and

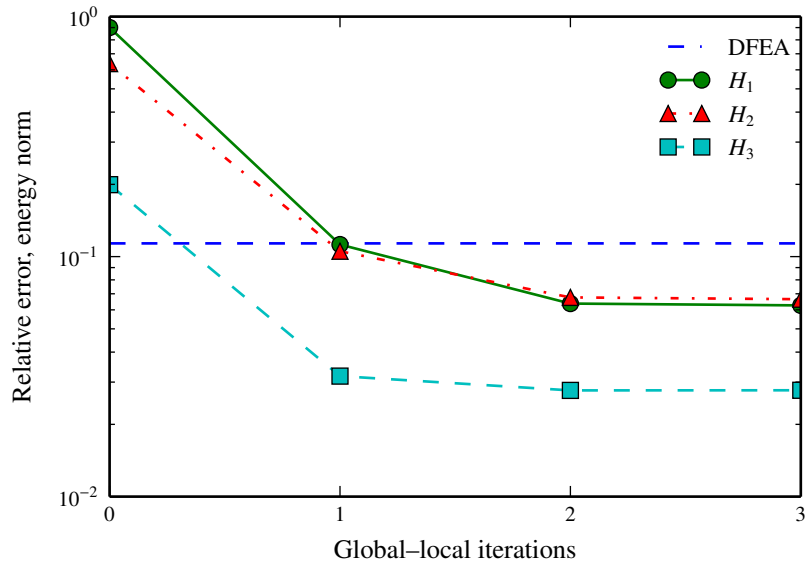
$$e_{E,\mathbf{u}}^r = \frac{\sqrt{|\mathcal{B}(\mathbf{u}_{gl}^{\text{ref}}, \mathbf{u}_{gl}^{\text{ref}}) - \mathcal{B}(\mathbf{u}_{gl}, \mathbf{u}_{gl})|}}{\sqrt{|\mathcal{B}(\mathbf{u}_{gl}^{\text{ref}}, \mathbf{u}_{gl}^{\text{ref}})|}}$$

for the elasticity problem, where $(\cdot)_{gl}^{\text{ref}}$ denotes the GFEM^{gl} *reference solution*, and $(\cdot)_{gl}$ denotes a GFEM^{gl} solution, while $\mathcal{B}(\cdot, \cdot)$ indicates the bilinear form associated with each problem. For comparison the error levels from an equivalent DFEA (once again an *hp*-GFEM DFEA with identical polynomial order and mesh size $h \approx 0.0078$) with respect to the GFEM^{gl} reference solution are also shown. It is important to note that initial, coarse-scale global problems at global mesh sizes H_1 and H_2 are too coarse to resolve material interfaces. Global mesh H_3 in fact matches the material interfaces; however, a mesh this coarse is unable to capture localized solution gradients in the neighborhood of the sharp thermal loading. Thus, in this problem boundary conditions on local domains can be especially poor, and the impact on global solution behavior is noticeable. With respect to the reference solution, GFEM^{gl} solutions from the coarsest two global meshes converge to a very similar and stable relative error level in the energy norm of roughly 2% and 7% in heat transfer and thermoelasticity problems, respectively. As global–local iterations are performed, error due to poor boundary conditions on fine-scale problems is reduced; therefore, local solution fidelity is ultimately what controls enriched global solution error after a few iterations. On the other hand the finest global mesh, which matches internal material interfaces, maintains a low and nearly constant error level with respect to the reference solution, even after iteration. It can also be observed that GFEM^{gl} solution quality may even exceed that of an equivalent direct simulation; special global–local enrichment degrees of freedom may be able to better represent localized gradients and singularities due to internal material interfaces.

Local or pointwise solution quantities are again compared in this numerical example. Convergence of von Mises stress at a point $(x, y) = (9.41, 0.28)$, denoted by a dot in Figure 3.16, on the surface of the laser-heated beam, and in the neighborhood of both the localized laser heating and material interface, after global–local iterations is shown in Figure 3.20. In all cases localized von Mises stress converges to a relative error level around or under 2%. For the coarsest global mesh H_1 , the effect of boundary conditions is improved consistently with iteration, resulting in a relative error level of well under 1%. At global mesh size H_2 , integration and discretization error, because the global mesh does *not* match material interfaces, likely skews the initial global solution such that localized von Mises stress is close to the reference value. While global solutions with the coarsest mesh H_1 show, in general, a smaller error with respect to the DFEA than a finer mesh H_2 , global mesh size may impact several GFEM^{gl} solution aspects, including the size of fine-scale, local problems, as well as the quality of the initial global solution, making pointwise convergence behavior potentially difficult to characterize. However, after iteration, the solution approaches a relative error level close to global mesh size H_3 . The fact that the global mesh conforms to internal material interfaces at mesh size H_3 leads to a steady error level in pointwise quantities, even after iteration.



(a) Heat transfer



(b) Thermoelasticity

Figure 3.19: Convergence of relative error in the energy norm of heterogeneous laser-heated beam GFEM^{gl} solutions at various global mesh refinement levels H after global–local iterations with respect to a GFEM^{gl} reference solution. Iteration zero represents the coarse-scale initial global solution. For comparison, the hp -GFEM DFEA is also shown.

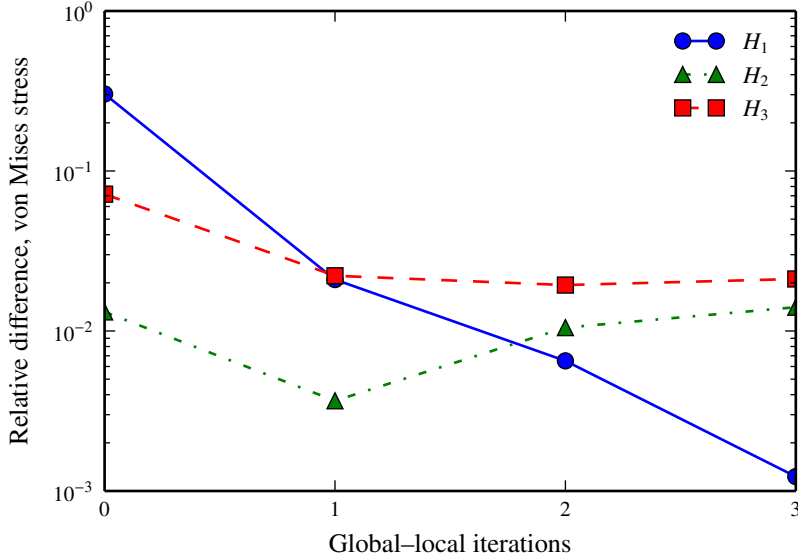


Figure 3.20: Pointwise convergence of von Mises stress in the heterogeneous laser-heated beam from GFEM^{gl} solutions at various global mesh refinement levels H after global–local iterations, with respect to a reference solution. Iteration zero represents the coarse-scale initial global solution.

3.2.4 L-shaped domain

The next numerical example is a three-dimensional L-shaped domain with a similar bi-material microstructural pattern to the square domain in Section 3.2.2, subjected to uniform, steady-state temperature boundary conditions on its top and right faces to induce a heat flux singularity at the reentrant inner corner. Only heat transfer is considered in this example. In this instance, the ratio of conductivities of each material phase is $\kappa_a/\kappa_b = 20$. Geometry and boundary conditions are described in Figure 3.21. This problem represents a more practical scenario where resolution of microstructural details is necessary only in a localized region surrounding a sharp solution gradient, and better demonstrates the important interaction between microstructural heterogeneity and structural-scale loading effects.

The global problem is meshed with 4-node GFEM tetrahedra and solved using GFEM^{gl} with sub-local problems, $\mathbf{p} = \{2, 2, 1\}$ globally, and, in sub-local problems, heavy localized mesh refinement to capture the material microstructure, with $\mathbf{p}_{loc} = \{2, 2, 1\}$; higher-order enrichment in the z -direction is unnecessary due to the nearly two-dimensional nature of the solution. In all cases, sub-local problems are solved in parallel, and only one global–local cycle is performed. To demonstrate the scale of the problem the coarse, global mesh and sample local problem are shown in Figure 3.22. The bi-material microstructure is adopted in the shaded region shown. Elsewhere, homogenized material properties are used, where the homogenized conductivity κ^* is computed by the rule of mixtures, that is,

$$\kappa^* = V_a \kappa_a + V_b \kappa_b,$$

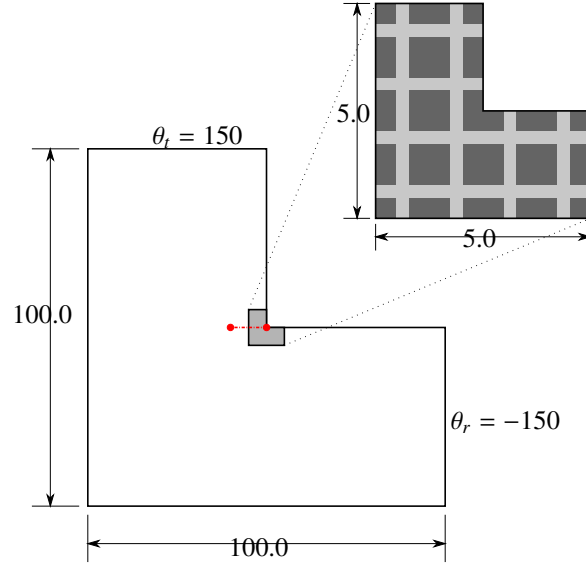


Figure 3.21: Geometry of the L-shaped domain with bi-material microstructure near the reentrant inner corner.

Table 3.6: Comparison of L-shaped domain solutions from various boundary conditions on the local problem(s).

Method	Global dofs	Energy ($\times 10^6$)	% difference
DFEA	1,676,652	3.376	–
DFEA, homogenized	10,120	3.440	1.91%
GFEM ^{gl} initial	768	3.537	4.79%
GFEM ^{gl} enriched	Dirichlet	770	0.26%
	mixed	770	0.28%

where V_a (V_b) is the volume fraction of phase a (b). Global–local enrichments are adopted only in the neighborhood of the edge singularity where the assumptions of the homogenization theory do not hold. Only two nodes of the coarse, global mesh are enriched with these functions. The reference or equivalent DFEA uses adaptive GFEM with $\mathbf{p}_{\text{DFEA}} = \{2, 2, 1\}$ and localized refinement around the reentrant corner. In contrast to previous examples, to demonstrate the impact of the material microstructure in the presence of a heat flux singularity, the problem is also solved using a DFEA with totally homogenized material parameters and $\mathbf{p}_{\text{homog}} = \{2, 2, 1\}$, and employing localized mesh refinement near the reentrant inner corner.

The first GFEM^{gl} simulations investigate the impact of applying different types of boundary conditions (Dirichlet or mixed) on, in this case, 2 sub-local problems. The solutions are also compared to the DFEA case using homogenized material properties throughout, as well as the coarse-scale, initial global solution using $\mathbf{p}_0 = \{1, 1, 1\}$. Pointwise temperature approaching the reentrant inner corner for all cases is plotted in Figure 3.23. Global energy comparisons of each solution are also presented in Table 3.6.

Despite a relatively poor initial global solution, GFEM^{gl} solutions employing both Dirichlet (temperature) and mixed (convective) boundary conditions on sub-local problems are nearly identical, with Dirichlet boundary conditions

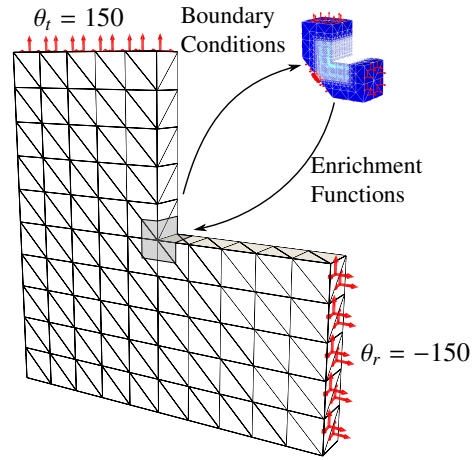


Figure 3.22: Coarse global mesh and a sub-local domain used to generate GFEM^{gl} enrichment functions for the L-shaped domain example. The assumptions of the homogenization theory are not valid in the neighborhood of the edge due to the presence of singularities.

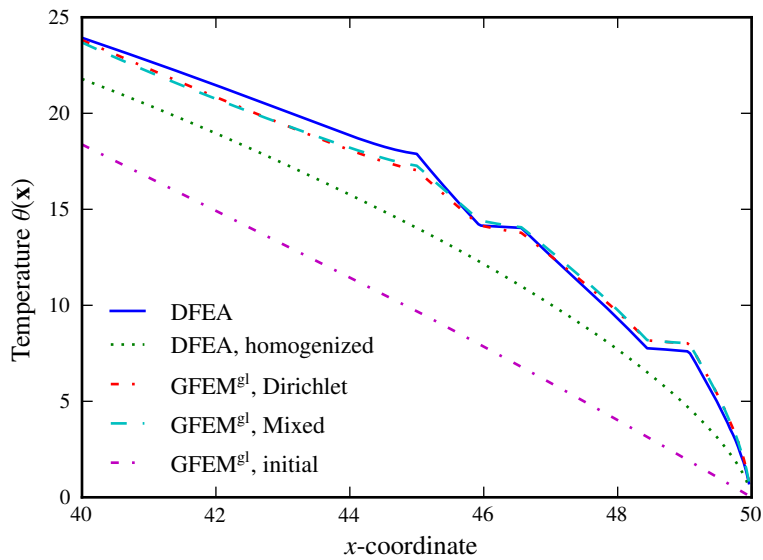


Figure 3.23: L-shaped domain temperature profile in approaching the reentrant corner at $x = 50$ (see dotted line in Figure 3.21), comparing DFEA, DFEA with homogenized material parameters, and all GFEM^{gl} boundary condition types.

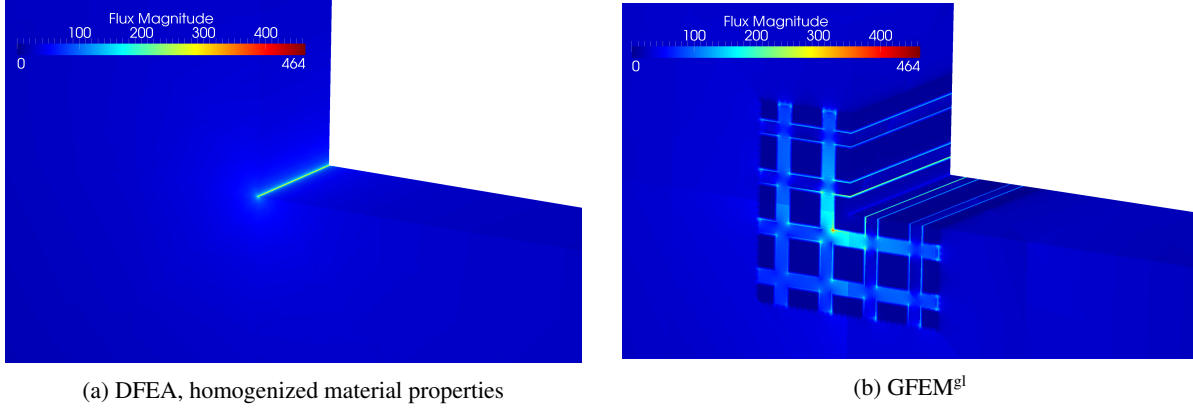


Figure 3.24: Magnitude of heat flux singularity at the reentrant inner corner of the L-shaped domain, demonstrating the impact of material heterogeneity on localized response. Compare to Figure 3.22 for scale.

giving just slightly better results relative to the reference DFEA. The DFEA with homogenized material parameters, on the other hand, leads to underestimation of the temperature in the neighborhood of the singularity at the reentrant inner corner, and this solution is clearly also unable to capture potentially important localized gradients. To further demonstrate the impact of material heterogeneity in the neighborhood of a sharp solution feature, contours of the singular flux field at the reentrant inner corner from both homogenized DFEA and GFEM^{gl} solutions are included in Figure 3.24. It is clear from this figure that the singularity pattern in the homogenized and multiscale solutions are completely different and that localized solution gradients can be captured by the GFEM^{gl} even across fine-scale problem boundaries. Furthermore, the GFEM^{gl} solution at the interface between homogenized and heterogeneous material properties does not show any spurious effects.

The effect of varying the number of (sub-)local problems used to generate global–local enrichment functions is also examined. This is accomplished by refining the global mesh, or decreasing the global mesh size H , around the corner in order to increase the number of seed patches, ω_α , $\alpha \in \mathcal{I}^{gl}$, in the global region from which sub-local problems are selected, but maintaining the same element size h in sub-local problems across cases. Equivalently, for each global mesh refinement level the ratio of structural-scale to fine-scale element size H/h decreases. Sub-local problems are solved in parallel on 24 CPUs, and only one global–local cycle is used. Table 3.7 shows the maximum, minimum, and average sizes of sub-local problems at the four coarsest global mesh sizes H .

Furthermore, in typical multiscale techniques, the memory requirements for saving fine-scale problem information may be substantial. In the GFEM^{gl}, as additional sub-local problems are extracted and solved, for a constant fine-scale mesh size h , the cost of solving each local problem actually decreases. However, it should be noted that in order to most efficiently iterate to improve sub-local boundary conditions, factorized stiffness matrices of each sub-local problem should be stored. The memory use in the GFEM^{gl} with varying numbers of sub-local problems is detailed in Table 3.8. The average memory requirement per sub-local problem drops steeply as the global mesh

Table 3.7: L-shaped domain GFEM^{gl} sub-local problem sizes. A greater number of sub-local problems indicates a finer global (coarse-scale) element size (H).

Method	(Sub-)local problems	(Sub-)local problem size		
		Smallest	Largest	Average
DFEA	–	–	1,676,652	–
GFEM ^{gl}	1	–	1,674,636	–
	2	1,348,208	1,348,208	1,348,208
	24	100,416	815,748	285,477
	161	568	274,820	44,764

Table 3.8: Memory usage in L-shaped domain solutions using the GFEM^{gl} for various numbers of sub-local problems. Overall memory use in GFEM^{gl} is bound by the storage of factorizations of sub-local problem stiffness matrices.

Method	Local problems	Memory use (GB)	
		Total	Per local problem
DFEA	–	2.14	2.14
GFEM ^{gl}	1	2.15	2.15
	2	3.03	1.51
	24	7.51	0.31
	161	7.70	0.05

refinement level is increased. However, when iterative improvement of boundary conditions is unnecessary, the memory requirements of the GFEM^{gl} decrease. Overall memory use in the parallel GFEM^{gl} is governed by the storage of factorized sub-local problem stiffness matrices, and a conservative upper bound on memory use by sub-local problems is given by the memory required in the largest sub-local problem multiplied by the number of processors used.

Pointwise temperature along a line approaching the reentrant inner corner is demonstrated in Figure 3.25 for the four *coarsest* global meshes (i.e., the smallest number of sub-local problems), while global error measures and solution times are given in Table 3.9 for all global meshes considered. While all solutions agree well with the DFEA, the case with 864 separate sub-local problems yields the most accurate result. Furthermore, Figure 3.25 shows that convergence to the reference solution as the number of sub-local problems is increased is observed not only in global measures but also in pointwise quantities. Thus, there is an apparent tradeoff between global-to-local mesh refinement

Table 3.9: Comparison of L-shaped domain solutions using the GFEM^{gl} for various numbers of sub-local problems. Times to solution (assembly and factorization) are also listed.

Method	Local problems	Global dofs	Energy ($\times 10^6$)	% diff.	Wall time (s)
DFEA	–	1,676,652	3.376	–	177.4
GFEM ^{gl}	1	770	3.385	0.29%	3126.8
	2	770	3.384	0.26%	837.7
	24	880	3.377	0.05%	281.6
	161	1,789	3.377	0.03%	60.8
	864	4,440	3.375	0.01%	30.2

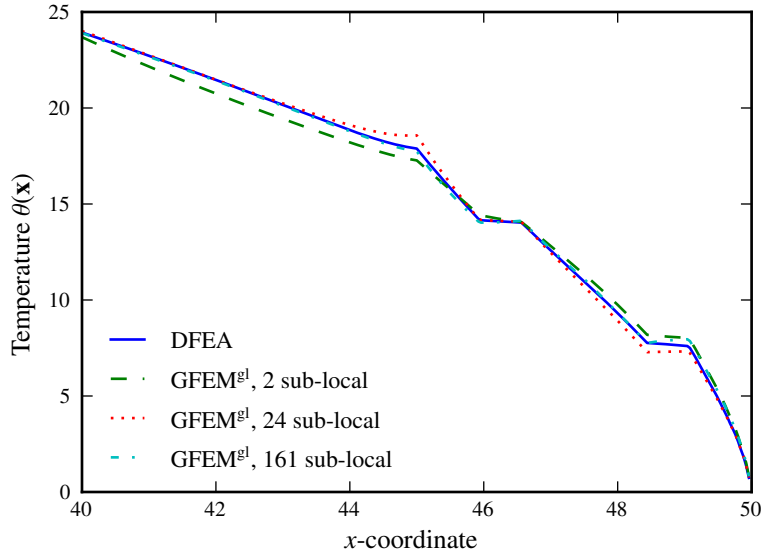


Figure 3.25: Temperature profile in L-shaped domain approaching the reentrant corner at $x = 50$ (see dotted line in Figure 3.21), comparing DFEA and GFEM^{gl} solutions with varying numbers of sub-local problems.

Table 3.10: Comparison of GFEM^{gl} parallel performance on 24 CPUs in L-shaped domain solutions with various numbers of sub-local problems. GFEM^{gl} solution times consider assembly, factorization, and solution of initial global and local problems, while DFEA solution times consider only the linear solve phase.

Method	Local problems	Solve (s)	Speedup	Efficiency
DFEA (serial)	–	1373.1	–	–
DFEA (parallel)	–	145.8	9.42	0.393
GFEM^{gl} (parallel)	24	267.1	5.14	0.214
	161	48.2	28.48	1.187
	864	17.8	76.97	3.207

ratio and solution accuracy. However, global mesh refinement increases the computational effort associated with solving the global problem itself, necessitating a detailed cost–benefit analysis of this idiosyncrasy of the GFEM^{gl} . As shown in Table 3.9, however, the increase in global problem size between the cases with 24 sub-local problems and 864 sub-local problems is modest at just a few thousand dofs. The solution using 864 sub-local problems is, perhaps counterintuitively, not only the most accurate but also the most efficient.

A more detailed analysis of the parallel performance of the GFEM^{gl} relative to DFEA combined with a highly optimized, parallel direct linear solver is provided in Table 3.10. In this case, only the three finest global mesh sizes are considered. GFEM^{gl} and DFEA parallel solutions (again, on 24 CPUs) are compared to a reference DFEA serial solution using a serial direct linear solver. Solve time in GFEM^{gl} encompasses the assembly and solution of the initial, coarse-scale global problem, assembly and solution of local problems, and solution of the enriched global problem. DFEA solve time, on the other hand, includes only the linear solve phase using an optimized, parallel direct linear

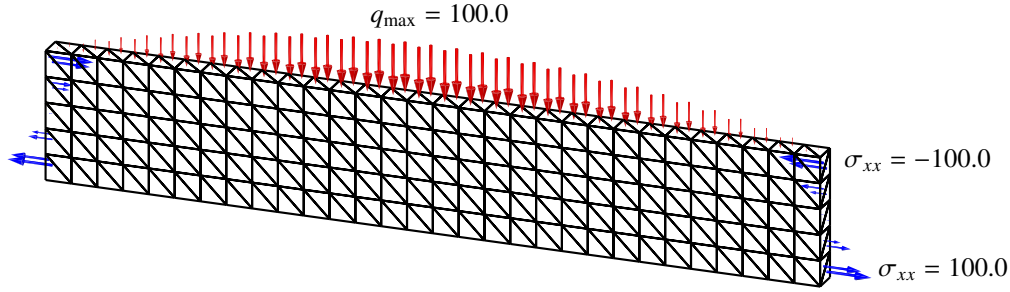


Figure 3.26: Mesh and thermomechanical boundary conditions on the heterogeneous beam.

Table 3.11: Thermoelasticity problem size details in degrees of freedom (dofs) for the heterogeneous beam compared to the equivalent hp -GFEM DFEA. In the GFEM^{gl} simulation 372 sub-local problems are solved.

Method	Problem size (dofs)
DFEA (hp -GFEM)	4,971,870
GFEM ^{gl} Initial global	11,160
Enriched global	12,276
Largest local	66,555
Smallest local	13,203
Average local	54,269

solver. GFEM^{gl} parallel solutions attain an efficiency of well over 100% in this example.

3.2.5 Heterogeneous beam under thermomechanical bending

The final example demonstrated is a heterogeneous beam of dimensions $30 \times 5 \times 1$ with material interfaces distributed throughout and subjected to uniform strong-axis bending tractions at both ends, along with a distributed heat flux on the top surface. Elsewhere, convective boundary conditions are applied. Geometry and boundary conditions are given in Figure 3.26. The structure of the two-phase heterogeneous material is random but defined in such a way that heavy, uniform mesh refinement in sub-local problems can resolve all internal material interfaces. Material properties of material phase a (b) are as follows: thermal conductivity $\kappa_a = 2.5$ ($\kappa_b = 10.0$) Young's modulus $E_a = 2.0 \times 10^5$ ($E_b = 10.0 \times 10^5$), Poisson's ratio $\nu_a = 0.3$ ($\nu_b = 0.25$), and coefficient of thermal expansion $\alpha_a = 2.0 \times 10^{-5}$ ($\alpha_b = 4.0 \times 10^{-5}$). Maintaining a coarse global mesh dimension $H = 1.0$, the characteristic “size” of the material microstructure requires a local mesh size $h = 0.125$ to resolve the material heterogeneity. Details regarding global and local problem sizes are listed in Table 3.11.

At a necessary mesh refinement level at the fine scale of $h = 0.125$, a DFEA approach is impractically expensive, as memory demands are far too high for the available computational resources. However, adopting a GFEM^{gl} approach, many smaller, independent sub-local problems allow for the resolution of material discontinuities at the fine scale, yet both the computational cost and memory requirements of each local problem are manageable. The global polynomial

Table 3.12: Wall times for each GFEM^{gl} thermoelasticity solution phase for the heterogeneous thermomechanical beam at $h = 0.125$.

	Wall time (s)			% of total time
	Assemble	Solve	Total	
Initial	1704.7	0.8	1705.5	35.1%
Local	138.2	283.9	442.1	8.7%
Enriched	2727.4	0.6	2728.0	56.2%
Total simulation time			4855.6	

order in the heat transfer (thermoelasticity) problem is $\mathbf{p}^\theta = \{2, 2, 2\}$ ($\mathbf{p}^u = \{3, 3, 3\}$), while in local problems, $\mathbf{p}_L^\theta = \{2, 2, 1\}$ ($\mathbf{p}_L^u = \{3, 3, 2\}$).

Contours of GFEM^{gl} solutions are shown in Figure 3.27 alongside results of an hp -GFEM direct simulation of the beam using homogenized, uniform material properties throughout. The homogenized hp -GFEM DFEA uses only a coarse, global mesh, $H = 1.0$ (identical to the global mesh in the GFEM^{gl} solution), and $\mathbf{p}_{\text{DFEA}}^\theta = \{2, 2, 2\}$, $\mathbf{p}_{\text{DFEA}}^u = \{3, 3, 3\}$. Both homogenized DFEA and GFEM^{gl} solutions capture the smooth, overall response of the structure. However, the GFEM^{gl} solution, enriched with detailed, fine-scale solutions, captures localized temperature and stress oscillations due to fine-scale material interfaces throughout the beam, even at the coarse, global scale.

A breakdown of solution times for this case is given in Table 3.12. Because of the high level of local mesh refinement relative to the coarse, global mesh, it is clear that global assembly is extraordinarily expensive relative to local problem computations. This additional expense stems from computing contributions from global–local enrichments, defined over the many highly hp -adapted subdomains, as well as obtaining the high-fidelity, enriched global temperature field for the calculation of thermal stress contributions. However, it is important to note that the GFEM^{gl} solution is still tractable on the computational resources used, while the equivalent DFEA far exceeds the available memory capacity.

3.3 Summary

The GFEM^{gl} enables effective resolution of microstructural effects on a coarse, structural-scale finite element mesh, which is required in order to capture intrinsically multiscale, coupled failure initiation and evolution in structures. GFEM^{gl} solution accuracy is demonstrated in global measures, such as energy, and also in pointwise quantities, like temperature, in the neighborhood of sharp gradients, and is found to be comparable to direct finite element analysis. The multiscale coupling is accomplished without the use of homogenized or upscaled material properties, which often fail to capture important localized behavior in the presence of, for example, singularities and other stress raisers. Fine-scale enrichment functions also effectively capture oscillatory, localized solution behavior across boundaries in

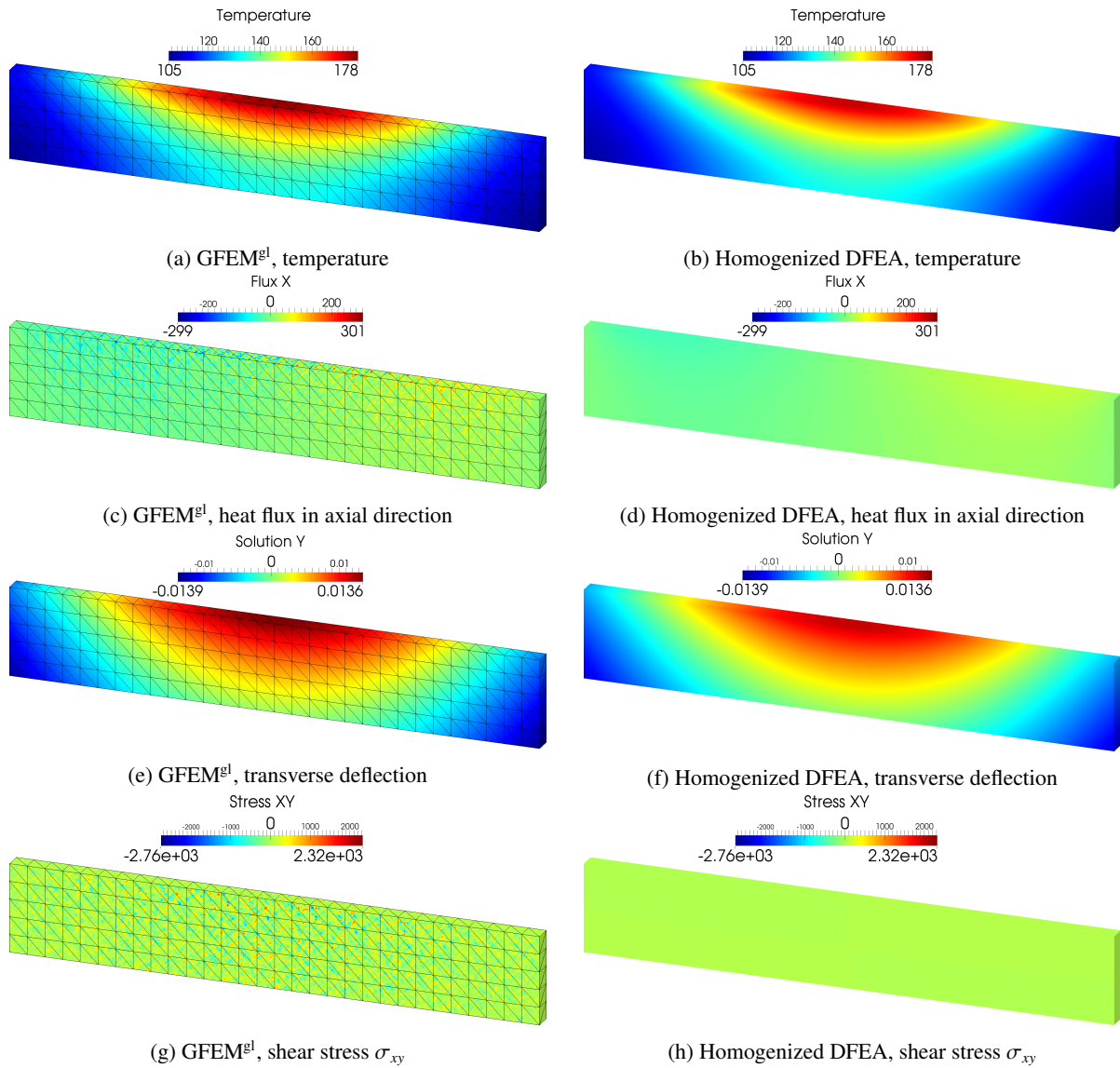


Figure 3.27: Heterogeneous beam solution contours from GFEM^{gl} simulations with $h = 0.125$, alongside solutions based on a DFEA using smooth, homogeneous material properties. The coarse-scale, global mesh is superimposed on GFEM^{gl} solutions.

the structural-scale problem. In the framework of the GFEM^{gl}, continuity among fine-scale solutions need not be enforced, nor are overly restrictive boundary conditions on fine-scale problems required, providing this method with flexibility in addition to its proven accuracy. Strategies are presented to improve boundary conditions on fine-scale problems, and carrying out multiple global–local iterations is shown to be an effective technique even in the presence of many sharp gradients due to microstructural features.

Furthermore, the examples demonstrated in this chapter highlight the efficiency of the GFEM^{gl}—it is rapidly parallelizable, since fine-scale sub-local problems are solved independently of one another, without communication. Such efficient parallelism is critical when dealing with problems of multiscale character, since, as shown in the examples presented, a large number of fine-scale problems is generally required in realistic simulations. Most importantly, the GFEM^{gl} obtains better efficiency than direct numerical simulation for the class of problems of interest, while maintaining nearly identical accuracy.

Chapter 4

GFEM^{gl} for nonlinear thermomechanical problems with time-dependent behavior

Previously, Chapter 2 described an efficient technique for modeling thermo-structural problems with the GFEM^{gl}. Work in this chapter focused solely on linear elastic structural response. In the classes of problems of interest, however, it is important to consider not only elastic but also *nonlinear, plastic* effects due to very localized thermomechanical loadings.

Strongly graded meshes in the neighborhood of localized heating phenomena are necessary to capture not only intense gradients in temperature, stress, and strain—as in previous chapters dealing with purely linear elastic material behavior—but also local residual deformations due to nonlinear effects. Adaptive methods are typically considered an optimal approach for problems of this nature [108, 126]. For instance, *hp*-adaptive FEM has been applied to computational modeling of laser welding processes in [85, 115], which utilize a posteriori error estimation to perform mesh refinement and unrefinement along the weld path. However, even when plasticity is confined to only a small region of the global structure, heavily adapted models may prove computationally expensive to solve, since *local* nonlinearities may govern the convergence behavior of the *global* nonlinear solution scheme. In general, classical approaches for solving high-fidelity, nonlinear problems such as domain decomposition-based solvers may experience convergence issues when nonlinear effects are extremely localized or otherwise unbalanced, and domain decomposition approaches aiming to address this issue is an active research area [11, 15, 103]. Another persistent issue in adaptive approaches is handling changing discretizations (i.e., remeshing or refinement/unrefinement) in between time or load steps. Adaptive simulations of nonlinear problems typically involve mapping or transfer of three-dimensional solutions as well as material state variables onto meshes which evolve in time, leading to significant computational overhead [67, 95, 104].

The GFEM^{gl} has been formulated for and applied to nonlinear, elasto-plastic problems by Kim et al. [64] and Gupta et al. [52], where it has proven effective in capturing localized plasticity in local problems while maintaining a coarse, uniform, structural-scale mesh, making global nonlinear solution iterations inexpensive. However, these works are limited to treating localized plastic behavior which is (i) confined to a fixed region of interest on the global structure and (ii) induced by uniform, monotonic, proportional structural loadings. In the class of problems under investigation, intense thermal gradients on the structure may vary significantly in both space and time, leading to thermomechanical behavior which is difficult to characterize a priori. Furthermore, both heating *and* cooling effects must be considered

in order to predict residual stresses and strains.

Building upon the multiphysics solution framework presented in Chapter 2, this chapter presents a novel GFEM^{gl} formulation to address these issues and treat the problem of coupled transient heat transfer and nonlinear thermoplasticity. The presented method can handle approximation spaces which evolve in time by updating enrichment functions generated from local boundary value problems at each time/load step in the analysis, while maintaining a *fixed global mesh*; thus, unlike typical *hp*-adaptive methods, it does not involve mapping of solutions and material state variables onto changing meshes. The quality of global–local enrichments may also be sensitive to boundary conditions applied on local problems at each time step of the analysis [51], so strategies for improving boundary conditions in the time-dependent, nonlinear problems of interest are also discussed. In Section 3.2 results from a few verification examples are included to demonstrate that the method achieves a comparable level of accuracy to traditional, direct analysis approaches. Many challenging, industrial-scale problems may require a high level of local fidelity which may be prohibitively expensive or difficult to achieve using a direct approach. Therefore, the presented method is finally applied to a representative example of this nature to highlight its parallelism and general applicability in application areas of interest.

4.1 Problem definition

In contrast with the problem formulation for linear thermoelasticity in Section 2.1, this chapter focuses on transient heat transfer problems and nonlinear thermoplasticity problems. The problem is defined over a domain $\Omega \in \mathbb{R}^3 \times [0, t_N]$ with a specified time interval $\{t | t \in [0, t_N]\}$. Just as in the previous case of linear thermoelasticity, the formulation is presented in a staggered sense.

4.1.1 Transient heat transfer

The transient heat transfer problem is defined over a domain $\Omega^\theta \in \mathbb{R}^3 \times [0, t_N]$, $\Omega^\theta = \Omega$, with boundary $\partial\Omega^\theta = \Gamma^\theta \cup \Gamma^f \cup \Gamma^c$, where $\Gamma^\theta \cap \Gamma^f = \emptyset$, $\Gamma^\theta \cap \Gamma^c = \emptyset$, and $\Gamma^c \cap \Gamma^f = \emptyset$. The strong form of the governing partial differential equation over a time interval $t \in [0, t_N]$ is given by

$$\rho c \frac{\partial \theta}{\partial t} - \nabla \cdot (\boldsymbol{\kappa} \nabla \theta) = Q(\mathbf{x}, t) \quad \text{in } \Omega^\theta, \quad (4.1)$$

where $\theta = \theta(\mathbf{x}, t)$ is the temperature field, $\boldsymbol{\kappa} = \boldsymbol{\kappa}(\mathbf{x})$ the thermal conductivity tensor, $\rho c = \rho(\mathbf{x})c(\mathbf{x})$ is the volumetric heat capacity, and $Q(\mathbf{x}, t)$ the internal heat source. As opposed to (2.1), time-dependency of the temperature field and thermal loads are considered.

Time-dependent boundary conditions on $\partial\Omega^\theta$ are given by

$$\begin{aligned}\theta &= \bar{\theta}(\mathbf{x}, t) \quad \text{on } \Gamma^\theta \\ -\kappa\nabla\theta \cdot \mathbf{n} &= \bar{f}(\mathbf{x}, t) \quad \text{on } \Gamma^f \\ -\kappa\nabla\theta \cdot \mathbf{n} &= h_c(\theta - \theta_\infty) \quad \text{on } \Gamma^c,\end{aligned}\tag{4.2}$$

where \mathbf{n} is the outward unit normal to Γ^f and Γ^c , \bar{f} and $\bar{\theta}$ are prescribed normal heat flux and temperature, respectively, h_c is the convective coefficient, and θ_∞ is the ambient temperature. Initial conditions at time $t = 0$ are

$$\theta(\mathbf{x}, 0) = \theta_0(\mathbf{x}).\tag{4.3}$$

4.1.2 Thermoplasticity

The thermoplasticity problem is again defined over $\Omega^u \in \mathbb{R}^3$, $\Omega^u = \Omega$, with boundary $\partial\Omega^u = \Gamma^u \cup \Gamma^t$, where $\Gamma^u \cap \Gamma^t = \emptyset$. Only quasistatic response is assumed; however, when dealing with highly transient thermal loadings, the dynamic effects of rapid thermal expansion and shrinkage may need to be considered in the thermomechanical response, which is left for future study.

The quasistatic or steady-state governing equations are given by

$$\begin{aligned}\nabla \cdot \boldsymbol{\sigma} &= -\mathbf{b}(\mathbf{x}, t) \quad \text{in } \Omega^u \\ \boldsymbol{\sigma} &= \mathbf{C} : \boldsymbol{\varepsilon}^m \\ \boldsymbol{\varepsilon}^m &= \boldsymbol{\varepsilon} - \boldsymbol{\varepsilon}^p - \boldsymbol{\varepsilon}^\theta \\ \boldsymbol{\varepsilon} &= \frac{1}{2}(\nabla\mathbf{u} + \nabla\mathbf{u}^T) \\ \boldsymbol{\varepsilon}^\theta &= \boldsymbol{\alpha}_\theta(\theta(\mathbf{x}, t) - \theta_\infty),\end{aligned}\tag{4.4}$$

with $\boldsymbol{\sigma}$ the Cauchy stress tensor, \mathbf{b} the body force, $\mathbf{C} = \mathbf{C}(\mathbf{x})$ Hooke's tensor of material moduli, and $\boldsymbol{\varepsilon}$, $\boldsymbol{\varepsilon}^m$, $\boldsymbol{\varepsilon}^p$, and $\boldsymbol{\varepsilon}^\theta$ the total, elastic mechanical, plastic, and thermal strain tensors, respectively. The reference temperature for the computation of thermal strains and the ambient temperature θ_∞ (used in convective heat transfer boundary conditions) are assumed to be the same in all cases. Plastic strain $\boldsymbol{\varepsilon}^p$ is a state variable defined at each material point in the domain; the J_2 plasticity model adopted in this study is defined in detail in the following section. $\mathbf{u} = \mathbf{u}(\mathbf{x}, t)$ is the (now time- or load-dependent) displacement field, and $\boldsymbol{\alpha}_\theta = \boldsymbol{\alpha}_\theta(\mathbf{x})$ denotes the tensor of thermal expansion coefficients. In all cases, isotropic thermal expansion is assumed, that is, $\boldsymbol{\alpha}_\theta = \alpha_\theta \mathbf{1}$. It is also important to note that in the context of thermoplasticity problems, t denotes pseudotime.

Table 4.1: Classical rate-independent J_2 flow theory.

Elastic stress-strain relationship:	$\boldsymbol{\sigma} = \mathbf{C} : \boldsymbol{\varepsilon}^n$
Elastic domain in stress space:	$\mathbb{E}_\sigma = \{(\boldsymbol{\sigma}, \alpha) \mid f(\boldsymbol{\sigma}, \alpha) \leq 0\}$
Associated flow rule and hardening law:	$\boldsymbol{\varepsilon}^p = \gamma \frac{\partial f}{\partial \boldsymbol{\sigma}}$ $\dot{\alpha} = \sqrt{\frac{2}{3}} \gamma$
Kuhn–Tucker loading/unloading conditions:	$\gamma \geq 0, f(\boldsymbol{\sigma}, \alpha) \leq 0, \gamma f(\boldsymbol{\sigma}, \alpha) = 0$
Consistency condition:	$\gamma \dot{f}(\boldsymbol{\sigma}, \alpha) = 0$

Boundary conditions on $\partial\Omega^u$ are

$$\begin{aligned} \mathbf{u}(\mathbf{x}, t) &= \bar{\mathbf{u}}(\mathbf{x}, t) \quad \text{on } \Gamma^u \\ \boldsymbol{\sigma}(\mathbf{x}, t) \cdot \mathbf{n} &= \bar{\mathbf{t}}(\mathbf{x}, t) \quad \text{on } \Gamma^t, \end{aligned} \quad (4.5)$$

where $\bar{\mathbf{u}}$ is the prescribed displacement, \mathbf{n} is the outward unit normal to Γ^t , and $\bar{\mathbf{t}}$ is the specified traction. Initial conditions at time $t = 0$ are denoted

$$\mathbf{u}(\mathbf{x}, 0) = \mathbf{u}_0(\mathbf{x}). \quad (4.6)$$

4.1.2.1 Plasticity model

Plastic deformations in the material are accounted for using the classical J_2 flow theory as detailed by Simo and Hughes [118] and included in Table 4.1. Only the rate-independent case with isotropic hardening is considered; however, viscoplastic effects become important in certain instances of the class of problems of interest, which may be a pertinent topic of future work. The von Mises yield criterion f is given by

$$f(\boldsymbol{\sigma}, \alpha) = \|\text{dev } \boldsymbol{\sigma}\| - \sqrt{\frac{2}{3}} \hat{K}(\alpha) \leq 0, \quad (4.7)$$

where α is the internal material hardening state variable, and the hardening model \hat{K} adopted herein is given by

$$\hat{K}(\alpha) = \sigma_y + K\alpha + (\sigma_\infty - \sigma_y) [1 - \exp(-\omega\alpha)], \quad (4.8)$$

with σ_y the yield stress and K the linear hardening parameter. σ_∞ and ω are the saturation stress and hardening exponent, respectively, associated with nonlinear hardening, based on the model originally proposed in [135] and also used in [32].

4.2 GFEM^{gl} formulation for coupled transient heat transfer and thermoplasticity

4.2.1 GFEM^{gl} for general time-dependent problems

In contrast to the steady-state form of the method presented in Section 2.2.1 of Chapter 2, GFEM^{gl} analyses of time-dependent or multi-step problems are most generally embodied by

- (i) establishing initial conditions, i.e., solving the *initial global problem*, then
- (ii) at each time or load step in the simulation $t = t_n, n = 0, \dots, N$,
 - (1) extracting and solving *local problems* based on boundary conditions from the global solution, and
 - (2) reanalyzing the *enriched global problem* based on local solutions at t_n .

The overall GFEM^{gl} algorithm for the coupled, time-dependent thermoplasticity problem is illustrated in Figure 4.1. Two primary issues unique to time-dependent or multi-step nonlinear GFEM^{gl} analyses implied by the steps above are

- (i) the choice of boundary conditions from the global solution on local problems at each time step t_n , so as to minimize error in local solutions, and
- (ii) the time-dependency of global–local enrichments used to approximate the global solution.

However, time evolution of the global approximation space is not unique to the GFEM^{gl}; this issue is analogous to *hp*-adaptive methods, where the global approximation changes in between time steps as a result of changing mesh refinement. Similarly, in G/XFEM analyses of dynamic fracture propagation [20, 25, 121], global enrichment spaces (i.e., mesh nodes enriched with Heaviside or singular functions) must vary in time to accommodate evolving crack paths.

A detailed GFEM^{gl} formulation for coupled transient heat transfer and nonlinear thermoplasticity follows, including a description of how local problem boundary conditions as well as time-dependent global approximation spaces are treated.

4.2.2 Transient heat transfer

As opposed to Section 2.3.1 in Chapter 2, time-dependency of the temperature field must be accounted for in discretizing the heat equation (4.1). Application of the GFEM^{gl} to transient heat transfer problems is the subject of work by O'Hara et al. [91–93]. In this formulation, the global governing PDE (4.1) is discretized spatially using GFEM and temporally using a finite difference scheme. In order to capture localized evolution of the solution in time, it is

1. Set initial conditions: $n = 0, t_0 = 0, \theta_0, \mathbf{u}_0$

2. At time $t = t_{n+1}$:

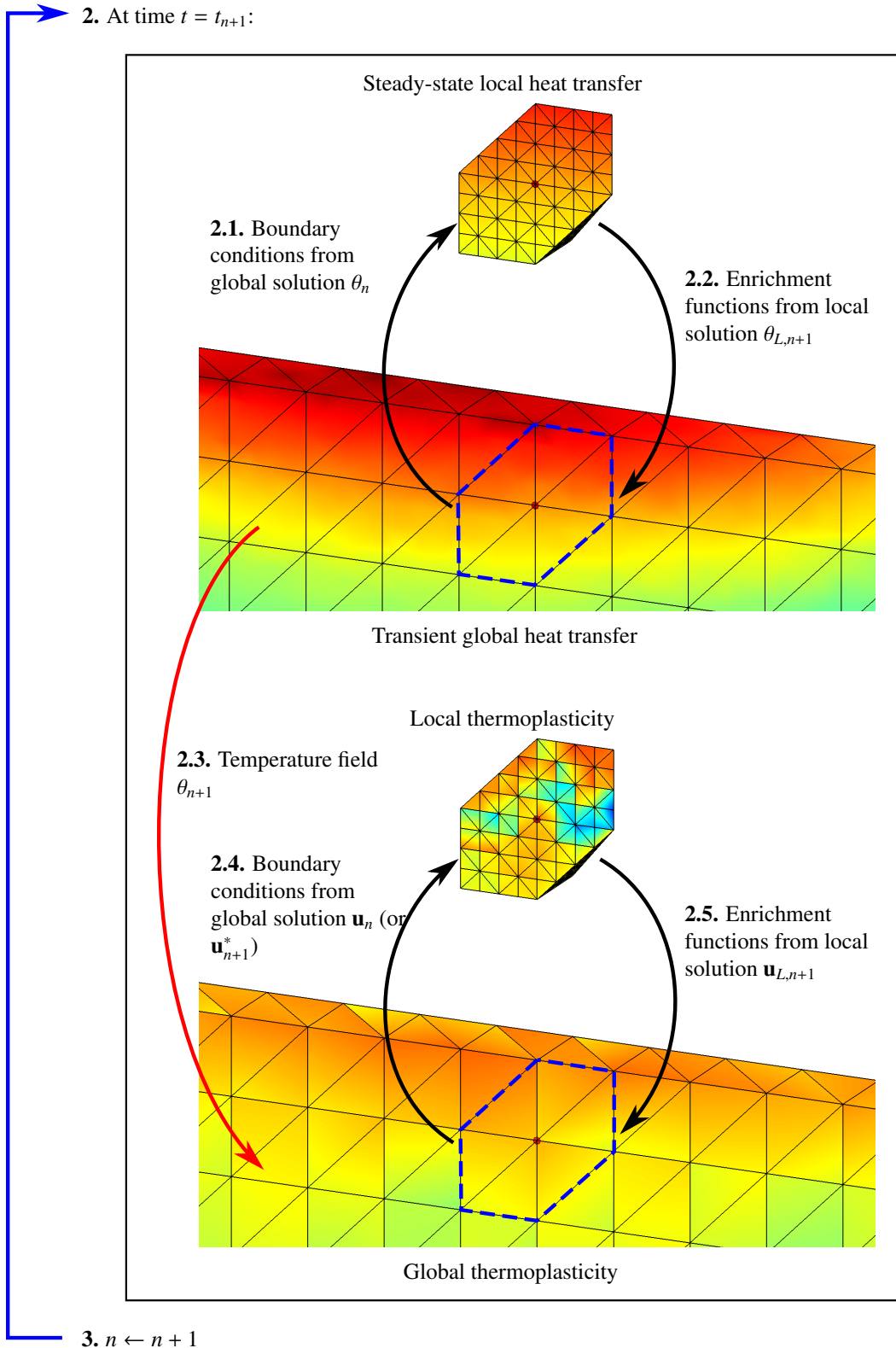


Figure 4.1: The GFEM^{gl} for time-dependent thermo-structural problems, as detailed in Section 4.2. The coarse-scale global problem and hp -adapted local problem are shown in each discipline.

generally necessary to update global–local shape functions at each time step, thereby introducing time-dependency into the global shape functions. Thus, the following transient formulation accommodates changing shape functions over the course of the transient solution.

4.2.2.1 Global problem

On the coarse-scale, global domain $\bar{\Omega}^\theta = \Omega^\theta \cup \partial\Omega^\theta$. The problem is formulated as: Find $\theta \in \mathbb{S}_G(\Omega^\theta) \subset \mathbb{S}_{GFEM}(\Omega^\theta)$ such that for all $\delta\theta \in \mathbb{S}_G(\Omega^\theta)$,

$$\begin{aligned} \int_{\Omega^\theta} \left(\rho c \frac{\partial\theta}{\partial t} \delta\theta + \nabla\theta \boldsymbol{\kappa} \nabla\delta\theta \right) d\Omega + \eta \int_{\Gamma^\theta} \theta \delta\theta d\Gamma + \int_{\Gamma^c} h_c \theta \delta\theta d\Gamma \\ = \int_{\Omega^\theta} Q \delta\theta d\Omega + \int_{\Gamma^f} \bar{f} \delta\theta d\Gamma + \eta \int_{\Gamma^\theta} \bar{\theta} \delta\theta d\Gamma + \int_{\Gamma^c} h_c \theta_\infty \delta\theta d\Gamma, \end{aligned} \quad (4.9)$$

where η is a penalty parameter for enforcement of Dirichlet boundary conditions.

The temperature drift $\frac{\partial\theta}{\partial t}$ is approximated using the α -method finite difference scheme,

$$\begin{aligned} \frac{\partial\theta}{\partial t} &= \frac{\theta_{n+1} - \theta_n}{\Delta t} \\ \theta_{n+\alpha} &= \alpha\theta_{n+1} + (1 - \alpha)\theta_n, \end{aligned} \quad (4.10)$$

where the notation $(\cdot)_n := (\cdot)(\mathbf{x}, t_n)$ is adopted. Parameter $0.0 \leq \alpha \leq 1.0$ determines the particular finite difference scheme (whether implicit or explicit), and Δt is the time step size, such that $\sum_{n=1}^N \Delta t_n = t_N$. Substituting (4.10) in (4.9), the temporally discretized weak form is given by

$$\begin{aligned} \int_{\Omega^\theta} \left(\frac{\rho c}{\Delta t} (\theta_{n+1} - \theta_n) \delta\theta + \nabla [\alpha\theta_{n+1} + (1 - \alpha)\theta_n] \boldsymbol{\kappa} \nabla\delta\theta \right) d\Omega \\ + \eta \int_{\Gamma^\theta} [\alpha\theta_{n+1} + (1 - \alpha)\theta_n] \delta\theta d\Gamma + \int_{\Gamma^c} h_c [\alpha\theta_{n+1} + (1 - \alpha)\theta_n] \delta\theta d\Gamma \\ = \int_{\Omega^\theta} [\alpha Q_{n+1} + (1 - \alpha)Q_n] \delta\theta d\Omega + \int_{\Gamma^f} [\alpha \bar{f}_{n+1} + (1 - \alpha)\bar{f}_n] \delta\theta d\Gamma \\ + \eta \int_{\Gamma^\theta} [\alpha \bar{\theta}_{n+1} + (1 - \alpha)\bar{\theta}_n] \delta\theta d\Gamma + \int_{\Gamma^c} h_c \theta_\infty \delta\theta d\Gamma. \end{aligned} \quad (4.11)$$

Adopting GFEM approximation (2.8) for the temperature field θ and rewriting in matrix form, while also considering potential time-dependency of shape functions,

$$\theta(\mathbf{x}, t_n) \approx \theta^{hp}(\mathbf{x}, t_n) = \bar{\mathbf{N}}_n^\theta(\mathbf{x}) \mathbf{d}^\theta, \quad (4.12)$$

where

$$\bar{\mathbf{N}}_n^\theta(\mathbf{x}) = [\bar{\mathbf{N}}_{n,1}^\theta(\mathbf{x}) \cdots \bar{\mathbf{N}}_{n,k}^\theta(\mathbf{x})], \quad \bar{\mathbf{N}}_{n,\alpha}^\theta = [N_\alpha(\mathbf{x}) \quad \phi_{n,\alpha 1}(\mathbf{x}) \cdots \phi_{n,\alpha m_\alpha}(\mathbf{x})],$$

and similarly for the temperature gradient $\nabla\theta$,

$$\nabla\theta(\mathbf{x}, t_n) \approx \nabla\theta^{hp}(\mathbf{x}, t_n) = \bar{\mathbf{B}}_n^\theta(\mathbf{x})\mathbf{d}^\theta = [\nabla \otimes \bar{\mathbf{N}}_n^\theta(\mathbf{x})]\mathbf{d}^\theta. \quad (4.13)$$

Substituting (4.12) and (4.13) into (4.11) and moving all known terms (those involving time t_n as well as prescribed quantities) to the right-hand side, the fully spatially and temporally discretized form of the transient heat transfer problem is

$$\left[\frac{1}{\Delta t} \mathbf{M}_{n+1}^\theta + \alpha \mathbf{K}_{n+1}^\theta \right] \mathbf{d}_{n+1}^\theta = \left[\frac{1}{\Delta t} \mathbf{M}_{n+1,n}^\theta - (1 - \alpha) \mathbf{K}_{n+1,n}^\theta \right] \mathbf{d}_n^\theta + \alpha \mathbf{f}_{\text{ext},n+1}^\theta + (1 - \alpha) \mathbf{f}_{\text{ext},n+1,n}^\theta, \quad (4.14)$$

where

$$\begin{aligned} \mathbf{M}_{n+1}^\theta &= \int_{\Omega^\theta} \rho c \bar{\mathbf{N}}_{n+1}^{\theta T} \bar{\mathbf{N}}_{n+1}^\theta \, d\Omega, \\ \mathbf{K}_{n+1}^\theta &= \int_{\Omega^\theta} \bar{\mathbf{B}}_{n+1}^{\theta T} \boldsymbol{\kappa} \bar{\mathbf{B}}_{n+1}^\theta \, d\Omega + \int_{\Gamma^c} h_c \bar{\mathbf{N}}_{n+1}^{\theta T} \bar{\mathbf{N}}_{n+1}^\theta \, d\Gamma, \\ \mathbf{M}_{n+1,n}^\theta &= \int_{\Omega^\theta} \rho c \bar{\mathbf{N}}_{n+1}^{\theta T} \bar{\mathbf{N}}_n^\theta \, d\Omega, \\ \mathbf{K}_{n+1,n}^\theta &= \int_{\Omega^\theta} \bar{\mathbf{B}}_{n+1}^{\theta T} \boldsymbol{\kappa} \bar{\mathbf{B}}_n^\theta \, d\Omega + \int_{\Gamma^c} h_c \bar{\mathbf{N}}_{n+1}^{\theta T} \bar{\mathbf{N}}_n^\theta \, d\Gamma, \\ \mathbf{f}_{\text{ext},n+1}^\theta &= \int_{\Omega^\theta} \bar{\mathbf{N}}_{n+1}^{\theta T} \mathcal{Q}_{n+1} \, d\Omega + \int_{\Gamma^f} \bar{\mathbf{N}}_{n+1}^{\theta T} \bar{f}_{n+1} \, d\Gamma + \eta \int_{\Gamma^g} \bar{\mathbf{N}}_{n+1}^{\theta T} \bar{\theta}_{n+1} \, d\Gamma + \int_{\Gamma^c} \bar{\mathbf{N}}_{n+1}^{\theta T} h_c \theta_\infty \, d\Gamma, \\ \mathbf{f}_{\text{ext},n+1,n}^\theta &= \int_{\Omega^\theta} \bar{\mathbf{N}}_{n+1}^{\theta T} \mathcal{Q}_n \, d\Omega + \int_{\Gamma^f} \bar{\mathbf{N}}_{n+1}^{\theta T} \bar{f}_n \, d\Gamma + \eta \int_{\Gamma^g} \bar{\mathbf{N}}_{n+1}^{\theta T} \bar{\theta}_n \, d\Gamma + \int_{\Gamma^c} \bar{\mathbf{N}}_{n+1}^{\theta T} h_c \theta_\infty \, d\Gamma. \end{aligned}$$

Thus, time-dependency of the global approximation space can be treated in a straightforward manner involving only one extra term, $\mathbf{M}_{n+1,n}^\theta \mathbf{d}_n^\theta$, on the right-hand side at each time step.

For simplicity, $\alpha = 1.0$ is chosen in all subsequent transient heat transfer GFEM^{gl} simulations, leading to the unconditionally stable, implicit backward Euler scheme. In this instance, (4.14) simplifies to

$$\left[\frac{1}{\Delta t} \mathbf{M}_{n+1}^\theta + \mathbf{K}_{n+1}^\theta \right] \mathbf{d}_{n+1}^\theta = \frac{1}{\Delta t} \mathbf{M}_{n+1,n}^\theta \mathbf{d}_n^\theta + \mathbf{f}_{\text{ext},n+1}^\theta. \quad (4.15)$$

4.2.2.2 Local problem(s)

Local problems defined on $\Omega_{L,i}^\theta$ are extracted from the global domain Ω^θ in the same manner as the GFEM^{gl} procedure presented in Section 2.3.1 of Chapter 2 for the case of steady-state heat transfer. Given the transient nature of the

global problem, local solutions should, however, be updated at each global time step $t = t_i$, $i = 0, \dots, N$ to reflect the time-evolution of localized effects. Because local solutions are only utilized to generate global–local enrichment functions with good approximation properties for the global problem, *transient effects in local problems are ignored*, which simplifies and reduces the computational effort required to solve. Thus, at a given time step t_{n+1} , the solving equations are of the same form as the steady-state heat transfer local problem presented in Section 2.3.1 of Chapter 2:

$$\mathbf{K}_L^\theta \mathbf{d}_{L,n+1}^\theta = \mathbf{f}_{\text{ext},L,n+1}^\theta, \quad (4.16)$$

where the left-hand side \mathbf{K}_L^θ remains constant in between time steps, just as in Equation (2.13). However, time-dependency of thermal loads and boundary conditions must be considered on the right-hand side, so that

$$\begin{aligned} \mathbf{f}_{\text{ext},L,n+1}^\theta = & \eta \int_{\partial\Omega_L^\theta \setminus (\partial\Omega_L^\theta \cap \partial\Omega^\theta)} \bar{\mathbf{N}}_L^{\theta T} \theta_n \, d\Gamma + \eta \int_{\partial\Omega_L^\theta \cap \Gamma^\theta} \bar{\mathbf{N}}_L^{\theta T} \bar{\theta}_{n+1} \, d\Gamma + \int_{\Omega_L^\theta} \bar{\mathbf{N}}_L^{\theta T} Q_{n+1} \, d\Omega \\ & + \int_{\partial\Omega_L^\theta \cap \Gamma^f} \bar{\mathbf{N}}_L^{\theta T} \bar{f}_{n+1} \, d\Gamma + \int_{\partial\Omega_L^\theta \cap \Gamma^c} h_c \bar{\mathbf{N}}_L^{\theta T} \theta_\infty \, d\Gamma. \end{aligned} \quad (4.17)$$

A key aspect of (4.17) is that boundary conditions on $\partial\Omega_L^\theta \cap \partial\Omega^\theta$, such as the prescribed heat flux $\bar{f}(\mathbf{x}, t)$ and temperature $\bar{\theta}(\mathbf{x}, t)$, are evaluated at current time $t = t_{n+1}$, whereas boundary conditions on $\partial\Omega_L^\theta \setminus (\partial\Omega_L^\theta \cap \partial\Omega^\theta)$ come from the transient global solution $\theta_n = \theta(\mathbf{x}, t_n)$ at the *previous* time step.

4.2.2.3 Global–local enrichment functions

The steady-state local problem (4.16) yields global–local enrichments for the transient global problem at time $t = t_n$

$$\phi_{n,\alpha}^{gl}(\mathbf{x}) = N_\alpha(\mathbf{x})\theta_L(\mathbf{x}, t_n). \quad (4.18)$$

Time-dependent shape functions at a given patch ω_α in the enriched global problem are thus given by

$$\bar{\mathbf{N}}_{n,\alpha}^\theta(\mathbf{x}) = \left[N_\alpha(\mathbf{x}) \quad \phi_{\alpha 1}(\mathbf{x}) \cdots \phi_{\alpha(m_\alpha-1)}(\mathbf{x}) \quad \phi_{n,\alpha}^{gl}(\mathbf{x}) \right],$$

where time-dependency is only assumed to arise in global–local shape functions. Temperature gradient $\bar{\mathbf{B}}_{n,\alpha}^\theta(\mathbf{x})$ follows in a straightforward manner.

4.2.3 Nonlinear thermoplasticity

Treating localized thermoplasticity with GFEM^{gl} using global–local shape functions which evolve in time bears analogies to heat transfer with time-dependent shape functions; however, additional challenges arise as a result of the non-

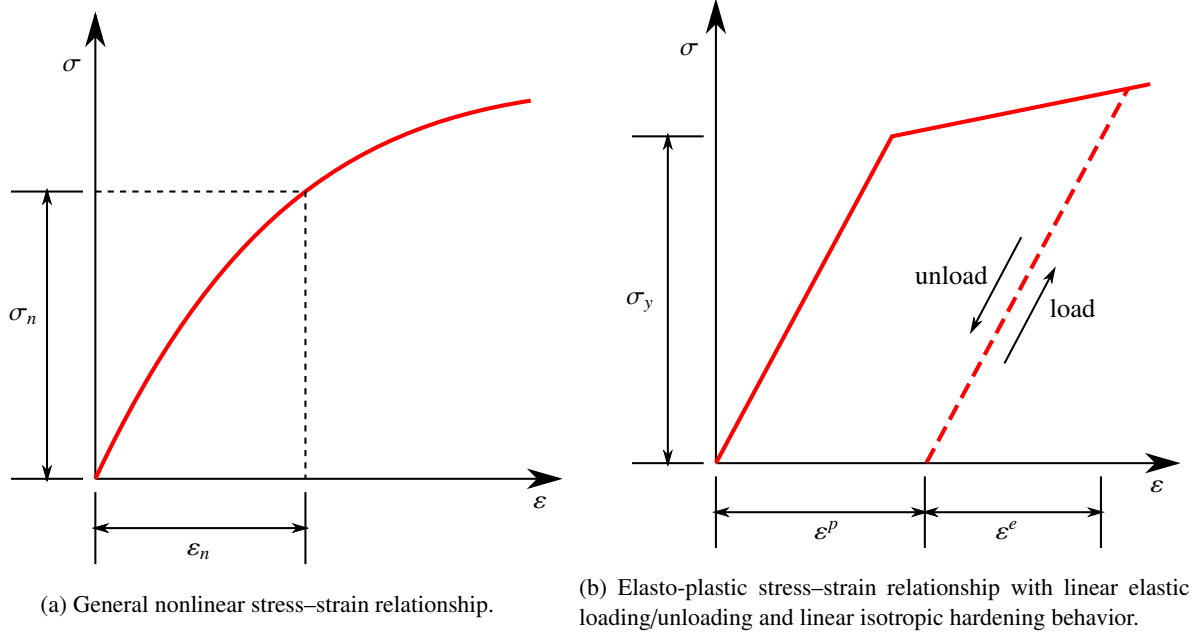


Figure 4.2: Nonlinear stress–strain relationships for, e.g., nonlinear elastic or elasto-plastic materials.

linear nature of the problem. In this section, strategies for accommodating time-dependent shape functions in the GFEM^{gl} are identified and formulated in detail for both

- (i) general nonlinear problems (for example, nonlinear elasticity) as well as
- (ii) the particular case of interest, thermo-elasto-plasticity.

The formulations presented are detailed in algorithm form in Appendix C.

4.2.3.1 General nonlinear global problem

The nonlinear problem defined by (4.4) is typically subdivided into several load or time steps, so that the displacement $\mathbf{u}_{n+1} := \mathbf{u}(\mathbf{x}, t_{n+1})$ is expressed incrementally as

$$\mathbf{u}_{n+1} = \mathbf{u}_n + \Delta \mathbf{u}_{n+1}. \quad (4.19)$$

Equilibrium must be satisfied in an incremental sense at each step. By substituting (4.19) in (4.4), the variational formulation of the nonlinear global problem is:

Find $\Delta \mathbf{u}_{n+1} \in \mathbb{S}_G(\Omega^u) \subset \mathbb{S}_{GFEM}(\Omega^u)$ such that, $\forall \delta \mathbf{u} \in \mathbb{S}_G(\Omega^u)$,

$$\int_{\Omega^u} \boldsymbol{\sigma}(\mathbf{u}_n + \Delta \mathbf{u}_{n+1}) : \boldsymbol{\varepsilon}(\delta \mathbf{u}) \, d\Omega + \eta \int_{\Gamma^u} (\mathbf{u}_n + \Delta \mathbf{u}_{n+1}) \cdot \delta \mathbf{u} \, d\Gamma = \int_{\Gamma^t} \bar{\mathbf{t}}_{n+1} \cdot \delta \mathbf{u} \, d\Gamma + \eta \int_{\Gamma^u} \bar{\mathbf{u}}_{n+1} \cdot \delta \mathbf{u} \, d\Gamma, \quad (4.20)$$

where η is a penalty parameter. Because nonlinearity arises in $\boldsymbol{\sigma}(\mathbf{u}_{n+1})$, as demonstrated, for example, in Figure 4.2a, an iterative Newton-Raphson procedure can directly be applied to solve (4.20) for $\Delta\mathbf{u}_{n+1}$. Linearizing (4.20) in this sense and rearranging all known terms (including prescribed loads or displacements and terms involving the previous time t_n or previous Newton-Raphson iteration) on the right-hand side,

$$\begin{aligned} \int_{\Omega^u} \boldsymbol{\varepsilon}(\Delta\mathbf{u}^{(i+1)}) : \mathbf{C}_{\text{tan}}^{(i)} : \boldsymbol{\varepsilon}(\delta\mathbf{u}) \, d\Omega + \eta \int_{\Gamma^u} \Delta\mathbf{u}^{(i+1)} \cdot \delta\mathbf{u} \, d\Gamma &= \int_{\Gamma^t} \bar{\mathbf{t}}_{n+1} \cdot \delta\mathbf{u} \, d\Gamma \\ &+ \eta \int_{\Gamma^u} (\bar{\mathbf{u}}_{n+1} - \mathbf{u}_{n+1}^{(i)}) \cdot \delta\mathbf{u} \, d\Gamma - \int_{\Omega^u} \boldsymbol{\sigma}(\mathbf{u}_n + \Delta\mathbf{u}_{n+1}^{(i)}) : \boldsymbol{\varepsilon}(\delta\mathbf{u}) \, d\Omega, \end{aligned} \quad (4.21)$$

where $(\cdot)^{(i)}$ signifies a quantity at Newton-Raphson iteration i , and $\mathbf{C}_{\text{tan}}^{(i)}$ represents the material tangent moduli at iteration i ,

$$\mathbf{C}_{\text{tan}}^{(i)} := \frac{\partial \boldsymbol{\sigma}(\mathbf{u}_{n+1}^{(i)})}{\partial \boldsymbol{\varepsilon}(\mathbf{u}_{n+1}^{(i)})}. \quad (4.22)$$

Observing that $\mathbf{u}_n|_{\Gamma^u} = \bar{\mathbf{u}}_n$, (4.21) simplifies further to

$$\begin{aligned} \int_{\Omega^u} \boldsymbol{\varepsilon}(\Delta\mathbf{u}^{(i+1)}) : \mathbf{C}_{\text{tan}}^{(i)} : \boldsymbol{\varepsilon}(\delta\mathbf{u}) \, d\Omega + \eta \int_{\Gamma^u} \Delta\mathbf{u}^{(i+1)} \cdot \delta\mathbf{u} \, d\Gamma &= \int_{\Gamma^t} \bar{\mathbf{t}}_{n+1} \cdot \delta\mathbf{u} \, d\Gamma \\ &+ \eta \int_{\Gamma^u} (\Delta\bar{\mathbf{u}}_{n+1} - \Delta\mathbf{u}_{n+1}^{(i)}) \cdot \delta\mathbf{u} \, d\Gamma - \int_{\Omega^u} \boldsymbol{\sigma}(\mathbf{u}_n + \Delta\mathbf{u}_{n+1}^{(i)}) : \boldsymbol{\varepsilon}(\delta\mathbf{u}) \, d\Omega, \end{aligned} \quad (4.23)$$

The total displacement increment at time t_{n+1} is updated at each iteration as

$$\Delta\mathbf{u}_{n+1}^{(i+1)} = \Delta\mathbf{u}_{n+1}^{(i)} + \Delta\mathbf{u}^{(i+1)}. \quad (4.24)$$

Combining the Newton-Raphson iteration (4.21), constitutive relations (4.4), and the J_2 -plasticity model of Table 4.1, the radial return mapping algorithm, as proposed in [118], to update the plastic deformation at each load step is detailed in Algorithm 4.1.

In contrast to Equations (2.19) and (2.20) in the linear thermoelasticity problem of Chapter 2, the nonlinear problem formulated in (4.23) leads to a GFEM approximation of the displacement (or strain) *increment*, rather than the total displacement (or strain), at time t_{n+1} , albeit of the same form,

$$\begin{aligned} \Delta\mathbf{u}(\mathbf{x}, t_{n+1}) &\approx \Delta\mathbf{u}^{hp}(\mathbf{x}, t_{n+1}) = \bar{\mathbf{N}}_{n+1}^u(\mathbf{x}) \Delta\mathbf{d}_{n+1}^u, \\ \boldsymbol{\varepsilon}(\Delta\mathbf{u}_{n+1}) &\approx \boldsymbol{\varepsilon}^{hp}(\Delta\mathbf{u}_{n+1}^{hp}) = \bar{\mathbf{B}}_{n+1}^u(\mathbf{x}) \Delta\mathbf{d}_{n+1}^u, \end{aligned} \quad (4.25)$$

with incremental solution coefficients $\Delta\mathbf{d}_{n+1}^u$. The total displacement and strain can then be reconstructed as the

Algorithm 4.1 Radial return mapping for classical rate-independent J_2 flow theory.

Compute the trial elastic state based on displacement $\mathbf{u}_{n+1}^{(i)}$ at iteration i ,

$$\begin{aligned}\boldsymbol{\varepsilon}_{n+1}^{m,\text{trial}} &= \boldsymbol{\varepsilon}(\mathbf{u}_{n+1}^{(i)}) - \boldsymbol{\varepsilon}_n^p - \boldsymbol{\varepsilon}_{n+1}^\theta \\ \boldsymbol{\sigma}_{n+1}^{\text{trial}} &= \mathbf{C} : \boldsymbol{\varepsilon}_{n+1}^{m,\text{trial}};\end{aligned}$$

if $f(\boldsymbol{\sigma}_{n+1}^{\text{trial}}, \alpha_n) \leq 0$ **then**

Admissible stress state—set the current plastic state to the previous state, and compute the elastic moduli:

$$\begin{aligned}\alpha_{n+1} &= \alpha_n \\ \boldsymbol{\varepsilon}_{n+1}^p &= \boldsymbol{\varepsilon}_n^p \\ \boldsymbol{\sigma}_{n+1} &= \boldsymbol{\sigma}_{n+1}^{\text{trial}} \\ \mathbf{C}_{\text{tan}}^{(i)} &= \mathbf{C}\end{aligned}$$

else

Inadmissible stress state—solve the (nonlinear) equation

$$f(\boldsymbol{\sigma}_{n+1}^{\text{trial}}, \alpha_n + \sqrt{\frac{2}{3}}\Delta\gamma^{(i)}) = 0$$

for $\Delta\gamma^{(i)} = \gamma^{(i)}\Delta t_{n+1}$;

Compute the updated plastic state and elasto-plastic tangent moduli:

$$\begin{aligned}\mathbf{n}_{n+1}^{(i)} &= \frac{\text{dev } \boldsymbol{\sigma}_{n+1}^{\text{trial}}}{\|\text{dev } \boldsymbol{\sigma}_{n+1}^{\text{trial}}\|} \\ \alpha_{n+1}^{(i)} &= \alpha_n + \sqrt{\frac{2}{3}}\Delta\gamma^{(i)} \\ \boldsymbol{\varepsilon}_{n+1}^{p(i)} &= \boldsymbol{\varepsilon}_n^p + \Delta\gamma^{(i)}\mathbf{n}_{n+1}^{(i)} \\ \boldsymbol{\varepsilon}_{n+1}^{m(i)} &= \boldsymbol{\varepsilon}(\mathbf{u}_{n+1}^{(i)}) - \boldsymbol{\varepsilon}_{n+1}^{p(i)} - \boldsymbol{\varepsilon}_{n+1}^\theta \\ \boldsymbol{\sigma}_{n+1}^{(i)} &= \mathbf{C} : \boldsymbol{\varepsilon}_{n+1}^{m(i)} \\ \mathbf{C}_{\text{tan}}^{(i)} &= \mathbf{C}_{\text{ep},n+1}^{(i)};\end{aligned}$$

end if

summation of all increments, that is,

$$\begin{aligned}\mathbf{u}^{hp}(\mathbf{x}, t_{n+1}) &= \sum_{j=0}^{n+1} \bar{\mathbf{N}}_j^{\mathbf{u}}(\mathbf{x}) \Delta \mathbf{d}_j^{\mathbf{u}}, \\ \boldsymbol{\varepsilon}^{hp}(\mathbf{u}_{n+1}^{hp}) &= \sum_{j=0}^{n+1} \bar{\mathbf{B}}_j^{\mathbf{u}}(\mathbf{x}) \Delta \mathbf{d}_j^{\mathbf{u}}.\end{aligned}\quad (4.26)$$

However, it is clear from (4.23) that the computation of $\boldsymbol{\sigma}(\mathbf{u}_n + \Delta \mathbf{u}_{n+1})$ at each integration point in $\Omega^{\mathbf{u}}$ involves the incremental reconstruction of total strain $\boldsymbol{\varepsilon}_{n+1}$ from each time step of the nonlinear solution. To avoid this computational overhead, it is convenient to store the total strain at the previous step $\boldsymbol{\varepsilon}_n$ as a state variable at each material point, such that

$$\boldsymbol{\varepsilon}(\mathbf{u}_{n+1}) \approx \boldsymbol{\varepsilon}^{hp}(\mathbf{u}_{n+1}^{hp}) = \boldsymbol{\varepsilon}_n + \bar{\mathbf{B}}_{n+1}^{\mathbf{u}}(\mathbf{x}) \Delta \mathbf{d}_{n+1}^{\mathbf{u}}. \quad (4.27)$$

Introducing (4.25) and (4.27) in (4.23), the discrete form of the problem at each Newton-Raphson iteration may be written as

$$\mathbf{K}_{\tan, n+1}^{\mathbf{u}(i)} \Delta \mathbf{d}^{\mathbf{u}(i+1)} = \mathbf{f}_{\text{ext}, n+1}^{\mathbf{u}} - \mathbf{f}_{\text{int}, n+1}^{\mathbf{u}(i)}, \quad (4.28)$$

where

$$\begin{aligned}\mathbf{K}_{\tan, n+1}^{\mathbf{u}(i)} &= \int_{\Omega^{\mathbf{u}}} \bar{\mathbf{B}}_{n+1}^{\mathbf{u}T} \mathbf{C}_{\tan}^{(i)} \bar{\mathbf{B}}_{n+1}^{\mathbf{u}} \, d\Omega + \eta \int_{\Gamma^{\mathbf{u}}} \bar{\mathbf{N}}_{n+1}^{\mathbf{u}T} \bar{\mathbf{N}}_{n+1}^{\mathbf{u}} \, d\Gamma, \\ \mathbf{f}_{\text{ext}, n+1}^{\mathbf{u}} &= \int_{\Gamma^{\mathbf{t}}} \bar{\mathbf{N}}_{n+1}^{\mathbf{u}T} \bar{\mathbf{t}}_{n+1} \, d\Gamma + \eta \int_{\Gamma^{\mathbf{u}}} \bar{\mathbf{N}}_{n+1}^{\mathbf{u}T} \bar{\mathbf{u}}_{n+1} \, d\Gamma, \\ \mathbf{f}_{\text{int}, n+1}^{\mathbf{u}(i)} &= \int_{\Omega^{\mathbf{u}}} \bar{\mathbf{B}}_{n+1}^{\mathbf{u}T} \boldsymbol{\sigma}(\boldsymbol{\varepsilon}_{n+1}) \, d\Omega + \eta \int_{\Gamma^{\mathbf{u}}} \bar{\mathbf{N}}_{n+1}^{\mathbf{u}T} \Delta \mathbf{d}_{n+1}^{\mathbf{u}} \, d\Gamma,\end{aligned}$$

and, from (4.4), $\mathbf{f}_{\text{int}, n+1}^{\mathbf{u}(i)}$ in (4.28) incorporates thermomechanical effects. From (4.24) and (4.26), the total solution at each iteration is updated discretely as

$$\mathbf{u}_{n+1}^{hp(i+1)} = \sum_{j=0}^n \bar{\mathbf{N}}_j^{\mathbf{u}}(\mathbf{x}) \Delta \mathbf{d}_j^{\mathbf{u}} + \bar{\mathbf{N}}_{n+1}^{\mathbf{u}} \Delta \mathbf{d}_{n+1}^{\mathbf{u}(i+1)} \quad \text{with} \quad \Delta \mathbf{d}_{n+1}^{\mathbf{u}(i+1)} = \Delta \mathbf{d}_{n+1}^{\mathbf{u}(i)} + \Delta \mathbf{d}_{n+1}^{\mathbf{u}(i+1)}. \quad (4.29)$$

4.2.3.2 Thermo-elasto-plastic global problem

The preceding holds for a general materially nonlinear problem (with or without time-dependent shape functions) based on an incremental Newton-Raphson solution scheme. However, the solution then depends recursively on all previous solution increments; thus, it requires saving each previous solution increment in the nonlinear analysis, $\Delta \mathbf{u}_j$, $j = 0, \dots, n$, comprised of solution coefficients $\Delta \mathbf{d}_j$ and time-dependent shape functions $\bar{\mathbf{N}}_j^{\mathbf{u}}$ at each step, as well as the previous total strain $\boldsymbol{\varepsilon}_n$ at each integration point in the domain. In three-dimensional, nonlinear solutions

involving many time steps and a large number of integration points, computer memory demands may therefore be substantial.

Instead, an explicit representation of the solution at the current time step *only in terms of shape functions from the current step* is sought, i.e., adopting (2.9), the GFEM approximations of the total displacement and strain fields, respectively, in matrix form are

$$\begin{aligned}\mathbf{u}_{n+1}^{(i)} &\approx \mathbf{u}_{n+1}^{hp(i)} = \bar{\mathbf{N}}_{n+1}^{\mathbf{u}}(\mathbf{x})\mathbf{d}_{n+1}^{\mathbf{u}(i)}, \\ \boldsymbol{\varepsilon}_{n+1}^{(i)} &\approx \boldsymbol{\varepsilon}_{n+1}^{hp(i)} = \bar{\mathbf{B}}_{n+1}^{\mathbf{u}}(\mathbf{x})\mathbf{d}_{n+1}^{\mathbf{u}(i)},\end{aligned}\quad (4.30)$$

where

$$\bar{\mathbf{N}}_{n+1}^{\mathbf{u}}(\mathbf{x}) = [\bar{\mathbf{N}}_{n+1,1}^{\mathbf{u}}(\mathbf{x}) \cdots \bar{\mathbf{N}}_{n+1,k}^{\mathbf{u}}(\mathbf{x})], \quad \bar{\mathbf{N}}_{n+1,\alpha}^{\mathbf{u}}(\mathbf{x}) = \left[\underbrace{\mathbf{N}_{\alpha 0}^{\mathbf{u}}(\mathbf{x})}_{\text{PoU}} \quad \underbrace{\mathbf{N}_{n+1,\alpha 1}^{\mathbf{u}}(\mathbf{x}) \cdots \mathbf{N}_{n+1,\alpha m_\alpha}^{\mathbf{u}}(\mathbf{x})}_{\text{Enrichment}} \right]$$

denotes the global shape functions, while

$$\bar{\mathbf{B}}_{n+1}^{\mathbf{u}}(\mathbf{x}) = [\bar{\mathbf{B}}_{n+1,1}^{\mathbf{u}}(\mathbf{x}) \cdots \bar{\mathbf{B}}_{n+1,k}^{\mathbf{u}}(\mathbf{x})], \quad \bar{\mathbf{B}}_{n+1,\alpha}^{\mathbf{u}}(\mathbf{x}) = \left[\underbrace{\mathbf{B}_{\alpha 0}^{\mathbf{u}}(\mathbf{x})}_{\text{PoU}} \quad \underbrace{\mathbf{B}_{n+1,\alpha 1}^{\mathbf{u}}(\mathbf{x}) \cdots \mathbf{B}_{n+1,\alpha m_\alpha}^{\mathbf{u}}(\mathbf{x})}_{\text{Enrichment}} \right],$$

indicates the strain-displacement matrix.

In the special case of elasto-plasticity, the total stress at the previous converged load step $\boldsymbol{\sigma}(\mathbf{u}_n)$ satisfies the von Mises yield criterion (4.7). Then, according to (4.4) and Table 4.1, $\boldsymbol{\sigma}$ is *linear elastic* in \mathbf{u}_n , such that

$$\boldsymbol{\sigma}(\mathbf{u}_{n+1}) = \boldsymbol{\sigma}(\mathbf{u}_n + \Delta\mathbf{u}_{n+1}) = \mathbf{C} : \boldsymbol{\varepsilon}^m(\mathbf{u}_n) + \boldsymbol{\sigma}(\Delta\mathbf{u}_{n+1}).$$

The elastic loading/unloading behavior is demonstrated graphically in Figure 4.2b (in this instance considering a linear elastic material model with linear isotropic hardening behavior). (4.21) may then be rewritten

$$\begin{aligned}\int_{\Omega^u} \boldsymbol{\varepsilon}(\Delta\mathbf{u}^{(i+1)}) : \mathbf{C}_{\text{tan}}^{(i)} : \boldsymbol{\varepsilon}(\delta\mathbf{u}) \, d\Omega + \eta \int_{\Gamma^u} \Delta\mathbf{u}^{(i+1)} \cdot \delta\mathbf{u} \, d\Gamma &= \int_{\Gamma^t} \bar{\mathbf{t}}_{n+1} \cdot \delta\mathbf{u} \, d\Gamma + \eta \int_{\Gamma^u} (\bar{\mathbf{u}}_{n+1} - \mathbf{u}_{n+1}^{(i)}) \cdot \delta\mathbf{u} \, d\Gamma \\ &- \int_{\Omega^u} \boldsymbol{\varepsilon}^m(\mathbf{u}_n) : \mathbf{C} : \boldsymbol{\varepsilon}(\delta\mathbf{u}) \, d\Omega - \int_{\Omega^u} \boldsymbol{\sigma}(\Delta\mathbf{u}_{n+1}^{(i)}) : \boldsymbol{\varepsilon}(\delta\mathbf{u}) \, d\Omega.\end{aligned}\quad (4.31)$$

A critical issue in (4.31) is representing the total solution $\mathbf{u}_{n+1}^{(0)}$ to begin Newton-Raphson iterations at the beginning of each new time or load step ($i = 1$). Traditionally, the previous converged total solution is used to begin the nonlinear

solution scheme, i.e., $\mathbf{u}_{n+1}^{(0)} = \mathbf{u}_n$. However,

$$\mathbf{u}_n \approx \bar{\mathbf{N}}_n^{\mathbf{u}} \mathbf{d}_n^{\mathbf{u}}$$

depends on previous shape functions $\bar{\mathbf{N}}_n^{\mathbf{u}}$, which are unavailable at the current time step, and previous converged solution coefficients $\mathbf{d}_n^{\mathbf{u}}$ are incompatible with shape functions $\bar{\mathbf{N}}_{n+1}^{\mathbf{u}}$ at the current step.

Linear recovery of total solution \mathbf{u}_n Instead, the *previous* total solution \mathbf{u}_n may be approximated using *current* global shape functions updated for time $t = t_{n+1}$,

$$\begin{aligned} \mathbf{u}_n &\approx \mathbf{u}_{n+1,n}^{hp} = \bar{\mathbf{N}}_{n+1}^{\mathbf{u}}(\mathbf{x}, t_{n+1}) \mathbf{d}_{n+1,n}^{\mathbf{u}}, \\ \boldsymbol{\varepsilon}_n &\approx \boldsymbol{\varepsilon}_{n+1,n}^{hp} = \bar{\mathbf{B}}_{n+1}^{\mathbf{u}}(\mathbf{x}, t_{n+1}) \mathbf{d}_{n+1,n}^{\mathbf{u}}, \end{aligned} \quad (4.32)$$

where the notation $(\)_{n+1,n}$ indicates a term involving shape functions from step $n + 1$ and quantities (e.g., strains, loads, or solutions) from step n . Because the previous converged state is *linear elastic* in \mathbf{u}_n , rewriting (4.20) at the previous step n and substituting linear elastic constitutive relations (4.4) yields

$$\int_{\Omega^{\mathbf{u}}} \boldsymbol{\varepsilon}^m(\mathbf{u}_n) : \mathbf{C} : \boldsymbol{\varepsilon}(\delta \mathbf{u}) \, d\Omega + \eta \int_{\Gamma^{\mathbf{u}}} \mathbf{u}_n \cdot \delta \mathbf{u} \, d\Gamma = \int_{\Gamma^t} \bar{\mathbf{t}}_n \cdot \delta \mathbf{u} \, d\Gamma + \eta \int_{\Gamma^{\mathbf{u}}} \bar{\mathbf{u}}_n \cdot \delta \mathbf{u} \, d\Gamma, \quad (4.33)$$

where

$$\boldsymbol{\varepsilon}^m(\mathbf{u}_n) = \boldsymbol{\varepsilon}(\mathbf{u}_n) - \boldsymbol{\varepsilon}_n^p - \boldsymbol{\varepsilon}_n^\theta.$$

Previous converged plastic and thermal strains $\boldsymbol{\varepsilon}_n^p$ and $\boldsymbol{\varepsilon}_n^\theta$ may then be applied as *linear elastic pre-strains* on the right-hand side of (4.33), so that

$$\int_{\Omega^{\mathbf{u}}} \boldsymbol{\varepsilon}(\mathbf{u}_n) : \mathbf{C} : \boldsymbol{\varepsilon}(\delta \mathbf{u}) \, d\Omega + \eta \int_{\Gamma^{\mathbf{u}}} \mathbf{u}_n \cdot \delta \mathbf{u} \, d\Gamma = \int_{\Gamma^t} \bar{\mathbf{t}}_n \cdot \delta \mathbf{u} \, d\Gamma + \eta \int_{\Gamma^{\mathbf{u}}} \bar{\mathbf{u}}_n \cdot \delta \mathbf{u} \, d\Gamma - \int_{\Omega^{\mathbf{u}}} (-\boldsymbol{\varepsilon}_n^p - \boldsymbol{\varepsilon}_n^\theta) : \mathbf{C} : \boldsymbol{\varepsilon}(\delta \mathbf{u}) \, d\Omega. \quad (4.34)$$

Substituting approximation (4.32) for \mathbf{u}_n and $\boldsymbol{\varepsilon}_n$ results in the discrete linear elastic system of equations

$$\mathbf{K}_{\text{elas},n+1}^{\mathbf{u}} \mathbf{d}_{n+1,n}^{\mathbf{u}} = \mathbf{f}_{\text{ext},n+1,n}^{\mathbf{u}} - \mathbf{f}_{\text{int},n+1,n}^{\mathbf{u}}, \quad (4.35)$$

with

$$\begin{aligned}\mathbf{K}_{\text{elas},n+1}^{\mathbf{u}} &= \int_{\Omega^{\mathbf{u}}} \bar{\mathbf{B}}_{n+1}^{\mathbf{u}T} \mathbf{C} \bar{\mathbf{B}}_{n+1}^{\mathbf{u}} \, d\Omega + \eta \int_{\Gamma^{\mathbf{u}}} \bar{\mathbf{N}}_{n+1}^{\mathbf{u}T} \bar{\mathbf{N}}_{n+1}^{\mathbf{u}} \, d\Gamma, \\ \mathbf{f}_{\text{ext},n+1,n}^{\mathbf{u}} &= \int_{\Gamma^{\mathbf{t}}} \bar{\mathbf{N}}_{n+1}^{\mathbf{u}T} \bar{\mathbf{t}}_n \, d\Gamma + \eta \int_{\Gamma^{\mathbf{u}}} \bar{\mathbf{N}}_{n+1}^{\mathbf{u}T} \bar{\mathbf{u}}_n \, d\Gamma, \\ \mathbf{f}_{\text{int},n+1,n}^{\mathbf{u}} &= \int_{\Omega^{\mathbf{u}}} \bar{\mathbf{B}}_{n+1}^{\mathbf{u}T} \mathbf{C} (-\boldsymbol{\varepsilon}_n^p - \alpha_\theta \theta_n) \, d\Omega.\end{aligned}$$

Although (4.35) has a residual-type quantity on the right-hand side, the internal force term contains only linear elastic pre-strains, leading to a total solution. The ‘recovered’ solution $\mathbf{u}_{n+1,n}^{hp}$ provides a robust starting point for the nonlinear solution algorithm at step $n + 1$, and the fully discrete form of the Newton-Raphson scheme for \mathbf{u}_{n+1} at each iteration $i > 0$ is then

$$\mathbf{K}_{\text{tan},n+1}^{\mathbf{u}(i)} \Delta \mathbf{d}^{\mathbf{u}(i+1)} = \mathbf{f}_{\text{ext},n+1}^{\mathbf{u}} - \mathbf{f}_{\text{int},n+1}^{\mathbf{u}(i)}, \quad (4.36)$$

with

$$\begin{aligned}\mathbf{K}_{\text{tan},n+1}^{\mathbf{u}(i)} &= \int_{\Omega^{\mathbf{u}}} \bar{\mathbf{B}}_{n+1}^{\mathbf{u}T} \mathbf{C}_{\text{tan}}^{(i)} \bar{\mathbf{B}}_{n+1}^{\mathbf{u}} \, d\Omega + \eta \int_{\Gamma^{\mathbf{u}}} \bar{\mathbf{N}}_{n+1}^{\mathbf{u}T} \bar{\mathbf{N}}_{n+1}^{\mathbf{u}} \, d\Gamma, \\ \mathbf{f}_{\text{ext},n+1}^{\mathbf{u}} &= \int_{\Gamma^{\mathbf{t}}} \bar{\mathbf{N}}_{n+1}^{\mathbf{u}T} \bar{\mathbf{t}}_{n+1} \, d\Gamma + \eta \int_{\Gamma^{\mathbf{u}}} \bar{\mathbf{N}}_{n+1}^{\mathbf{u}T} \bar{\mathbf{u}}_{n+1} \, d\Gamma, \\ \mathbf{f}_{\text{int},n+1}^{\mathbf{u}(i)} &= \int_{\Omega^{\mathbf{u}}} \bar{\mathbf{B}}_{n+1}^{\mathbf{u}T} \boldsymbol{\sigma}(\mathbf{u}_{n+1}^{(i)}) \, d\Omega.\end{aligned}$$

The approximate total solution $\mathbf{u}_{n+1}^{hp(i+1)}$ can then be expressed in a convenient form *involving only shape functions from the current step* $t = t_{n+1}$, as

$$\mathbf{u}_{n+1}^{hp(i)} = \bar{\mathbf{N}}_{n+1}^{\mathbf{u}} \mathbf{d}_{n+1}^{\mathbf{u}(i+1)} \quad \text{with} \quad \mathbf{d}_{n+1}^{\mathbf{u}(i+1)} = \mathbf{d}_{n+1}^{\mathbf{u}(i)} + \Delta \mathbf{d}^{\mathbf{u}(i+1)}, \quad (4.37)$$

where $\mathbf{d}_{n+1}^{\mathbf{u}(0)} = \mathbf{d}_{n+1,n}^{\mathbf{u}}$. Thus, time-dependency of the global approximation space may be handled automatically, and representing the total solution in the updated space at step $t = t_{n+1}$ involves *no additional computational cost or storage* compared to a discretization which remains constant in between time steps.

Linear prediction of total solution \mathbf{u}_{n+1} A disadvantage of recovering the previous converged state \mathbf{u}_n is that (4.34) involves the temperature from the previous time $t = t_n$, which therefore requires storage of the heat transfer solution from both previous and current time steps. Instead, a strategy based on a linear elastic ‘prediction’ of the solution at

the current time $t = t_{n+1}$ is detailed as follows: At the initial Newton-Raphson iteration $i = 1$ of time t_{n+1} ,

$$\begin{aligned}\mathbf{C}_{\text{tan}}^{(0)} &= \mathbf{C}, \\ \mathbf{u}_{n+1}^{(1)} &:= \mathbf{u}_n + \Delta \mathbf{u}^{(1)}.\end{aligned}$$

Substituting the above into (4.31) yields

$$\begin{aligned}\int_{\Omega^u} \boldsymbol{\varepsilon}(\Delta \mathbf{u}^{(1)}) : \mathbf{C} : \boldsymbol{\varepsilon}(\delta \mathbf{u}) \, d\Omega + \eta \int_{\Gamma^u} \Delta \mathbf{u}^{(1)} \cdot \delta \mathbf{u} \, d\Gamma &= \int_{\Gamma^t} \bar{\mathbf{t}}_{n+1} \cdot \delta \mathbf{u} \, d\Gamma + \eta \int_{\Gamma^u} (\bar{\mathbf{u}}_{n+1} - (\mathbf{u}_{n+1}^{(1)} - \Delta \mathbf{u}^{(1)})) \cdot \delta \mathbf{u} \, d\Gamma \\ &\quad - \int_{\Omega^u} (\boldsymbol{\varepsilon}(\mathbf{u}_{n+1}^{(1)} - \Delta \mathbf{u}^{(1)}) - \boldsymbol{\varepsilon}_n^p - \boldsymbol{\varepsilon}_{n+1}^\theta) : \mathbf{C} : \boldsymbol{\varepsilon}(\delta \mathbf{u}) \, d\Omega,\end{aligned}$$

then rearranging and simplifying further,

$$\begin{aligned}\int_{\Omega^u} \boldsymbol{\varepsilon}(\mathbf{u}_{n+1}^{(1)}) : \mathbf{C} : \boldsymbol{\varepsilon}(\delta \mathbf{u}) \, d\Omega + \eta \int_{\Gamma^u} \mathbf{u}_{n+1}^{(1)} \cdot \delta \mathbf{u} \, d\Gamma &= \int_{\Gamma^t} \bar{\mathbf{t}}_{n+1} \cdot \delta \mathbf{u} \, d\Gamma + \eta \int_{\Gamma^u} \bar{\mathbf{u}}_{n+1} \cdot \delta \mathbf{u} \, d\Gamma \\ &\quad + \int_{\Omega^u} (\boldsymbol{\varepsilon}_n^p + \boldsymbol{\varepsilon}_{n+1}^\theta) : \mathbf{C} : \boldsymbol{\varepsilon}(\delta \mathbf{u}) \, d\Omega,\end{aligned}\quad (4.38)$$

which is linear in *total solution* iterate $\mathbf{u}_{n+1}^{(1)}$, based on the application of $\boldsymbol{\varepsilon}_n^p$ as a linear elastic pre-strain on the right-hand side. Rather than ‘recovering’ previous solution $\mathbf{u}_{n+1,n}$ as proposed above, $\mathbf{u}_{n+1}^{(1)}$ is equivalent to a linear elastic ‘predictor’ or trial state of the classical RRA [118] at load increment $n + 1$. Substituting (4.30) into (4.38) results in the discrete linear system of equations at iteration $i = 1$

$$\mathbf{K}_{\text{elas},n+1}^u \mathbf{d}_{n+1}^{u(1)} = \mathbf{f}_{\text{ext},n+1}^u - \mathbf{f}_{\text{int},n+1}^{u(0)},\quad (4.39)$$

with

$$\mathbf{f}_{\text{int},n+1}^{u(0)} = \int_{\Omega^u} \bar{\mathbf{B}}_{n+1}^{uT} \mathbf{C} (-\boldsymbol{\varepsilon}_n^p - \boldsymbol{\alpha}_\theta \theta_{n+1}) \, d\Omega.$$

The fully discrete form of the Newton-Raphson scheme for \mathbf{u}_{n+1} at each iteration $i > 1$ is given by (4.36), and the approximate total solution $\mathbf{u}_{n+1}^{hp(i+1)}$ is similarly given by (4.37).

4.2.3.3 Local problem(s)

A local domain $\Omega_L^u \subseteq \Omega^u$ is chosen just as previously described in the linear thermoelasticity formulation of Section 2.3.2 of Chapter 2. The *nonlinear* local thermoplasticity problem is divided into time steps or increments in the same manner as the global problem, so that, at $t = t_{n+1}$, it is formulated as follows:

Find $\Delta \mathbf{u}_{L,n+1} \in \mathbb{S}_L(\Omega_L^u) \subset \mathbb{S}_{GFEM}(\Omega_L^u)$ such that, $\forall \delta \mathbf{u}_L \in X_L^{hp}(\Omega_L^u)$,

$$\begin{aligned} \int_{\Omega_L^u} \boldsymbol{\sigma}(\mathbf{u}_{L,n} + \Delta \mathbf{u}_{L,n+1}) : \boldsymbol{\varepsilon}(\delta \mathbf{u}_L) \, d\Omega + \eta \int_{\partial \Omega_L^u \setminus (\partial \Omega_L^u \cap \Gamma^t)} (\mathbf{u}_{L,n} + \Delta \mathbf{u}_{L,n+1}) \cdot \delta \mathbf{u}_L \, d\Gamma \\ = \eta \int_{\partial \Omega_L^u \setminus (\partial \Omega_L^u \cap \partial \Omega^u)} \mathbf{u}_n \cdot \delta \mathbf{u}_L \, d\Gamma + \eta \int_{\partial \Omega_L^u \cap \Gamma^u} \bar{\mathbf{u}}_{n+1} \cdot \delta \mathbf{u}_L \, d\Gamma + \int_{\partial \Omega_L^u \cap \Gamma^t} \bar{\mathbf{t}}_{n+1} \cdot \delta \mathbf{u}_L \, d\Gamma. \end{aligned} \quad (4.40)$$

A key aspect of problem (4.40) is the use of the generalized FEM solution of the global problem \mathbf{u}_n at the previous time step as a displacement boundary condition on $\partial \Omega_L^u \setminus (\partial \Omega_L^u \cap \partial \Omega^u)$; tractions or spring boundary conditions are also permitted.

The local total displacement, displacement increment, and total strain fields, respectively, may be approximated as

$$\begin{aligned} \Delta \mathbf{u}_L(\mathbf{x}, t_{n+1}) &\approx \Delta \mathbf{u}_L^{hp}(\mathbf{x}, t_{n+1}) = \bar{\mathbf{N}}_L^u(\mathbf{x}) \Delta \mathbf{d}_{L,n+1}^u, \\ \mathbf{u}_L(\mathbf{x}, t_{n+1}) &\approx \mathbf{u}_L^{hp}(\mathbf{x}, t_{n+1}) = \bar{\mathbf{N}}_L^u(\mathbf{x}) \mathbf{d}_{L,n+1}^u, \\ \boldsymbol{\varepsilon}(\mathbf{u}_{L,n+1}) &\approx \boldsymbol{\varepsilon}_L^{hp}(\mathbf{u}_{L,n+1}^{hp}) = \bar{\mathbf{B}}_L^u(\mathbf{x}) \mathbf{d}_{L,n+1}^u, \end{aligned} \quad (4.41)$$

where, in the local problem, shape functions are *independent* of time t . Applying a Newton-Raphson iteration scheme to the nonlinear problem (4.40) in an analogous manner to the global problem (4.21), the discrete system of equations at iteration $i + 1$ is given by

$$\mathbf{K}_{\tan,L}^{\mathbf{u}(i)} \Delta \mathbf{d}_L^{\mathbf{u}(i+1)} = \mathbf{f}_{\text{ext},L,n+1}^{\mathbf{u}} - \mathbf{f}_{\text{int},L,n+1}^{\mathbf{u}(i)}, \quad (4.42)$$

with

$$\begin{aligned} \mathbf{K}_{\tan,L}^{\mathbf{u}(i)} &= \int_{\Omega_L^u} \bar{\mathbf{B}}_L^{\mathbf{u}T} \mathbf{C}_{\tan}^{(i)} \bar{\mathbf{B}}_L^{\mathbf{u}} \, d\Omega + \eta \int_{\partial \Omega_L^u \setminus (\partial \Omega_L^u \cap \Gamma^t)} \bar{\mathbf{N}}_L^{\mathbf{u}T} \bar{\mathbf{N}}_L^{\mathbf{u}} \, d\Gamma, \\ \mathbf{f}_{\text{ext},L,n+1}^{\mathbf{u}} &= \eta \int_{\partial \Omega_L^u \setminus (\partial \Omega_L^u \cap \partial \Omega^u)} \bar{\mathbf{N}}_L^{\mathbf{u}T} \mathbf{u}_n \, d\Gamma + \eta \int_{\partial \Omega_L^u \cap \Gamma^u} \bar{\mathbf{N}}_L^{\mathbf{u}T} \bar{\mathbf{u}}_{n+1} \, d\Gamma + \int_{\partial \Omega_L^u \cap \Gamma^t} \bar{\mathbf{N}}_L^{\mathbf{u}T} \bar{\mathbf{t}}_{n+1} \, d\Gamma, \\ \mathbf{f}_{\text{int},L,n+1}^{\mathbf{u}(i)} &= \int_{\Omega_L^u} \bar{\mathbf{B}}_L^{\mathbf{u}T} \boldsymbol{\sigma}(\mathbf{u}_{L,n+1}) \, d\Omega, \end{aligned}$$

and the total solution at each iteration is updated as

$$\mathbf{u}_{L,n+1}^{hp(i+1)} = \bar{\mathbf{N}}_L^u \mathbf{d}_{L,n+1}^{\mathbf{u}(i+1)} \quad \text{with} \quad \mathbf{d}_{L,n+1}^{\mathbf{u}(i+1)} = \mathbf{d}_{L,n+1}^{\mathbf{u}(i)} + \Delta \mathbf{d}_L^{\mathbf{u}(i+1)}.$$

4.2.3.4 Improving local boundary conditions

As described in previous chapters, the quality of an enriched global GFEM^{gl} solution is sensitive to the quality of boundary conditions provided by the global problem—especially in time-dependent or multi-step analyses, since

error arising from local problem boundary conditions is propagated from time step to time step. In (4.40), boundary conditions $\mathbf{u}_n \approx \mathbf{u}_n^{hp}$ from the previous global time step may provide a poor estimate of the global solution at the current time step, but traditional approaches for improving boundary conditions, such as performing multiple global–local iterations or using a large ‘buffer zone’ [51], may be prohibitively expensive in nonlinear problems involving many time steps. The GFEM^{el}, however, is targeted at problems exhibiting localized plasticity, so that nonlinearity at a given load step is concentrated, for example, under a sharp loading, while the behavior of the majority of the global domain is linear elastic. Therefore, an estimate or prediction of the global solution $\mathbf{u}_{n+1}^* \approx \mathbf{u}_{n,n+1}^{hp}$ at the current time step t_{n+1} based on shape functions from the *previous* time step t_n may be used to provide improved local problem boundary conditions,

$$\begin{aligned}\mathbf{u}_{n+1}^* &\approx \mathbf{u}_{n,n+1}^{hp} = \tilde{\mathbf{N}}_n^{\mathbf{u}}(\mathbf{x})\mathbf{d}_{n,n+1}^{\mathbf{u}}, \\ \boldsymbol{\varepsilon}_{n+1}^* &\approx \boldsymbol{\varepsilon}_{n,n+1}^{hp} = \tilde{\mathbf{B}}_n^{\mathbf{u}}(\mathbf{x})\mathbf{d}_{n,n+1}^{\mathbf{u}},\end{aligned}\quad (4.43)$$

where $(\)_{n,n+1}$ indicates a computation of quantities at time $t = t_{n+1}$ using shape functions from the previous step, $t = t_n$. Two variations are possible: *Linear elastic* prediction of the global solution $\mathbf{u}_{n,n+1}^{hp,\text{lin}}$, based on (4.39), substituting shape functions $\tilde{\mathbf{N}}_n^{\mathbf{u}}$ and $\tilde{\mathbf{B}}_n^{\mathbf{u}}$,

$$\mathbf{u}_{n,n+1}^{hp,\text{lin}} = \tilde{\mathbf{N}}_n^{\mathbf{u}}\mathbf{d}_{n,n+1}^{\text{lin}},$$

leading to the linear system of equations

$$\mathbf{K}_{\text{elas},n}^{\mathbf{u}}\mathbf{d}_{n,n+1}^{\text{lin}} = \mathbf{f}_{\text{ext},n,n+1}^{\mathbf{u}} - \mathbf{f}_{\text{int},n,n+1}^{\mathbf{u}},\quad (4.44)$$

or *nonlinear* prediction of the global solution $\mathbf{u}_{n,n+1}^{hp,\text{nl}}$, based on (4.36), using shape functions $\tilde{\mathbf{N}}_n^{\mathbf{u}}$ and $\tilde{\mathbf{B}}_n^{\mathbf{u}}$,

$$\mathbf{K}_{\text{tan},n}^{\mathbf{u}(i)}\Delta\mathbf{d}^{\mathbf{u}(i+1)} = \mathbf{f}_{\text{ext},n,n+1}^{\mathbf{u}} - \mathbf{f}_{\text{int},n,n+1}^{\mathbf{u}(i)},\quad (4.45)$$

where the total solution is then given by

$$\mathbf{u}_{n,n+1}^{hp,\text{nl}(i+1)} = \tilde{\mathbf{N}}_n^{\mathbf{u}}\mathbf{d}_{n,n+1}^{\mathbf{u}(i+1)} \quad \text{with} \quad \mathbf{d}_{n,n+1}^{\mathbf{u}(i+1)} = \mathbf{d}_{n,n+1}^{\mathbf{u}(i)} + \Delta\mathbf{d}^{\mathbf{u}(i+1)}.$$

The nonlinear improvement strategy is substantially more expensive than the linear prediction, involving, in general, several Newton-Raphson iterations.

4.2.3.5 Global–local enrichment functions

Based on the two global problem formulations presented, two different time-dependent global–local enrichments are proposed for nonlinear problems to treat incremental or total approximations of the global solution. In either case, time-dependent shape functions at a given patch ω_α in the global problem are of the form

$$\bar{\mathbf{N}}_{n+1,\alpha}^{\mathbf{u}}(\mathbf{x}) = \left[\mathbf{N}_{\alpha 0}^{\mathbf{u}}(\mathbf{x}) \quad \mathbf{N}_{\alpha 1}^{\mathbf{u}}(\mathbf{x}) \cdots \mathbf{N}_{\alpha(m_\alpha-1)}^{\mathbf{u}}(\mathbf{x}) \quad \mathbf{N}_{n+1,\alpha}^{\mathbf{u},gl}(\mathbf{x}) \right],$$

that is, time-dependency in the global shape functions is assumed to arise only in terms involving global–local enrichments. Strain–displacement matrix $\bar{\mathbf{B}}_{n+1,\alpha}^{\mathbf{u}}(\mathbf{x})$ follows in a straightforward manner.

Incremental global–local enrichments In the case of general nonlinear global problems based on an incremental approximation of the solution at each time step, such as (4.25), global shape functions $\bar{\mathbf{N}}_{n+1}^{\mathbf{u}}$ should possess good approximation properties to represent the *incremental change* in the solution, or the evolution of the solution in between time steps, rather than the total solution itself. Thus, a new global–local enrichment based on the increment in the local solution over the interval $[t_n, t_{n+1}]$ is adopted,

$$\phi_{n+1,\alpha}^{gl}(\mathbf{x}) = N_\alpha(\mathbf{x}) \Delta \mathbf{u}_L(\mathbf{x}, t_{n+1}), \quad (4.46)$$

where the local displacement increment is given in (4.41).

Total global–local enrichments When approximating the *total* solution at each time step in the global problem, as in (4.30) or (4.32), global–local enrichments are of the traditional form at $t = t_{n+1}$,

$$\phi_{n+1,\alpha}^{gl}(\mathbf{x}) = N_\alpha(\mathbf{x}) \mathbf{u}_L(\mathbf{x}, t_{n+1}), \quad (4.47)$$

and the local solution \mathbf{u}_L is given in (4.41).

4.3 Numerical examples

A few numerical examples are included in the following section to explore the robustness, efficiency, and accuracy of the proposed GFEM^{gl}. In verification examples, GFEM^{gl} solutions are compared to a reference solution based on an optimal direct finite element analysis (DFEA) approach, *hp*-GFEM, which is equivalent to *hp*-adaptive FEM. Additionally, to demonstrate the applicability of the method to industrial-scale problems, a larger, realistic problem is presented for which a direct analysis approach would be impractical. In the following examples, a fixed mesh

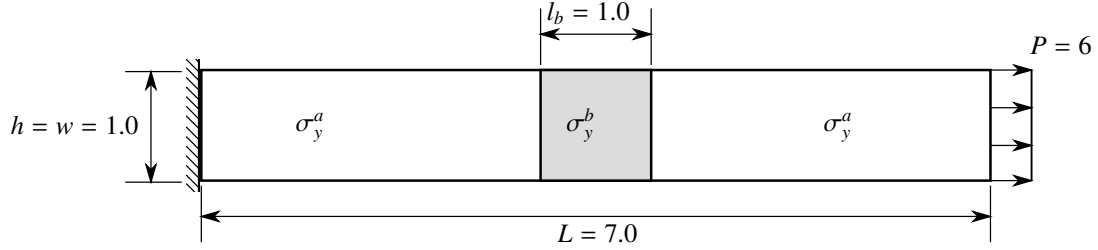


Figure 4.3: Geometry and boundary conditions of the elasto-plastic bi-material bar.

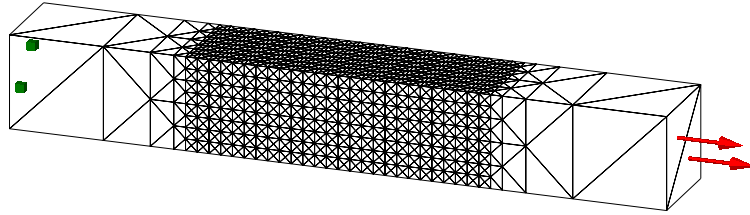


Figure 4.4: hp -GFEM mesh of the bi-material bar problem.

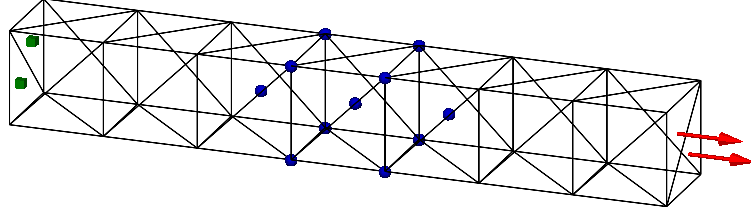
geometry is used in all time steps of hp -GFEM reference solutions and GFEM^{gl} global and local problems, that is, no mesh adaptivity is performed in between time steps. Furthermore, unless otherwise specified, all GFEM^{gl} nonlinear examples utilize the linear prediction strategy (4.39) to represent the total solution at each new time step, and boundary conditions on local problems are updated based on a linear prediction of the total solution (4.44).

4.3.1 Bi-material bar with confined plastic region

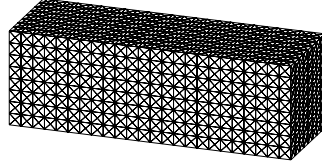
The first numerical example is a verification problem subject to *only* mechanical (i.e., no thermomechanical) loadings, for the purpose of testing each of the above GFEM^{gl} formulations for nonlinear problems with time-dependent shape functions.

The example is a bar of dimensions $1 \times 7 \times 1$ under uniform tension $P = 6$ with a soft region in the center, designed to induce localized plasticity. The bar geometry and boundary conditions are illustrated in Figure 4.3. The bar has uniform Young's modulus and Poisson's ratio $E = 4$ and $\nu = 0.0$, respectively, while the yield stress in the "stiff" region is $\sigma_y^a = 12.0$ and in the "soft" region $\sigma_y^b = 4.0$. The material has a bilinear hardening model with plastic tangent modulus $E_{\text{tan}} = 0.25$. The tensile load P is applied in 10 equal increments or load steps, λP , $\lambda = 0.1, 0.2, \dots, 1.0$, then the bar is subsequently unloaded in 10 equal increments, resulting in $N = 20$ total load steps. This problem is based on a very similar problem originally solved using the GFEM^{gl} formulation proposed in [64].

In this study, the problem is solved using both hp -GFEM (DFEA), for reference, and GFEM^{gl}, based on the formulations detailed in the above sections. hp -GFEM and GFEM^{gl} (global and local) meshes for this problem are shown in Figures 4.4 and 4.5, respectively. Reference hp -GFEM solutions use a uniform polynomial order $p_{hp} = \{2, 2, 2\}$ and heavy mesh refinement in the soft region to capture plastic deformation, while GFEM^{gl} solutions similarly



(a) GFEM^{gl} global problem. Spherical glyphs represent global nodes enriched with the local solution.



(b) GFEM^{gl} local problem.

Figure 4.5: Meshes used to solve the bi-material bar problem with the GFEM^{gl}.

use $\mathbf{p} = \mathbf{p}_{loc} = \{2, 2, 2\}$. There is no global mesh refinement, while uniform mesh refinement in the local problem, $\Omega_L = \{\mathbf{x} \mid 2.0 < x < 5.0\}$, is performed to match that of the *hp*-GFEM global mesh. the *hp*-GFEM global problem consists of 111,372 dofs, while the GFEM^{gl} global problem and local problem have, respectively, 501 and 103,404. In each case the global solution is enforced as a mixed- or spring-type boundary condition on the local domain; it is furthermore important to note that in this problem, boundary conditions on local problems *only* come from the global solution (all other local boundaries have homogeneous Neumann conditions). The problem is solved using the variety of GFEM^{gl} algorithms presented above:

- (i) GFEM^{gl} based on time-dependent, *incremental* enrichments (4.46) and local problem boundary conditions from
 - (a) the solution at the previous step \mathbf{u}_n or
 - (b) *linear prediction* of the next solution increment, $\Delta \mathbf{u}_{n,n+1}^{\text{lin}}$;
- (ii) GFEM^{gl} based on time-dependent, *total* enrichments (4.47) and local problem boundary conditions from
 - (a) the solution at the previous step \mathbf{u}_n ,
 - (b) *linear prediction* of the solution $\mathbf{u}_{n,n+1}^{\text{lin}}$, i.e., from (4.44), or
 - (c) *nonlinear prediction* of the solution $\mathbf{u}_{n,n+1}^{\text{nl}}$, i.e., from (4.45);
- (iii) GFEM^{gl} based on *time-independent* enrichment functions. Enrichment functions are generated from the nonlinear solution of the local problem $\mathbf{u}_{L,\text{max}}$ with boundary conditions from a *linear* solution of the global problem at the maximum load step, i.e., $\lambda_{\text{max}} = 1.0$; this is the strategy proposed in [52, 64], which is included here for comparison.

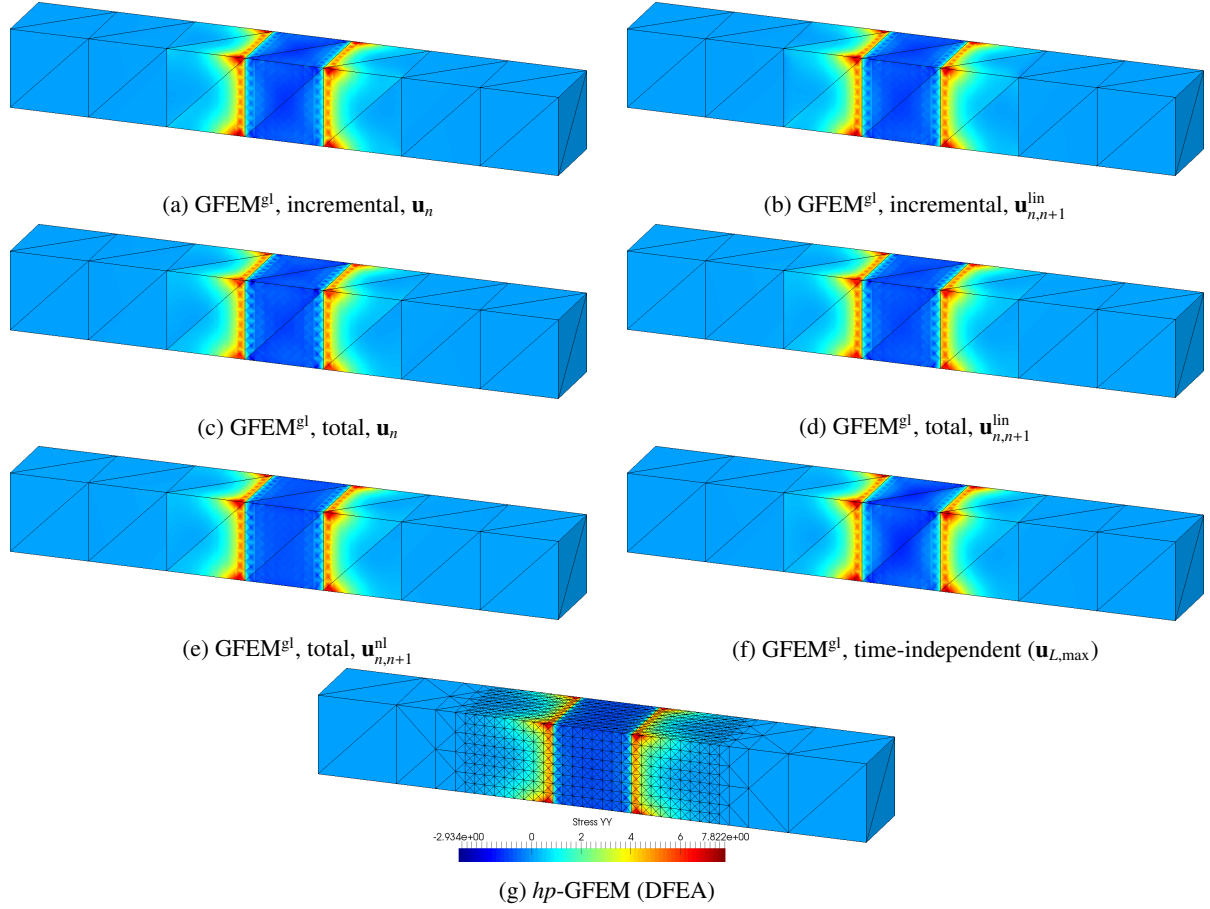


Figure 4.6: Contours of residual axial stress σ_{yy} in the bi-material bar problem from GFEM^{gl} and hp -GFEM solutions at the final load step.

Qualitative contour plots of the residual axial stress field σ_{yy} at $t = t_N$, when the bar is fully unloaded, are shown in Figure 4.6. Load–displacement curves from each global–local enrichment strategy—incremental, total, and time-independent—are included in Figures 4.7, 4.8, and 4.9, respectively, with the hp -GFEM solution superimposed in each case for comparison. Displacement and applied load are both evaluated at $\mathbf{x} = (0.5, 7.0, 0.5)$. Very good agreement of all solutions with the hp -GFEM reference is observed for this verification problem.

In order to investigate the accuracy of each specific approach, the relative errors in maximum axial displacement u_y^{\max} at the end of the bar, $\mathbf{x} = (0.5, 7.0, 0.5)$, from each solution are compared in Table 4.2. It is clear that updating the local solution at each time or load step leads to more accurate global solutions, as all GFEM^{gl} strategies involving time-dependent shape functions give better results than the time-independent enrichment functions from a single local solution at maximum load. Nonlinear solutions based on both incremental and total enrichments give similar results; a linear approximation of global boundary conditions at t_{n+1} leads to slight improvements in the observed maximum displacement. As expected, a *nonlinear* estimate of local problem boundary conditions at the current time step gives

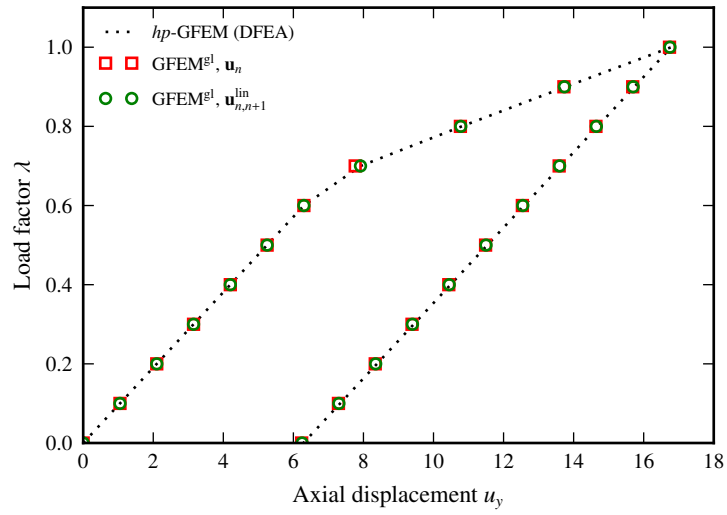


Figure 4.7: GFEM^{el} load–displacement curve of the bi-material bar problem based on incremental enrichments, compared to *hp*-GFEM.

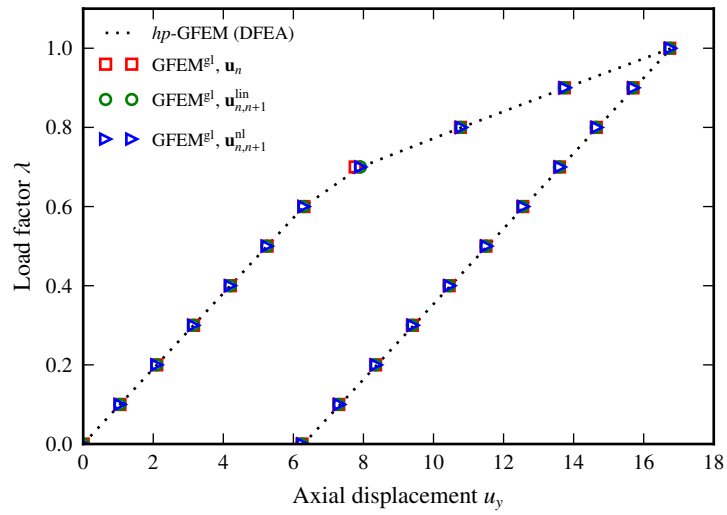


Figure 4.8: GFEM^{el} load–displacement curve of the bi-material bar problem based on total enrichments, compared to *hp*-GFEM.

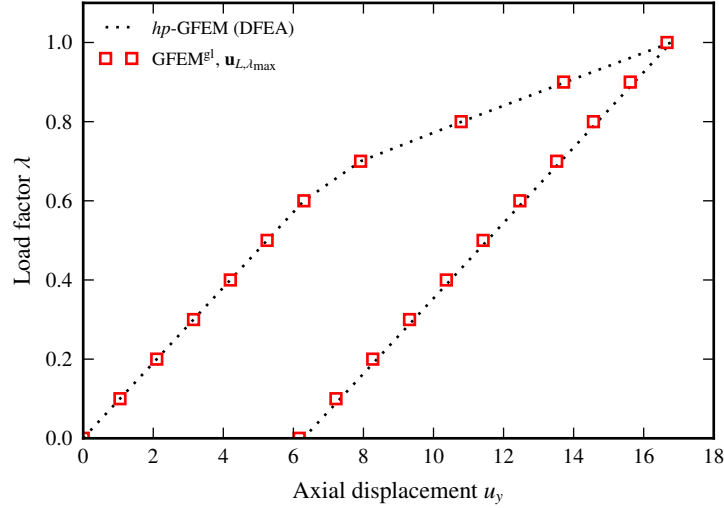


Figure 4.9: GFEM^{gl} load–displacement curve of the bi-material bar problem based on global–local enrichments computed from the ultimate load step, $\lambda = \lambda_{\max} = 1.0$, compared to hp -GFEM.

Table 4.2: Comparison of maximum axial displacements u_y^{\max} obtained from GFEM^{gl} solutions of the bi-material bar, relative to the hp -GFEM reference.

Method	Global dofs	u_y^{\max}	% difference
hp -GFEM (DFEA)	111,372	16.79	–
GFEM ^{gl} , coarse global	468	15.63	6.895%
total, \mathbf{u}_n	501	16.74	0.262%
total, $\mathbf{u}_{n,n+1}^{\text{lin}}$	501	16.75	0.246%
total, $\mathbf{u}_{n,n+1}^{\text{nl}}$	501	16.77	0.118%
incremental, \mathbf{u}_n	501	16.74	0.297%
incremental, $\mathbf{u}_{n,n+1}^{\text{lin}}$	501	16.75	0.225%
time-independent ($\mathbf{u}_{L,\max}$)	501	16.67	0.720%

Table 4.3: Comparison of Newton-Raphson iterations required for convergence of the GFEM^{gl} global bi-material bar problem, relative to the *hp*-GFEM reference. Unloading begins at load step 10. A blank space in the table indicates a linear (elastic) step. The *total* number of global iterations at each step—that is, including nonlinear prediction of boundary conditions—are given.

Load step	Global iterations						
	<i>hp</i> -GFEM	total, \mathbf{u}_n	total, $\mathbf{u}_{n,n+1}^{\text{lin}}$	total, $\mathbf{u}_{n,n+1}^{\text{nl}}$	incr., \mathbf{u}_n	incr., $\mathbf{u}_{n,n+1}^{\text{lin}}$	$\mathbf{u}_{L,\text{max}}$
1							
2							
3							
4							
5							
6							
7	4	4	3	7	4	4	4
8	4	4	4	8	4	4	4
9	4	4	4	8	4	4	4
10	4	4	3	9	4	4	4
11		3					
12		2					
13							
14							
15							
16							
17							
18							
19							
20							

the best result. However, as previously noted, this strategy comes at the cost of performing *two* nonlinear solutions of the global problem at each time step.

The total number of Newton-Raphson iterations required for convergence at each load step in global problems is included in Table 4.3; local iterations required are given in Table 4.4. Although nonlinear boundary condition prediction requires, in general, multiple nonlinear solution iterations to converge, thus increasing the number of global assembly/solution cycles, it should be noted from Table 4.4 that these more accurate boundary conditions lead to fewer overall Newton-Raphson iterations in the local problem, relative to linear boundary condition prediction. However, this is a problem-dependent behavior, as the global problem itself is relatively small and inexpensive to solve, and furthermore, local problem boundary conditions *only* come from the global solution—no prescribed, external boundary conditions are applied—thus, the quality and behavior of local solutions is entirely dependent upon the quality of the global solution. Furthermore, from Table 4.3, nonlinear behavior is observed at unloading steps 11 and 12 when local boundary conditions from \mathbf{u}_n are used with the total solution approach. This behavior may be attributed to a combination of the lagging local boundary condition and corresponding recovery of the total global solution; on the other hand, this “residual” nonlinear behavior is not observed when adopting an incremental approach in the global

Table 4.4: Comparison of Newton-Raphson iterations required for convergence of the GFEM^{gl} local bi-material bar problem, relative to the hp -GFEM reference. Unloading begins (in the global problem) at step 10. A blank space in the table indicates a linear (elastic) step.

Load step	Local iterations				
	total, \mathbf{u}_n	total, $\mathbf{u}_{n,n+1}^{\text{lin}}$	total, $\mathbf{u}_{n,n+1}^{\text{nl}}$	incr., \mathbf{u}_n	incr., $\mathbf{u}_{n,n+1}^{\text{lin}}$
1					
2					
3					
4					
5					
6					
7			3	3	3
8	3	4	4	3	4
9	4	4	4	4	4
10	4	4	4	4	4
11	4	4		4	4
12					
13					
14					
15					
16					
17					
18					
19					
20					

Table 4.5: Thermo-elasto-plastic laser-heated beam material properties.

Property	Value	Units
Young's modulus E	10.15×10^6	psi
Poisson's ratio ν	0.33	–
Yield stress σ_y	40.0×10^3	psi
Saturation stress σ_∞	45.0×10^3	psi
Plastic modulus K	0.0	psi
Hardening exponent ω	75.0	–
Thermal expansion coefficient α_θ	1.283×10^{-5}	$^\circ\text{F}^{-1}$
Thermal conductivity κ	1.87	$\frac{\text{ft-lbf}}{\text{s-in-}^\circ\text{F}}$
Heat capacity ρc	16.2	$\frac{\text{ft-lbf}}{\text{in}^3\text{-}^\circ\text{F}}$

problem.

4.3.2 Thermo-elasto-plastic laser-heated beam

While the previous example serves as verification for the implementation of time-dependent shape functions for elasto-plastic problems, the following example is a verification problem for time-dependent thermoplasticity problems involving transient heating solved with GFEM^{gl}. In all cases, an hp -GFEM direct analysis is used as a reference for comparison. The problem is very similar in nature to the homogeneous laser-heated beam of Section 2.5.2 of Chapter 2 on linear thermoelasticity. However, in this case, two types of *transient*, localized thermal boundary conditions are applied:

- (i) stationary, localized heating followed by cooling to room temperature; and
- (ii) a moving, localized heating.

The beam is of dimensions 12 in \times 0.5 in \times 0.24 in, and is fixed against axial deformations in all load scenarios. Initial conditions in the heat transfer and thermoplasticity are $\theta_0 = \theta_\infty$ and $\mathbf{u}_0 = \mathbf{0}$. Its thermal and mechanical material properties are summarized in Table 4.5. In GFEM^{gl} solutions of the problem, the same fixed, coarse-scale global mesh consisting of four-node tetrahedral elements (global element size $H = 0.5$) is used irrespective of the nature of thermal boundary conditions applied, whether stationary or moving. GFEM^{gl} local problems are meshed with four-node tetrahedral elements for local adaptive mesh refinement. On the other hand, the hp -GFEM global mesh must be adapted for each load case of interest. In this and all other thermoplasticity problems presented in this chapter, only *total* global–local enrichments, based on linear recovery of the total solution, are considered. The effect of boundary conditions on local problems from \mathbf{u}_n and $\mathbf{u}_{n,n+1}^{\text{lin}}$, as detailed in Section 4.2.3.4, is examined in GFEM^{gl} solutions in each load case.

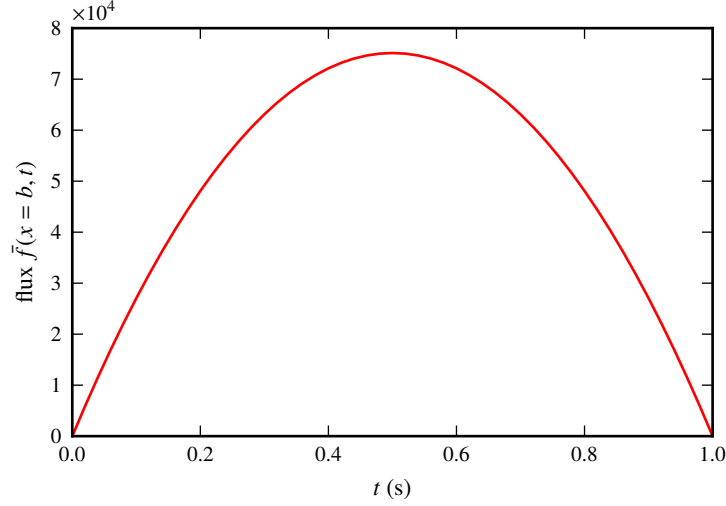


Figure 4.10: Time evolution of the maximum magnitude (at $x = 9.3$) of the stationary laser flux applied to the thermo-elasto-plastic laser-heated beam.

4.3.2.1 Stationary laser heating

The stationary laser heating applied to the front surface of the beam ($z = 0.24$ in) is characterized by

$$\tilde{f}(\mathbf{x}, t) = \frac{I_0}{2\pi a^2} g(t) \exp\left(\frac{-(x-b)^2}{2a^2}\right), \quad 8.0 \leq x \leq 10.0, \quad \text{where}$$

$$g(t) = \begin{cases} -\frac{t}{t_{\max}} \left(\frac{t}{t_{\max}} - 2.0\right) & \text{if } t < 2t_{\max} \\ 0.0 & \text{otherwise.} \end{cases}$$

Parameter $I_0 = 295 \frac{\text{ft-lbf}}{\text{s}}$ is the laser flux intensity, $a = 0.025$ in is the laser focus, or width, and $b = 9.3$ in dictates the x -coordinate of the center of the flux. The temporal variation of the applied flux magnitude is denoted $g(t)$, and $t_{\max} = 0.5$ s is the time at which the laser flux reaches a maximum. The time evolution of the maximum magnitude of the applied laser flux (i.e., at the focus point, $x = b$) is illustrated in Figure 4.10. Convection boundary conditions are applied elsewhere, at an ambient temperature of $\theta_{\infty} = 70$ °F.

The sharply varying laser flux requires high local solution fidelity—accomplished in hp -GFEM via localized adaptive mesh refinement, and in GFEM^{el} by global–local enrichments from the solution of an adapted local problem—in order to predict not only intense temperature and stress gradients, but also localized, residual plastic deformation in the beam due to the heating. The GFEM^{el} global heat transfer problem has $\mathbf{p}^{\theta} = \{2, 2, 2\}$ ($\mathbf{p}^{\mathbf{u}} = \{3, 3, 3\}$ for thermo-plasticity) and a global mesh size $H = 0.5$. The local problem is chosen in a region of the beam in the neighborhood of the sharp applied flux, $8.0 \leq x \leq 10.5$, which has local adaptive mesh refinement such that local mesh size $h = 0.0625$ and $\mathbf{p}_L^{\theta} = \{2, 2, 2\}$ ($\mathbf{p}_L^{\mathbf{u}} = \{3, 3, 3\}$ for thermoplasticity). Temperature and spring boundary conditions are applied on

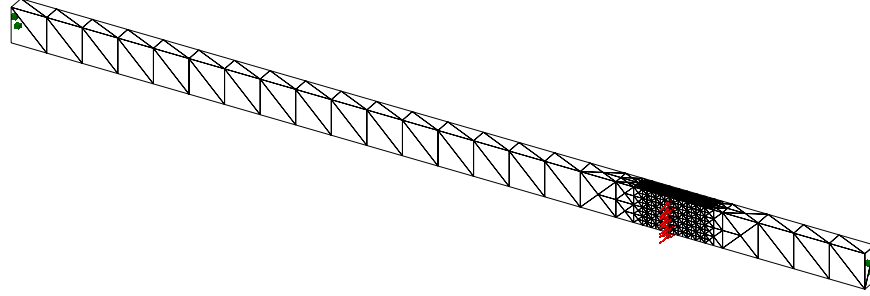
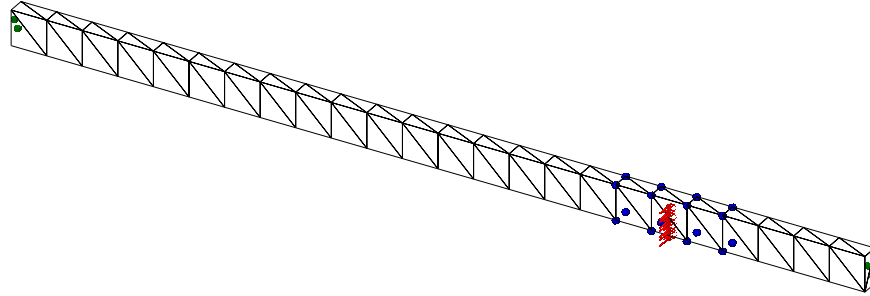
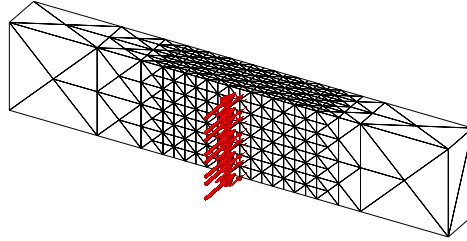


Figure 4.11: hp -GFEM mesh of the thermo-elasto-plastic beam subjected to stationary laser heating.



(a) GFEM^{gl} global problem. Spherical glyphs represent global nodes enriched with the local solution.



(b) GFEM^{gl} local problem.

Figure 4.12: Meshes used to solve the thermo-elasto-plastic laser-heated problem with the GFEM^{gl} (stationary heating).

heat transfer and thermoplasticity local problems, respectively. The hp -GFEM direct analysis is designed to achieve approximately equivalent solution fidelity to GFEM^{gl} solutions; it has a coarse global mesh size away from the sharp heating $H = 0.5$ and localized global mesh refinement in the neighborhood of the sharp flux such that $H = 0.0625$, with a uniform polynomial order throughout $\mathbf{p}^\theta = \{2, 2, 2\}$ ($\mathbf{p}^u = \{3, 3, 3\}$ in the thermoplasticity problem). Both GFEM^{gl} and hp -GFEM simulations are carried out over 32 time/load steps, with $\Delta t = 0.125$ s the time step size in the transient heat transfer problem, so that $0.0 \leq t \leq 4.0$. The hp -GFEM mesh geometry and boundary conditions are shown in Figure 4.11, while the corresponding GFEM^{gl} local and global meshes are shown in Figure 4.12.

Results from two GFEM^{gl} solution strategies are included: one based on time-dependent shape functions, as formulated in Section 4.2.3, and the other based on time-independent shape functions. Time-dependent global–local enrichments in thermoplasticity problems are generated from local solutions using boundary conditions from both \mathbf{u}_n and $\mathbf{u}_{n,n+1}^{\text{lin}}$, as described in Section 4.2.3.4. Time-independent global–local enrichments come from the solution of a

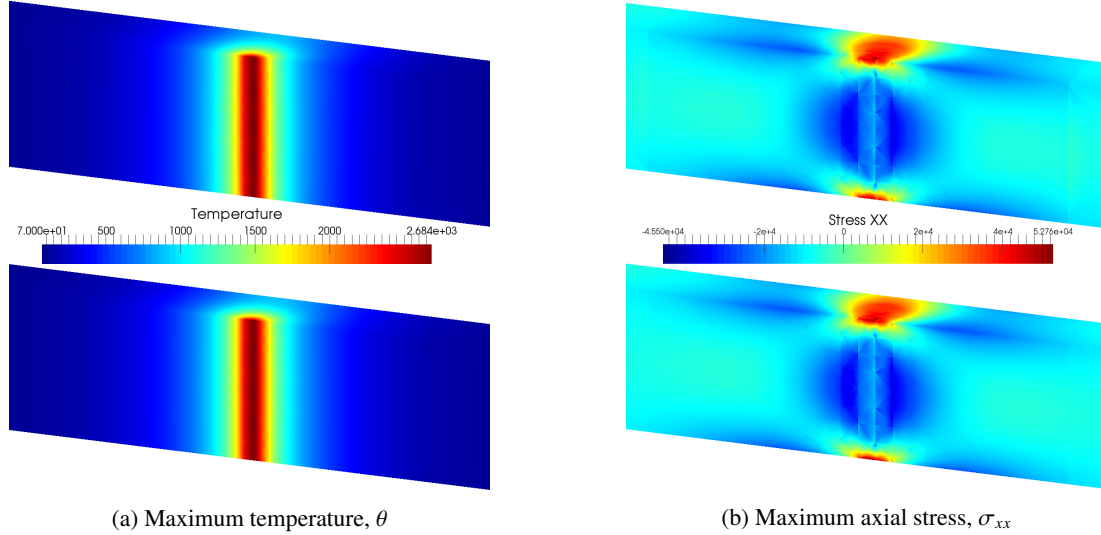


Figure 4.13: Contours of maximum temperature and axial stress in the thermo-elasto-plastic laser-heated beam problem from GFEM^{gl} (top) and *hp*-GFEM (bottom) solutions. The GFEM^{gl} stress contour shown has local problem boundary conditions from $\mathbf{u}_{n,n+1}^{\text{lin}}$.

single steady-state local problem at the maximum thermal load step (i.e., $t = t_{\text{max}}$), which is analogous to the strategy described previously in Section 4.3.1 and originally presented in [64].

Qualitative, three-dimensional contours of the maximum temperature and corresponding maximum axial stress from *hp*-GFEM and GFEM^{gl} solutions (based on local boundary conditions from $\mathbf{u}_{n,n+1}^{\text{lin}}$) are shown in Figure 4.13. Figure 4.14 shows enriched global and corresponding local thermoplasticity problem solution contours at the maximum temperature step from each choice of local problem boundary conditions (\mathbf{u}_n and $\mathbf{u}_{n,n+1}^{\text{lin}}$). It can be observed, qualitatively, that a linear global solution at each new load step may lead to a much improved estimate of global solution behavior on local problem boundaries, and accurate boundary conditions on local problems generally lead to high-quality enriched global solutions.

The pointwise maximum temperature and von Mises stress along the central axis of the beam, $y = 0.25$, at a depth $z = 0.22$, just beneath the surface, are plotted in Figure 4.15. The reference *hp*-GFEM solution is shown for comparison with GFEM^{gl} simulations using time-dependent shape functions. The maximum temperature distribution is nearly identical for both *hp*-GFEM and GFEM^{gl} simulations. Pointwise maximum von Mises stresses along the centerline of the beam also show a good agreement; due to the generous size of the local domain chosen in this example, local boundary conditions from \mathbf{u}_n and $\mathbf{u}_{n,n+1}^{\text{lin}}$ yield very similar results, though $\mathbf{u}_{n,n+1}^{\text{lin}}$ compares slightly better to *hp*-GFEM results near the intense stress gradient where the sharp laser heating is applied. A localized oscillation in the stress field near $x = 9.24$ in both GFEM^{gl} simulations likely arises due to the coarse global mesh chosen in this example and the proximity of this point to a global mesh edge.

In contrast, Figure 4.16 shows a comparison between pointwise maximum temperature and von Mises stress

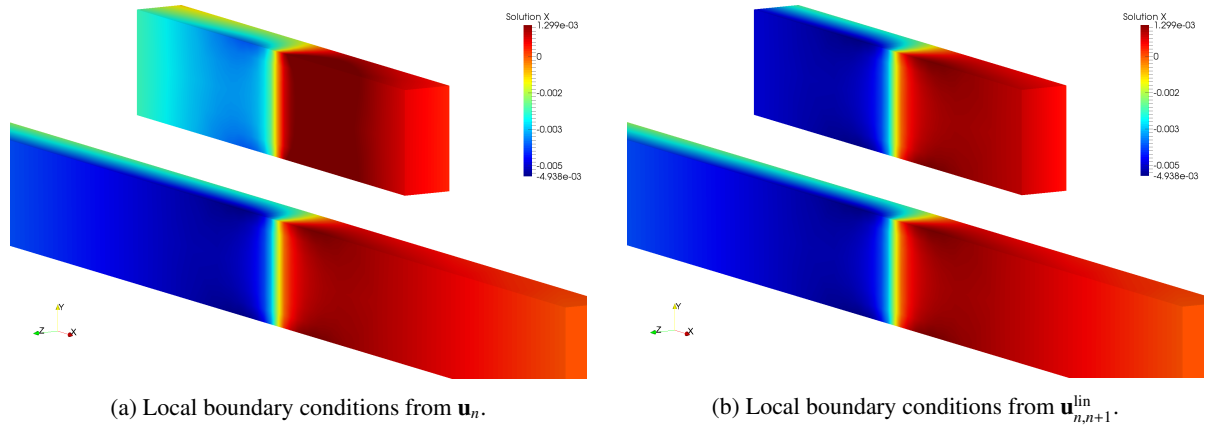
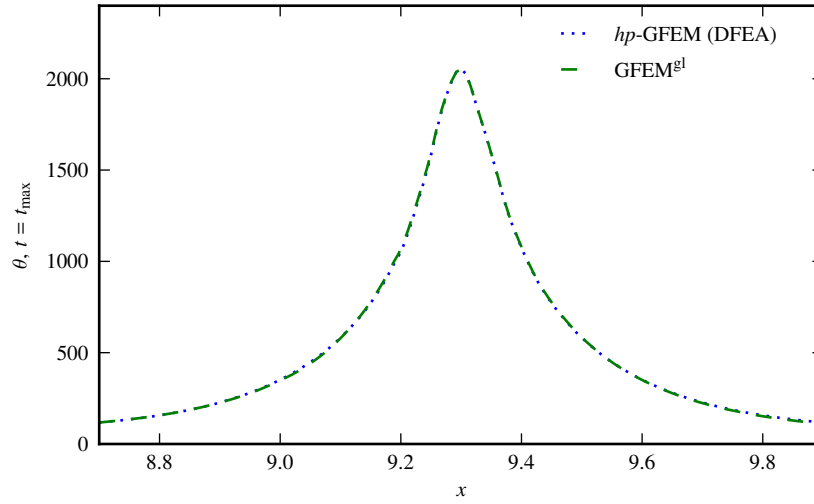


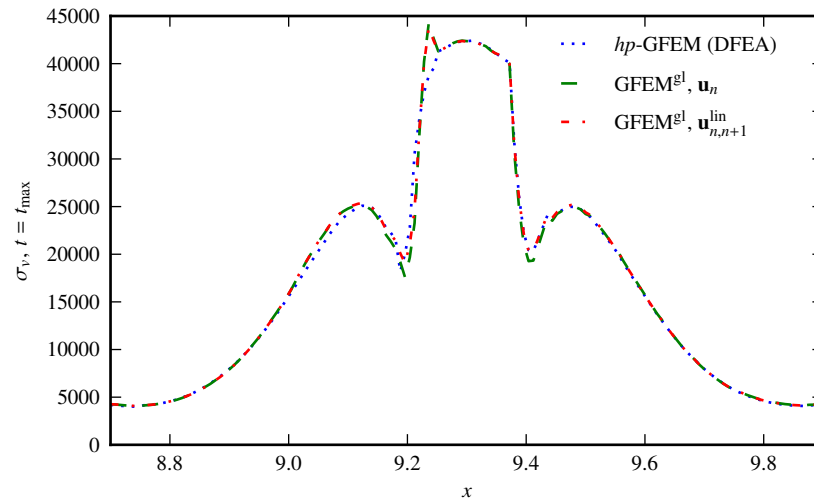
Figure 4.14: Contours of axial displacement u_x at the maximum temperature load step in the thermo-elasto-plastic laser-heated beam problem from GFEM^{gl} local (top) and corresponding enriched global (bottom) solutions with different choices of local boundary conditions.

in a GFEM^{gl} simulation based on time-independent shape functions (that is, global–local enrichments from a local solution at maximum thermal load). Global–local enrichments from the maximum thermal load are able to effectively capture the localized behavior of the transient temperature field. However, it is clear from Figure 4.16b that time-independent shape functions cannot adequately characterize the more complex time evolution of thermal stresses from the multiphysics solution field.

Of interest in this verification problem is the accuracy, relative to direct analysis, of prediction of residual deformations using GFEM^{gl}. Thus, following the transient heat transfer solution, the beam is cooled back to its initial state (ambient temperature $\theta_\infty = 70.0$ °F). The residual deformed shapes of *hp*-GFEM reference and all GFEM^{gl} solutions (based on both time-dependent and time-independent shape functions) are shown for qualitative comparison in Figure 4.17. Pointwise residual displacements u_y in the vertical direction, near the top of the beam ($y = 0.48$), as well as u_z in the out-of-plane direction, along the central axis of the beam ($y = 0.25$), are shown in Figure 4.18. Again included for contrast in Figure 4.19 are plots of residual deformations resulting from GFEM^{gl} simulations of the same problem with *time-independent* shape functions. Although both GFEM^{gl} solutions with time-dependent enrichments show similar qualitative behavior, local boundary conditions from $\mathbf{u}_{n,n+1}^{\text{lin}}$ offer a noticeable improvement over boundary conditions from \mathbf{u}_n in the prediction of residual deformations when compared to the DFEA reference solution. Figures 4.17 and 4.19 further reinforce that time-independent shape functions in thermoplasticity problems are not suitable for capturing residual deformations due to highly localized thermal stresses which evolve significantly in time.

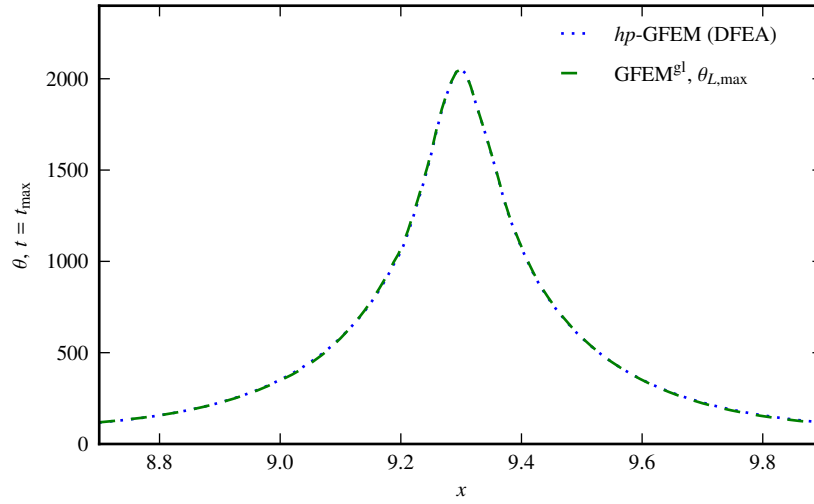


(a) Maximum temperature, θ

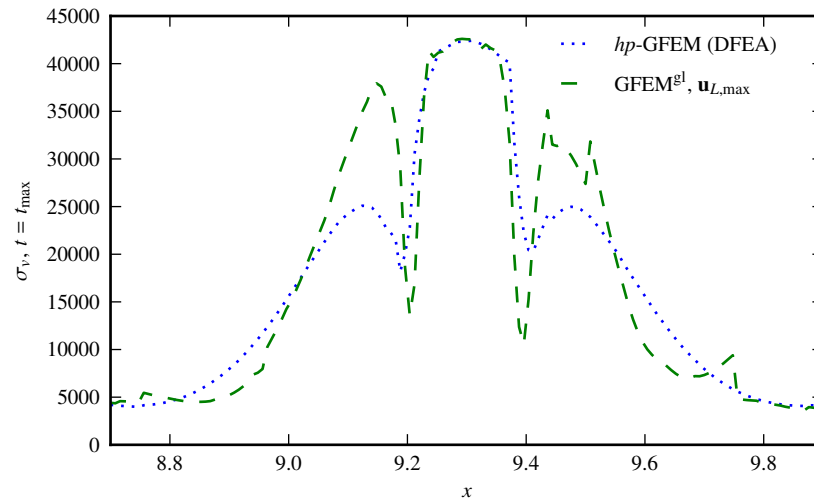


(b) Maximum von Mises stress, σ_v

Figure 4.15: Pointwise maximum temperature and von Mises stress along the central axis ($y = 0.25, z = 0.22$) of the thermo-elasto-plastic laser-heated beam from the hp -GFEM reference and $GFEM^{gl}$ solutions with time-dependent shape functions.



(a) Maximum temperature, θ



(b) Maximum von Mises stress, σ_v

Figure 4.16: Pointwise maximum temperature and von Mises stress along the central axis ($y = 0.25, z = 0.22$) of the thermo-elasto-plastic laser-heated beam from the hp -GFEM reference and GFEM^{el} solutions with *time-independent* shape functions.

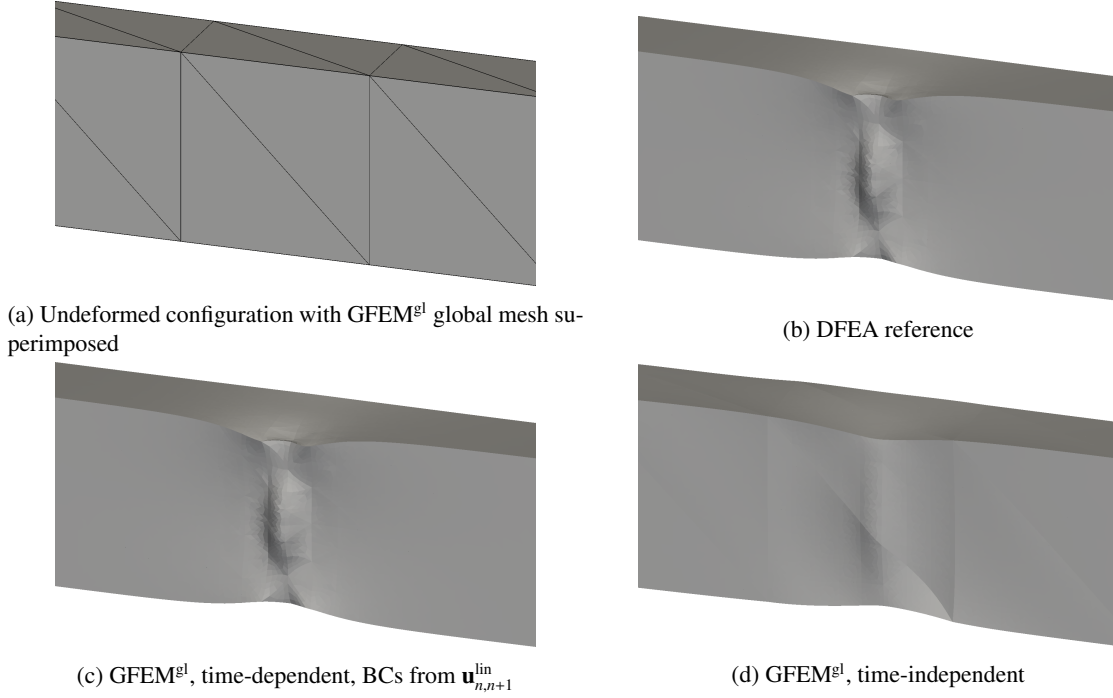


Figure 4.17: Residual deformed configurations of the thermo-elasto-plastic laser-heated beam from *hp*-GFEM and GFEM^{gl} solutions. The coarse, global mesh used in GFEM^{gl} analyses is shown on the undeformed configuration for comparison.

4.3.2.2 Moving laser heating

The moving laser heating applied to the front surface of the beam ($z = 0.24$ in) is characterized by

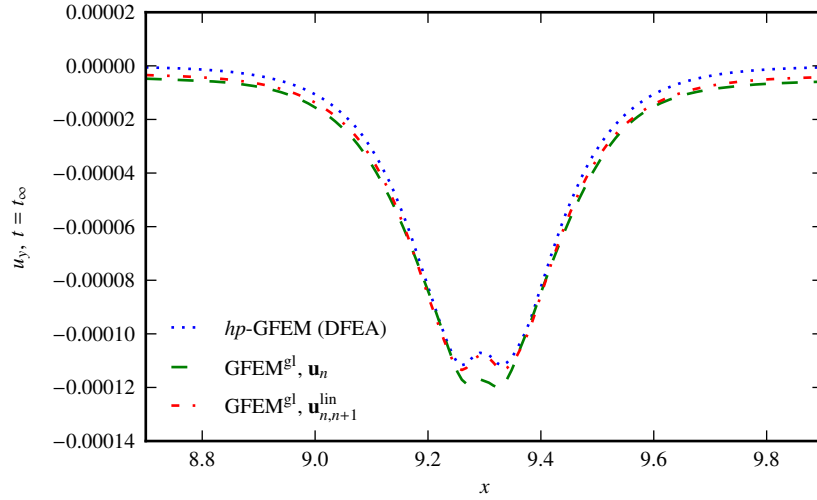
$$\bar{f}(\mathbf{x}, t) = \frac{I_0}{2\pi a^2} g(t) \exp\left(\frac{-(x - b(t))^2}{2a^2}\right), \quad 8.0 \leq x \leq 12.0, \quad \text{where}$$

$$g(t) = 1.0 - \exp(-\gamma t),$$

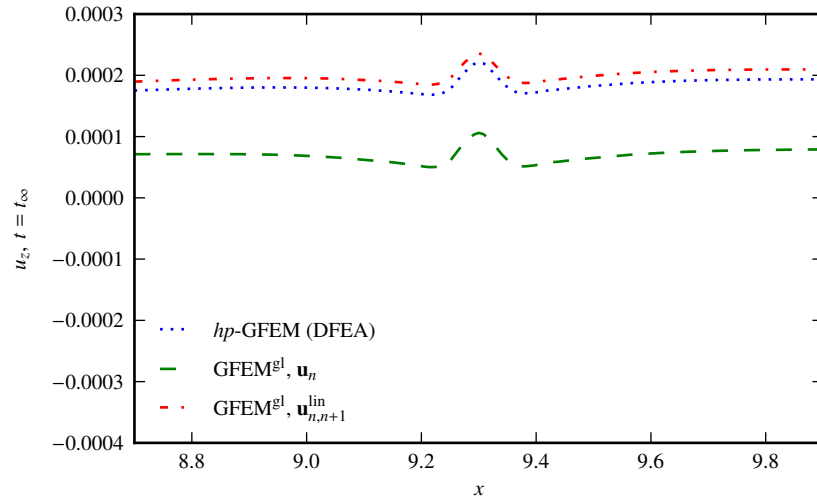
$$b(t) = 9.25 + v_x t.$$

Parameter $I_0 = 125 \frac{\text{ft-lbf}}{\text{s}}$ is the laser flux intensity, $a = 0.025$ in is the laser focus or width, and $b(t)$ dictates the spatial variation of the flux in time, with $v_x = 0.125$ in/s the constant velocity of the applied laser heating. The temporal variation of the applied heat flux magnitude is denoted $g(t)$, which increases in time, with $\gamma = 3.0$. The time-rise of the maximum applied laser flux (i.e., at the focus point, $x = 9.25 + 0.125t$) is shown in Figure 4.20. Convection boundary conditions with ambient temperature $\theta_\infty = 70$ °F are applied elsewhere on the domain.

Time-dependent shape functions are necessary in this case to capture the local spatial evolution of the transient heat flux. As in the previous load case, the GFEM^{gl} global heat transfer problem has $\mathbf{p}^\theta = \{2, 2, 2\}$ (thermoplasticity has $\mathbf{p}^u = \{3, 3, 3\}$). In order to accommodate the moving flux in this case, the local problem is chosen as a larger region in

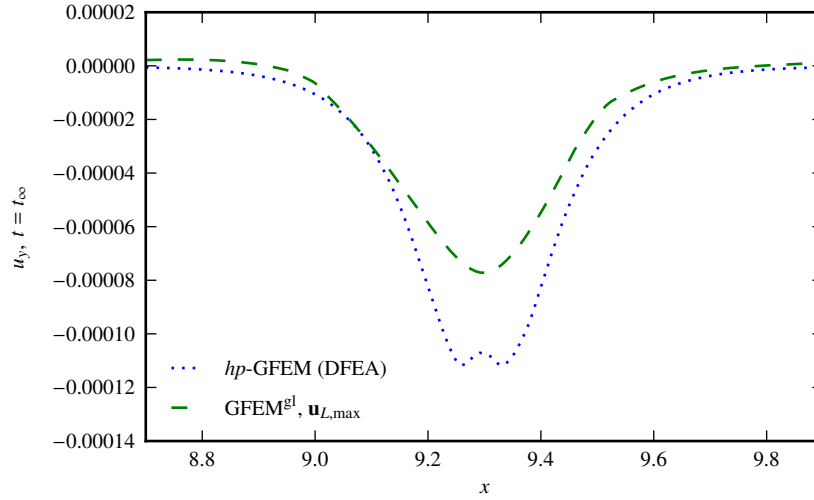


(a) Residual vertical displacement, u_y

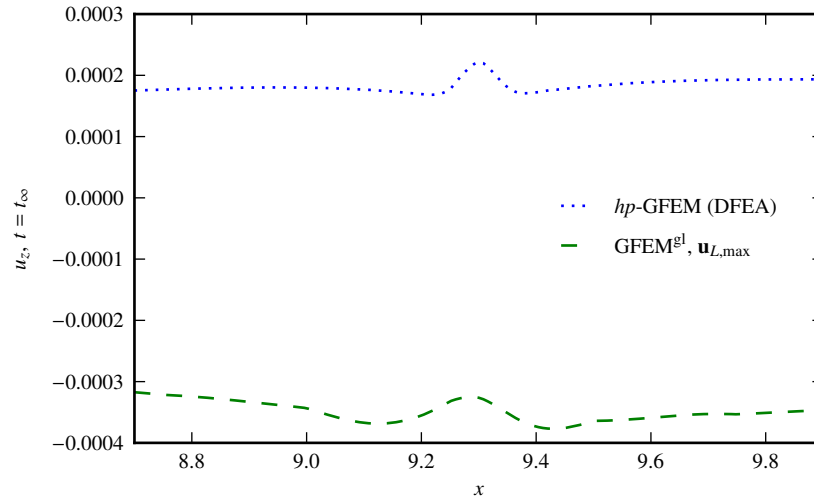


(b) Residual out-of-plane displacement, u_z

Figure 4.18: Pointwise residual displacements, after cooling to room temperature, of the thermo-elasto-plastic laser-heated beam from the hp -GFEM reference and GFEM^{gl} solutions with time-dependent shape functions. Vertical displacement u_y is measured at $y = 0.48$, $z = 0.22$, while out-of-plane displacement u_z is measured at $y = 0.25$, $z = 0.22$.



(a) Residual vertical displacement, u_y



(b) Residual out-of-plane displacement, u_z

Figure 4.19: Pointwise residual displacements, after cooling to room temperature, of the thermo-elasto-plastic laser-heated beam from the hp -GFEM reference and a $GFEM^{gl}$ solution with *time-independent* shape functions. Vertical displacement u_y is measured at $y = 0.48$, $z = 0.22$, while out-of-plane displacement u_z is measured at $y = 0.25$, $z = 0.22$.

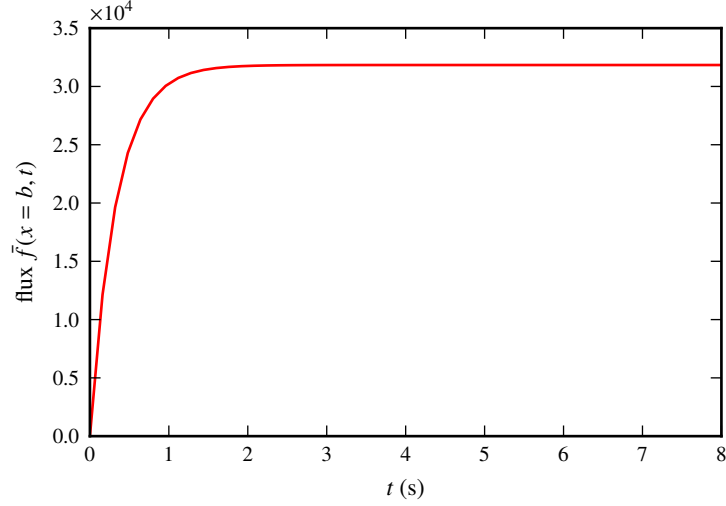


Figure 4.20: Time evolution of the maximum magnitude (at $x = 9.25 + 0.125t$) of the moving laser flux applied to the thermo-elasto-plastic laser-heated beam.

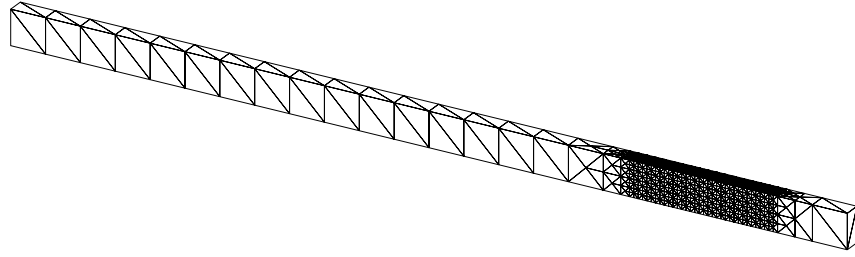
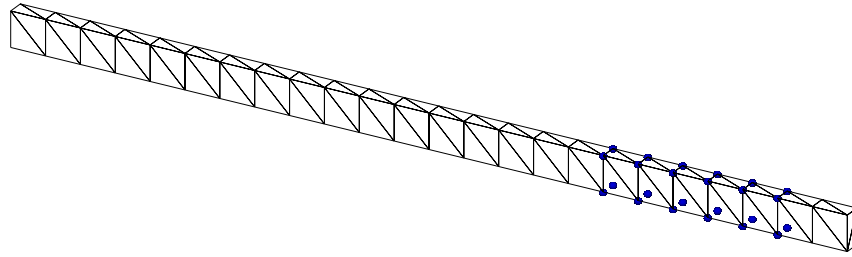


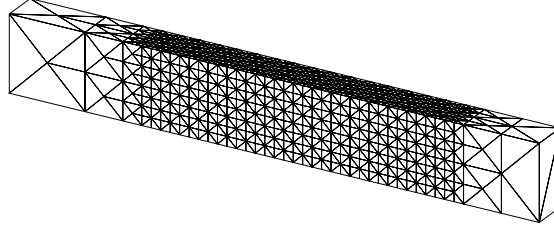
Figure 4.21: hp -GFEM mesh of the thermo-elasto-plastic beam subjected to moving laser heating.

the global domain, $8.0 < x < 11.5$, where once again the local mesh size $h = 0.0625$, and $\mathbf{p}_L^\theta = \{2, 2, 2\}$ ($\mathbf{p}_L^u = \{3, 3, 3\}$ for thermoplasticity). Temperature (spring) boundary conditions are applied on the heat transfer (thermoplasticity) local problem. Similarly, the hp -GFEM direct analysis has localized global mesh refinement along the path of the sharp, applied flux, so that $H = 0.0625$ locally, and a uniform polynomial order throughout $\mathbf{p}^\theta = \{2, 2, 2\}$ ($\mathbf{p}^u = \{3, 3, 3\}$ in the thermoplasticity problem). Each simulation has 32 time/load steps, with $\Delta t = 0.25$ s the time step size in the transient heat transfer problem, so that $0.0 \leq t \leq 8.0$. Mesh geometries are depicted in Figures 4.21 and 4.22, corresponding to hp -GFEM and GFEM^{gl} simulations, respectively.

In this case, to accommodate the sharp laser heating as it propagates along the axis of the beam, the local problem is chosen to be larger than the previous, stationary scenario. The GFEM^{gl} for transient heat transfer and thermoplasticity could be adapted to accommodate moving local problem meshes, so as to maintain as small a local problem size as possible surrounding the localized loadings of interest. However, it is also important to note that to predict localized residual deformations, stresses, and strains, global–local enrichment functions are necessary in all regions of the



(a) GFEM^{gl} global problem. Spherical glyphs represent global nodes enriched with the local solution.



(b) GFEM^{gl} local problem.

Figure 4.22: Meshes used to solve the thermo-elasto-plastic laser-heated problem with the GFEM^{gl} (moving heat flux).

structure *previously or currently* affected by localized heating and corresponding plastic effects.

The temperature distribution $\theta(\mathbf{x}, t)$ along the central axis of the beam at $y = 0.25$, $z = 0.2$ at various times t , comparing hp -GFEM DFEA and GFEM^{gl} solutions, is given in Figure 4.23, and the corresponding quasistatic axial stresses $\sigma_{xx}(\mathbf{x}, t)$ are shown in Figure 4.24. As in the previous load case, the temperature field from the transient GFEM^{gl} solution and stress fields from the thermoplasticity solution match the hp -GFEM reference solution well at all time steps of the analysis. At the final time step, a slight discrepancy is observed when local boundary conditions from \mathbf{u}_n are used; the local problem is large in this example in order to accommodate the moving heat flux, but as the sharp heating approaches the right boundary, the effects of inaccurate boundary conditions impact the solution more significantly. Additionally, global stresses at this step approach yield ($\sigma_y = 4.0 \times 10^4$); thus, plastic behavior may not be extremely localized any longer. Contour plots of the accrued plastic strain at the final load step are given in Figure 4.25 for the hp -GFEM reference and GFEM^{gl} solutions. It can be observed in this case that the GFEM^{gl} predicts very similar nonlinear material behavior, even on a coarse, global mesh.

GFEM^{gl} solutions are shown to be accurate; however, the computational efficiency of the proposed approach is also of interest. Table 4.6 compares the wall time spent assembling and solving the global nonlinear thermoplasticity problem until convergence of the residual at a single time step, $t = 0.75$, in GFEM^{gl} and hp -GFEM reference solutions. A parallel assembly and parallel direct linear solver are used. As expected, assembly of the GFEM^{gl} global nonlinear problem is slightly more expensive than the hp -GFEM reference in order to accurately integrate global–local enrichments; however, there are roughly 50 times fewer degrees of freedom in the GFEM^{gl} global problem, leading to vastly

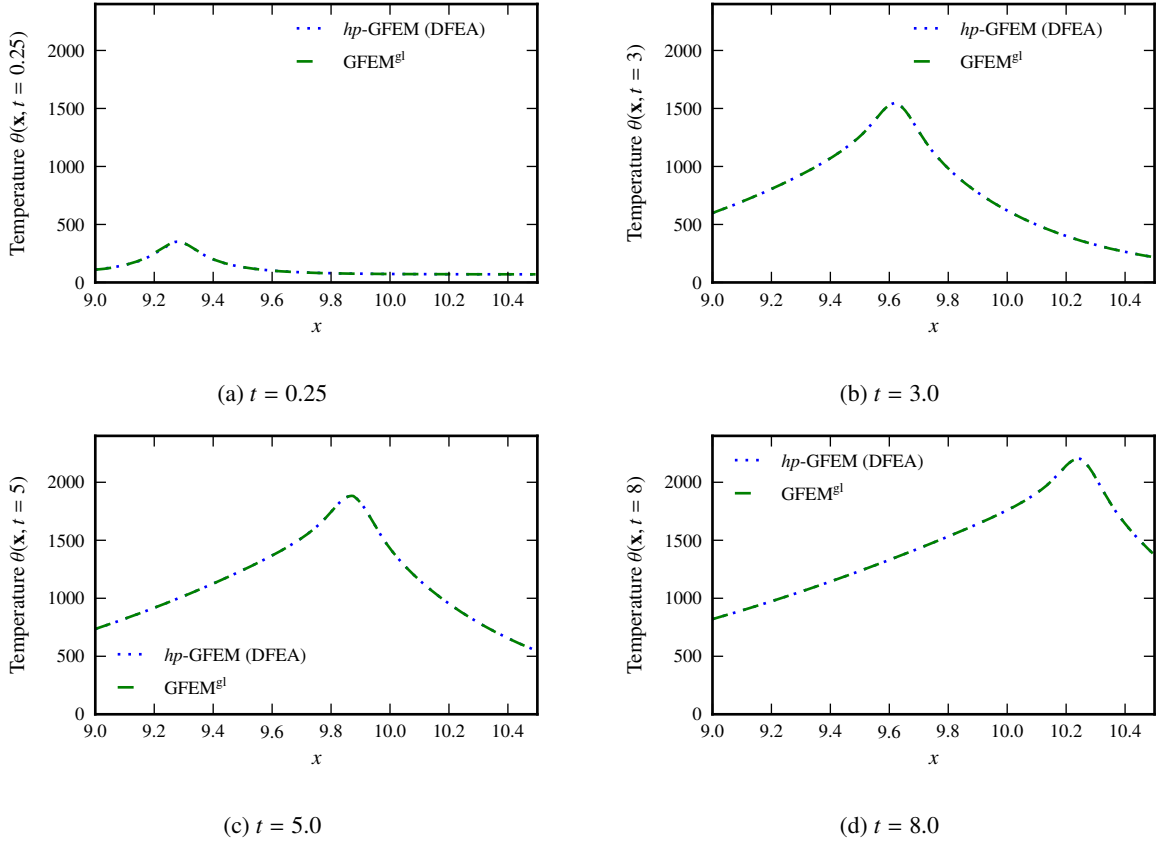


Figure 4.23: Temperature profiles along the central axis of the thermo-elasto-plastic laser-heated beam subjected to a transient, moving laser flux at various times t . The temperature is taken at depth $z = 0.2$. hp -GFEM and $GFEM^{gl}$ solutions are plotted together for comparison.

Table 4.6: Wall time spent assembling/solving the global nonlinear laser-heated beam problem (moving flux) at $t = 0.75$; $GFEM^{gl}$ vs. hp -GFEM reference.

	Problem size (dofs)	Iterations	Wall time (s)		
			Assemble	Solve	Total
hp -GFEM (DFEA)	153,090	3	16.90	33.38	50.29
$GFEM^{gl}$ global	3,072	2	23.87	0.03	23.91

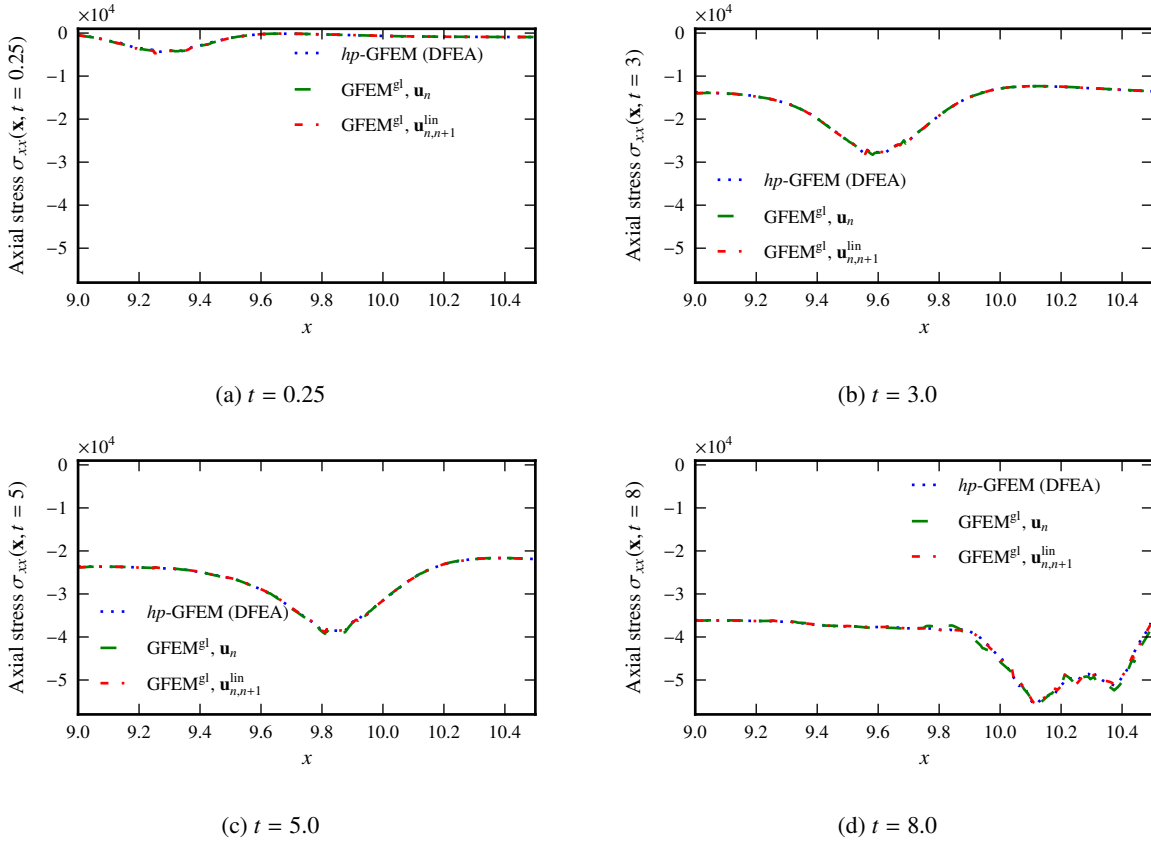


Figure 4.24: Axial stress profiles along the central axis of the thermo-elasto-plastic laser-heated beam subjected to a transient, moving laser flux at various times t . The temperature is taken at depth $z = 0.2$. hp -GFEM and $GFEM^{gl}$ solutions are plotted together for comparison.

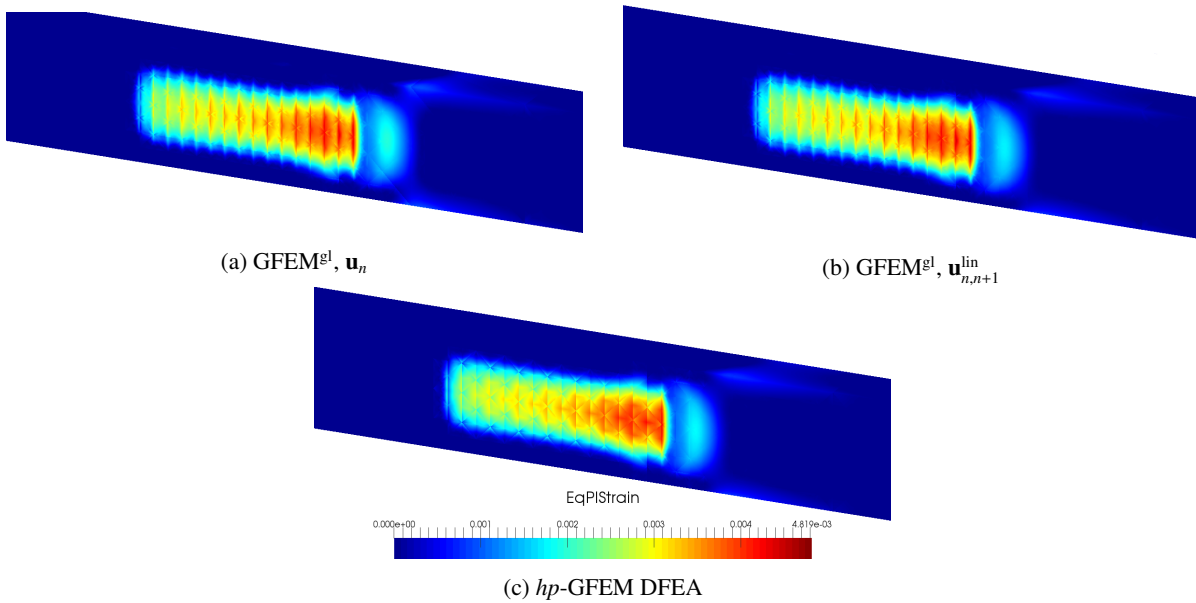


Figure 4.25: Contours of equivalent plastic strain $\bar{\epsilon}^P$ at the final time/load step for the thermo-elasto-plastic laser-heated beam subjected to a moving laser heating.

Table 4.7: Thermo-elasto-plastic heterogeneous beam material properties.

Property	Phase a	Phase b
Young's modulus E	2.0×10^5	10.0×10^5
Poisson's ratio ν	0.30	0.30
Yield stress σ_y	1000	2000
Plastic modulus K	6000	6000
Thermal expansion coefficient α_θ	2.0×10^{-5}	4.0×10^{-5}
Thermal conductivity κ	2.0	10.0

Table 4.8: Thermoplasticity problem size details in degrees of freedom (dofs) for the heterogeneous beam compared to the equivalent hp -GFEM DFEA. In the GFEM^{gl} simulation 372 sub-local problems are solved.

Method	Problem size (dofs)
DFEA (hp -GFEM)	381,150
GFEM ^{gl} Initial global	11,160
Enriched global	12,276
Largest local	6,450
Smallest local	1,650
Average local	5,368

reduced factorization and solution times and overall lower computational cost per global load step.

4.3.3 Heterogeneous thermo-elasto-plastic beam

This problem is analogous to the heterogeneous thermoelastic beam of Section 3.2.5 of Chapter 3. Thus, the problem geometry and boundary conditions are exactly as described in Figure 3.26: a beam with random, heterogeneous material throughout is subjected to uniform bending, as well as a heat flux on its top surface. However, in this chapter, thermo-elasto-plastic material properties are adopted. The presence of sharp material interfaces at the fine scale may therefore lead to very localized plastic deformations; the goal of the GFEM^{gl} is to capture this local behavior.

The characteristic size of the microstructure is increased, relative to the thermoelastic example of Section 3.2.5, in order to compare GFEM^{gl} results with an equivalent hp -GFEM solution (DFEA). Material properties of each phase a and b are summarized in Table 4.7. A linear hardening model ($\omega = 0$, $\sigma_\infty = \sigma_y$) is used in the plastic response of the structure.

The GFEM^{gl} global mesh size $H = 1.0$, the number of local problems is 372, local mesh size $h = 0.25$, and in the thermoplasticity problem, global and local polynomial orders are $\mathbf{p}^u = \{3, 3, 3\}$ and $\mathbf{p}_L^u = \{3, 3, 3\}$, respectively (one polynomial order lower is adopted in heat transfer analysis). The equivalent DFEA reference solution has a uniform global mesh size $H = 0.25$ and $\mathbf{p}_{ref}^u = \{3, 3, 3\}$. Global and local problem sizes are detailed in Table 4.8. the DFEA leverages a parallel assembly and parallel direct linear solver; GFEM^{gl} local problems are solved in parallel,

Table 4.9: Comparison of GFEM^{gl} solution of the heterogeneous thermo-elasto-plastic beam to the equivalent *hp*-GFEM DFEA.

Method	Heat energy ($\times 10^4$)	Strain energy	$e_{E,\theta}^{r,\text{diff}}$	$e_{E,\mathbf{u}}^{r,\text{diff}}$
<i>hp</i> -GFEM (DFEA)	5.041	31.99	–	–
GFEM ^{gl} initial	4.769	62.76	0.232	0.981
enriched	5.036	32.03	0.029	0.032

Table 4.10: Comparison of wall times of *hp*-GFEM DFEA and each GFEM^{gl} thermoplasticity solution phase for the heterogeneous thermomechanical beam. The problems are solved on a parallel machine with 24 CPUs.

	Wall time (s)			Speedup
	Assemble	Solve	Total	
<i>hp</i> -GFEM (DFEA, serial)	99.32	379.34	478.65	–
<i>hp</i> -GFEM (DFEA)	7.81	55.20	63.01	7.60
GFEM ^{gl} initial	1.24	0.41		
local	–	31.73		
enriched	11.51	0.64	45.54	10.51

while global problems are assembled and solved in parallel on a machine with 24 CPUs. The parallel assembly implementation is discussed in detail in Appendix B.

Relative difference in the energy norm of the GFEM^{gl} parallel solution with respect to the equivalent DFEA reference is given in Table 4.9. Internal energy and work of internal forces (strain energy) are compared in the heat transfer and thermoplasticity problem, respectively. Relative differences $e_{E,\theta}^{r,\text{diff}}$ and $e_{E,\mathbf{u}}^{r,\text{diff}}$ are computed based on Equations (2.27) and (2.28) from Chapter 2. Globally, a good agreement of both DFEA and GFEM^{gl} solutions is observed, with a relative difference in the energy norm in each case of around or under 3%, while, according to Table 4.8, roughly 30 times fewer degrees of freedom are required in the global GFEM^{gl} problem. Furthermore, a qualitative comparison of the von Mises stress contours from each solution is shown in 4.26. Local stress concentrations due to sharp material interfaces may cause localized plastic deformation, thus inducing nonlinear behavior *globally*.

A comparison of solution times from DFEA and GFEM^{gl} solution is given in Table 4.10, and the number of Newton-Raphson iterations required to solve in each case is given in Table 4.11. Table 4.11 shows that nonlinearity

Table 4.11: Newton-Raphson iterations required to solve the heterogeneous thermo-elasto-plastic beam problem with each method.

		Iterations
<i>hp</i> -GFEM (DFEA)		2
GFEM ^{gl} initial		1 (<i>linear elastic</i>)
	local	1 (362 of 372 local problems)
		2 (10 of 372 local problems)
	enriched	2

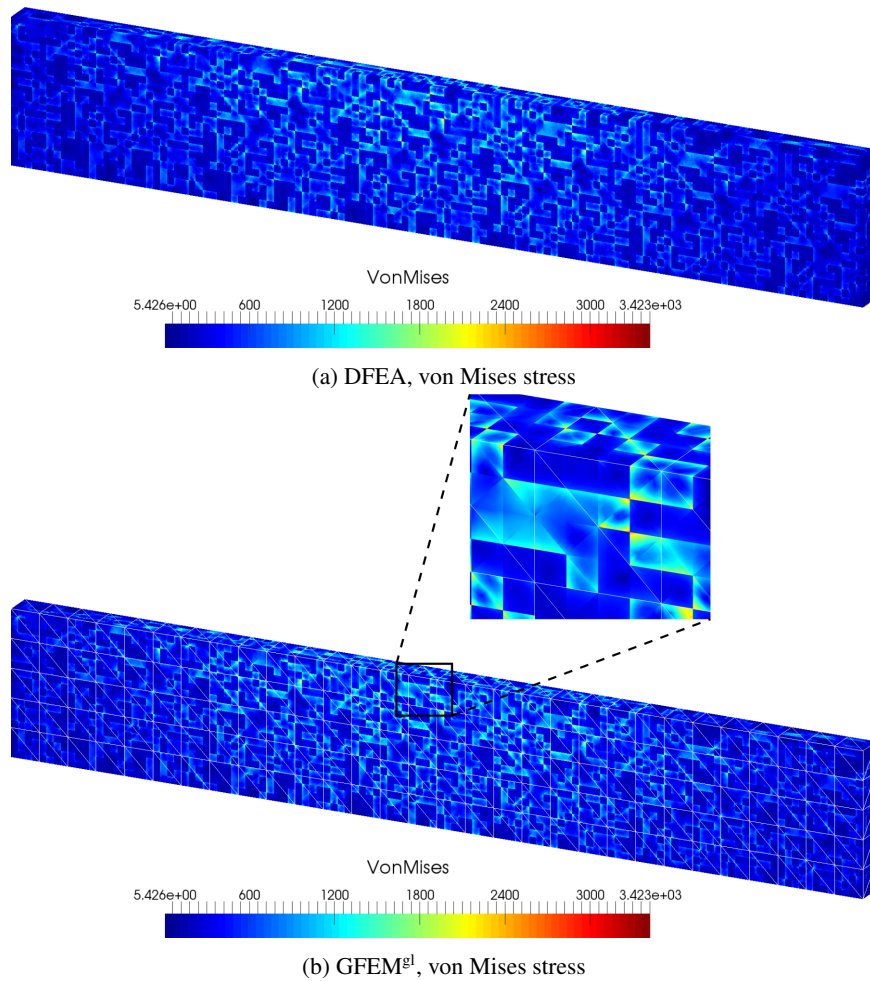


Figure 4.26: Heterogeneous thermo-elasto-plastic beam von Mises stress contours from (a) hp -GFEM DFEA reference and (b) GFEM^{el} solutions. The coarse-scale, global mesh is superimposed on the GFEM^{el} solution, as well as an enlarged view of a local stress concentration due to a material interface.

Table 4.12: Comparison of wall times for assembly of the global heterogeneous thermo-elasto-plastic beam thermo-plasticity problem in both GFEM^{gl} and *hp*-GFEM DFEA on 24 CPUs.

	Assembly wall time (s)	Speedup
<i>hp</i> -GFEM (DFEA, serial)	99.32	–
GFEM ^{gl} enriched (serial)	210.86	–
<i>hp</i> -GFEM (parallel)	7.81	12.71
GFEM ^{gl} enriched (parallel)	11.51	18.32

exists in this problem at the global scale. The very fine, uniform mesh of the direct finite element analysis, required to capture localized nonlinear behavior, makes each nonlinear solution iteration expensive. GFEM^{gl}, on the other hand, maintains a coarse, global mesh, drastically reducing the cost of each global Newton-Raphson iteration. Moreover, in this example problem, fine-scale nonlinearity exists in only very few (10 out of 372 total) local problems, in which more than one Newton-Raphson iteration is required for convergence. Because the vast majority of local problems (362 of 372 total) have only linear elastic behavior, convergence of the local solution is observed in just one iteration; thus, locally *linear* fine-scale behavior can be resolved in the global problem without the need to iterate in the expensive, highly refined local problem. Owing to these significant advantages over direct analysis, from Table 4.10, analyzing this problem with the GFEM^{gl} with parallel *nonlinear* sub-local problems results in a 25% time savings in comparison, and a better parallel speedup with respect to the equivalent serial, direct simulation.

Table 4.12 examines the parallel and serial global assembly times for the heterogeneous beam (see Appendix B for parallel assembly details). Since global integration of element matrices is performed over the heavily refined, fine-scale problem mesh, each global GFEM^{gl} element involves the evaluation of global–local shape functions as well as material properties at many fine-scale integration points. Because global element computations are relatively expensive, scalability of the parallel global assembly for this problem is in general comparable to or better than *hp*-GFEM DFEA.

4.3.4 Hat-stiffened panel

The final example presented is a representative structure with realistic geometry that might be encountered in, for example, aerospace applications: a three-dimensional, thin panel structure with two ‘hat’ stiffeners along the bottom surface to provide additional reinforcement. The panel geometry is illustrated in Figure 4.27, and the material properties are summarized in Table 4.13. A linear hardening model (i.e., $\omega = 0$, $\sigma_\infty = \sigma_y$) for the plastic response of the structure is chosen. Unless otherwise noted, dimensions are given in inches. Additional dimensions include the panel thickness, $t_{\text{panel}} = 0.0625$, and the thickness and depth of the stiffeners, $t_{\text{stiff}} = 0.032$ and $d_{\text{stiff}} = 1.0$, respectively. The stiffeners are joined to the panel by 40 full spot welds and 4 half-spot welds at the global boundary which intersects the stiffeners, each of radius $r_{\text{weld}} = 0.07$.

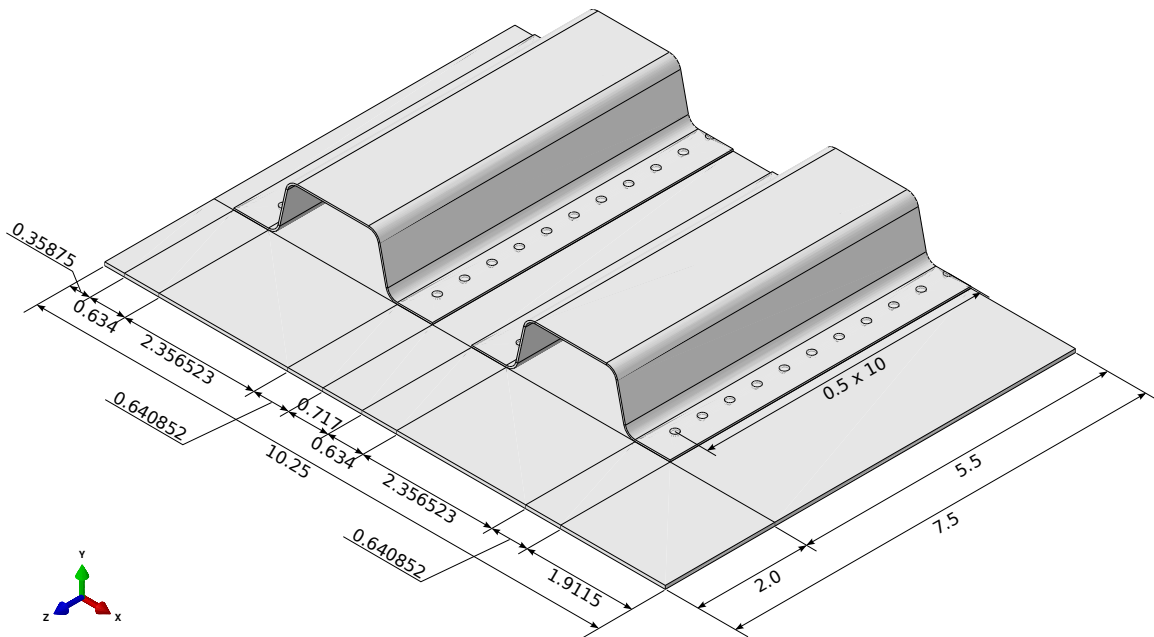


Figure 4.27: Geometry of the hat-stiffened panel problem. Overall size of the panel in-plane is 10.0×7.5 .

Table 4.13: Hat-stiffened panel material properties.

Property	Value	Units
Young's modulus E	17.1×10^3	ksi
Poisson's ratio ν	0.325	–
Yield stress σ_y	152.0	ksi
Plastic modulus K	420.0	ksi
Thermal expansion coefficient α_θ	4.28×10^{-6}	$^\circ\text{F}^{-1}$
Thermal conductivity κ	0.8755	$\frac{\text{ft}\cdot\text{lb}}{\text{s}\cdot\text{in}\cdot^\circ\text{F}}$
Heat capacity ρc	14.0384	$\frac{\text{ft}\cdot\text{lb}}{\text{in}^3\cdot^\circ\text{F}}$

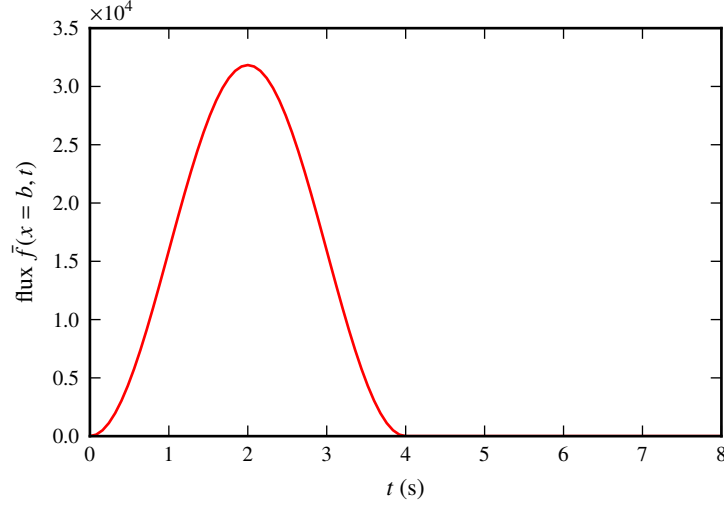


Figure 4.28: Time variation of peak flux intensity (i.e., at $x = b$, $z_{min} \leq z \leq z_{max}$) applied to the hat-stiffened panel problem in each local region of interest.

A constant normal pressure $p_0 = 2.0$ psi and steady heat flux $\bar{f}_0 = 5.0 \frac{\text{ft-lbf}}{\text{s-in}^2}$ are applied to the panel surface. The edges of the panel are held at a constant temperature $\bar{\theta}_\infty = 70^\circ \text{F}$. Spring boundary conditions are applied along the two frontmost panel edges in Figure 4.27, while displacement boundary conditions preventing in-plane displacement (i.e., symmetry boundary conditions) are applied along the rear panel and stiffener edges. To induce sharp thermomechanical gradients, a series of local, transient heat fluxes are applied at various locations on the panel surface. The applied heat flux is given by a Gaussian function, spatially, with an impulse variation in time, denoted $g(t)$,

$$\bar{f}(\mathbf{x}, t) = \frac{I_0}{2\pi a^2} g(t) h(z) \exp\left(\frac{-(x-b)^2}{2a^2}\right) + \bar{f}_0, \quad 0.0 \leq t \leq 4.0, \quad \text{where}$$

$$g(t) = \frac{1 - \cos\left(\frac{\pi t}{2}\right)}{2},$$

$$h(z) = \begin{cases} \exp(-(z - z_{min})^2) & \text{if } z < z_{min} \\ 1.0 & \text{if } z_{min} \leq z \leq z_{max} \\ \exp(-(z - z_{max})^2) & \text{if } z > z_{max}. \end{cases}$$

In all cases, $I_0 = 80.0 \frac{\text{ft-lbf}}{\text{s}}$ is the intensity, $a = 0.02$ in gives the width or radius of the heat flux, b determines the center of the applied flux in the transverse (x -) direction, and z_{min} and z_{max} dictate the spatial length of the flux. The time variation of the peak flux intensity is included in Figure 4.28. Details on the size and location of each localized heating in terms of other parameters $\{z_{min}, z_{max}, b\}$ are included in Table 4.14.

Table 4.14: Hat-stiffened panel sharp flux locations.

Load case	z_{min}	z_{max}	b
A	3.4	3.8	6.4
B	4.1	4.4	3.0

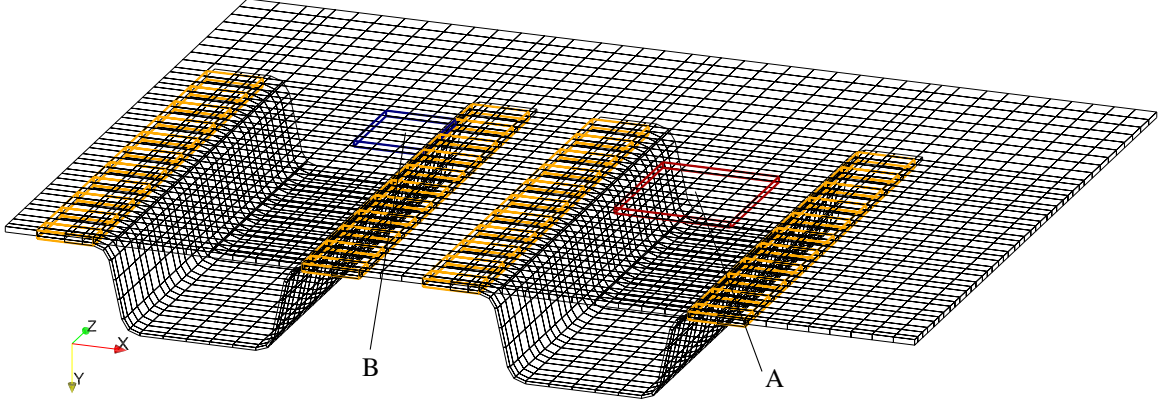
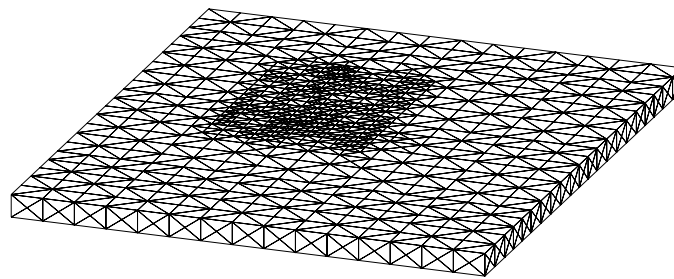


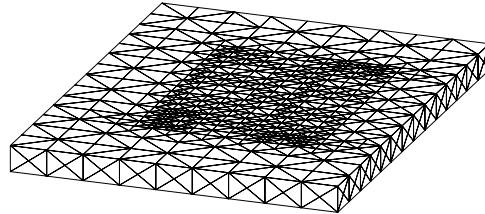
Figure 4.29: Global hexahedral mesh and local problem regions in the hat-stiffened panel problem: critical local regions subjected to sharp heating effects, and 44 local regions along the stiffener connections containing spot welds.

The FE mesh of the panel consists entirely of structured, 8-node hexahedral elements, which is shown in Figure 4.29—the figure also indicates critical local regions A and B which are subjected to a sharp, local heating, and the local regions containing each spot weld or half-spot weld. In order to maintain a coarse, global structural mesh regardless of localized features such as sharp geometry of the spot weld connections or applied thermal loadings, the GFEM^{gl} is utilized to insert this information into the global model via the solution of local problems. Local problems are discretized using 4-node *tetrahedral* elements, so that unstructured local meshes can represent detailed geometry, and adaptive mesh refinement may be used to capture localized phenomena of interest. A discussion on incorporating global–local enrichments defined on a tetrahedral mesh into a global approximation space based on a partition of unity from hexahedral elements can be found in [92], and is also the subject of ongoing work [68]. The local problem meshes used to treat sharp applied heatings are shown in Figure 4.30, and cutaway views of typical unstructured tetrahedral local problem meshes designed to fit the geometry of full and half-spot welds, respectively, are illustrated in Figure 4.31.

The GFEM discretization has a linear polynomial approximation in the heat transfer global and local problems, $\mathbf{p}^g = \{1, 1, 1\}$ and $\mathbf{p}_L^g = \{1, 1, 1\}$, while the global thermo-structural problem has a quadratic approximation, $\mathbf{p}^u = \{2, 2, 2\}$ and $\mathbf{p}_L^u = \{2, 2, 2\}$. Total global–local enrichments and linear prediction of the solution at each time step are utilized to solve the global problem. Global and local problem size details are given in Table 4.15. The GFEM^{gl} enriched global model is nearly identical in size to the coarse, global mesh, differing by only about 1%. On the other hand, a hypothetical, equivalent direct analysis with a specially tailored mesh to represent all fine-scale features would

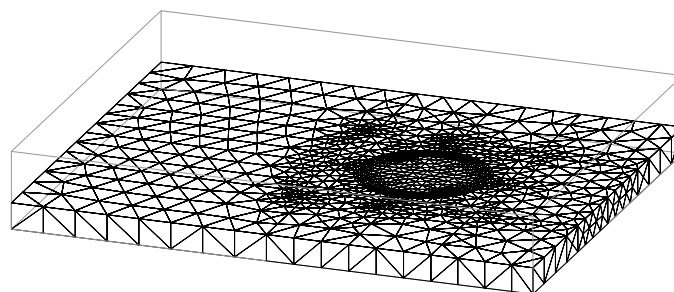


(a) Flux region A

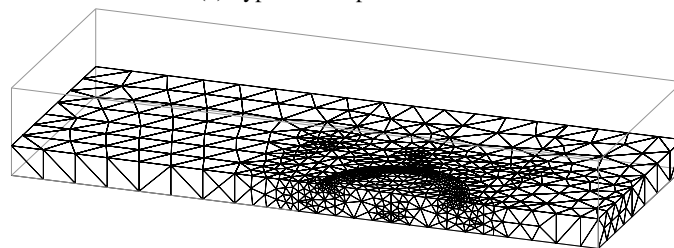


(b) Flux region B

Figure 4.30: Tetrahedral local problem meshes used in each sharp flux case for the hat-stiffened panel problem.



(a) Typical full spot weld mesh



(b) Typical half-spot weld mesh

Figure 4.31: Cutaway view of typical tetrahedral local problem meshes used in regions with spot welds in the hat-stiffened panel problem. A specially-tailored unstructured mesh is used locally to fit the weld geometry.

Table 4.15: Hat-stiffened panel GFEM^{gl} problem size details in degrees of freedom (dofs). In each analysis local problems for 40 full spot welds, 4 half-spot welds, and 1 local region are solved. The estimated equivalent DFEA thermoplasticity problem size is roughly 4.5 million dofs.

		Problem size (dofs)	
		Heat transfer	Thermoplasticity
DFEA (<i>estimate</i>)		370,000	4,500,000
Initial global		27,888	209,160
Enriched global (A)		28,480	210,936
Enriched global (B)		28,436	210,804
Local	Full spot weld	7,966	95,592
	Half-spot weld	4,179	50,148
	Region A	5,807	69,684
	Region B	5,965	71,580

result in approximately 4.5 million degrees of freedom in the global thermoplasticity problem, or roughly a 2000% increase in global problem size relative to the coarse problem. Furthermore, detailed geometry of the the spot welds and sharp applied heat fluxes would pose significant mesh generation challenges.

The simulation consists of 20 time steps in the heating phase and 5 in the cooling phase for a total of 25 time/load steps and a simulation time of 25 seconds. In the heating phase, $0.0 \leq t \leq 5.0$, the time step size is $\Delta t = 0.25$ s, while in the cooling phase, $5.0 < t \leq 25.0$, the time step is substantially larger, $\Delta t = 4.0$, since variation of the temperature field is mostly smooth and material behavior is elastic in this interval.

Figure 4.32 shows the localized nature of temperature distributions in the panel due to each sharp applied flux case at the maximum load step ($t = 2.5$) from GFEM^{gl} simulations.

Because a DFEA is impractically expensive, GFEM^{gl} results are instead compared to a direct simulation on the coarse, global hexahedral mesh, in order to demonstrate the localized solution fidelity possible with GFEM^{gl}. Figure 4.33 gives the internal heat energy and strain energy from GFEM^{gl} and coarse global direct analyses. Both global models capture the overall response of the structure reasonably well; large errors in the transient heat transfer solution exist near the peak heat flux, since the coarse mesh is unable to account for the sharp applied heating, which is due to both discretization error and numerical integration error in the sharp, Gaussian function.

From an engineering perspective, however, localized quantities such as stress, strain, and plastic deformation due to the sharp heating and detailed connection geometry are of specific interest. Figures 4.34 and 4.35 show a zoom-in on the localized peak and residual von Mises stress in the panel surface, resulting from a sharp flux applied in Regions A and B, respectively, for both GFEM^{gl} and coarse-scale analyses of the problem. In Region A, the coarse analysis yields a sharp stress gradient and residual localized stress, which is likely due to the close proximity of the applied, sharp heat flux to a global mesh edge. However, stresses are substantially higher than expected due to the low fidelity of local plastic deformation prediction. GFEM^{gl}, on the other hand, gives a more realistic stress distribution, as well as

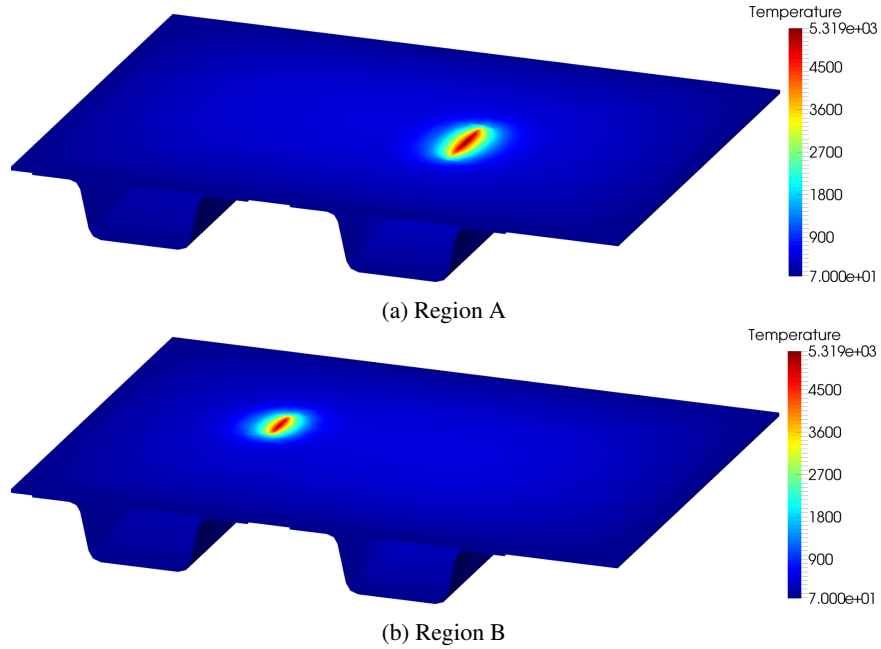
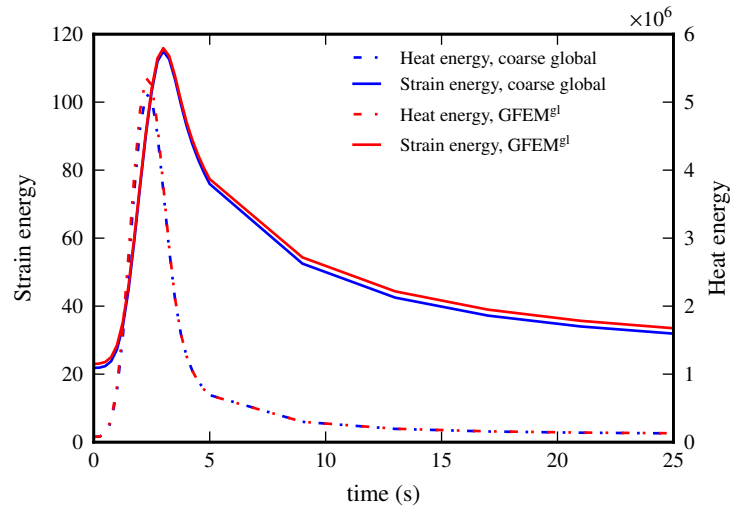


Figure 4.32: GFEM^{gl} global temperature contours at the maximum heat flux ($t = 2.5$) in the hat-stiffened panel problem.

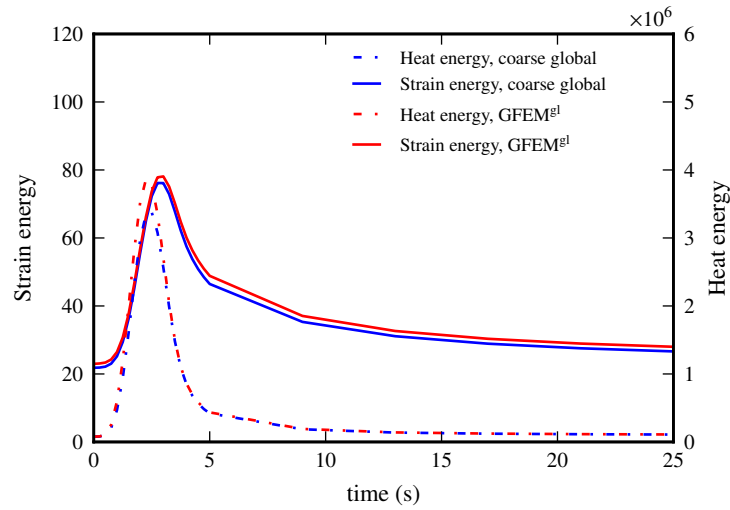
a sharper resolution of the residual stress due to localized plasticity. Region B, however, shows significantly different localized behavior, both at the maximum and residual steps. The GFEM^{gl} gives a good resolution of the complex interaction between the panel and spot weld connections to the stiffener in the neighborhood of the localized heat flux. Moreover, the GFEM^{gl} predicts a sharp, localized residual stress field underneath the applied heat flux, while the coarse, global analysis is unable to capture this effect.

Figures 4.36 and 4.37 show the analogous von Mises stress distributions on a cutaway view in each stiffener connection, only at maximum load ($t = 2.5$), in each sharp flux case. In Region A, local stress is concentrated in the panel and thus is remote relative to the stiffener connections; while localized stresses still exist at the spot weld connections, they are low in magnitude. On the other hand, comparing Figures 4.37a and 4.37b, the sharp flux in Region B is applied much closer to a stiffener, leading to substantially higher stresses and localized plasticity in the spot weld connections. In contrast to Figure 4.36, high local fidelity in the thermoplasticity problem is necessary in this case to accurately resolve sharp stress gradients in the welded connections, which might lead to localized failure in the panel.

Table 4.16 details the total wall times required for solution of the thermoplasticity problem on 24 CPUs with GFEM^{gl} while the coarse global solution times are also included for reference; only results from Region A are included. In the GFEM^{gl}, local problems are assembled and solved in parallel, while both the coarse-scale and GFEM^{gl} enriched global problems use a parallel assembly routine and parallel direct sparse linear solver. Global factoriza-



(a) Region A



(b) Region B

Figure 4.33: Strain energy and internal heat energy in the hat-stiffened panel problem, GFEM^{gl} vs. coarse scale hexahedral mesh.

Table 4.16: Wall times required for GFEM^{gl} simulation of the hat-stiffened panel problem; sharp flux in Region A. The times for the coarse scale global problem are also included for reference.

	Wall time (s)			
	Local assemble/solve	Assemble	Solve	Total
Coarse global	–	66.2	379.5	445.6
GFEM ^{gl}	1231.6	6148.7	440.9	7821.1

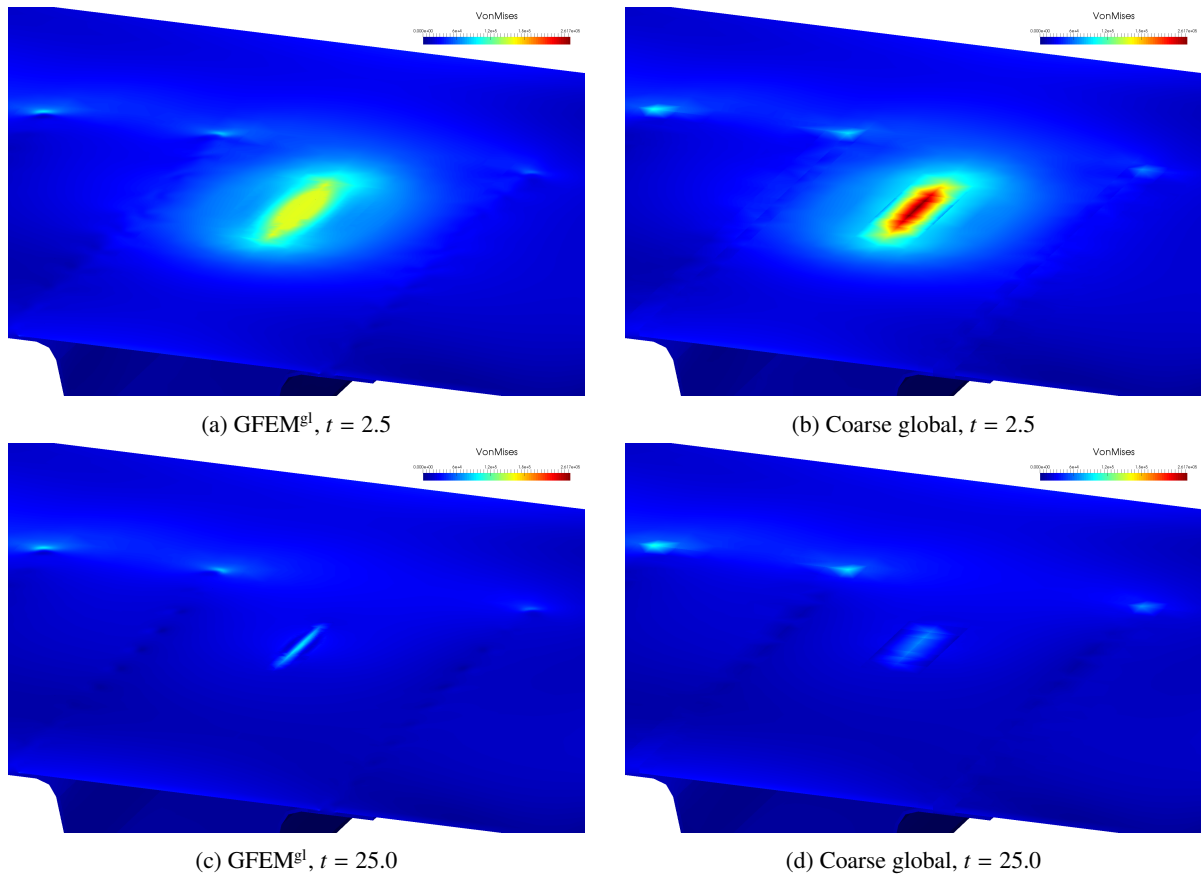


Figure 4.34: Von Mises stress contours in the panel at maximum load ($t = 2.5$) and final ($t = 25.0$) time steps from GFEM^{gl} and coarse global simulations of the hat-stiffened panel problem; sharp flux in Region A.

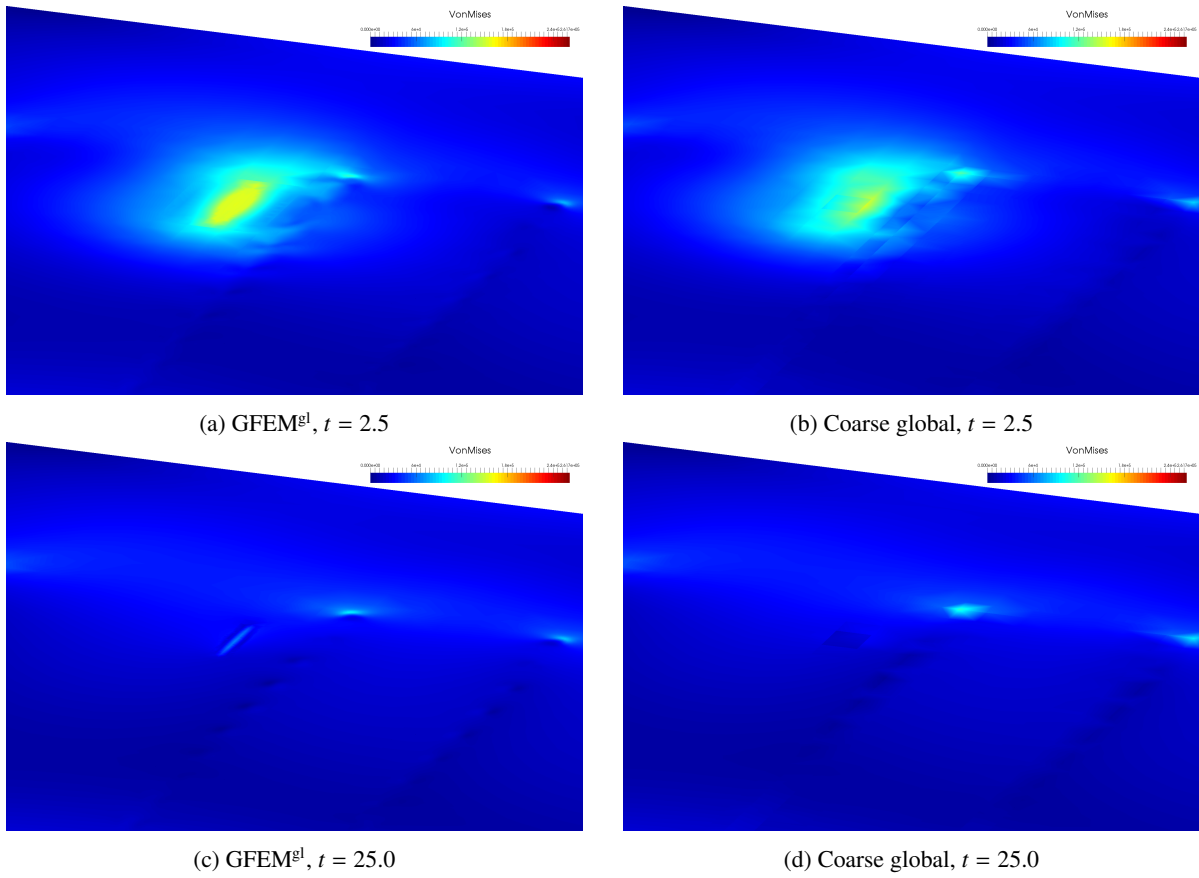


Figure 4.35: Von Mises stress contours in the panel at maximum load ($t = 2.5$) and final ($t = 25.0$) time steps from GFEM^{gl} and coarse global simulations of the hat-stiffened panel problem; sharp flux in Region B.

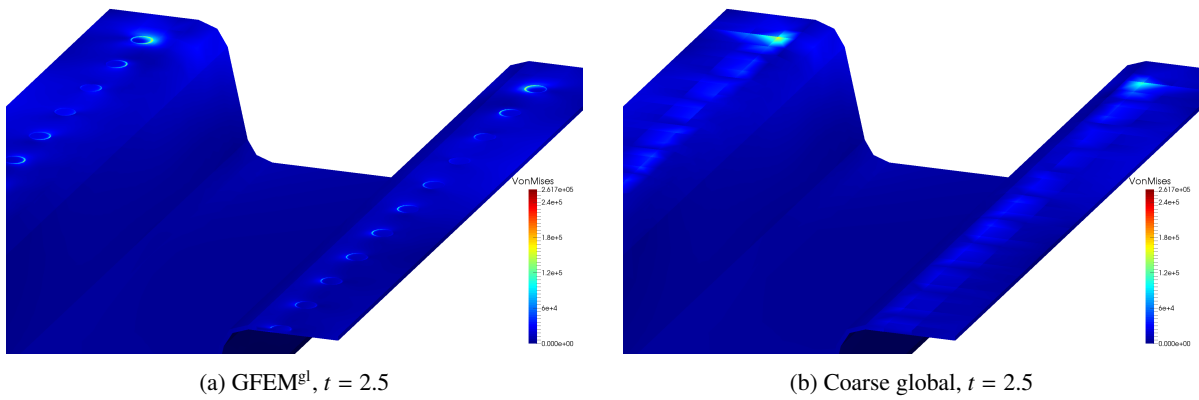


Figure 4.36: Cutaway view of von Mises stress contours in the stiffeners at maximum load ($t = 2.5$) from GFEM^{gl} and coarse global simulations of the hat-stiffened panel problem; sharp flux in Region A.

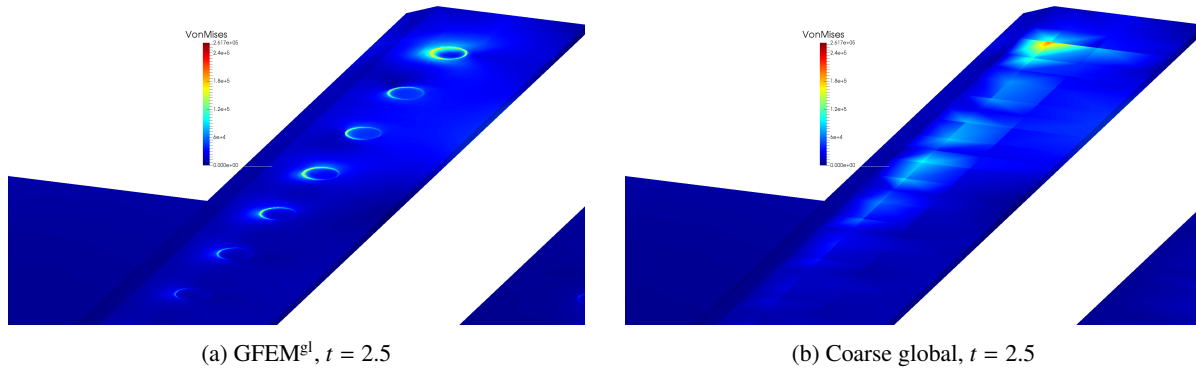


Figure 4.37: Cutaway view of von Mises stress contours in the stiffeners at maximum load ($t = 2.5$) from GFEM^{gl} and coarse global simulations of the hat-stiffened panel problem; sharp flux in Region B.

tion and solution times in both coarse global and GFEM^{gl} simulations are comparable, since global problem sizes are comparable, but the large computational expense associated with solving local problems and, furthermore, the costly assembly of GFEM^{gl} enriched global problems are evident. More efficient numerical integration strategies for assembling global–local enrichments could partially reduce this cost, which is explored in [116] and warrants further study. Regardless, it is also worth noting that an equivalent DFEA of the problem would result in over 4 million dofs, or a problem size increase of over 20 times relative to the coarse mesh; thus, the computational cost associated with assembly and solution of the problem would increase substantially—and likely eclipse that of the GFEM^{gl}—to reach a comparable fidelity.

4.3.4.1 Steady-state: parallel study

To assess the parallel strong scaling performance of the GFEM^{gl} in this example, the peak sharp flux located in Region B is applied and a parallel steady-state, nonlinear analysis is carried out on various numbers of threads. The *overall* speedup of the GFEM^{gl}, considering all aspects of assembly and solution of both global and local problems, versus the number of processors is shown in Figure 4.38. Despite the relatively small number of local problems solved in this example, reasonable gains in speedup are observed as additional threads are added. A good parallel efficiency (0.92) is observed with 4 threads, while parallel performance degrades as additional CPUs are added, resulting in an efficiency of 0.64 and speedup of 15.45 on 24 threads. This decrease in efficiency may be attributed to a *load imbalance* among threads due to several factors—specifically, the small number of local problems relative to the number of threads, small discrepancies in the sizes of individual local problems, and, importantly, unbalanced nonlinear behavior among local problems. For instance, a noticeable decrease in parallel efficiency occurs between 16 and 20 threads; when 20 threads are utilized in the analysis, the parallel computation time is in fact bound by the *serial* wall time spent solving a single nonlinear local problem.

In [63], a load balance heuristic for parallel solution of local problems is established, based purely on local problem

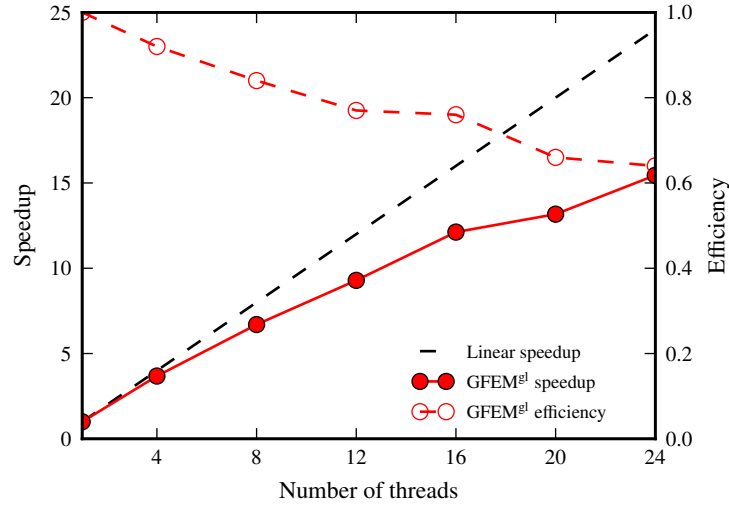
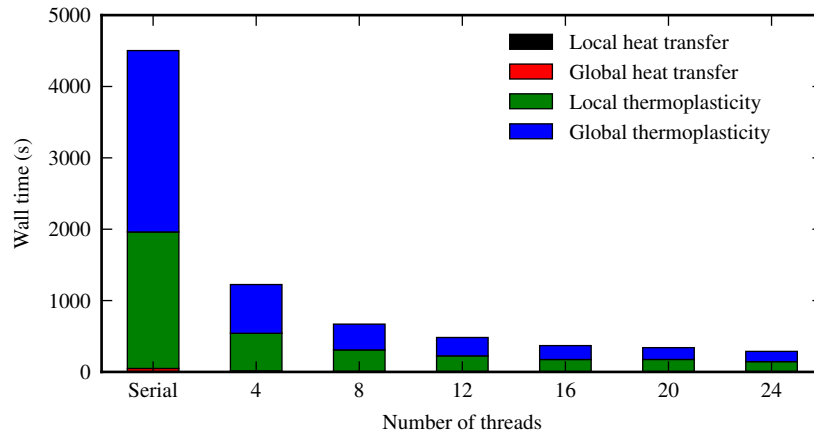


Figure 4.38: GFEM^{gl} parallel speedup in the steady-state hat-stiffened panel problem, relative to a serial GFEM^{gl} simulation. The GFEM^{gl} simulation utilizes a parallel assembly and parallel direct sparse solver, and has 45 local problems which are analyzed in parallel.

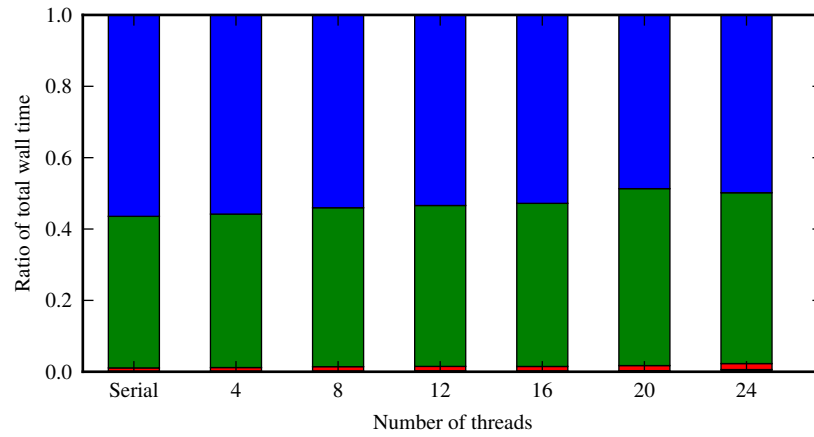
sizes in dofs, and is applied only to linear problems. Strategies such as sorting local problems in descending order of cost are identified, yielding improvements in parallel performance. Nonlinear problems, on the other hand, present a challenge in achieving a good parallel load balance, since it is difficult or impossible to determine where nonlinear behavior may occur a priori; even small local problems may necessitate several nonlinear iterations to converge, so that problem size alone may not offer a good prediction of the computational cost.

Development of strategies to account for the additional cost of localized nonlinearities in parallel computations requires further investigation. It is reasonable to speculate, however, that by subdividing local problems into smaller local domains (as in, e.g., [63, 106]), better parallel efficiency might be observed, although errors in local problem boundary conditions could lead to less accurate global solutions.

A breakdown of solution time spent in each phase of the problem is given in Figure 4.39. Based on Figure 4.39a, it can be observed that, as expected, the computational cost of the thermoplasticity problem vastly outweighs that of the heat transfer problem. Moreover, Figure 4.39b shows that parallel assembly and solution of local problems scale nearly evenly with parallel assembly and solution of the enriched global problem; at least up to the number of CPUs considered in this study, neither local problems nor the enriched global problem present a specific bottleneck in the strong scaling of the overall GFEM^{gl} simulation time for this example.



(a) Total solution wall times.



(b) Ratio of wall time in each solution phase to total solution wall time.

Figure 4.39: Parallel vs. serial solution wall times spent in each solution phase in the steady-state hat-stiffened panel problem. Total wall times as well as the proportion of total solution wall time spent in each solution phase are shown.

4.4 Summary

A novel GFEM^{gl} formulation for the analysis of materially nonlinear, coupled thermo-structural problems subjected to localized, transient heating effects is presented in this chapter. GFEM enrichment functions are generated on the fly via the solution of *hp*-adapted local boundary value problems, enabling fine-scale features to be represented on a coarse, fixed, structural-scale mesh. To account for the evolution of localized solution features in time, local solutions must be updated at each time or load step of the analysis, leading to time-dependency of global–local enrichment functions, and, therefore, time-dependency of the global approximation space. Several strategies for handling time-dependent, numerically generated shape functions and ensuring convergence of solution iterations at each time or load step of the nonlinear analysis are thus identified. Unlike traditional adaptive meshing strategies, the GFEM^{gl} does not require additional computational effort to map global solutions or nonlinear material state variables between time or load steps, from one global discretization or approximation space to the next, since the global mesh remains constant. Since the quality of numerical global–local enrichment functions can be sensitive to the accuracy of local problem boundary conditions from the global solution, a simple strategy based on linearly updating local boundary conditions at each step in the nonlinear, thermo-elasto-plastic problems of interest is also introduced.

The methods developed in this work are applied to a few representative problems of interest exhibiting localized, nonlinear thermomechanical effects in the form of sharp applied loadings as well as internal material interfaces and heterogeneity, in the interest of assessing robustness, accuracy, and computational efficiency. In terms of accuracy, GFEM^{gl} solutions compare favorably with equivalent direct approaches (*hp*-adaptive GFEM) in representing localized temperature gradients, thermomechanical stresses and strains, and residual deformations, while maintaining a coarse global mesh. The reference direct analysis approaches, however, employ highly adapted meshes, and global convergence is often governed by extremely localized nonlinearities, leading to expensive nonlinear solution iterations. Because localized nonlinearities are treated in GFEM^{gl} local problems, and GFEM^{gl} global problem sizes are also generally orders of magnitude smaller than equivalent direct analyses, global nonlinear solution iterations are inexpensive. The GFEM^{gl} also provides excellent meshing flexibility relative to a direct analysis approach, since localized loads or geometric features need only be captured in local problems. Furthermore, GFEM^{gl} local problems are *intrinsically parallelizable*, so that analysis of fine-scale solution features on adapted local meshes is computationally efficient; thus, the GFEM^{gl} may achieve reduced solution times relative to DFEA, even when a high level of fidelity in localized regions of interest is required at the global scale.

Chapter 5

Contributions and prospects for future work

The preceding chapters have presented several extensions to the generalized finite element method with the primary goal of application to large-scale, nonlinear thermo-structural problems featuring localized phenomena in mind. Here, a summary of the main novel contributions of the work, as well as a broad overview of potential future extensions, is given.

5.1 Contributions

- (i) The first noteworthy contribution of this thesis is a framework for analysis of multiphysics (i.e., coupled thermo-mechanical) problems exhibiting localized solution behavior in *hp*-GFEM and GFEM^{gl}, as presented in [107]. The framework enables efficient coupling of physics when sharp variations in multiphysics solution quantities of interest may occur *within coarse, structural-scale elements* due to the use of special GFEM enrichment functions.
- (ii) This work also introduces a GFEM^{gl} for modeling localized, structural-scale thermal and thermo-mechanical effects induced by fine-scale material heterogeneity, as published in [106]. The impact of local variation in material properties may be important to consider in the global response of the structure, especially in regions where *typical homogenization approaches are not valid*, such as in the neighborhood of highly localized gradients and singularities. The GFEM^{gl} approach
 - (a) allows for a level of fidelity which may be prohibitively computationally expensive or memory-intensive on given computational resources when using a direct method, such as adaptive finite element analysis, and
 - (b) is straightforward to implement on parallel computers, while providing excellent parallel efficiency relative to equivalent direct analysis approaches.

Moreover, the method is quite flexible and generic, as it has been shown to be applicable to *nonlinear as well as transient problems*.

- (iii) Also presented in this thesis is the extension of GFEM and GFEM^{gl} to nonlinear thermoplasticity problems *subjected to localized, transient thermal effects*. Building on the GFEM^{gl} heat transfer formulation introduced in

[90–93], in this work, thermo-elasto-plastic problems of interest are effectively modeled using coarse, structural-scale meshes via the use of *time-dependent GFEM^{sl} enrichment functions*. The time-dependent shape functions are able to represent localized temperature and resulting thermal stress/strain fields, as well as localized residual deformations, which are crucial considerations in life prediction of structures in the target application areas. The method allows for global approximation spaces which evolve in time to capture localized phenomena *without requiring a mapping of global three-dimensional solutions and nonlinear material state variables*, for instance, between changing meshes, as is typical of traditional *hp*-adaptive approaches to problems of a similar nature, and poses a substantial computational overhead.

5.2 Future directions

Based on results as well as persistent limitations observed during the course of this work, several potential future directions or extensions of the research are necessary to continue progress toward practical and realistic applications of the methods developed.

5.2.1 Improved physics

Analysis methods developed and presented in this thesis may benefit tremendously from the introduction of more complex or realistic physics to the problem at hand. Extension of the GFEM^{sl} framework presented in this thesis to account for additional physics effects will likely prove both challenging and interesting. A few of the most important of these extensions are summarized.

5.2.1.1 Realistic material models

In this study, simple J_2 plasticity and linear heat transfer are considered. However, in practical applications areas of interest, i.e., structures in extreme, multiphysics loading scenarios, more sophisticated material constitutive models are necessary to characterize the physics of the problem.

For instance, as cited in [12], in the application area of computational welding mechanics, consideration of *rate-dependent, thermo-viscoplastic effects* is of utmost importance in satisfactorily describing material behavior at elevated temperatures, potentially upwards of two-thirds of the melting point. Furthermore, examining *temperature-dependent thermal and mechanical properties*, including nonlinear heat transfer, may likely drastically impact nonlinear response of the structures of interest [69, 70].

Similar issues are well-cited in the application area of structural analysis of hypersonic air vehicles, where localized, rate-dependent plastic effects can significantly alter the response of the global structure in extreme aero-thermo-

structural environments [128]. As in the case of laser welding, temperature-dependent variation of material properties in this class of problems is likely to have a marked influence on overall structural behavior, and is a requirement for realistic structural models.

5.2.1.2 Large deformations

Hypersonic flight vehicle structures are typically comprised of very thin plate members. Deformations due to rapid, local heating of the structure are thus known to lead to geometrically nonlinear phenomena such as *local buckling*, for example, in between structural stiffeners. In other areas of interest, such as computational weld mechanics, practical finite element models must be able to predict residual structural distortion in the interest of identifying the potential for, e.g., buckling or instability [21]. Therefore, consideration of large deformations in the structure is a necessary component of future work in this area.

5.2.1.3 Transient dynamic response

Typically, a quasistatic thermomechanical response is considered sufficient in the application area of computational modeling of laser welding [69]. In the case of hypersonic flight vehicles, however, extremely rapid temperature changes and aerodynamic pressure loads on the structure due to, e.g., shock interactions, may lead to transient dynamic effects. Accounting for transient effects due to localized loadings in the context of the GFEM^{gl} is an intriguing future direction of research.

5.2.1.4 Thermomechanical fracture

A crucial consideration in the life prediction of structures in the application areas of interest in this work is fracture nucleation and propagation. For instance, Tzou [132] attempts to characterize the evolution of fractures due to thermal shock loading from a transient heat source. Related to the previous point on consideration of dynamic response, modeling dynamic fracture in structures subjected to extremely localized, shock thermal loadings is an important direction of future research, and the coupled framework developed as part of this study, in conjunction with previous work with GFEM for three-dimensional crack propagation is well-suited to this application.

5.2.2 Multiple spatial scales

Aside from introducing more sophisticated physics into the problems examined herein, this study has highlighted the formidable parallel performance and applicability of the GFEM^{gl} to problems of an intrinsically coupled multi-scale character—especially relative to traditional direct approaches, which prove to be prohibitively computationally expensive in the context of large-scale problems requiring extreme fidelity at the global scale. It has been shown

that additional computational power alone may not be sufficient to solve challenging multiscale, multiphysics problems; thus, the development of effective, scalable multiscale analysis techniques is necessary to take advantage of high-performance computing resources.

One potentially interesting future extension is *the introduction of multiple—i.e., more than two—spatial scales* into the GFEM^{gl} framework. By introducing multiple hierarchies of computationally manageable fine-scale, local problems, the GFEM^{gl} may prove to be an effective tool for bridging micro- or material-scale effects to the structural or component level.

5.2.2.1 Numerical integration of global GFEM^{gl} weak form

Even in a simple, two-scale approach, the cost of numerically integrating the global system of equations, which depends on numerical enrichment functions defined over fine-scale, local meshes, is significant. The introduction of additional spatial scales into the hierarchy would lead to a disparity between local and global mesh sizes of potentially arbitrarily many orders of magnitude; thus, the traditional approach of performing numerical integration over the local mesh would become impracticable due to prohibitive computational cost.

To reduce the cost of assembling global–local enrichments and thus accelerate global solution times, simplified or optimized numerical integration approaches are necessary. Work by Schweitzer and Wu [116] has preliminarily investigated this issue, albeit in the context of the global–local approach with enrichments stemming from a particle method in local problems.

5.2.3 Efficient linear solvers

The parallel version of the GFEM^{gl} bears similarities to, for example, domain-decomposition based methods, which attempt to make large-scale, high-fidelity problems more tractable by subdividing them into computationally manageable, parallelizable subdomains. GFEM^{gl} incurs little to no communication cost among intrinsically parallelizable local problems, making it very conducive to high-performance computing applications. However, in order to better understand the competitiveness of the method as it is applied to large-scale problems in the applications of interest, relative to available approaches, *a direct comparison to available parallel approaches, like multigrid or domain-decomposition methods, is necessary.*

5.2.4 Integration with practical analysis tools

The transition of methods developed herein to design practice is, unfortunately, a nontrivial task, as it requires more than simply providing a computer implementation of these methods to practicing engineers and scientists. Several additional method developments are necessary.

5.2.4.1 Nonintrusive implementation

Related to the incorporation of more realistic or complex physical behavior into the framework developed during this study, practical applications of the method in an engineering context also require robust software tools. Mature, widely-used analysis codes have large libraries of material models, loads and boundary conditions, element formulations, and efficient solvers. As discussed in [50, 105], *nonintrusively incorporating the method into an established (i.e., commercial) analysis software package*, is necessary to enable more rapid and accessible transition of the GFEM^{gl} to industrial applications, and designing an efficient and robust algorithm to do so is an important topic of future research.

5.2.4.2 Dimensionally reduced models

Fully three-dimensional models are prohibitively expensive for large-scale problems; however, the kinematic assumptions of dimensionally reduced structural elements such as plates, shells, beams, etc., cannot satisfactorily capture localized thermomechanical behavior of interest. Furthermore, adaptive localized mesh refinement, an optimal solution strategy in the classes of problems of interest, is difficult—or perhaps impossible—when dealing with meshes of plates, shells, or even three-dimensional hexahedral elements. Therefore, another key aspect in the potential application of the subject methods to industrial-scale problems is the *compatibility of the GFEM^{gl} with commonly-used, practical structural element formulations* such as plates and shells. Souloumiac and others [122] and Duan and others [21], for instance, propose a method for coupling solid and dimensionally reduced models, in the application area of weld mechanics, in order to predict global-scale residual distortions due to highly localized, thermo-elasto-plastic effects. The superposition-based *hp-d* method of Krause and Rank [112] has previously been extended to the coupling of locally three-dimensional and globally two-dimensional approximations in [33, 34]—an analogous extension of the GFEM^{gl} is also likely possible.

Appendix A

Thermomechanical coupling implementation for GFEM

This segment presents a detailed description of specific issues relating to the computational implementation of one-way coupling for thermomechanical problems in a GFEM framework, introduced in Chapter 2, with special emphasis on maintaining computational efficiency.

A.1 *hp*-GFEM coupling

Coupling two physics problems with the *hp*-version of GFEM is the most straightforward case because in this instance one finite element in the heat transfer problem corresponds to exactly one finite element in the thermo-structural problem. The integration order for assembly of the stiffness matrix over element i_{el}^u in the thermomechanical problem is chosen based upon the maximum equivalent polynomial order,

$$p_{eq} = \max\{p_{eq}(\phi_{ai}), p_{eq}(\mathbf{b}), p_{eq}(\theta)\}, \quad (\text{A.1})$$

where $\phi_{ai}(\mathbf{x})$ are structural problem shape functions, $\mathbf{b}(\mathbf{x})$ the structural problem body force, and $\theta(\mathbf{x})$ the temperature field. The polynomial order of the temperature field $p_{eq}(\theta(\mathbf{x}))$ is easily obtained as the maximum p -order of the heat transfer problem shape functions over the patches covering element i_{el}^θ .

Once the integration order has been obtained for i_{el}^u , evaluation of the temperature field at the integration points is direct, since integration points in each element i_{el}^θ in the heat transfer problem and i_{el}^u in the structural problem are identical; no expensive searching for individual elements in the mesh and inverse mapping of integration points to physical coordinates is required. The detailed algorithm for assembly and solution, accounting for thermal stress contributions, in this case is straightforward and is detailed in Algorithm A.1. The mesh correspondence and exchange of information between problems is also illustrated in Figure A.1.

Algorithm A.1 Assembly and solution of hp -GFEM global thermoelasticity problems considering multiphysics temperature effects.

```

for finite element  $i_{\text{el}}^{\text{u}} < n_{\text{els}}$  in the structural mesh do
  get the corresponding element  $i_{\text{el}}^{\theta}$  in the heat transfer problem;
  determine the integration rule  $\{\xi\}_{i_{\text{el}}}$  based on (A.1);
  for each integration point  $\xi_j, j < n_{\text{pts}}$  do
    obtain temperature field  $\theta$  in  $i_{\text{el}}^{\theta}$  at  $\xi_j$ , and compute thermal strain  $\varepsilon_{\theta}$  from (2.3);
    compute contributions from  $i_{\text{el}}^{\text{u}}$  at  $\xi_j$  in weak form (2.21);
     $j \leftarrow j + 1$ ;
  end for
   $i_{\text{el}}^{\text{u}} \leftarrow i_{\text{el}}^{\text{u}} + 1$ ;
end for
solve linear system (2.23);

```

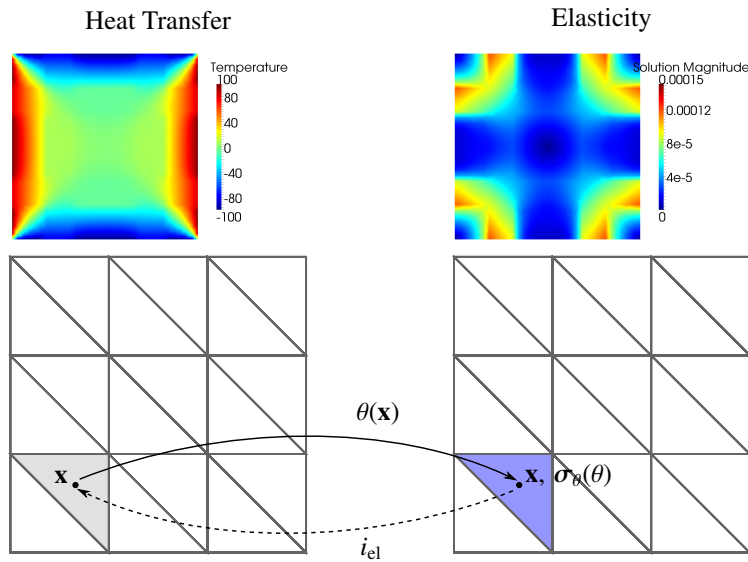


Figure A.1: Algorithm showing communication between physics problems in the hp -GFEM case to obtain thermal stress contributions. Dashed arrows represent corresponding data in each problem, while solid arrows represent exchange of physical quantities between the physics problems.

A.2 GFEM^{gl} coupling

As previously discussed, the GFEM^{gl} introduces additional complexities in the multiphysics coupling framework. Because a sequential coupling is adopted, the most accurate, enriched global heat transfer solution θ^E is used to compute thermal stress contributions in each of the initial global, local, and enriched global structural problems, as described previously in Section 2.3.2. However, θ^E is represented using global–local shape functions from the solution of hp -adapted heat transfer local problems, which are defined over the refined local mesh.

Additional assumptions are therefore adopted in the GFEM^{gl} to maintain computational efficiency and compatibility with the multiphysics coupling framework. Not only are the global heat transfer and structural mesh geometries identical, but the *local problem meshes* must also have the same one-to-one correspondence of elements. Just as in the

hp-GFEM, only the geometry of the mesh must be the same, however, and arbitrary choice of enrichment functions is possible.

A.2.1 Global thermo-structural problems

The coupling procedures for both initial and enriched global problems are virtually the same. However, in the application of interest, the heat transfer problem is typically subject to extremely sharp and localized thermal boundary conditions. It has been shown that these sharp thermal loadings, when applied on a coarse, global mesh, can lead to large integration errors (as well as significant pollution error in the initial global solution) [90, 93]. Once these integration errors are treated in the GFEM^{el} heat transfer local and enriched global solutions, the refined local mesh of the heat transfer problem may be used to accurately integrate thermal stress contributions, even in the coarse-scale, global structural problem. While in general the use of this fine integration mesh results in a large number of quadrature points, it allows for exact integration of thermal stress contributions, and the effort required is comparable to a direct finite element analysis at the same level of fidelity. In realistic problems, it is further expected that the assembly effort in the region where global–local enrichments are required will be comparable to the effort associated with the remainder of the global domain. Although it is not a focus of present work, alternative, *inexact but less expensive* integration techniques have been in active development [116]. The local mesh elements nested within each coarse-scale global element are denoted *descendants* of that global element. The exchange of data between physics problems for computing thermal stress contributions (using nested local elements) is described graphically in Figure A.2.

The detailed description of thermoelastic problem assembly and solution, considering multiphysics effects, in initial and enriched global problems is given in Algorithm A.2.

A.2.2 Local thermo-structural problems

Assembly of structural local problems is similar to the global problems; however, local problems are required to communicate with the global structural and heat transfer problems in order to obtain the global temperature field, θ^E , for thermal stress contributions at integration points in the refined local mesh. As described pictorially in Figure A.3, each local structural mesh element i_{el}^u is a nested descendant of the corresponding global element i_{el}^u . Thus, it is a simple task to determine the coarse-scale, global element corresponding to each local descendant. Some additional computational effort is incurred in this case, since an inverse mapping is required to obtain the corresponding integration point in the global element. The assembly and solution algorithm adopted in the thermoelastic problem is described in detail in Algorithm A.3.

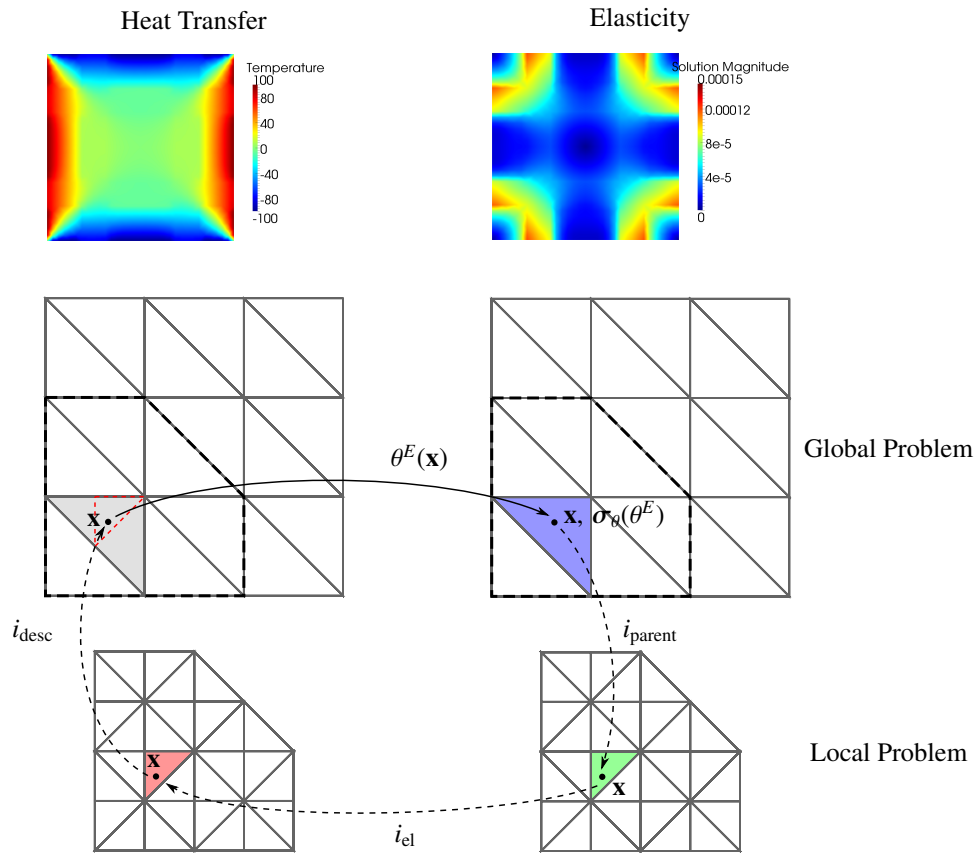


Figure A.2: Algorithm showing communication between GFEM^{el} global thermo-structural problem and global heat transfer problems to obtain thermal stress contributions. Dashed arrows represent a corresponding data in each problem, while solid arrows represent exchange of physical quantities between the physics problems.

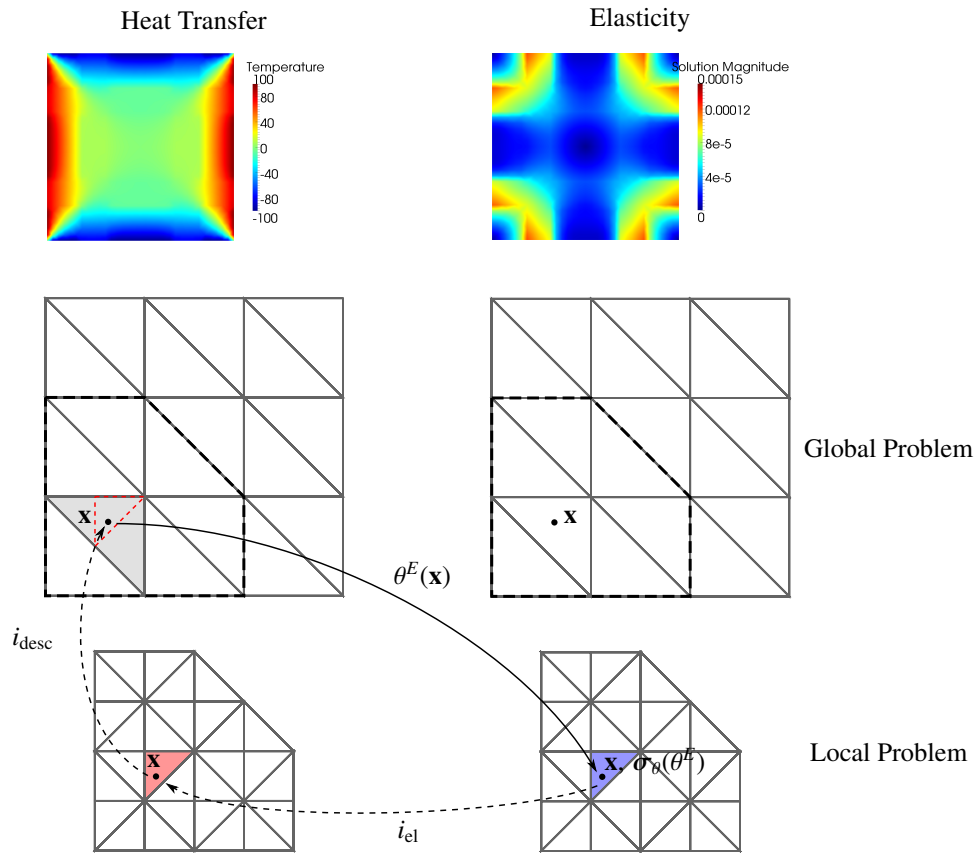


Figure A.3: Algorithm showing communication between GFEM^{el} local thermo-structural problems and the global heat transfer problem to obtain thermal stress contributions. Dashed arrows represent corresponding data in each problem, while solid arrows represent exchange of physical quantities between the physics problems.

Algorithm A.2 Assembly and solution, considering multiphysics temperature effects, of GFEM^{gl} initial and enriched global thermoelasticity problems.

for finite element $i_{\text{el}}^{\text{u}} < n_{\text{els}}$ in the global structural mesh **do**
 get the corresponding *global* element i_{el}^{θ} in the global heat transfer problem;
 get the list of nested local elements of i_{el}^{u} , $\{j_{\text{desc}}^{\text{uL}}\}_{i_{\text{el}}}$;
for each descendant $j_{\text{desc}}^{\text{uL}} < n_{\text{descs}}$ **do**
 get the corresponding *local* descendant $j_{\text{desc}}^{\theta\text{L}}$ in the local heat transfer problem;
 determine the descendant integration points $\{\xi\}_{j_{\text{desc}}}$;
for each integration point ξ_k , $k < n_{\text{pts}}$ **do**
 find the corresponding *global* integration point η_k in i_{el}^{θ} by inverse mapping the physical coordinate \mathbf{x}_k ;
 obtain temperature field θ^E using $j_{\text{desc}}^{\theta\text{L}}$ at η_k in i_{el}^{θ} , and compute thermal strain ε_{θ} from (2.3);
 compute contributions from $j_{\text{desc}}^{\text{uL}}$ at η_k to i_{el}^{u} at ξ_k in weak form (2.21);
 $k \leftarrow k + 1$;
end for
 $j_{\text{desc}}^{\text{uL}} \leftarrow j_{\text{desc}}^{\text{uL}} + 1$;
end for
 $i_{\text{el}}^{\text{uL}} \leftarrow i_{\text{el}}^{\text{uL}} + 1$;
end for
 solve linear system (2.23);

Algorithm A.3 Assembly and solution, considering multiphysics temperature effects, of GFEM^{gl} local thermoelasticity problems.

for finite element $i_{\text{el}}^{\text{uL}} < n_{\text{els}}^{\text{L}}$ in the local structural mesh **do**
 get the corresponding *local* element $i_{\text{el}}^{\theta\text{L}}$ in the local heat transfer problem;
 get the corresponding *global* element $i_{\text{parent}}^{\theta}$ in the global heat transfer problem;
 determine the local integration rule $\{\xi\}_{i_{\text{el}}}$;
for each integration point ξ_j , $j < n_{\text{pts}}$ **do**
 find the corresponding *global* integration point η_j in $i_{\text{parent}}^{\theta}$ by inverse mapping the physical coordinate \mathbf{x}_j .
 obtain temperature field θ^E using $i_{\text{el}}^{\theta\text{L}}$ at η_j in $i_{\text{parent}}^{\theta}$, and compute thermal strain ε_{θ} from (2.3);
 compute contributions from $i_{\text{el}}^{\text{uL}}$ at ξ_j in weak form (2.24);
 $j \leftarrow j + 1$;
end for
 $i_{\text{el}}^{\text{uL}} \leftarrow i_{\text{el}}^{\text{uL}} + 1$;
end for
 solve linear system (2.25);

Appendix B

GFEM^{gl} parallel improvements

This appendix details implementational improvements related to parallel performance of the GFEM^{gl}, as used in Chapters 3 and 4. All parallel algorithms are implemented in C++ using OpenMP [94].

B.1 Sub-local problem boundary condition computation

As described in detail and demonstrated in Chapter 3, the GFEM^{gl} based on sub-local problems can resolve very localized behavior on a coarse-scale, structural mesh via the efficient, parallel solution of many fine-scale, local problems. These local problems are subject to boundary conditions from the global solution, which may come from

- (i) a coarse-scale, initial global analysis, defined on a coarse, quasi-uniform mesh and based on only analytical or polynomial global shape functions, or
- (ii) a previous enriched global GFEM^{gl} solution, such as from a previous time or load step, or a previous global–local iteration.

Mapping global solutions onto the boundary of fine scale problems can be computationally expensive, especially when the global solution involves numerical global–local enrichment functions which are defined over highly adapted fine-scale meshes. Based on the topology and hierarchy of GFEM^{gl} local and global meshes, optimized strategies for computing boundary conditions on sub-local problems are devised so as to incur little to no additional computational cost.

B.1.1 Boundary conditions from coarse-scale solution

When fine-scale boundary conditions come from a coarse-scale, initial global analysis based only on analytically-defined shape functions and a coarse, global mesh, computation is straightforward and inexpensive; fine-scale elements are directly descended from a coarse-scale element, which is stored as part of the local problem data structure. The mapping of boundary conditions onto local problems from a coarse-scale, global solution is demonstrated in Figure B.1 and described in Algorithm B.1.

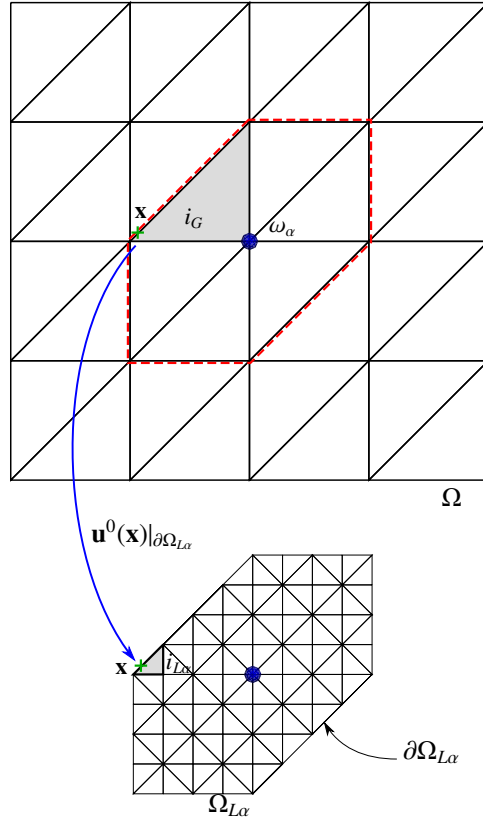


Figure B.1: Coarse-scale computation of boundary conditions on sub-local problems *without* global–local enrichment functions in the global problem.

Algorithm B.1 Assembly of sub-local problem boundary condition contributions on a given local problem from a coarse, global solution.

for each *local* element face $i_{L\alpha}^{\text{BC}}$ on the boundary $\partial\Omega_{L\alpha} \setminus (\partial\Omega_{L\alpha} \cap \partial\Omega)$ of local problem $\Omega_{L\alpha}$ **do**
 get the corresponding *global* volume element i_G in the global problem which contains $i_{L\alpha}$;
 for each local integration point ξ_j , $j < n_{\text{pts}}$ on face $i_{L\alpha}^{\text{BC}}$ **do**
 compute the corresponding global coordinate $\mathbf{x}_j(\xi_j)$;
 evaluate the coarse-scale, global solution $u^0(\mathbf{x}_j)$ in i_G ;
 compute boundary condition contributions from $u^0(\mathbf{x}_j)$ as in, e.g., (2.15);
 end for
end for

B.1.2 Boundary conditions from enriched global solution

When boundary conditions on sub-local problems come from global solutions based on global–local enrichment functions, computation of boundary condition quantities becomes substantially more involved. A naïve or ‘brute force’ approach (equivalent to the approach described in the above section for coarse-scale global solutions) consists of expensive searching for local elements and mapping of global to local coordinates based on a given *global* coordinate \mathbf{x} in order to evaluate global–local enrichment functions. However, as mesh adaptivity in fine-scale problems increases, this approach quickly becomes extremely inefficient (see, for instance, 3.3 in Chapter 3) or even unreliable, resulting in overall GFEM^{gl} solution time bottlenecks due to local problem boundary computations.

Instead, the *hierarchical topology of the underlying adapted local meshes*, on which global–local enrichments are defined, may be used to devise an optimized approach for computing global–local boundary conditions on fine-scale problems. In all cases, local meshes are adapted such that they are compatible in regions in which they overlap on the global domain. A single *master descendant* is defined (denoted i_{GL} in Algorithm B.2), which then can be used to link a given sub-local element to its geometrically corresponding elements in all other fine-scale problems. The mesh of master descendants covering all sub-local domains is equivalent to the mesh of an unsubdivided, monolithic local problem—that is, in terms of local domains,

$$\Omega_{L,\text{master}} = \bigcup_{\alpha} \Omega_{L\alpha}.$$

Figure B.2 describes the optimized approach and illustrates the fine-scale mesh correspondence graphically. The topology of the boundary of local problem $\Omega_{L\alpha}$ is identified on both the coarse global and intersecting sub-local problem meshes—it is important to note that the boundary of $\Omega_{L\alpha}$ is interior to these intersecting problems. Algorithm B.2 gives a detailed explanation of the procedure. Figure B.3 illustrates the mesh of master descendants corresponding to Figure B.2.

B.1.3 Numerical example: transient heat transfer

To verify the implementation and demonstrate the improvements in computational efficiency associated with leveraging the algorithm presented, the laser-heated beam example of Section 4.3.2.1 in Chapter 4 is solved; however, in this case, only the transient heat transfer problem is considered. Furthermore, 6 levels of global mesh refinement are performed on the global domain in the neighborhood of the sharp, stationary applied laser flux. The resulting local domain has 10 additional levels of localized mesh refinement surrounding the sharp flux location in GFEM^{gl} simulations. In parallel GFEM^{gl} simulations with sub-local problems, the local domain is subdivided into 250 sub-local problems. The global polynomial order is $\mathbf{p} = \{2, 2, 2, \}$ while in the local problem, $\mathbf{p}_{loc} = \{3, 3, 3\}$. The transient

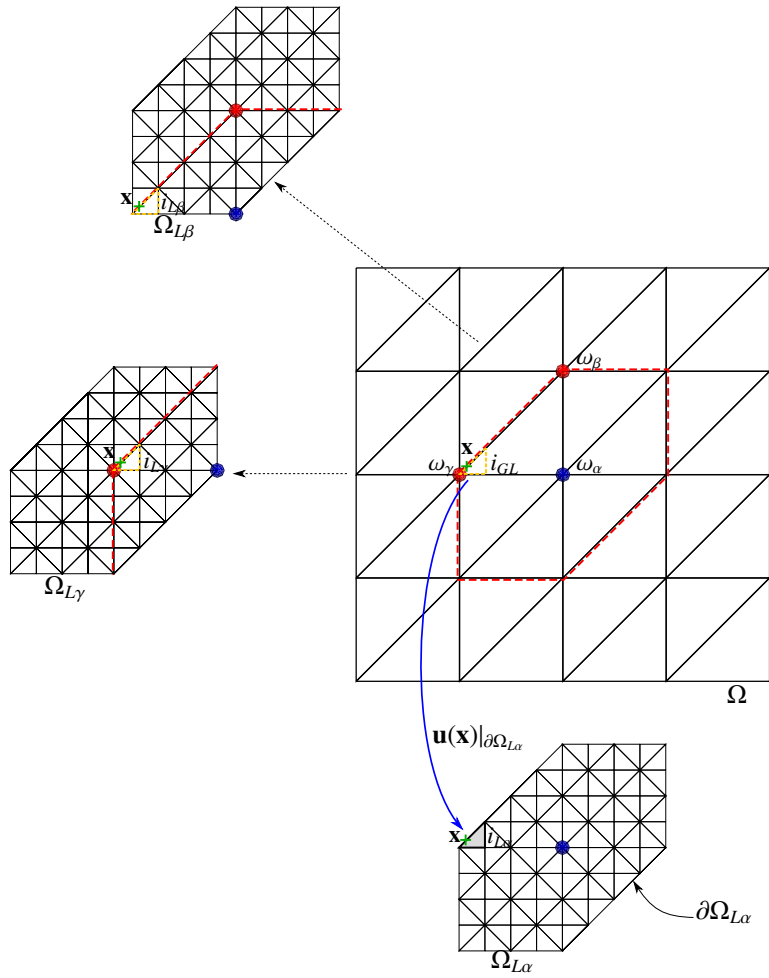


Figure B.2: Local problem descendant relationships for optimized computation of boundary conditions on sub-local problems *with* global–local enrichment functions in the global problem, based on nested mesh topology in sub-local problems (i.e., when conducting multiple global–local iterations, or in time-dependent problems). The optimized approach avoids expensive searching and mapping of fine-scale solutions onto the sub-local boundaries.

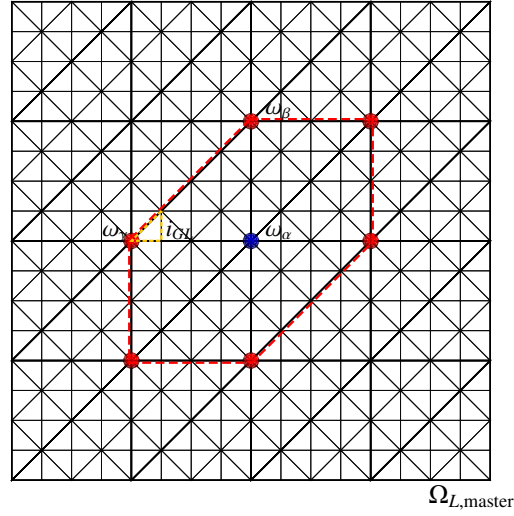


Figure B.3: Fine-scale, master descendant mesh associated with Figure B.2, used to determine the geometric correspondence of fine-scale elements for efficient computation of sub-local boundary conditions.

Algorithm B.2 Assembly of sub-local problem boundary condition contributions on a given local problem from an enriched global GFEM^{gl} solution.

for each *local* element face $i_{L\alpha}^{\text{BC}}$ on the boundary $\partial\Omega_{L\alpha} \setminus (\partial\Omega_{L\alpha} \cap \partial\Omega)$ of local problem $\Omega_{L\alpha}$ **do**
 get the corresponding *global* volume element i_G in the global problem which contains $i_{L\alpha}$;
 get the *master descendant* i_{GL} which corresponds to $i_{L\alpha}$;
for each local integration point ξ_j , $j < n_{\text{pts}}$ on face $i_{L\alpha}^{\text{BC}}$ **do**
 compute the corresponding global coordinate $\mathbf{x}_j(\xi_j)$;
for each enriched global node ω_k , $k < n_{\text{nods}}$ (where $\omega_\alpha \in \{\omega_k\}$) of element i_G **do**
 evaluate the solution $u_{Lk}(\mathbf{x}_j)$, of each corresponding sub-local problem Ω_{Lk} , using ξ_j and descendant i_{GL} ;
 compute global–local shape functions at the integration point, as in, e.g., (4.18),

$$\phi_{\alpha k}^{\text{gl}} = \varphi_\alpha u_{Lk};$$

end for
 calculate the global solution $u(\mathbf{x}_j)$ in i_G based on global–local shape functions;
 compute boundary condition contributions from $u(\mathbf{x}_j)$ as in, e.g., (4.17);
end for
end for

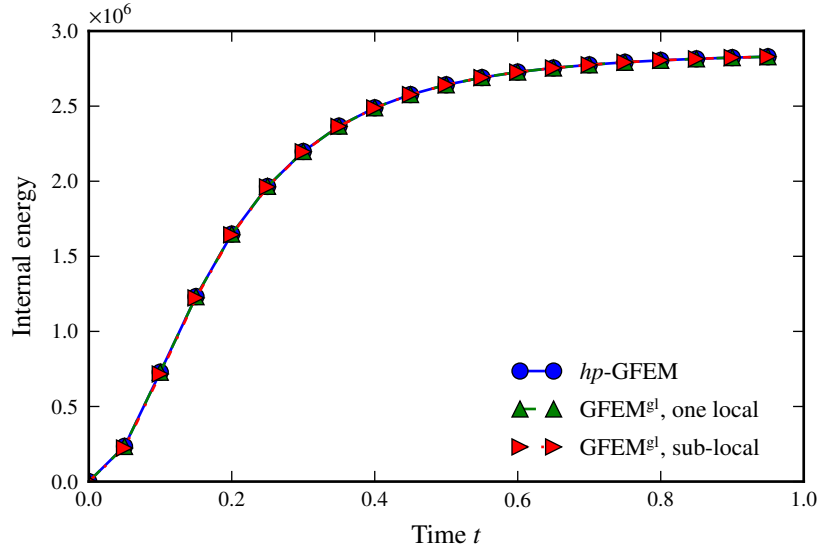


Figure B.4: Internal energies of GFEM^{gl} and hp -GFEM transient heat transfer solutions of the laser-heated beam.

analysis is carried out over the interval $t \in [0, 1]$ in 20 uniform time steps, so that $\Delta t = 0.05$. For comparison, an ‘equivalent’ direct hp -GFEM analysis is also included. Both GFEM^{gl} and hp -GFEM simulations leverage a parallel implementation on a machine with 24 computing cores.

The internal energies of GFEM^{gl} and hp -GFEM solutions at each time step are given in Figure B.4.

Figure B.5 shows the wall times required for solution of the problem under each method when ‘brute force’ computation of local boundary conditions is used. Despite the good accuracy of all approaches adopted to solve the problem, the expensive searching and mapping of GFEM^{gl} enriched global solutions onto sub-local problem boundaries bottlenecks the overall solution time, so that any benefit of a parallel implementation is lost due to computational overhead.

Figure B.6 compares the wall time required for assembly of local problems in each GFEM^{gl} simulation, now considering optimized computation of local boundary conditions. It is an important distinction that the monolithic GFEM^{gl} local problem uses a parallel assembly algorithm on 24 threads, while each of 250 GFEM^{gl} sub-local problems utilizes a serial assembly routine on each thread; the assembly of sub-local problems experiences a slight overhead with respect to the monolithic local problem because of this as well as the extra expense associated with overlapping sub-local regions (see, e.g., Figure B.2). Immense gains in assembly efficiency are observed by adopting the optimized numerical integration strategy on sub-local boundaries described above, and the benefits are expected to increase as the ratio H/h between global and local mesh sizes increases.

In contrast with Figure B.5, Figure B.7 compares overall transient simulation wall times when computation of sub-local problem boundary conditions is optimized. As expected, in this instance the parallel GFEM^{gl} with sub-local

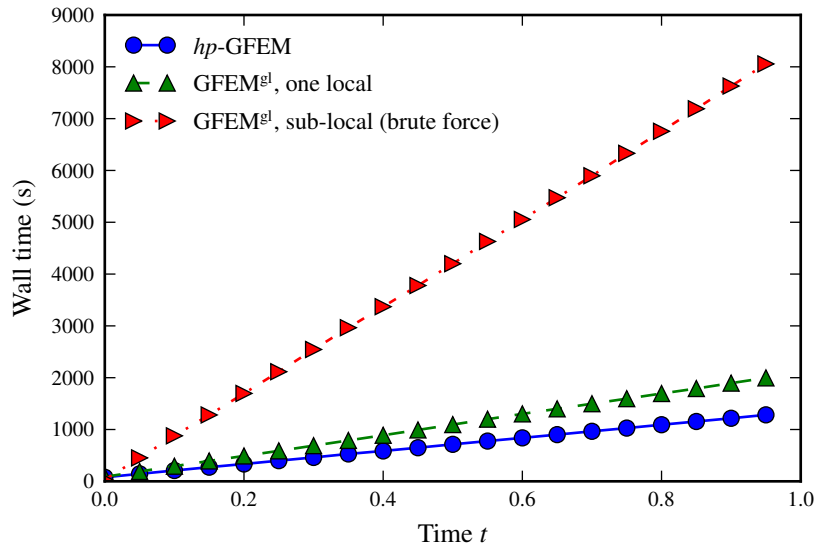


Figure B.5: Cumulative wall time required for transient heat transfer simulation of the laser-heated beam, brute force computation of local problem boundary conditions.

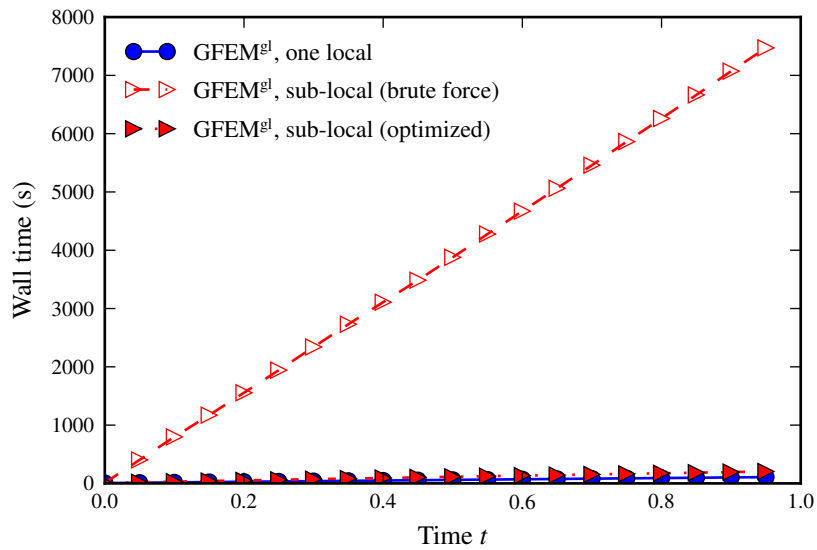


Figure B.6: Cumulative wall time required for assembly of local problems in GFEM^{gl} transient heat transfer simulations of the laser-heated beam. The monolithic GFEM^{gl} local problem utilizes a parallel assembly on 24 threads, while sub-local problems are each assembled (in serial) on one thread in the team of 24 total threads.

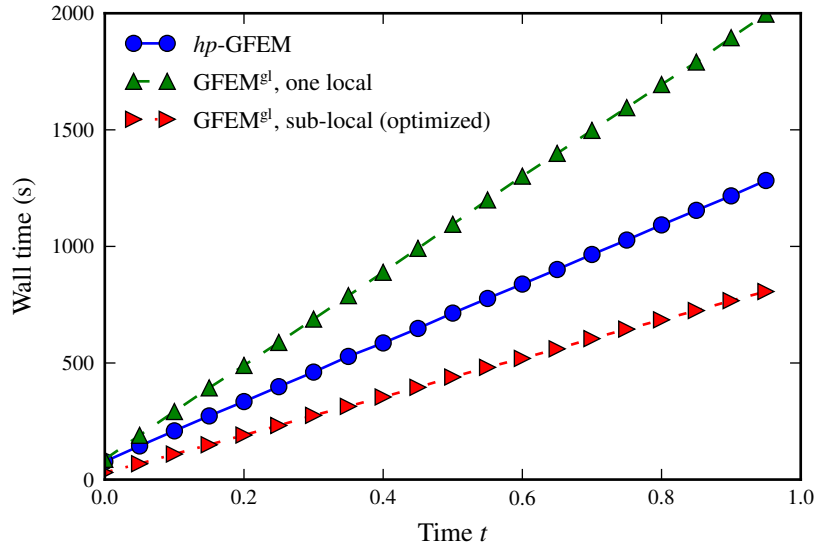


Figure B.7: Cumulative wall time required for transient heat transfer simulation of the laser-heated beam, optimized computation of local problem boundary conditions.

Table B.1: Comparison of parallel efficiency of hp -GFEM and $GFEM^{gl}$ transient heat transfer solutions of the laser-heated beam at a single time step ($t = 0.1$) on 24 CPUs. $GFEM^{gl}$ solution times consider assembly, factorization, and solution of local problems, while DFEA solution times consider only the linear solve phase.

Method	Solve (s)	Speedup	Efficiency
hp -GFEM DFEA (serial)	551.11	–	–
hp -GFEM DFEA (parallel)	83.73	6.58	0.274
$GFEM^{gl}$	78.59	7.01	0.292
$GFEM^{gl}$, sub-local	27.11	20.33	0.847

problems outperforms both hp -GFEM and $GFEM^{gl}$ simulations in terms of total wall time required.

Table B.1 compares the parallel efficiency of $GFEM^{gl}$ approaches with respect to the hp -GFEM solution using an optimized, parallel direct sparse solver at a single time step ($t = 0.1$) of the transient solution. The solution times shown are exclusive of time spent assembling the global problem; that is, they include hp -GFEM times for factorization and solution of the global system of equations, while $GFEM^{gl}$ times include assembly, factorization, and solution of local problems, as well as factorization and solution of the global problem. The parallel $GFEM^{gl}$ with sub-local problems yields the best speedup with respect to the serial DFEA.

Even further gains in computational efficiency are possible in $GFEM^{gl}$ transient heat transfer problems, with or without sub-local problems. Because no time scale is associated with the linear, steady-state local problems, and their respective spatial discretizations remain constant at each time step of the analysis, the factorized system of equations for each local or sub-local domain may be stored and reused at each global time step. In this instance, only external loads require updating, and solution of local problems involves only a forward and backward substitution on

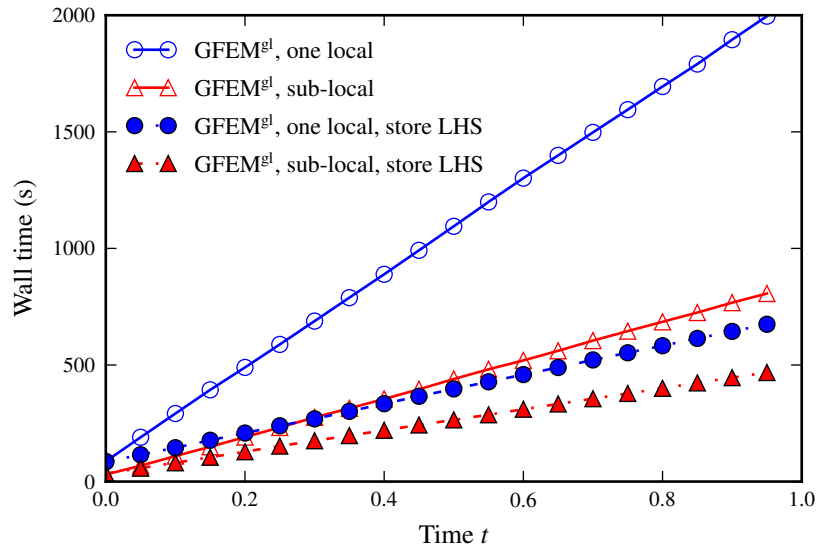


Figure B.8: Comparison of wall times for transient heat transfer simulations of the laser-heated beam with (store LHS) and without storage of (sub-)local problem factorizations. The monolithic GFEM^{gl} local problem utilizes a parallel assembly on 24 threads, while sub-local problems are each assembled (in serial) on one thread in the team of 24 total threads.

the factorized linear system. Figure B.8 shows overall solution wall times when local factorizations are stored and reused at each time step. While the monolithic local problem leads to an improved solution time, even relative to the analysis utilizing parallel sub-local problems, it is again important to distinguish that the local problem utilizes a parallel assembly algorithm and parallel direct sparse solver. In general, however, monolithic local problems may be *prohibitively large* to be solved on given computational resources. Although this strategy allows for faster computation times, the storage overhead associated with all local or sub-local problem factorizations may be extremely large; thus, a careful consideration of computation time versus memory usage is important. Furthermore, the strategy is only generally applicable to linear problems (i.e., importantly, *not* the elasto-plastic problems with multiple load steps that are also of interest in this study). Regardless, the GFEM^{gl} with sub-local problems is capable of providing good computational efficiency without incurring additional storage overhead.

B.2 Parallel assembly

Three parallel assembly strategies are compared, based on findings by Jarzebski et al. [57]:

- (i) OpenMP critical regions (`critical`), which are implemented in the global assembly routine, asserting that only one thread at a time may assemble its contributions into the global matrices,
- (ii) OpenMP atomic updates (`atomic`), which reduces the overhead associated with critical regions, and can be

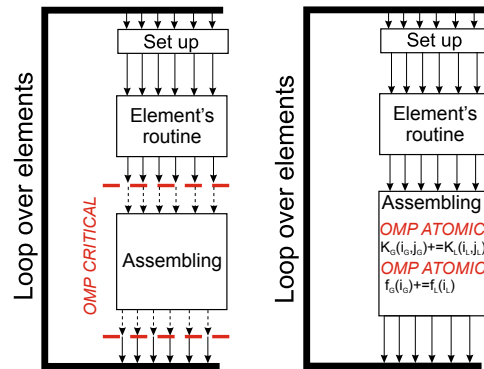


Figure B.9: Different OpenMP parallel assembly strategies considered: atomic updating (atomic) versus critical region (critical), from [57].

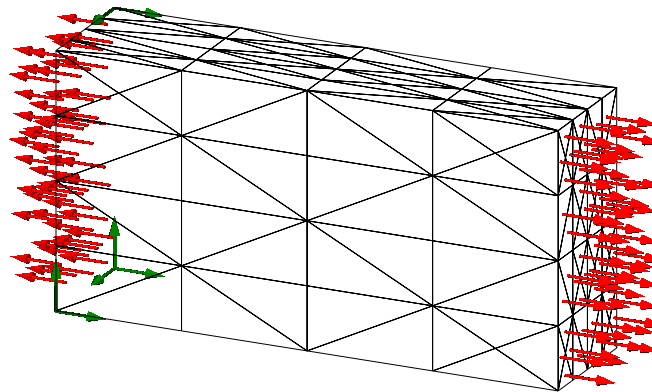


Figure B.10: Simple parallel assembly benchmark problem; a 4-node tetrahedral mesh of a linear elastic domain under uniform tension.

applied to a single update operation in the global matrices,

(iii) and an element coloring scheme [13],

each in order to avoid race conditions in the global stiffness matrix and load vector(s).

B.2.1 Tetrahedral mesh

Figure B.10 shows a very simple, linear elasticity ‘benchmark’ problem used to assess the scalability of each global assembly approach. The model consists of 1,208 four-node tetrahedral GFEM elements. Two global polynomial orders of the approximation are considered, $p = 5$ (33,075 global degrees of freedom) and $p = 6$ (52,920). A high polynomial order is chosen so that individual element computations are expensive relative to the cost of assembly of element contributions into the global matrices—i.e., each element contribution involves many integration points.

Figure B.11 shows parallel assembly speedup results with global polynomial orders $p = 5$ and $p = 6$ for each of the strategies implemented. The global serial CPU times for assembly are 12.16 and 102.86 seconds, respectively. It is clear that use of a critical region, which requires explicit synchronization of all threads during each assembly operation, gives a poor speedup of roughly 2 or less for $p = 5$ and 7 or less when $p = 6$. Scalability likely reaches an upper bound due to the serial execution time required during the assembly operation.

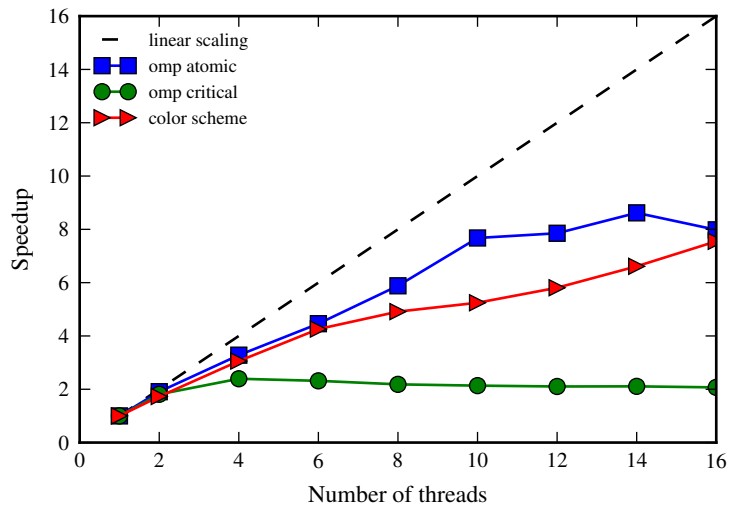
The element coloring scheme avoids race conditions altogether by ensuring that all elements assembled in a given color do not share a global node, i.e., no two elements of a single color will simultaneously write to a single location in memory. However, there are several limitations inherent in this approach. First, there is a substantial overhead associated with computing the mesh coloring, especially for dense tetrahedral mesh topologies where many elements may share a single node. (It should be noted, however, that this overhead time is not included in the numerical results shown.) Second, it is also possible that a mesh coloring may require a very large number of colors; the number of elements of a given color may therefore be fewer than the number of processors available for the assembly operation. In this instance a suboptimal speedup is expected, which proves true in the examples shown, as the parallel speedup reaches an upper bound of roughly 8. The element coloring scheme generally yields a better speedup than the critical region approach, however. Specific performance aspects of the coloring scheme are detailed in Section B.2.3.

Atomic updating, which is a simplified critical region optimized for update operations on a given shared memory location, provides the best speedup for the test examples shown. While $p = 5$ seems to reach a bottleneck, when $p = 6$ globally, the approach scales well relative to the ideal, linear scaling.

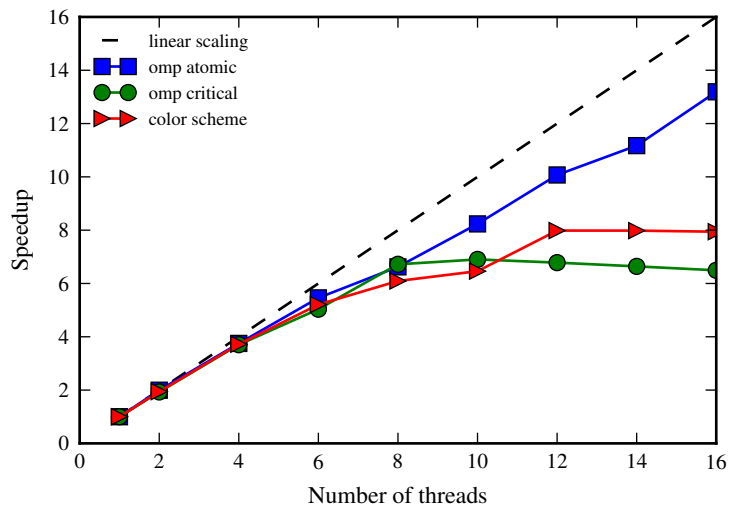
B.2.2 Hexahedral mesh

Figure B.12 shows the same linear elasticity ‘benchmark’ problem, now meshed with 1,000 eight-node hexahedral GFEM elements, for comparison with the previous tetrahedral mesh. A global polynomial order $p = 4$ is used in this case, resulting in 83,160 degrees of freedom.

Parallel assembly speedup results for this example are included in Figure B.13. For reference, the serial CPU time for assembly of the hexahedral benchmark problem is 26.52 seconds. A very similar behavior of the parallel assembly strategy utilizing a critical region is observed in this case, again due to the serial bottleneck. However, in this case the atomic update and mesh coloring give very similar speedup results. The improved performance of the coloring scheme, relative to atomic updating, may be attributed to the nature of the hexahedral mesh; in this case, fewer elements are connected to each node, resulting in fewer colors, or, equivalently, fewer race conditions.



(a) $p = 5$



(b) $p = 6$

Figure B.11: Speedup in parallel assembly for the benchmark problem with 4-node tetrahedral elements for various global polynomial orders of the approximation.

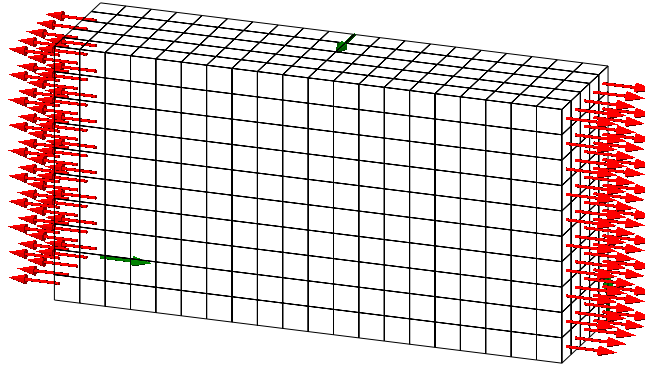


Figure B.12: Simple parallel assembly benchmark problem; an 8-node hexahedral mesh of a linear elastic domain under uniform tension.

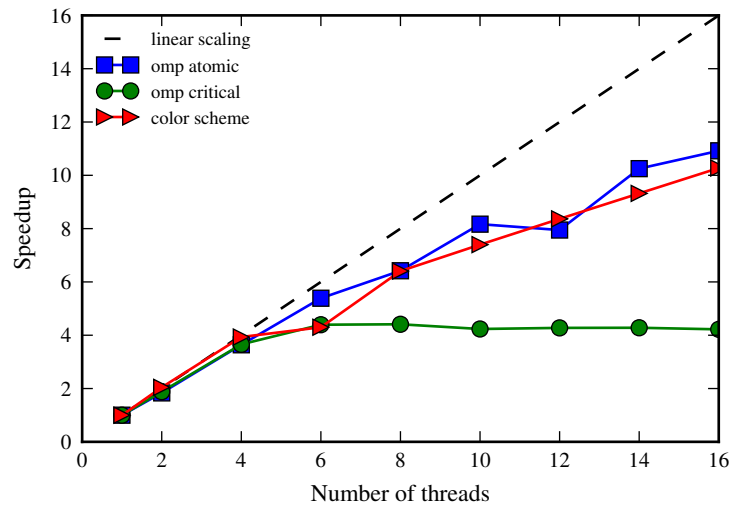


Figure B.13: Speedup in parallel assembly for the benchmark problem with 8-node hexahedral elements.

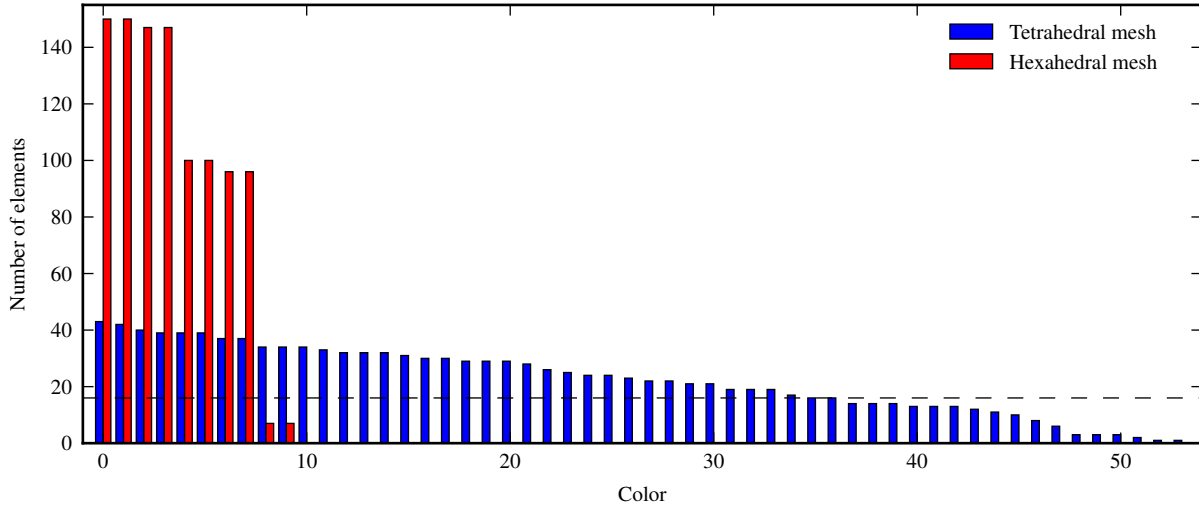


Figure B.14: Comparison of the number of elements per color in each mesh considered for the benchmark problem. The dashed horizontal line indicates the maximum number of CPUs on which the parallel assembly was tested in the examples shown. The tetrahedral mesh has a total of 1,208 elements, while the hexahedral mesh has 1,000.

B.2.3 Element coloring scheme performance

Figure B.14 compares the number of elements per color in both the structured tetrahedral and structured hexahedral meshes. While the tetrahedral mesh requires 54 colors, with a maximum of number of elements $n_{el} = 43$ in the largest color, the hexahedral mesh needs only 10 colors, with 150 elements in the largest color.

The dashed horizontal line in the figure indicates the maximum number of threads, $N = 16$, for which parallel assembly results are shown in both of these sample meshes. Out of 54 colors in the tetrahedral mesh, 17 have fewer elements than threads, $n_{el} < N$, which greatly diminishes the efficiency of the parallel assembly, as (sometimes multiple) threads remain idle during the assembly of these colors. On the other hand, just 2 of 10 colors in the hexahedral mesh have $n_{el} < N$, while most colors have $n_{el} \gg N$, due to the connectivity structure of the mesh, resulting in fewer elements connected per node; thus, the coloring scheme achieves a substantially better speedup on the hexahedral mesh than in the tetrahedral case.

Appendix C

GFEM^{gl} nonlinear solution algorithms for time-dependent shape functions

This appendix provides the nonlinear solution strategies for GFEM^{gl} thermoplasticity problems presented in Chapter 4 in detailed algorithm form, for ease of implementational reproduction, as follows:

- (i) A nonlinear solution algorithm C.1 based on reconstruction of the total solution from separate approximations at each increment, or the ‘incremental’ approach.
- (ii) Algorithm C.2 based on recovering the previous converged solution at time $t = t_n$ in the updated approximation space at $t = t_{n+1}$ from a linear elastic solution, or the linear ‘recovery’ approach.
- (iii) Algorithm C.3 based on predicting the total solution at the current time step $t = t_{n+1}$ in the updated approximation space from a linear elastic solution, or the linear ‘prediction’ approach.

Algorithm C.1 Nonlinear GFEM^{gl} solution algorithm based on an incremental approach.

for all $t \in t_0, \dots, t_N$ **do**

if updating local problem boundary conditions **then**

 Compute (4.44),

$$\Delta \mathbf{d}_{n,n+1}^{\mathbf{u},\text{lin}} \leftarrow \left(\mathbf{K}_{\text{elas},n}^{\mathbf{u}} \right)^{-1} \left(\mathbf{f}_{\text{ext},n,n+1}^{\mathbf{u}} - \mathbf{f}_{\text{int},n,n+1}^{\mathbf{u}} \right);$$

$$\mathbf{u}_{n,n+1}^{\text{hp},\text{lin}} = \sum_{j=0}^n \bar{\mathbf{N}}_j^{\mathbf{u}}(\mathbf{x}) \Delta \mathbf{d}_j^{\mathbf{u}} + \bar{\mathbf{N}}_n^{\mathbf{u}} \Delta \mathbf{d}_{n,n+1}^{\mathbf{u},\text{lin}}$$

end if

 Solve local problems, update global–local shape functions,

$$\phi_{n+1,\alpha}^{gl}(\mathbf{x}) = N_\alpha(\mathbf{x}) \Delta \mathbf{u}_L(\mathbf{x}, t_{n+1});$$

$i \leftarrow 0$;

repeat

 Assemble and solve (4.28),

$$\Delta \mathbf{d}^{\mathbf{u}(i+1)} \leftarrow \left(\mathbf{K}_{\text{tan},n+1}^{\mathbf{u}(i)} \right)^{-1} \left(\mathbf{f}_{\text{ext},n+1}^{\mathbf{u}} - \mathbf{f}_{\text{int},n+1}^{\mathbf{u}(i)} \right);$$

 Update the total solution according to (4.29),

$$\Delta \mathbf{d}_{n+1}^{\mathbf{u}(i+1)} \leftarrow \Delta \mathbf{d}_{n+1}^{\mathbf{u}(i)} + \Delta \mathbf{d}^{\mathbf{u}(i+1)};$$

$$\mathbf{u}_{n+1}^{\text{hp}(i+1)} = \sum_{j=0}^n \bar{\mathbf{N}}_j^{\mathbf{u}}(\mathbf{x}) \Delta \mathbf{d}_j^{\mathbf{u}} + \bar{\mathbf{N}}_{n+1}^{\mathbf{u}} \Delta \mathbf{d}_{n+1}^{\mathbf{u}(i+1)};$$

$i \leftarrow i + 1$;

until convergence

end for

Algorithm C.2 Nonlinear GFEM^{gl} solution algorithm based on linear recovery of the previous converged solution.

for all $t \in t_0, \dots, t_N$ **do**

if updating local problem boundary conditions **then**

 Compute (4.44),

$$\mathbf{d}_{n,n+1}^{\mathbf{u},\text{lin}} \leftarrow (\mathbf{K}_{\text{elas},n}^{\mathbf{u}})^{-1} (\mathbf{f}_{\text{ext},n,n+1}^{\mathbf{u}} - \mathbf{f}_{\text{int},n,n+1}^{\mathbf{u}});$$

$$\mathbf{u}_{n,n+1}^{\text{hp},\text{lin}} = \tilde{\mathbf{N}}_n^{\mathbf{u}} \mathbf{d}_{n,n+1}^{\mathbf{u},\text{lin}}$$

end if

 Solve local problems, update global–local shape functions,

$$\phi_{n+1,\alpha}^{\text{gl}}(\mathbf{x}) = N_\alpha(\mathbf{x}) \mathbf{u}_L(\mathbf{x}, t_{n+1});$$

$i \leftarrow 0$;

 Solve linear elastic problem at the previous (converged) step with current shape functions (4.35),

$$\mathbf{d}_{n+1,n}^{\mathbf{u}} \leftarrow (\mathbf{K}_{\text{elas},n+1}^{\mathbf{u}})^{-1} (\mathbf{f}_{\text{ext},n+1,n}^{\mathbf{u}} - \mathbf{f}_{\text{int},n+1,n}^{\mathbf{u}});$$

$$\mathbf{d}_{n+1}^{\mathbf{u}(0)} \leftarrow \mathbf{d}_{n+1,n}^{\mathbf{u}};$$

repeat

 Assemble and solve (4.28),

$$\Delta \mathbf{d}_{n+1}^{\mathbf{u}(i+1)} \leftarrow (\mathbf{K}_{\text{tan},n+1}^{\mathbf{u}(i)})^{-1} (\mathbf{f}_{\text{ext},n+1}^{\mathbf{u}} - \mathbf{f}_{\text{int},n+1}^{\mathbf{u}(i)});$$

 Update the total solution (4.37),

$$\mathbf{d}_{n+1}^{\mathbf{u}(i+1)} \leftarrow \mathbf{d}_{n+1}^{\mathbf{u}(i)} + \Delta \mathbf{d}_{n+1}^{\mathbf{u}(i+1)};$$

$$\mathbf{u}_{n+1}^{\text{hp}(i)} = \tilde{\mathbf{N}}_{n+1}^{\mathbf{u}} \mathbf{d}_{n+1}^{\mathbf{u}(i+1)};$$

$i \leftarrow i + 1$;

until convergence

end for

Algorithm C.3 Nonlinear GFEM^{gl} solution algorithm based on linear prediction of the total solution at the current time step.

for all $t \in t_0, \dots, t_N$ **do**

if updating local problem boundary conditions **then**

 Compute (4.44),

$$\mathbf{d}_{n,n+1}^{\mathbf{u},\text{lin}} \leftarrow (\mathbf{K}_{\text{elas},n}^{\mathbf{u}})^{-1} (\mathbf{f}_{\text{ext},n,n+1}^{\mathbf{u}} - \mathbf{f}_{\text{int},n,n+1}^{\mathbf{u}});$$

$$\mathbf{u}_{n,n+1}^{hp,\text{lin}} = \tilde{\mathbf{N}}_n^{\mathbf{u}} \mathbf{d}_{n,n+1}^{\mathbf{u},\text{lin}}$$

end if

 Solve local problems, update global–local shape functions,

$$\phi_{n+1,\alpha}^{gl}(\mathbf{x}) = N_\alpha(\mathbf{x}) \mathbf{u}_L(\mathbf{x}, t_{n+1});$$

$i \leftarrow 1$;

 Solve linear elastic problem for the total solution at the current step (4.39),

$$\mathbf{d}_{n+1}^{\mathbf{u}(1)} = (\mathbf{K}_{\text{elas},n+1}^{\mathbf{u}})^{-1} (\mathbf{f}_{\text{ext},n+1}^{\mathbf{u}} - \mathbf{f}_{\text{int},n+1}^{\mathbf{u}(0)});$$

repeat

 Assemble and solve (4.28),

$$\Delta \mathbf{d}_{n+1}^{\mathbf{u}(i+1)} \leftarrow (\mathbf{K}_{\text{tan},n+1}^{\mathbf{u}(i)})^{-1} (\mathbf{f}_{\text{ext},n+1}^{\mathbf{u}} - \mathbf{f}_{\text{int},n+1}^{\mathbf{u}(i)});$$

 Update the total solution (4.37),

$$\mathbf{d}_{n+1}^{\mathbf{u}(i+1)} \leftarrow \mathbf{d}_{n+1}^{\mathbf{u}(i)} + \Delta \mathbf{d}_{n+1}^{\mathbf{u}(i+1)};$$

$$\mathbf{u}_{n+1}^{hp(i)} = \tilde{\mathbf{N}}_{n+1}^{\mathbf{u}} \mathbf{d}_{n+1}^{\mathbf{u}(i+1)};$$

$i \leftarrow i + 1$;

until convergence

end for

References

- [1] A.M. Aragon, C.A. Duarte, and P.H. Geubelle. Generalized finite element enrichment functions for discontinuous gradient fields. *International Journal for Numerical Methods in Engineering*, 82(2):242–268, 2010. doi: 10.1002/nme.2772.
- [2] I. Babuška and J.M. Melenk. The partition of unity method. *International Journal for Numerical Methods in Engineering*, 40:727–758, 1997.
- [3] I. Babuška and T. Strouboulis. *The Finite Element Method and its Reliability*. Numerical Mathematics and Scientific Computation. Oxford Science Publications, New York, 2001.
- [4] I. Babuška, G. Caloz, and J.E. Osborn. Special finite element methods for a class of second order elliptic problems with rough coefficients. *SIAM Journal on Numerical Analysis*, 31(4):945–981, 1994.
- [5] Ivo Babuška and Robert Lipton. L^2 -global to local projection: an approach to multiscale analysis. *Mathematical Models and Methods in Applied Sciences*, 21(11):2211–2226, 2011. ISSN 0218-2025. doi: 10.1142/S0218202511005714.
- [6] Randolph E. Bank, Todd F. Dupont, and Harry Yserentant. The Hierarchical Basis Multigrid Method. *Numerische Mathematik*, 52(4):427–458, 1988. ISSN 0029-599X. doi: 10.1007/BF01462238.
- [7] T. Belytschko and T. Black. Elastic crack growth in finite elements with minimal remeshing. *International Journal for Numerical Methods in Engineering*, 45:601–620, 1999.
- [8] T. Belytschko, S. Loehnert, and J.-H. Song. Multiscale aggregating discontinuities: A method for circumventing loss of material stability. *International Journal for Numerical Methods in Engineering*, 73(6):869–894, 2008. doi: 10.1002/nme.2156.
- [9] T. Belytschko, R. Gracie, and G. Ventura. A review of extended/generalized finite element methods for material modeling. *Modelling and Simulations in Materials Science and Engineering*, 17:043001, 2009. doi: 10.1088/0965-0393/17/4/043001.
- [10] Ted Belytschko, Stefan Loehnert, and Jeong-Hoon Song. Multiscale aggregating discontinuities: A method for circumventing loss of material stability. *International Journal for Numerical Methods in Engineering*, 73(6):869–894, 2008. ISSN 00295981. doi: 10.1002/nme.2156.
- [11] Xiao-Chuan Cai and David E. Keyes. Nonlinearly Preconditioned Inexact Newton Algorithms. *SIAM Journal on Scientific Computing*, 24(1):183–200, 2002. ISSN 1064-8275. doi: 10.1137/S106482750037620X.
- [12] C. Carmignani, R. Mares, and G. Toselli. Transient finite element analysis of deep penetration laser welding process in a singlepass butt-welded thick steel plate. *Computer Methods in Applied Mechanics and Engineering*, 179, 1999.
- [13] Cris Cecka, Adrian J. Lew, and E. Darve. Assembly of finite element methods on graphics processors. *International Journal for Numerical Methods in Engineering*, 85(5):640–669, 2011. ISSN 00295981. doi: 10.1002/nme.2989.

- [14] M. Cloirec, N. Moës, G. Marckmann, and P. Cartraud. Two-scale analysis of cracks using the extended finite element method. In D.R.J. Owen, E. Onate, and B. Suarez, editors, *VIII International Conference on Computational Plasticity Fundamentals and Application –COMPLAS 2005*, pages 483–485, Barcelona, Spain, 2005. CIMNE.
- [15] Philippe Cresta, Olivier Allix, Christian Rey, and Stéphane Guinard. Nonlinear localization strategies for domain decomposition methods: Application to post-buckling analyses. *Computer Methods in Applied Mechanics and Engineering*, 196(8):1436–1446, 2007. ISSN 00457825. doi: 10.1016/j.cma.2006.03.013.
- [16] D. D’Ambrosio. Numerical prediction of laminar shock/shock interactions in hypersonic flow. *Journal of Spacecraft and Rockets*, 40(2):153–161, 2003.
- [17] René de Borst. Challenges in computational materials science: Multiple scales, multi-physics and evolving discontinuities. *Computational Materials Science*, 43(1):1–15, 2008. ISSN 09270256. doi: 10.1016/j.commatsci.2007.07.022.
- [18] Hashmi Ben Dhia and Guillaume Rateau. The Arlequin method as a flexible engineering design tool. *International Journal for Numerical Methods in Engineering*, 62(11):1442–1462, 2005. ISSN 0029-5981. doi: 10.1002/nme.1229.
- [19] A.Th. Diamantoudis and G.N. Labeas. Stress intensity factors of semi-elliptical surface cracks in pressure vessels by global-local finite element methodology. *Engineering Fracture Mechanics*, 72:1299–1312, 2005.
- [20] Q. Duan, J.H. Song, T. Menouillard, and T. Belytschko. Element-local level set method for three-dimensional dynamic crack growth. *International Journal for Numerical Methods in Engineering*, 80(12):15201543, 2009. doi: 10.1002/nme.2665.
- [21] Y. G. Duan, Y. Vincent, F. Boitout, J. B. Leblond, and J. M. Bergheau. Prediction of welding residual distortions of large structures using a local/global approach. *Journal of Mechanical Science and Technology*, 21(10):1700–1706, 2007. ISSN 1738-494X. doi: 10.1007/BF03177397.
- [22] C.A. Duarte and I. Babuška. Mesh-independent p -orthotropic enrichment using the generalized finite element method. *International Journal for Numerical Methods in Engineering*, 55(12):1477–1492, 2002. doi: 10.1002/nme.557.
- [23] C.A. Duarte and D.-J. Kim. Analysis and applications of a generalized finite element method with global–local enrichment functions. *Computer Methods in Applied Mechanics and Engineering*, 197(6-8):487–504, 2008. doi: 10.1016/j.cma.2007.08.017.
- [24] C.A. Duarte, I. Babuška, and J.T. Oden. Generalized finite element methods for three dimensional structural mechanics problems. *Computers and Structures*, 77:215–232, 2000. doi: 10.1016/S0045-7949(99)00211-4.
- [25] C.A. Duarte, O.N. Hamzeh, T.J. Liszka, and W.W. Tworzydło. A generalized finite element method for the simulation of three-dimensional dynamic crack propagation. *Computer Methods in Applied Mechanics and Engineering*, 190(15–17):2227–2262, 2001. doi: 10.1016/S0045-7825(00)00233-4.
- [26] C.A. Duarte, D.-J. Kim, and I. Babuška. A Global-Local Approach for the Construction of Enrichment Functions for the Generalized FEM and Its Application to Three-Dimensional Cracks. In V.M.A. Leitão, C.J.S. Alves, and C.A. Duarte, editors, *Advances in Meshfree Techniques*, volume 5 of *Computational Methods in Applied Sciences*, pages 1–26. Springer, Dordrecht, The Netherlands, 2007. ISBN 978-1-4020-6094-6.
- [27] C.A.M. Duarte and J.T. Oden. hp clouds – A meshless method to solve boundary-value problems. Technical Report 95-05, TICAM, The University of Texas at Austin, May 1995.
- [28] C.A.M. Duarte and J.T. Oden. hp clouds – An hp meshless method. *Numerical Methods for Partial Differential Equations*, 12:673–705, 1996. doi: 10.1002/(SICI)1098-2426(199611)12:6<673::AID-NUM3>3.0.CO;2-P.
- [29] C.A.M. Duarte and J.T. Oden. An hp adaptive method using clouds. *Computer Methods in Applied Mechanics and Engineering*, 139:237–262, 1996. doi: 10.1016/S0045-7825(96)01085-7.

- [30] Marc Duflo. The extended finite element method in thermoelastic fracture mechanics. *International Journal for Numerical Methods in Engineering*, 74(5):827–847, 2008. ISSN 00295981. doi: 10.1002/nme.2197.
- [31] L.J. Durlofsky, Y. Efendiev, and V. Ginting. An adaptive local global multiscale finite volume element method for two-phase flow simulations. *Advances in Water Resources*, 30(3):576–588, 2007. ISSN 03091708. doi: 10.1016/j.advwatres.2006.04.002.
- [32] A. Düster and E. Rank. A p -version finite element approach for two- and three-dimensional problems of the J_2 flow theory with non-linear isotropic hardening. *International Journal for Numerical Methods in Engineering*, 53(1):49–63, 2002. ISSN 00295981. doi: 10.1002/nme.391.
- [33] A. Düster, A. Niggel, and E. Rank. Applying the hp - d version of the FEM to locally enhance dimensionally reduced models. *Computer Methods in Applied Mechanics and Engineering*, 196(37-40):3524–3533, 2007. ISSN 00457825. doi: 10.1016/j.cma.2006.10.018.
- [34] Alexander Düster. *High order finite elements for three-dimensional, thin-walled nonlinear continua*. PhD thesis, Technische Universität München, 2002.
- [35] Y. Efendiev and T. Hou. Multiscale finite element methods for porous media flows and their applications. *Applied Numerical Mathematics*, 57(5-7):577–596, 2007. ISSN 01689274. doi: 10.1016/j.apnum.2006.07.009.
- [36] Charbel Farhat, Michel Lesoinne, Patrick LeTallec, Kendall Pierson, and Daniel Rixen. FETI-DP: a dual-primal unified FETI method—part I: A faster alternative to the two-level FETI method. *International Journal for Numerical Methods in Engineering*, 50(7):1523–1544, 2001. ISSN 0029-5981. doi: 10.1002/nme.76.
- [37] F. Feyel and J. Chaboche. FE^2 multiscale approach for modelling the elastoviscoplastic behaviour of long fibre SiC/Ti composite materials. *Computer Methods in Applied Mechanics and Engineering*, 183(3):309–330, 2000.
- [38] Frédéric Feyel. A multilevel finite element method (FE^2) to describe the response of highly non-linear structures using generalized continua. *Computer Methods in Applied Mechanics and Engineering*, 192(28-30):3233–3244, 2003. ISSN 00457825. doi: 10.1016/S0045-7825(03)00348-7.
- [39] J Fish. The s -version of the finite element method. *Computers & Structures*, 43(3):539–547, 1992.
- [40] J. Fish and Z. Yuan. Multiscale enrichment based on partition of unity. *International Journal for Numerical Methods in Engineering*, 62:1341–1359, 2005.
- [41] P. P. Friedmann, K. G. Powell, J. J. McNamara, B. J. Thuruthimattam, and R. Bartels. Hypersonic aerothermoelastic studies for reusable launch vehicles, 2004. AIAA 2004-1590.
- [42] P. P. Friedmann, K. G. Powell, J. J. McNamara, B. J. Thuruthimattam, and R. Bartels. Three-dimensional aeroelastic and aerothermoelastic behavior in hypersonic flow, 2005. AIAA 2005-2175.
- [43] M.G.D. Geers, V.G. Kouznetsova, and W.A.M. Brekelmans. Multi-scale computational homogenization: Trends and challenges. *Journal of Computational and Applied Mathematics*, 234(7):2175–2182, 2010. ISSN 03770427. doi: 10.1016/j.cam.2009.08.077.
- [44] Lionel Gendre, Olivier Allix, Pierre Gosselet, and François Comte. Non-intrusive and exact global/local techniques for structural problems with local plasticity. *Computational Mechanics*, 44(2):233–245, 2009. ISSN 0178-7675. doi: 10.1007/s00466-009-0372-9.
- [45] S. Ghosh and S. Moorthy. Three dimensional Voronoi cell finite element model for microstructures with ellipsoidal heterogeneities. *Computational Mechanics*, 34:510–531, 2004.
- [46] S. Ghosh, K. Lee, and S. Moorthy. Multiple scale analysis of heterogeneous elastic structures using homogenization theory and Voronoi cell finite element method. *International Journal of Solids and Structures*, 32(1): 27–62, 1995.

- [47] S. Ghosh, J. Bai, and P. Raghavan. Concurrent multi-level model for damage evolution in microstructurally debonding composites. *Mechanics of Materials*, 39(3):241–266, 2007.
- [48] Somnath Ghosh, Kyunghoon Lee, and Prasanna Raghavan. A multi-level computational model for multi-scale damage analysis in composite and porous materials. *International Journal of Solids and Structures*, 38(14): 2335–2385, 2001. ISSN 00207683. doi: 10.1016/S0020-7683(00)00167-0.
- [49] P.-A. Guidault, O. Allix, L. Champaney, and C. Cornuault. A multiscale extended finite element method for crack propagation. *Computer Methods in Applied Mechanics and Engineering*, 197:381–399, 2008.
- [50] P. Gupta, J.P. Pereira, D.-J. Kim, C.A. Duarte, and T. Eason. Analysis of three-dimensional fracture mechanics problems: A non-intrusive approach using a generalized finite element method. *Engineering Fracture Mechanics*, 90:41–64, 2012. ISSN 0013-7944. doi: 10.1016/j.engfracmech.2012.04.014.
- [51] V. Gupta, D.-J. Kim, and C.A. Duarte. Analysis and improvements of global-local enrichments for the generalized finite element method. *Computer Methods in Applied Mechanics and Engineering*, 245–246:47–62, 2012. doi: 10.1016/j.cma.2012.06.021.
- [52] V. Gupta, D.-J. Kim, and C.A. Duarte. Extensions of the two-scale generalized finite element method to nonlinear fracture problems. *International Journal for Multiscale Computational Engineering*, 11(6):581–596, 2013. doi: 10.1615/IntJMultCompEng.2013005685.
- [53] R. R. Heldenfels. Structural Prospects for Hypersonic Air Vehicles. *Aircraft Engineering and Aerospace Technology*, 38(11):18–20, 1966. ISSN 0002-2667. doi: 10.1108/eb034205.
- [54] Thomas Y. Hou and Xiao-Hui Wu. A multiscale finite element method for elliptic problems in composite materials and porous media. *Journal of Computational Physics*, 134(1):169–189, 1997. ISSN 00219991. doi: 10.1006/jcph.1997.5682.
- [55] Ning Hu, Xian-zhong Guo, and I. Norman Katz. Multi- p preconditioners. *SIAM Journal on Scientific Computing*, 18(6):1676–1697, 1997. ISSN 1064-8275. doi: 10.1137/S1064827595279368.
- [56] Thomas J.R. Hughes, Gonzalo R. Feijóo, Luca Mazzei, and Jean-Baptiste Quinicy. The variational multiscale method—a paradigm for computational mechanics. *Computer Methods in Applied Mechanics and Engineering*, 7825(98), 1998.
- [57] P. Jarzebski, K. Wisniewski, and R. L. Taylor. On parallelization of the loop over elements in FEAP. *Computational Mechanics*, 56(1):77–86, 2015. ISSN 0178-7675. doi: 10.1007/s00466-015-1156-z.
- [58] Meysam Joulaian and Alexander Düster. Local enrichment of the finite cell method for problems with material interfaces. *Computational Mechanics*, 52(4):741–762, 2013. ISSN 01787675. doi: 10.1007/s00466-013-0853-8.
- [59] A.R. Khoei, S. Moallemi, and E. Haghghat. Thermo-hydro-mechanical modeling of impermeable discontinuity in saturated porous media with X-FEM technique. *Engineering Fracture Mechanics*, 96:701–723, December 2012. ISSN 00137944. doi: 10.1016/j.engfracmech.2012.10.003.
- [60] Rooh. A. Khurram and Arif Masud. A multiscale/stabilized formulation of the incompressible Navier–Stokes equations for moving boundary flows and fluid–structure interaction. *Computational Mechanics*, 38(4-5):403–416, 2006. ISSN 0178-7675. doi: 10.1007/s00466-006-0059-4.
- [61] D.-J. Kim, C.A. Duarte, and J.P. Pereira. Analysis of interacting cracks using the generalized finite element method with global-local enrichment functions. *Journal of Applied Mechanics*, 75(5):051107, 2008. doi: 10.1115/1.2936240.
- [62] D.-J. Kim, J.P. Pereira, and C.A. Duarte. Analysis of three-dimensional fracture mechanics problems: A two-scale approach using coarse generalized FEM meshes. *International Journal for Numerical Methods in Engineering*, 81(3):335–365, 2010. doi: 10.1002/nme.2690.

- [63] D.-J. Kim, C.A. Duarte, and N.A. Sobh. Parallel simulations of three-dimensional cracks using the generalized finite element method. *Computational Mechanics*, 47(3):265–282, 2011. doi: 10.1007/s00466-010-0546-5.
- [64] D.-J. Kim, C. A. Duarte, and S. P. Proenca. A generalized finite element method with global-local enrichment functions for confined plasticity problems. *Computational Mechanics*, 50(5):563–578, 2012. ISSN 0178-7675. doi: 10.1007/s00466-012-0689-7.
- [65] V. Kouznetsova, M. G. D. Geers, and W. A. M. Brekelmans. Multi-scale constitutive modelling of heterogeneous materials with a gradient-enhanced computational homogenization scheme. *International Journal for Numerical Methods in Engineering*, 54(8):1235–1260, 2002. ISSN 0029-5981. doi: 10.1002/nme.541.
- [66] B. P. Lamichhane and B. I. Wohlmuth. Mortar finite elements for interface problems. *Computing*, 72(3-4): 333–348, 2004. ISSN 0010-485X. doi: 10.1007/s00607-003-0062-y.
- [67] Nam-Sua Lee and Klaus-Jürgen Bathe. Error indicators and adaptive remeshing in large deformation finite element analysis. *Finite Elements in Analysis and Design*, 16(2):99–139, 1994. ISSN 0168874X. doi: 10.1016/0168-874X(94)90044-2.
- [68] H. Li and C.A. Duarte. A multiscale generalized FEM for the simulation of spot welds in large structures. In *13th US National Congress on Computational Mechanics*, San Diego, CA, July 26-30 2015.
- [69] L.-E. Lindgren. Numerical modelling of welding. *Computer Methods in Applied Mechanics and Engineering*, 195(48-49):6710–6736, 2006. ISSN 00457825. doi: 10.1016/j.cma.2005.08.018.
- [70] Lars-Erik Lindgren and Lennart Karlsson. Deformations and stresses in welding of shell structures. *International Journal for Numerical Methods in Engineering*, 25(2):635–655, 1988. ISSN 0029-5981. doi: 10.1002/nme.1620250223.
- [71] J. T. Liu, S. T. Gu, E. Monteiro, and Q. C. He. A versatile interface model for thermal conduction phenomena and its numerical implementation by XFEM. *Computational Mechanics*, 53(4):825–843, 2013. ISSN 0178-7675. doi: 10.1007/s00466-013-0933-9.
- [72] W.K. Liu and C. McVeigh. Predictive multiscale theory for design of heterogeneous materials. *Computational Mechanics*, 42(2):147–170, 2008. doi: 10.1007/s00466-007-0176-8.
- [73] O. Lloberas-Valls, D.J. Rixen, A. Simone, and L.J. Sluys. Domain decomposition techniques for the efficient modeling of brittle heterogeneous materials. *Computer Methods in Applied Mechanics and Engineering*, 200(13-16):1577–1590, 2011. ISSN 00457825. doi: 10.1016/j.cma.2011.01.008.
- [74] S. Loehnert and T. Belytschko. A multiscale projection method for macro/microcrack simulations. *International Journal for Numerical Methods in Engineering*, 71(12):1466–1482, 2007.
- [75] Michael Macri and Suvranu De. An octree partition of unity method (OctPUM) with enrichments for multiscale modeling of heterogeneous media. *Computers & Structures*, 86(7-8):780–795, 2008. ISSN 00457949. doi: 10.1016/j.compstruc.2007.06.001.
- [76] Michael Macri and Andrew Littlefield. Enrichment based multiscale modeling for thermo-stress analysis of heterogeneous material. *International Journal for Numerical Methods in Engineering*, 93(11):1147–1169, 2013. ISSN 00295981. doi: 10.1002/nme.4420.
- [77] Karel Matouš, Mohan G. Kulkarni, and Philippe H. Geubelle. Multiscale cohesive failure modeling of heterogeneous adhesives. *Journal of the Mechanics and Physics of Solids*, 56(4):1511–1533, 2008. doi: 10.1016/j.jmps.2007.08.005.
- [78] C. McVeigh and W.K. Liu. Linking microstructure and properties through a predictive multiresolution continuum. *Computer Methods in Applied Mechanics and Engineering*, 197(41-42):3268–3290, 2008.
- [79] C. McVeigh, F. Vernerey, W.K. Liu, and L.C. Brinson. Multiresolution analysis for material design. *Computer Methods in Applied Mechanics and Engineering*, 195(37-40):5053–5076, 2006.

- [80] J.M. Melenk and I. Babuška. The partition of unity finite element method: Basic theory and applications. *Computer Methods in Applied Mechanics and Engineering*, 139:289–314, 1996.
- [81] W.F. Mitchell. The hp -multigrid method applied to hp -adaptive refinement of triangular grids. *Numerical Linear Algebra with Applications*, 17(1):211–228, 2010. doi: doi10.1002/nla.700.
- [82] N. Moës, J. Dolbow, and T. Belytschko. A finite element method for crack growth without remeshing. *International Journal for Numerical Methods in Engineering*, 46:131–150, 1999.
- [83] N. Moës, A. Gravouil, and T. Belytschko. Non-planar 3D crack growth by the extended finite element and level sets – Part I: Mechanical model. *International Journal for Numerical Methods in Engineering*, 53(11): 2549–2568, 2002.
- [84] N. Moës, M. Cloirec, P. Cartraud, and J.-F. Remacle. A computational approach to handle complex microstructure geometries. *Computer Methods in Applied Mechanics and Engineering*, 192:3163–3177, 2003.
- [85] J. Montalvo-Urquizo, Z. Akbay, and A. Schmidt. Adaptive finite element models applied to the laser welding problem. *Computational Materials Science*, 46(1):245–254, 2009. ISSN 09270256. doi: 10.1016/j.commatsci.2009.02.037.
- [86] G. A. Moraitis and G. N. Labeas. Residual stress and distortion calculation of laser beam welding for aluminum lap joints. *Journal of Materials Processing Technology*, 198(1-3):260–269, 2008. ISSN 09240136. doi: 10.1016/j.jmatprotec.2007.07.013.
- [87] J. R. Moselle, A. R. Wieting, M.S. Holden, and C. Glass. Studies of aerothermal loads generated in regions of shock/shock interaction in hypersonic flow, 1988. AIAA-88-0477.
- [88] A.K. Noor. Global-local methodologies and their applications to nonlinear analysis. *Finite Elements in Analysis and Design*, 2:333–346, 1986.
- [89] J.T. Oden, C.A. Duarte, and O.C. Zienkiewicz. A new cloud-based hp finite element method. *Computer Methods in Applied Mechanics and Engineering*, 153:117–126, 1998. doi: 10.1016/S0045-7825(97)00039-X.
- [90] P. O’Hara, C.A. Duarte, and T. Eason. Generalized finite element analysis of three-dimensional heat transfer problems exhibiting sharp thermal gradients. *Computer Methods in Applied Mechanics and Engineering*, 198 (21–26):1857–1871, 2009. doi: 10.1016/j.cma.2008.12.024.
- [91] P. O’Hara, C.A. Duarte, and T. Eason. Transient analysis of sharp thermal gradients using coarse finite element meshes. *Computer Methods in Applied Mechanics and Engineering*, 200(5–8):812–829, 2011. doi: 10.1016/j.cma.2010.10.005.
- [92] P. O’Hara, C.A. Duarte, T. Eason, and J. Garzon. Efficient analysis of transient heat transfer problems exhibiting sharp thermal gradients. *Computational Mechanics*, 51(5):743–764, 2013. doi: 10.1007/s00466-012-0750-6.
- [93] Patrick James O’Hara. *A Multi-Scale Generalized Finite Element Method for Sharp, Transient Thermal Gradients*. PhD thesis, University of Illinois at Urbana-Champaign, 2010.
- [94] OpenMP. Open multi-processing application programming interface. <http://openmp.org/wp/>.
- [95] M. Ortiz and J.J. Quigley. Adaptive mesh refinement in strain localization problems. *Computer Methods in Applied Mechanics and Engineering*, 90(1-3):781–804, 1991. ISSN 00457825. doi: 10.1016/0045-7825(91) 90184-8.
- [96] C. Oskay and J. Fish. On calibration and validation of eigendeformation-based multiscale models for failure analysis of heterogeneous systems. *Computational Mechanics*, 42(2):181–195, 2008.
- [97] Caglar Oskay. Variational multiscale enrichment for modeling coupled mechano-diffusion problems. *International Journal for Numerical Methods in Engineering*, 89(6):686–705, 2012. ISSN 00295981. doi: 10.1002/nme.3258.

- [98] Caglar Oskay. Variational multiscale enrichment method with mixed boundary conditions for modeling diffusion and deformation problems. *Computer Methods in Applied Mechanics and Engineering*, 264:178–190, September 2013. ISSN 00457825. doi: 10.1016/j.cma.2013.05.022.
- [99] I. Özdemir, W. A. M. Brekelmans, and M. G. D. Geers. Computational homogenization for heat conduction in heterogeneous solids. *International Journal for Numerical Methods in Engineering*, 73(2):185–204, 2008. ISSN 00295981. doi: 10.1002/nme.2068.
- [100] I. Özdemir, W.A.M. Brekelmans, and M.G.D. Geers. FE² computational homogenization for the thermo-mechanical analysis of heterogeneous solids. *Computer Methods in Applied Mechanics and Engineering*, 198(3-4):602–613, 2008. ISSN 00457825. doi: 10.1016/j.cma.2008.09.008.
- [101] A. K. Pandey, P. Dechaumphai, and E. A. Thornton. Finite element thermo-viscoplastic analysis of aerospace structures. Technical report, NASA Langley Research Center, Hampton, VA, USA, 1990.
- [102] Ajay K. Pandey. Thermoviscoplastic response of engine-cowl leading edge subjected to an oscillating shock-shock interaction. *Journal of Spacecraft and Rockets*, 30(6):771–773, November 1993. ISSN 0022-4650. doi: 10.2514/3.26387.
- [103] Julien Pebre, Christian Rey, and Pierre Gosselet. A Nonlinear Dual-Domain Decomposition Method: Application to Structural Problems with Damage. *International Journal for Multiscale Computational Engineering*, 6(3):251–262, 2008. ISSN 1543-1649. doi: 10.1615/IntJMultCompEng.v6.i3.50.
- [104] D. Perić, Ch. Hochard, M. Dutko, and D.R.J. Owen. Transfer operators for evolving meshes in small strain elasto-plasticity. *Computer Methods in Applied Mechanics and Engineering*, 137(3-4):331–344, 1996. ISSN 00457825. doi: 10.1016/S0045-7825(96)01070-5.
- [105] J. Plews, C.A. Duarte, and T. Eason. An improved non-intrusive global-local approach for sharp thermal gradients in a standard FEA platform. *International Journal for Numerical Methods in Engineering*, 91(4):426–449, 2012. doi: 10.1002/nme.4279.
- [106] J.A. Plews and C.A. Duarte. Bridging multiple structural scales with a generalized finite element method. *International Journal for Numerical Methods in Engineering*, 102(3–4):180–201, 2015. doi: 10.1002/nme.4703.
- [107] J.A. Plews and C.A. Duarte. Generalized finite element approaches for analysis of localized thermo-structural effects. *International Journal for Numerical Methods in Engineering*, 2015. doi: 10.1002/nme.4942.
- [108] W. Rachowicz, J. T. Oden, and L. Demkowicz. Toward a universal h - p adaptive finite element strategy, Part 3. Design of h - p meshes. *Computer Methods in Applied Mechanics and Engineering*, 77:181–212, 1989.
- [109] F.K.F. Radtke, A. Simone, and L.J. Sluys. A computational model for failure analysis of fibre reinforced concrete with discrete treatment of fibres. *Engineering Fracture Mechanics*, 77(4):597–620, 2010. doi: 10.1016/j.engfracmech.2009.11.014.
- [110] F.K.F. Radtke, A. Simone, and L.J. Sluys. A partition of unity finite element method for obtaining elastic properties of continua with embedded thin fibres. *International Journal for Numerical Methods in Engineering*, 84(6):708–732, 2010. doi: 10.1002/nme.2916.
- [111] P. Raghavan and S. Ghosh. Concurrent multi-scale analysis of elastic composites by a multi-level computational model. *Computer Methods in Applied Mechanics and Engineering*, 193(6-8):497–538, 2004. ISSN 00457825. doi: 10.1016/j.cma.2003.10.007.
- [112] E. Rank and R. Krause. A Multiscale Finite-Element Method. *Computers & Structures*, 64(1-4):139–144, 1997. ISSN 1557-170X.
- [113] J. Rannou, A. Gravouil, and M.C Baietto-Dubourg. A local multigrid X-FEM strategy for 3-D crack propagation. *International Journal for Numerical Methods in Engineering*, 77:581–600, 2009. doi: 10.1002/nme.2427.

- [114] R. Rolfes, J. Noack, and M. Taeschner. High performance 3D-analysis of thermo-mechanically loaded composite structures. *Composite Structures*, 46(4):367–379, 1999. ISSN 02638223. doi: 10.1016/S0263-8223(99)00101-4.
- [115] H Runnemalm and S Hyun. Three-dimensional welding analysis using an adaptive mesh scheme. *Computer Methods in Applied Mechanics and Engineering*, 189(2):515–523, 2000. ISSN 00457825. doi: 10.1016/S0045-7825(99)00304-7.
- [116] Marc Alexander Schweitzer and Sa Wu. Numerical Integration of On-the-Fly-Computed Enrichment Functions in the PUM. In M. Griebel and M. A. Schweitzer, editors, *Lecture Notes in Computational Science and Engineering: Meshfree Methods for Partial Differential Equations VII*, volume 100, pages 247–267. Springer International Publishing, Switzerland, 2015. doi: 10.1007/978-3-319-06898-5_13.
- [117] A M Sharan, D Dhar, and R Seshadri. Heat transfer/thermal stress analysis of semiconductors under transient conditions. *Modelling and Simulation in Materials Science and Engineering*, 5(3):245–258, 1997. ISSN 0965-0393. doi: 10.1088/0965-0393/5/3/004.
- [118] J.C. Simo and T.J.R. Hughes. *Computational Inelasticity*. Springer, 1998. ISBN: 0-387-97520-9.
- [119] A. Simone, C.A. Duarte, and E. Van der Giessen. A generalized finite element method for polycrystals with discontinuous grain boundaries. *International Journal for Numerical Methods in Engineering*, 67(8):1122–1145, 2006. doi: 10.1002/nme.1658.
- [120] Jeong-Hoon Song and Ted Belytschko. Multiscale aggregating discontinuities method for micro–macro failure of composites. *Composites Part B: Engineering*, 40(6):417–426, 2009. doi: 10.1016/j.compositesb.2009.01.007.
- [121] Jeong-Hoon Song, Hongwu Wang, and Ted Belytschko. A comparative study on finite element methods for dynamic fracture. *Computational Mechanics*, 42(2):239–250, 2008. ISSN 0178-7675. doi: 10.1007/s00466-007-0210-x.
- [122] B. Souloumiac, F. Boitout, and J.M. Bergheau. A New Local-Global Approach for the Modelling of Welded Steel Components Distortions. In *Mathematical Modelling of Weld Phenomena 6*, Graz, Austria, 2002. ISBN 978-1-902653-56-3.
- [123] T. Strouboulis, K. Copps, and I. Babuška. The generalized finite element method. *Computer Methods in Applied Mechanics and Engineering*, 190:4081–4193, 2001.
- [124] N. Sukumar, D. Chopp, N. Moës, and T. Belytschko. Modeling holes and inclusions by level sets in the extended finite element method. *Computer Methods in Applied Mechanics and Engineering*, 190:6183–6200, 2001.
- [125] S. Suresh, A. E. Giannakopoulos, and M. Olsson. Elastoplastic analysis of thermal cycling: Layered materials with sharp interfaces. *Journal of the Mechanics and Physics of Solids*, 42(6):979–1018, 1994. ISSN 00225096. doi: 10.1016/0022-5096(94)90081-7.
- [126] B. Szabo and I. Babuška. *Finite Element Analysis*. John Wiley and Sons, New York, 1991.
- [127] E. A. Thornton. Thermal structures – four decades of progress. *Journal of Aircraft*, 29(3):485–498, 1992. ISSN 0021-8669.
- [128] Earl A. Thornton and J. D. Kolenski. Viscoplastic response of structures for intense local heating. *Journal of Aerospace Engineering*, 7(1):50–71, 1994.
- [129] Earl A. Thornton, J. Tinsley Oden, W. Woytek Tworzydło, and Sung-Kie Youn. Thermoviscoplastic analysis of hypersonic structures subjected to severe aerodynamic heating. *Journal of Aircraft*, 27(9):826–835, September 1990. ISSN 0021-8669. doi: 10.2514/3.45943.
- [130] S.A. Tsirkas, P. Papanikos, and Th. Kermanidis. Numerical simulation of the laser welding process in butt-joint specimens. *Journal of Materials Processing Technology*, 134(1):59–69, 2003. ISSN 09240136. doi: 10.1016/S0924-0136(02)00921-4.

- [131] T. L. Turner and R. L. Ash. Analysis of the thermal environment and thermal response associated with thermal-acoustic testing, 1990. AIAA-90-0975-CP.
- [132] Da Yu Tzou. Fracture path emanating from a rapidly moving heat source—the effect of thermal shock waves under high rate response. *Engineering Fracture Mechanics*, 41(1):111–125, 1992. ISSN 00137944. doi: 10.1016/0013-7944(92)90100-S.
- [133] Jörg F. Unger. An FE²-X¹ approach for multiscale localization phenomena. *Journal of the Mechanics and Physics of Solids*, 61(4):928–948, 2013. ISSN 00225096. doi: 10.1016/j.jmps.2012.12.010.
- [134] T.J. Vaughan and C.T. McCarthy. Micromechanical modelling of the transverse damage behaviour in fibre reinforced composites. *Composites Science and Technology*, 71(3):388–396, 2011. doi: 10.1016/j.compscitech.2010.12.006.
- [135] E. Voce. A practical strain-hardening function. *Metallurgica*, 51:219–226, 1955.
- [136] J.D. Whitcomb. Iterative global/local finite element analysis. *Computers and Structures*, 40:1027–1031, 1991.
- [137] A. R. Wieting. Experimental study of shock wave interference heating on a cylindrical leading edge, 1987. NASA Technical Memorandum 100484.
- [138] Allan R. Wieting, Pramote Dechaumphai, Kim S. Bey, Earl A. Thornton, and Ken Morgan. Application of integrated fluid-thermal-structural analysis methods. *Thin-Walled Structures*, 11(1-2):1–23, January 1991. ISSN 02638231. doi: 10.1016/0263-8231(91)90008-7.
- [139] Jin Xu, C.K. Lee, and K.H. Tan. An XFEM frame for plate elements in yield line analyses. *International Journal for Numerical Methods in Engineering*, 96(3):150–175, 2013. ISSN 00295981. doi: 10.1002/nme.4535.
- [140] D. S. Yang, H. W. Zhang, S. Zhang, and M. K. Lu. A multiscale strategy for thermo-elastic plastic stress analysis of heterogeneous multiphase materials. *Acta Mechanica*, 226:1549–1569, 2015. ISSN 0001-5970. doi: 10.1007/s00707-014-1269-z.
- [141] Zheng Yuan and Jacob Fish. Multiple scale eigendeformation-based reduced order homogenization. *Computer Methods in Applied Mechanics and Engineering*, 198(2126):2016 – 2038, 2009. doi: 10.1016/j.cma.2008.12.038.
- [142] Arash Zamani, Robert Gracie, and M. Reza Eslami. Higher order tip enrichment of eXtended Finite Element Method in thermoelasticity. *Computational Mechanics*, 46(6):851–866, 2010. ISSN 0178-7675. doi: 10.1007/s00466-010-0520-2.
- [143] H. W. Zhang, Y. Liu, S. Zhang, J. Tao, J. K. Wu, and B. S. Chen. Extended multiscale finite element method: its basis and applications for mechanical analysis of heterogeneous materials. *Computational Mechanics*, 53(4):659–685, 2013. ISSN 0178-7675. doi: 10.1007/s00466-013-0924-x.